AlGaN quantum dots grown by molecular beam epitaxy for ultraviolet light emitting diodes

Samuel Matta

THÈSE POUR OBTENIR LE GRADE DE DOCTEUR DE L'UNIVERSITÉ DE MONTPELLIER

En physique

École doctorale I2S

Unité de recherche L2C-UMR 5221

AlGaN quantum dots grown by molecular beam epitaxy for ultraviolet light emitting diodes

Présentée par Samuel MATTA

Le 02 mai 2018

Sous la direction de Bernard GIL et Julien BRAULT

Devant le jury composé de

Lucyna FIRLEJ, Professeur, L2C Université de Montpellier, France	Présidente
Maria TCHERNYCHEVA, Directeur de Recherche, CNRS - Université Paris sud, France	Rapporteur
Sergey IVANOV, Professeur, Ioffe Physical-Technical Institute of RAS, St. Petersburg, Russia	Rapporteur
Guillaume CASSABOIS, Professeur, L2C - Université de Montpellier, France	Examinateur
Guy FEUILLET, Directeur de Recherche, CEA – LETI, Grenoble, France	Examinateur
Bernard GIL, Directeur de Recherche, L2C - Université de Montpellier, France	Directeur de Thèse
Julien BRAULT, Chargé de Recherche, CNRS - CRHEA, Valbonne, France	Encadrant de Thèse

‘‘In the middle of difficulty lies opportunity’’

Albert Einstein

To my parents and my brother……

Acknowledgments

Without any doubt the last three years have been incredibly a rewarding experience in which I learned a lot and met amazing people, not only on the scientific level but also on the personal one. This thesis would have never been possible without the support of a long list of people. I would like to express my sincere gratitude to all of them.

First and foremost, I wish to thank my advisors, **Bernard GIL** and **Julien BRAULT** for their availability, their help and their patience throughout the three years. **Bernard GIL**, you were always available to answer my questions although all your different responsibilities and busy schedules. I am really proud to do my PhD under your guidance and to learn from your huge research expertise. I would like to thank you for your trust, the freedom you gave me to move on and for encouraging my research along the three years. **Julien BRAULT**, I have been extremely lucky to have a supervisor who cared so much about my work, and who responded to my questions and queries so promptly. I would also like to thank you for teaching me how to approach science from a better perspective. I couldn't have done this without your support and patience.

I would also like to thank my committee members, **Lucyna FIRLEJ**, **Maria TCHERNYCHEVA**, **Sergey IVANOV, Guillaume CASSABOIS and Guy FEUILLET** for serving as my committee members. I also want to thank you for letting my defense be an enjoyable moment, for your brilliant comments and for your amazing report, thanks to you.

I want to express my gratitude to **Mathieu LEROUX**, I cannot thank you enough for always taking the time to explain things and for your constructive criticism, and thanks to this I had a better in-depth understanding of my results. I also thank you for always pushing me to look on the small hidden details in order to have a better understanding of the results. **Jean MASSIES,** thank you for always being open for discussions on epitaxy, for being an open source of MBE knowledge and always taking the time to explain me about growth.

Benjamin DAMILANO, thank you for all the fruitful discussions that we had not just about physics and quantum dots but also about salsa. I will never forget that you were picking my parking place. **Mohamed AL KHALFIOUI,** I would like to thank you for the invaluable discussions that we had especially on the LED electrical characterizations. **Jesús ZUNIGA-PEREZ**, I'll always be grateful for you being a source of inspiration and motivation. Besides being a great researcher you always cared about the students careers. You also provided me with

useful information and suggestions for my future. **Philippe VENNEGUES,** thank you for all the discussions that we had and your TEM expertise, it was a pleasure to work with you. Also, I will never forget every evening when you were telling me to go home and stop working. **Maxim KORYTOV,** I was really lucky to work with you, your knowledge and expertise to characterize quantum dots by TEM helped me a lot in my work. **Fabrice SEMOND,** I would like to thank you for all our fruitful discussions on MBE and the useful information and suggestions for my future career. **Yvon CORDIER,** It was a pleasure to drink the coffee with you every morning and to have interesting discussions.

Olivier TOTTEREAU, thank you for your patient and technical help with SEM and EDX. Your immediate availability will always be appreciated. **Aimeric COURVILLE**, thank you for your constant presence and for unhesitatingly always taking the time to share your knowledge on MOCVD growth and the AFM equipment. **Denis LEFEBVRE,** your professional MBE technical support will always be appreciated, thanks to you I learned a lot. **Sébastien CHENOT,** I would like to thank you for all the clean room processing that you made for me, thanks to you we fabricated the first UV LED in CRHEA. **Virginie BRANDLI**, my office mate, it was a real pleasure to be with you in the same office, thank you for your continuous support during the three years. Your advices helped me to get over some difficult times. **Stéphane VEZIAN**, thank you for all the endless laughs we had together specially in the MBE room. I will never forget that you are the best ‘‘pêcheur d’échantillon’’ I ever met.

I thank **Maud NEMOZ, Marc PORTAIL, Boris POULET, Luan NGUYEN, Christian MORHAIN** for their help, advice and forming me on the different equipment. **Stéphanie RENNESON, and Blandine ALLOING** your smile, positive energy and moral support were always making my day.

I acknowledge **Jean-Yves DUBOZ** and **Philippe BOUCAUD** for their competent direction of the CRHEA laboratory. Jean-Yves also provided helpful insights and critical ideas onto my thesis work. I am also thankful to **Eric DREZET**, **Patrick CHALBET**, **Michèle PEFFERKORN, Anne-Marie GALIANA and Isabelle CERUTTI** for their IT and administrative support and easy solving of everyday problems.

I thank my fellow lab mates and friends for all the fun we had in the last three years. In particular, I would like to thank **Michel KHOURY** and **Rami KHAZAKA,** I have to say that both of you were a source of motivation for me when I arrived in CRHEA, Michel the patents generating machine and Rami the publication generating machine. Thank you for the amazing time we had together inside and outside the lab. **Stanislav BODNAR**, the crazy Russian friend, you succeeded to convince me to go to the gym for two months. I also thank **Roy DAGHER**, **Peinan NI**, **Fulvio CARUSO**, **Gema TABARES, Rémi COMYN** and **Esther LUSIA** for being

awesome colleagues. A special thanks to the new PhD generation ‘‘Bon application team’’ **Victor FAN ARCARA, Ramy MANTACH, Mario FERRARO, Gauthier BRIERE, Rajat SAWANT and Philipp JOHN** for all the amazing moments and the fun we had, starting from the lunch time, the trip to Italy … and ending with the open space, a lot of memories and good times, thank you all.

Also, **Adrien MICHON, Eric FRAYSSINET, Maxime HUGUES, Jean-Michel CHAUVEAU, Patrice GENEVET, Philippe DE MIERRY, Nathalie CALIN** and many others who are too numerous to mention individually are all greatly acknowledged for their contributions whether for technical training, answering questions or giving advice.

This thesis work is the result of a strong collaboration with **L2C laboratory**. First of all I would like thank **Pierre LEFEVRE** the director of L2C for giving me this opportunity. I also thank in particular **Thi-Huong NGO, Thi Quynh Phuong VUONG, and Pierre VALVIN** for all their help and the TRPL characterizations. I also express my gratitude to **Sylvie CONTRERAS** for all the electrical characterizations. It was a real pleasure to work with you all.

This PhD was financially supported by the ANR Project (ANR-14-CE26–0025-01) “NANOGANUV.” that I would like to acknowledge.

Last but not least, I would like to thank all my friends and family especially my **mother, father and brother**, to whom this thesis is dedicated, for their endless love and continuous support throughout those three years and my life in general.

Samuel MATTA

Résumé substantiel (Extended abstract in French)

Ce manuscrit de thèse concerne l'élaboration des nanostructures (boîtes quantiques (BQs)) à base de matériaux semi-conducteurs (Al,Ga)N pour développer des sources de lumière (ex: les diodes électroluminescentes (DELs)) qui émettent dans l'ultraviolet (UV). L'objectif est d'étudier les mécanismes de croissance, par épitaxie par jets moléculaires ainsi que les propriétés structurales et optiques des BQs $Al_yGa_{1-y}N$ dans une matrice $Al_xGa_{1-x}N$ (0001) (avec x > y). Cette étude a été réalisée dans le but de développer un procédé de croissance et d'étudier le potentiel des BQs $Al_yGa_{1-y}N$ en tant que nouvelle voie pour la réalisation d'émetteurs UV plus efficaces, et plus spécifiquement pour les DELs UV. Ces travaux s'inscrivent dans le cadre du projet ANR NANOGANUV (N° ANR-14-CE26-0025-01).

L'émission de la lumière a connu une révolution au début des années 1990 avec l'introduction de matériaux semi-conducteurs à base de nitrure. Les nitrures d'éléments III, appelé composés III-N, (GaN, AlN, InN et leurs alliages) sont des semi-conducteurs à bande interdite directe présents sous de multiples formes dans la vie de tous les jours dans des applications optoélectroniques et électroniques modernes (ex : DEL, laser, transistor etc..). Grâce à leur large bande interdite qui varie entre 0,69 eV pour InN et 6,1 eV pour l'AlN, ils sont devenus les matériaux de choix pour couvrir une grande partie du spectre électromagnétique en partant du proche infrarouge et en couvrant le visible, en utilisant les alliages (In,Ga)N, jusqu'à atteindre la gamme ultraviolette, en utilisant les alliages (Al,Ga)N.

La recherche sur les III-N a progressé rapidement après la première démonstration de DELs bleues à haute puissance en 1994 [1], une invention qui a conduit à l'attribution du prix Nobel de physique en 2014 [2]. Ces dispositifs ont réussi à atteindre des rendements quantiques externes très élevés, dépassant 80 % [3]. Après l'introduction réussie de ces matériaux pour les émetteurs visibles, les DELs UV ont commencé à attirer l'attention et sont à présent considérées comme la prochaine technologie pour remplacer les lampes à vapeur de mercure. Aujourd'hui, l'utilisation du mercure est devenue une préoccupation majeure due à sa toxicité qui pose des problèmes de santé publique et environnementaux (recyclage). De plus, les lampes à mercure souffrent de plusieurs limitations techniques telles que leur grande taille, leur courte durée de vie, et une gamme de longueurs d'onde discrète. En conséquence, le rôle des DELs UV devient de plus en plus important avec un taux de croissance du marché de 34 % par an [4].

Les alliages (Al,Ga)N permettent de couvrir une grande partie de la gamme UV, en ajustant l'émission de bande interdite de 3,4 eV (soit 365 nm, en utilisant le GaN) à 6,1 eV (soit 203 nm, en utilisant l'AlN).

Le développement des DELs UV est motivé par l'étendue des applications industrielles possibles dans les différentes gammes UV telles que :

- La polymérisation et l'impression 3D dans la gamme UVA (400 - 320 nm).
- La croissance des plantes et la photothérapie dans la gamme UVB (320 - 280 nm).
- La purification de l'eau et de l'air dans la gamme UVC (< 280 nm).

Cependant, l'efficacité des DELs UV diminue fortement vers les courtes longueurs d'onde (elle est typiquement inférieure à 10 % dans l'UVC) [5]. Cette chute est due en partie à la faible qualité structurale de la région active avec des densités de dislocations supérieures à 10^9 cm^{-2} et qui agissent comme des centres de recombinaison non-radiatifs. Notre approche pour s'affranchir de l'effet de la qualité cristalline médiocre sur l'efficacité des DELs UV est d'utiliser des boîtes quantiques (c.à.d des îlots tridimensionnelles (3D) de taille nanométrique) comme région active à la place des puits quantiques actuellement utilisés. Grâce à cette approche, les excitons sont confinés à l'intérieur des BQs (selon les trois directions de l'espace) et donc leur probabilité de se recombiner non-radiativement avec les dislocations est minimisée.

Ce manuscrit est composé de cinq chapitres**. Le chapitre I** introduit les propriétés de base des matériaux d'éléments trois à base de nitrure. En particulier, leurs propriétés cristallines et élastiques ainsi que leurs structures de bande sont présentées. Ensuite, l'effet du champ électrique interne (F_{int}) dans ces matériaux est discuté. Dans une seconde partie, l'état de l'art des émetteurs UV est décrit avec les différents défis techniques et les différentes approches proposées pour améliorer leur efficacité. La dernière partie du chapitre consiste à introduire le concept de croissance épitaxiale en utilisant la technique de croissance par épitaxie sous jets moléculaires (EJM ou MBE pour Molecular Beam Epitaxy) pour les matériaux nitrures et en mettant l'accent sur les BQs.

Le chapitre II se focalise sur les propriétés des BQs GaN fabriquées par épitaxie par jets moléculaires en utilisant une source plasma (N_2, appelée PAMBE) ou ammoniac (NH_3, appelée NH_3-MBE) comme source d'azote. Le rôle de la contrainte épitaxiale et de l'énergie de surface sur la formation et les propriétés optiques des BQs ont été étudiés. Le travail a été réalisé dans le but d'étudier l'effet de la localisation des porteurs dans les BQs sur les efficacités radiatives et de choisir la meilleure approche de croissance pour l'émission dans l'UV. Dans un premier temps, l'influence de la contrainte épitaxiale sur la formation et les morphologies (taille, densité) des BQs a été étudiée en fabriquant des BQs GaN sur différentes couches tremplins d'$Al_xGa_{1-x}N$

(avec 0,5 ≤ x ≤ 0,7; soit un désaccord de paramètre de maille ($\frac{\Delta a}{a} = \frac{a_{GaN} - a_{Al_xGa_{1-x}N}}{a_{Al_xGa_{1-x}N}}$) compris entre 1,2 % ≤ Δa/a ≤ 1,7 %). Dans cette étude, nous avons montré qu'en augmentant le désaccord de paramètre de maille (Δa/a), entre le plan des BQs et la couche tremplin d'$Al_xGa_{1-x}N$, on favorise la formation de BQs plus petites avec une densité plus élevée (jusqu'à dix fois plus grande) et des distributions en taille plus homogènes. Cependant, les mesures de photoluminescence (PL) ont montré une modification de la réponse optique des BQs à cause du champ électrique interne (F_{int}) qui induit un fort décalage vers les plus grandes longueurs d'onde (décalage vers le rouge) lorsque la concentration en Al de la matrice $Al_xGa_{1-x}N$ augmente (un décalage de 3,22 eV à 2,95 eV pour les BQs GaN crues par PAMBE et de 3,36 à 2,97 eV pour les BQs GaN développées par NH_3-MBE, en augmentant la composition x_{Al} du tremplin d'$Al_xGa_{1-x}N$ de 0,5 à 0,7). En effet, nous avons montré que la discontinuité du champ électrique interne augmente alors de 3 à 5,3 MV / cm en augmentant x_{Al} de 0,5 à 0,7. De plus, les mesures de PL en fonction de la puissance d'excitation du laser nous ont permis de conclure que plus les BQs sont petites moins leurs propriétés optiques sont modifiées par F_{int}, c.à.d que F_{int} a moins d'influence sur leurs structures de bande. D'autre part, une comparaison de la formation de BQs GaN en utilisant la croissance par PAMBE ou NH_3-MBE a permis d'étudié l'influence du procédé de croissance sur la contribution du coût en énergie de surface (Δγ), qui est fortement modifié en utilisant des sources N_2 ou NH_3. Il a été montré que le processus de croissance est mieux contrôlé en utilisant la croissance par PAMBE, conduisant à la formation de BQs GaN avec des densités plus importantes et une meilleure uniformité de taille qu'en utilisant NH_3-MBE. En termes de propriétés optiques, les BQs GaN formées par PAMBE ont montré des intensités de PL jusqu'à trois fois plus élevées et une largeur à mi-hauteur plus petite que les BQs GaN formées par NH_3-MBE. Enfin, les mesures de photoluminescence résolue en temps (TRPL) combinées aux mesures de PL en fonction de la température nous ont permis de déterminer les efficacités quantiques internes (IQE) des BQs GaN / $Al_xGa_{1-x}N$ (0001). Des valeurs d'IQE d'environ 50 % ont été obtenues à basse température avec la possibilité d'atteindre un rapport d'intensité intégré de PL entre 300 K et 9 K allant jusqu'à 75 %. Ces résultats ont confirmé le confinement efficace des porteurs dans les BQs GaN.

Le chapitre III est consacré à l'étude de la croissance et des propriétés optiques des BQs $Al_{0.1}Ga_{0.9}N$ / $Al_{0.5}Ga_{0.5}N$, en montrant les différents défis pour obtenir des BQs efficaces. Le changement de la procédure de croissance, notamment l'étape de recuit post-croissance, a montré une modification de la forme des BQs. Plus précisément, on obtient des BQs de forme allongée avec un recuit à 740°C et des BQs symétriques avec un recuit à une température proche ou supérieure à 800°C. La variation de la quantité déposée d'$Al_{0,1}Ga_{0,9}N$ de 10,5 MC à 6 MC (1 MC ~ 0,26 nm) a montré la capacité de couvrir la gamme de l'UVA profond, en passant de 340

nm (3,65 eV) à 324 nm (3,83 eV). En plus, une bande supplémentaire qui émet vers des longueurs d'onde plus grandes (énergies plus basses) a également été observée pour les BQs formées avec un recuit à 740°C. En combinant les caractérisations morphologiques et optiques, cette bande a été attribuée à une fluctuation de composition des BQs dans la région active, induisant la formation d'une famille additionnelle de BQs avec une composition en Al inférieure à la composition nominale de 10 %: plus précisément la composition a été estimée à une valeur proche de l'alliage GaN. Egalement, des hauteurs plus grandes pour cette seconde famille de BQs a été observée par rapport à la famille principale de BQs $Al_{0,1}Ga_{0,9}N$ (dont la composition est estimée à une valeur égale ou légèrement supérieure à la concentration nominale). De plus, un champ électrique interne d'environ 2 MV / cm a été estimé pour le système des BQs $Al_{0,1}Ga_{0,9}N$ / $Al_{0,5}Ga_{0,5}N$. Enfin, il a été démontré qu'en faisant un recuit à plus haute température ($\geq$ 800°C) l'émission de PL de cette famille supplémentaire de BQs (BQs riche en Ga ou (Al)GaN) diminue très fortement. De plus, cette étape de recuit a fortement impacté la forme des BQs et conduit à une amélioration de leur efficacité radiative d'un facteur 3.

Après avoir défini les conditions de croissance optimisées pour les nanostructures $Al_{0,1}Ga_{0,9}N$ / $Al_{0,5}Ga_{0,5}N$ (0001), **le chapitre IV** a été centré sur les BQs $Al_yGa_{1-y}N$ ($0 \leq y \leq 0,4$) formées sur des matrices $Al_xGa_{1-x}N$ (0001) ($0,5 \leq x \leq 0,7$), dans le but d'aller plus loin dans l'UV. En faisant varier les conditions de croissance des BQs $Al_yGa_{1-y}N$, on a étudié la gamme accessible d'émission en longueurs d'onde. L'influence de la variation de la composition en Al dans la matrice $Al_xGa_{1-x}N$ sur la formation de BQs $Al_{0,1}Ga_{0,9}N$ a aussi été étudiée. On a montré qu'en augmentant la composition x_{Al} de la couche tremplin $Al_xGa_{1-x}N$ (conduisent à augmenter aussi F_{int}), l'émission de PL ne se décale pas vers le rouge (contrairement aux BQs GaN). Au contraire, un léger décalage vers le bleu (UV) a été observé et attribué à la formation de BQs avec des hauteurs légèrement plus petites lorsque x_{Al} augmente. Ce résultat montre que l'émission d'énergie de PL des BQs $Al_{0,1}Ga_{0,9}N$ est presque insensible à F_{int} en raison de leur faible hauteur ($h \leq 2,5$ nm). Les mesures de PL en fonction de la température nous ont aussi permis de conclure qu'une taille modérée de BQs $Al_yGa_{1-y}N$ insérées dans une barrière $Al_xGa_{1-x}N$ avec un contraste chimique modéré (Δ_{x-y}) est nécessaire pour améliorer l'efficacité radiative avec des rapports I(300K) / I(9K) atteignant 46 % dans le cas des BQs $Al_{0,1}Ga_{0,9}N$ / $Al_{0,6}Ga_{0,4}N$ (0001). Ensuite, la variation de la composition dans les BQs $Al_yGa_{1-y}N$ ainsi que la quantité de matière déposée nous ont permis d'obtenir une large gamme de longueurs d'onde d'émission accessibles. En ajustant ces conditions de croissance, l'émission de la longueur d'onde des BQs a été déplacée de l'UVA vers l'UVC, atteignant des longueurs d'onde minimales autour de 270 - 275 nm (pour les applications de purification de l'eau et de l'air) avec un rendement radiatif de 30 % contre 0,5 % dans une structure similaire à base de puits quantiques. Les différentes dynamiques de recombinaison ont également été étudiées en utilisant des mesures de

photoluminescence résolues en temps (TRPL). En allant des BQs GaN à des BQs $Al_yGa_{1-y}N$, le temps de déclin radiatif diminue fortement, de l'ordre de la µs (pour GaN) jusqu'à la ns (pour $Al_{0,4}Ga_{0,6}N$). L'IQE à basse température a également été estimée, en utilisant les mesures de TRPL, atteignant des valeurs comprises entre 50 % et 66 %.

Dans le dernier chapitre, nous avons montré la possibilité de fabriquer des dispositifs DELs à base de BQs $Al_yGa_{1-y}N$ injectées électriquement couvrant une émission du bleu-violet jusqu'à l'UVB (de 415 nm à 305 nm). Les caractéristiques d'électroluminescence (EL) des BQs GaN / $Al_{0.5}Ga_{0.5}N$ ont montré une émission dans la gamme bleu-UVA (de 450 nm à 360 nm). La difficulté d'obtenir une émission à plus courte longueur d'onde, en utilisant des BQs GaN (0001), est principalement liée à l'influence du champ électrique interne et à la hauteur des BQs qui est limitée par la quantité minimale déposée (~ 6 MCs) pour les fabriquer. Dans un second temps, des DELs UV à base de BQs $Al_{0,1}Ga_{0,9}N$ et $Al_{0,2}Ga_{0,8}N$ ont été fabriquées pour la première fois, montrant la possibilité d'aller jusque dans la gamme UVB. Pour les DELs à base de BQs $Al_{0,1}Ga_{0,9}N$, une émission dans la gamme UVA (entre 325 nm et 335 nm) a été montrée, tandis que pour les DELs à base de BQs $Al_{0,2}Ga_{0,8}N$, une émission jusqu'à la gamme UVB (entre 305 nm et 320 nm) a été observée. Les caractéristiques électriques des différentes DELs $Al_yGa_{1-y}N$ ont aussi été étudiées. A ce stade, les performances de ces DELs sont encore modestes mais le résultat important est que ces dispositifs montrent la possibilité d'utiliser les BQs en tant que région active pour la réalisation de dispositifs injectés électriquement émettant dans la gamme UV.

Références

[1] S. Nakamura, T. Mukai, and M. Senoh, Appl. Phys. Lett., 64, 1687 (1994).

[2] "The Nobel Prize in Physics" (2014). http://www.nobelprize.org/nobel_prizes/physics/laureates/2014/

[3] Y. Narukawa, M. Ichikawa, D. Sanga, M. Sano, T. Mukai, J. phys. D: Appl phys 43, 354002 (2010).

[4] http://www.semiconductor-today.com/news_items/2017/jun/ledinside_150617.shtml

[5] M. Kneissl, III-Nitride Ultraviolet Emitters, Springer International Publishing (2016).

Table of Contents

List of Acronyms

QD	Quantum dots
QW	Quantum well
LED	Light emitting diode
UV	Ultraviolet
MBE	Molecular beam epitaxy
NH_3-MBE	Ammonia assisted MBE
PAMBE	Plasma assisted MBE
TDs	Threading dislocations
ML	Monolayer
IQE	Internal quantum efficiency
EQE	External quantum efficiency
F_{int}	Internal electric field
x_{Al}	Aluminium concentration in the template
y_{Al}	QDs aluminium concentration
n.c.	Nominal concentration
PL	Photoluminescence
FWHM	Full width half maximum
TRPL	Time resolved photoluminescence
QCSE	Quantum confined stark effect
AFM	Atomic force microscopy
SEM	Scanning electron microscopy
STEM	Scanning transmission electron microscopy
HAADF	High-angle annular dark-field imaging
EDX	Energy dispersive X-ray
XRD	X-ray diffraction

Introduction

Light emission faced a revolution in the early 1990s with the introduction of III-V semiconductor materials based on nitride. III-nitride materials (GaN, AlN, InN and their alloys) are direct band gap semiconductors very suitable for modern optoelectronics and electronics applications (e.g.: light emitting diode (LED), laser etc ...) thanks to their remarkable properties. The most important one is undoubtedly their large band gap which varies from 0.69 eV for InN to 3.4 eV for GaN till reaching 6.1 eV for AlN (Figure 1). Thanks to the band gap engineering concept, developed on traditional III-V semiconductors (arsenides, phosphides), they became a promising material to cover a large part of the spectral range, starting from the near infrared and visible range, using $In_xGa_{1-x}N$ alloys, and ending in the ultraviolet range, using $Al_xGa_{1-x}N$ alloys.

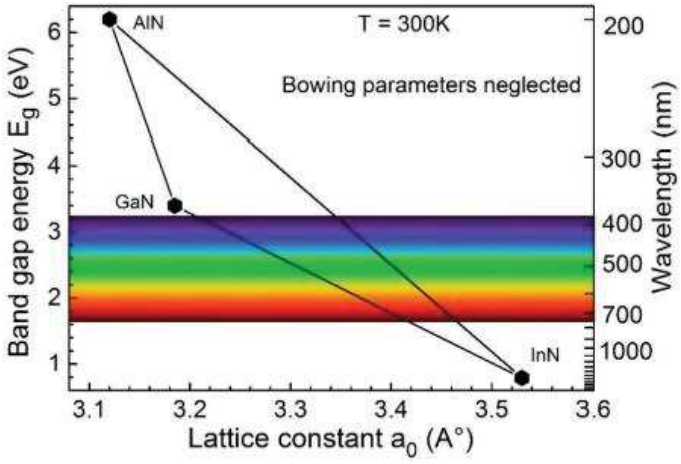

Figure 1. Band gap energies versus in-plane lattice constants of wurtzite AlN, GaN and InN semiconductors at room temperature.

In the late 1960s, the first report on single crystalline GaN was published by Maruska and Tietjen [1]. However, at this stage, the low crystalline quality and the residual n-type doping were an obstacle to the development of III-nitride devices. Later, the revolution (in the early 1990s) came thanks to the development of a growth process (metal organic vapor phase epitaxy (MOVPE)) and achievements of high quality GaN materials and later on development of p-type doping. These breakthroughs opened the path to the fabrication of (In,Ga)N blue light emitting diodes (LEDs) which became the fundamental component at the origin of the fabrication of white LEDs. Thanks to this invention, new generations of energy efficient, environmentally friendly and bright light sources were created, which paved the way for multiple applications. This technology was pioneered by Isamu Akasaki, Hiroshi Amano and Shuji Nakamura who received the Nobel Prize in Physics in 2014 [2] for their contributions [3, 4, 5].

III-nitride research then progressed rapidly: after the first demonstration of high power blue LEDs in 1994 [6], very high external quantum efficiencies exceeding 80 % were reached fifteen years later [7]. Besides LEDs, III-nitride materials also attracted the attention for number of other optoelectronic and electronic devices, such as laser diodes [8], ultraviolet photodetectors [9] and high electron mobility transistors (HEMT) [10]. This last one also opened the way for different high power and RF applications. Today, III-nitride materials are present in many sectors of the semiconductor industry driven by different applications such as lighting, RF, power, laser, data storage etc …. According to Yole development, III-nitride market reached around $ 16 billion in 2016 and will reach $ 20 billion by 2020 [11].

After the successful introduction of III-nitride semiconductors for visible emitters, ultraviolet (UV) LEDs started to attract a lot of attentions and are considered as the next technology to replace mercury vapor lamps. The use of mercury is a main concern as it is a toxic material which brings environmental problems. Moreover, mercury lamps suffer from several technical limitations such as short lifetime, large sizes and fixed wavelengths [12]. As a consequence, the role of UV LEDs became more and more important with an actual market growth rate of 34 % per year [13].

(Al,Ga)N alloys are the materials of choice for the fabrication of UV LEDs as they can cover a large part of the UV range by tuning the band gap emission from 3.4 eV (i.e. 365 nm), using GaN, to 6.1 eV (i.e. 203 nm), using AlN.

UV LEDs are motivated by a wide range of industrial applications, in the different UV regions, such as:

- UV curing and 3D printing in the **UVA range (400 - 320 nm)**
- Plant growth and phototherapy **UVB range (320 - 280 nm)**
- Water and air purifications in the **UVC range (< 280 nm)**

Contrary to (In,Ga)N blue LEDs which already showed very high external quantum efficiencies (EQE), UV LEDs suffer from a significant decrease of the EQE while going towards shorter wavelengths, typically below 10 % in the UVB and UVC ranges [14]. This is mainly due to the poor electrical characteristics (due to the low p-doping efficiencies for (Al,Ga)N layers) and the low structural quality of (Al,Ga)N materials due to the high density of dislocations which act as non radiative recombination centers. Our approach to overcome the effect of the reduced crystalline quality on the UV LED efficiency, i.e. on the radiative efficiency, is to use three dimensional (3D) quantum dots (QDs) (which are nanometer-sized islands) as the active region of LEDs instead of 2D quantum wells (QWs). Using this approach, the carriers are trapped inside

the QDs along the three spatial directions and thus the probability to recombine non-radiatively with surrounding defects is reduced.

The main target of this thesis was to develop a fabrication process for QDs by studying the epitaxial growth, the structural and optical properties of (Al,Ga)N QDs and investigating their potential as a novel route to fabricate efficient UV emitters (emitting between 270 nm and 400 nm).

This thesis is divided into five chapters and is structured as follows:

- **Chapter I** will introduce the basic properties of III-nitride materials underlying this work. In particular, their crystal and elastic properties as well as the band structures will be presented. Afterwards, the effect of the electric field in those materials will be discussed. In a second part, the state of the art of III-nitride ultraviolet emitters will be presented along with the different technical issues and the different approaches proposed to improve their efficiencies will be reviewed. The chapter ends by introducing the concept of epitaxial growth as well as the molecular beam epitaxy (MBE) growth technique specificities for nitride materials and with a particular focus on quantum dots (QDs).
- **Chapter II** will focus on GaN QDs properties grown by plasma MBE (PAMBE) and ammonia MBE (NH_3-MBE). The role of the epitaxial strain and the surface energy on the QD growth and optical properties will be studied. This work has been carried out with the aim to study the carrier localization inside the QDs on the radiative efficiency and choose the best approach for UV emission.
- **Chapter III** will be dedicated to study the growth and the optical properties of $Al_{0.1}Ga_{0.9}N$ QDs. This chapter will discuss the different growth challenges and the influence of growth conditions on the QDs shape and optical properties, in particular the wavelength range and the radiative efficiency.
- **Chapter IV** will be dedicated to the study of $Al_yGa_{1-y}N$ QDs ($0 \leq y \leq 0.4$) with the aim to go deeper in the UV range. By varying the $Al_yGa_{1-y}N$ QDs growth conditions, the range of accessible wavelengths emission will be investigated. As a result, the possibility to tune the emission wavelength from the blue down to the UVC range will be presented with the ability to reach high radiative efficiencies compared to quantum wells.
- **Chapter V** will present the demonstration of electrically injected $Al_yGa_{1-y}N$ QD-based UV LED prototypes, and discuss their main electro-optical properties. We will show the possibility to fabricate QD-based LEDs emitting in the whole UVA range, using GaN and $Al_{0.1}Ga_{0.9}N$ QDs, and down to 305 nm in the UVB range with $Al_{0.2}Ga_{0.8}N$ QDs active regions.

Finally, a general conclusion and perspectives of this work will be presented.

References

[1] H. P. Maruska and J. J. Tietjen, Appl. Phys. Lett. 15, 327 (1969).

[2] "The Nobel Prize in Physics" (2014). http://www.nobelprize.org/nobel_prizes/physics/laureates/2014/

[3] H. Amano, N. Sawaki, Y Toyoda and I. Akasaki, Appl. Phys. Lett., 48, 353 (1986).

[4] H. Amano, M. Kito, K. Hiramatsu and I. Akasaki, Jpn. J. Appl. Phys. 28, L2112 (1989).

[5] S. Nakamura, T. Mukai, M. Senoh and N. Iwasa, Jpn. J. Appl. Phys. 31, L139 (1992)

[6] S. Nakamura, T. Mukai, and M. Senoh, Appl. Phys. Lett., 64, 1687 (1994).

[7] Y. Narukawa, M. Ichikawa, D. Sanga, M. Sano, T. Mukai, J. phys. D: Appl phys 43, 354002 (2010).

[8] S. Nakamura, M. Senoh, S. Nagahama, N. Iwasa, T. Yamada, T. Matsushita, H. Kiyoku, and Y. Sugimoto, Jpn. J. Appl. Phys., 35, L217 (1996).

[9] M. Razeghi and A. Rogalski, J. Appl. Phys., 79, 7433 (1996).

[10] M. Asif Khan, J. N. Kuznia, D. T. Olson, W. J. Schaff, J. W. Burm, and M. S. Shur, Appl. Phys. Lett., 65, 1121 (1994).

[11]Yole développement and KnowMade, http://www.yole.fr/III-N_PatentWatch_KnowMade.aspx#.Wofp8tThCHv

[12] Y. Muramoto, M. Kimura, and S. Nouda, Semicond. Sci. Technol. 29, 084004 (2014).

[13] http://www.semiconductor-today.com/news_items/2017/jun/ledinside_150617.shtml

[14] M. Kneissl, III-Nitride Ultraviolet Emitters, Springer International Publishing (2016).

Table of Contents

I. Overview on nitrides for ultraviolet emission

This first chapter will introduce the basic properties of III-nitride materials which are necessary to understand the nature of these materials and will give important fundamentals to introduce the subject of my PhD thesis. In the first part, a background on III-nitride materials properties will be presented by giving some notions on the crystal and elastic properties as well as the band structures. We will then investigate the effect of the electric field in those materials. In the second part, the state of the art of III-nitride ultraviolet emitters will be presented with the different technical issues and the proposed approaches to improve their efficiencies. In the third part, the concept of epitaxial growth will be presented as well as the growth technique using molecular beam epitaxy for nitride materials and more specifically for quantum dots.

I.1 Background on III-nitride properties

I.1.1 Crystal properties

The III-nitride materials (AlN, GaN, InN) can be crystallized in three distinct phases: wurtzite, zinc blende and rock salt. However for epitaxial growth, only the first two phases can be grown, as the rock salt phase needs very high pressures (> 12 GPa) [1] to be induced. Concerning the first two phases, the wurtzite phase is known to be the most stable thermodynamically and has usually a better structural quality compared to the zinc blende which is a metastable phase.

In this work, only the wurtzite crystal structure is used. It has a hexagonal unit cell and belongs to the $P6_3mc$ space group which corresponds to two compact hexagonal sublattices shifted by $u = \frac{3}{8}c$ for the ideal structure (with c the lattice parameter along the (0001) axis (cf. Figure I-1(b)), whereas the zinc blende structure belongs to the $F\bar{4}3m$ space group and consists of two face-centered cubic sublattices formed respectively of metal and nitrogen atoms, separated from each other's by $\frac{a\sqrt{3}}{4}$, with a the lattice parameter (cf. Figure I-1(a)).

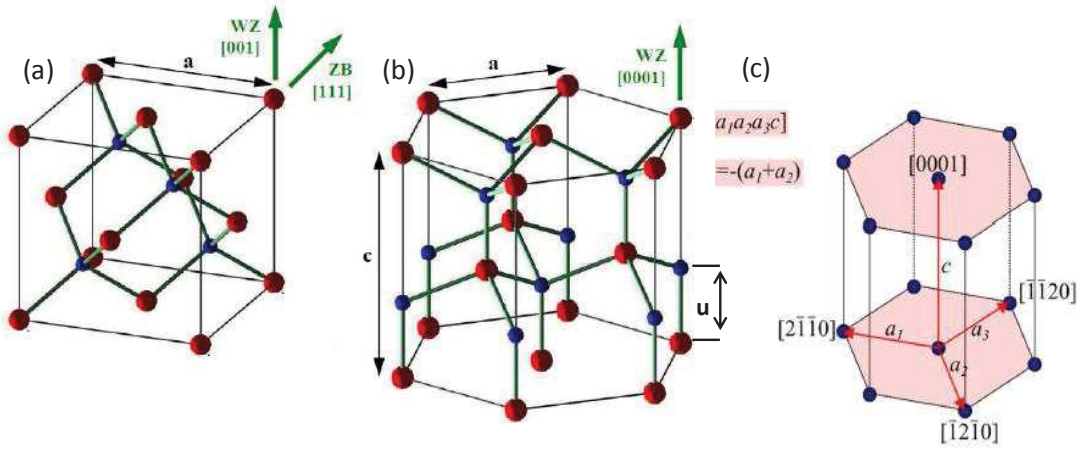

Figure I-1. Atomic structure of III-nitride a) zinc blende and b) wurtzite crystal phases [2]. The red and blue spheres indicate the metal and N atoms respectively. c) Representation of the crystallographic axes of the wurtzite structure.

For the wurtzite and zinc blende structures, each group III atom is surrounded by four nitrogen atoms. The two structures can be constructed by a particular stacking sequence of diatomic planes. As we can see on Figure I-2(a), the wurtzite structure has an oriented sequence of AB-AB along the [0001] axis. On the other hand, the zinc blende structure is presented by an ABC-ABC sequence along the [111] axis (cf. Figure I-2(b)).

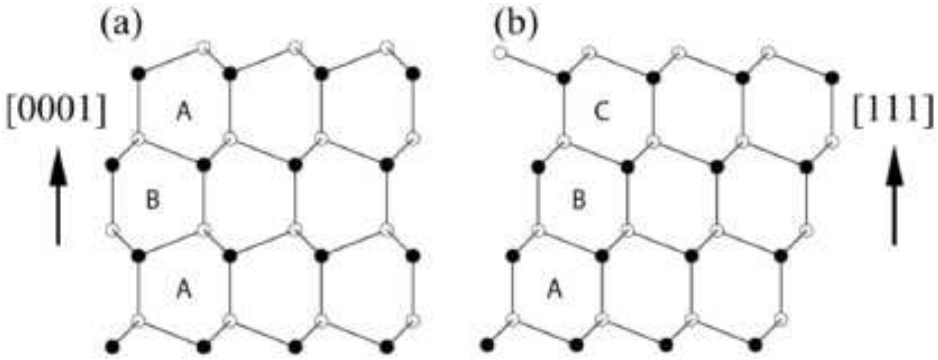

Figure I-2. Stacking sequence of a) wurtzite (0001) structure (seen along the [11-20] azimuth), and b) zinc blende (111) structure (seen along the [1-10] azimuth).

For hexagonal structures, the lattice points are usually indexed by a set of four integers denoted by (h k i l) known as the Miller-Bravais indices and are related to the vectors $\overrightarrow{a_1}$, $\overrightarrow{a_2}$, $\overrightarrow{a_3}$ and $\vec{c}$, respectively. The first three vectors are rotated by 120° to each other and their sum must be equal to zero (i.e. i = - (h + k)). The fourth one is perpendicular to the hexagonal base and represents the [0001] axis (cf. Figure I-1(c)).

The lattice parameters that define the wurtzite structures are mainly c, a and u parameters which are representing the edge and the height of the hexagonal cell and the bond length respectively (Figure I-1(b)). The different parameters for GaN and AlN are summarized in table

I-1. We can note the differences between the lattice parameters as well as the c/a and u/c ratios for the different nitride materials. For an ideal wurtzite structure, u/c and a/c ratios are 0.375 and 1.633 respectively, which means that GaN ratios are closer to those of an ideal wurtzite structure than AlN ones. This structural nuance between nitride materials induce significant differences in the spontaneous polarization, as it will be discussed in the next part.

Table I-1: Lattice parameters for GaN and AlN at 300K [3, 4].

	c (Å)	a (Å)	c/a	u/c	Thermal expansion coefficients (10^{-6} K^{-1})
GaN	5.185	3.189	1.626	0.377	α_c=3.17 / α_a=5.59
AlN	4.982	3.112	1.600	0.382	α_c=5.3 / α_a=4.2

The lattice parameters also depend on the material temperature, so they can evolve as a function of the temperature which will add thermal stresses in the case of heteroepitaxy. The thermal expansion coefficients are also summarized in table I-1. The effect of these stresses appears mainly while cooling the sample after growth, which can create some cracks especially during the growth of AlN or $Al_xGa_{1-x}N$ with high Al composition on GaN. These cracks can be limited by adding an intercalated AlN layer [5, 6, 7].

The lattice parameters in the case of ternary alloys, such as $Al_xGa_{1-x}N$ alloys, can be calculated by linear interpolation assuming Vegard's law [8]:

$$a(Al_xGa_{1-x}N) = x.\,a(AlN) + (1-x).\,a(GaN) \quad \text{(I-1)}$$

$$c(Al_xGa_{1-x}N) = x.\,c(AlN) + (1-x).\,c(GaN) \quad \text{(I-2)}$$

In epitaxy, one of the main reasons impacting the crystalline quality of the grown layers is the host substrate. As the target of this thesis is to grow $Al_xGa_{1-x}N$ nanostructures with high Al content, AlN substrates would be the more adapted choice, especially for ultraviolet applications due to its transparency in this emission range. Although AlN substrates are available in the market, the price and crystalline quality are not yet good enough to compete with other substrates. For the choice of the substrates, different parameters should be taken into account such as the lattice parameter, defect density, thermal expansion coefficient, the orientation etc… The most commonly used substrates for the fabrication of optoelectronic devices are sapphire, SiC and Si (111). The lattice parameters as well as the thermal coefficients are summarized in table I-2.

SiC substrate appears as the most suitable substrate for nitride materials as the lattice mismatch with GaN and AlN is smaller compared to sapphire and Si. Moreover, its thermal and electrical conductivities are very good. The most important drawback is the high price.

Si (111) substrate is an interesting choice because of its low cost and availability in large diameter plates (up to 12"). However, the important problems related to the epitaxy of III-nitride on Si (111) are the large lattice mismatch, which degrades the III-N materials quality, and the strong thermal expansion coefficients mismatch which leads to strongly stressed layers and the appearance of cracks.

Today, the most commonly used substrate is sapphire (0001). It remains the substrate of choice due to its availability, low cost and the high thermal stability. Furthermore, it is transparent in the visible and ultraviolet ranges. Also, efficient blue LEDs are successfully produced using this substrate. However, this substrate suffers from different problems as the poor thermal conductivity and the strong lattice mismatch with GaN and AlN, which induce a high defect density (> $10^8 cm^{-2}$).

Table I-2 : Lattice parameters and thermal expansion coefficients for different substrates (Al_2O_3, SiC and Si)[13].

	Al_2O_3 (0001)	**6H-SiC (0001)**	**Si(111)**
Lattice parameter a (Å)	$\frac{4.7589}{\sqrt{3}} = 2.747$	3.0806	5.43 x $\frac{\sqrt{2}}{2}$ = 3.84
In-plane lattice mismatch with AlN (a_{AlN}- a_{sub}) / a_{sub} (%)	13	1	-18.9
In-plane lattice mismatch with GaN (a_{GaN}- a_{sub}) / a_{sub} (%)	16 (compressive)	3.5 (compressive)	-17 (Tensile)
Thermal expansion coefficient α (10^{-6} K^{-1})	7.3	4.46	3.59

Different crystal planes can be used for the growth of the materials and the epitaxial layers are generally named according to the crystal plane. The majority of III-N hetero-structures are grown on sapphire (0001) c-plane which is known as the “polar plane”. Other growth planes are also possible and referred as “nonpolar” or “semipolar”. For non polar growth planes, the direction is perpendicular to the c-plane. Among them, the (1-100) and (11-20) planes which are named m-plane and a-plane, respectively. The semipolar planes are at an intermediate angle different than 90° and 0° with the c-axis, e.g. the (20-21) plane. Figure I-3 presents some examples of the different growth orientations.

Most of III-nitride heterostructures are grown along the [0001] polar orientation. However, one of the aspects of this orientation is the presence of strong electric fields induced by polarization discontinuities at interfaces (cf. part I.1.2.2) which can strongly impact the optoelectronic properties (inducing a red shift of the wavelength emission). For semipolar and

nonpolar orientations, the influence of the polarization field is reduced, which is good for ultraviolet applications. However, the most important drawback is the small substrate size.

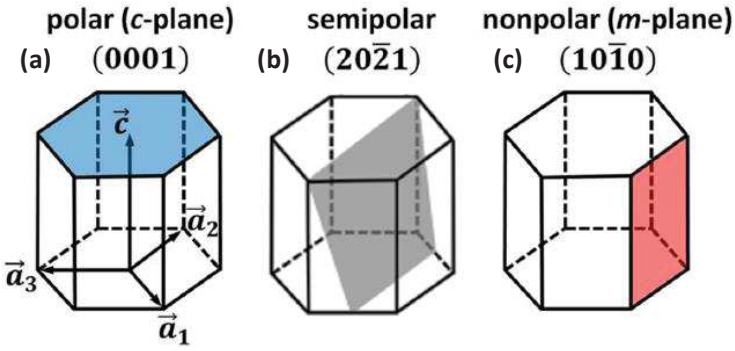

Figure I-3. Examples of different crystal plane orientations: (a) polar, (b) semipolar (20-21) and (c) nonpolar (10-10) planes [9].

The [0001] and [000$\bar{1}$] directions are different from each others. The [0001] direction is designated as positive direction with the vector pointing from a metal atom (i.e. Al, Ga) to a nitrogen atom (N). This direction is referred as metal polarity. For the opposite direction [000$\bar{1}$], the vector points towards the metal atom and the direction is referred as nitrogen polarity (Figure I-4). In general, the polarity affects the surface properties as well as the optical properties. The quality of N-polar layers are generally lower compared to metal polar ones, in particular regarding the surface roughness and the impurities concentration [10, 11, 12].

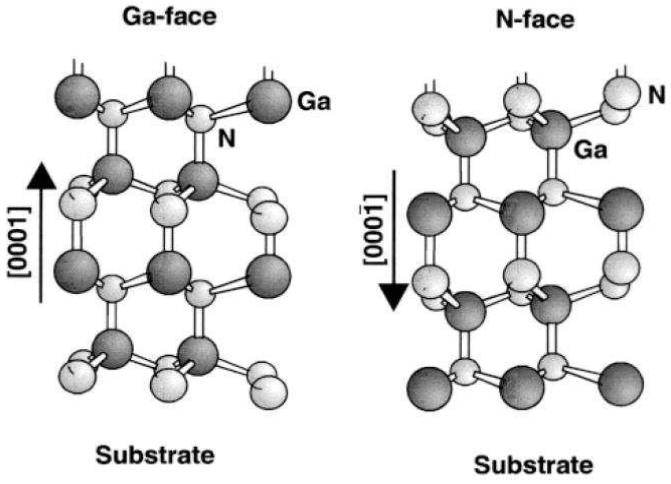

Figure I-4. Schematics illustrating the polarity in a GaN wurtzite structure: a) metal-polar and b) N-polar [13].

I.1.2 Elastic properties

I.1.2.1 Strain and stress

III nitride materials are obtained mainly by hetero-epitaxy. As mentioned before, they are grown generally on a host substrate which presents different lattice and thermal expansion parameters, in most of the cases on a sapphire substrate. Moreover, the III-N elements have also very different lattice parameters compared to each others. These make the epitaxial layers undergo considerable stresses and deformations. In general, it leads to a biaxial stress in the growth plane. This generated stress can be either compressive or tensile. For example, in the case of growing (Al,Ga)N on AlN, (i.e. $a_{(Al,Ga)N} > a_{AlN}$), the (Al,Ga)N layer will be lattice-strained on the AlN layer and an elastic energy will be generated and stored in the (Al,Ga)N epilayer due to the compressive stress (Figure I-5(b)). After a certain thickness, called critical thickness, this stored energy can be relaxed by forming dislocations (plastic relaxation, cf. Figure I-5(c)) or through a shape transition and the formation of a 3D layer (elastic relaxation). In the framework of the linear elasticity theory, the critical thickness for both the plastic and elastic relaxation is inversely proportional to the square value of the lattice mismatch.

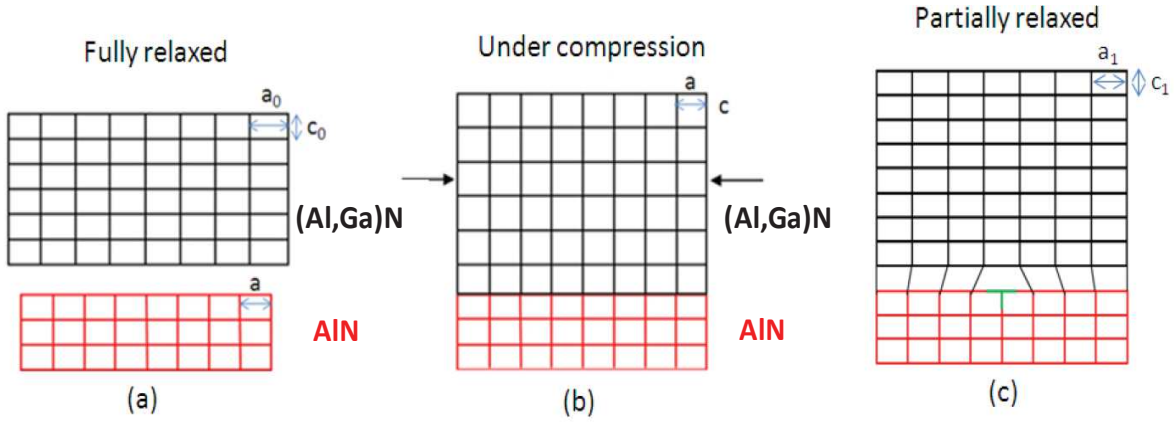

Figure I-5. Schematic diagram for different epilayer growth situations in the case of an (Al,Ga)N layer grown on AlN: a) fully relaxed (Al,Ga)N layer (before growth), b) compressively strained, and c) partially relaxed by plastic relaxation and the formation of dislocations (T).

In a wurtzite hetero-epitaxial growth, due to the induced stress, the in-plane lattice parameter (a) of the epilayer is adapted with that of the substrate parameter at the initial stage of growth. As a consequence, the out of plane parameter (c) changes depending on the a-parameter. In a linear elasticity regime, the a and c parameters relation as well as the stress-strain relation are related together by Hooke's law:

$$\vec{\sigma} = C.\vec{\varepsilon} \qquad \text{(I-3)}$$

Where $\vec{\sigma}$ and $\vec{\varepsilon}$ are the stress and strain tensors and C is the fourth-order elastic coefficient tensor. By using Voigt notation [14] for hexagonal system, this tensor can be written in the form of a 6 x 6 matrix (eq. I-4).

To simplify the notation and eq. I-4, we replaced the indices {xx, yy, zz, yz, xz, xy} by {1, 2, 3, 4, 5, 6} respectively. In the following, the components of the deformation tensor will be as followed:

- Stress tensor along the main axes : $\sigma_1 = \sigma_{xx}$; $\sigma_2 = \sigma_{yy}$; $\sigma_3 = \sigma_{zz}$
- Shear stress : $\sigma_4 = \sigma_{yz}$; $\sigma_5 = \sigma_{xz}$; $\sigma_6 = \sigma_{xy}$
- Strain tensor along the main axes : $\varepsilon_1 = \varepsilon_{xx}$; $\varepsilon_2 = \varepsilon_{yy}$; $\varepsilon_3 = \varepsilon_{zz}$
- Shear strain tensors : $\varepsilon_4 = 2.\varepsilon_{yz}$; $\varepsilon_5 = 2.\varepsilon_{zx}$; $\varepsilon_6 = 2.\varepsilon_{xy}$

$$\begin{pmatrix}\sigma_1\\ \sigma_2\\ \sigma_3\\ \sigma_4\\ \sigma_5\\ \sigma_6\end{pmatrix} = \begin{pmatrix} C_{11} & C_{12} & C_{13} & 0 & 0 & 0 \\ C_{12} & C_{11} & C_{13} & 0 & 0 & 0 \\ C_{13} & C_{13} & C_{33} & 0 & 0 & 0 \\ 0 & 0 & 0 & C_{44} & 0 & 0 \\ 0 & 0 & 0 & 0 & C_{44} & 0 \\ 0 & 0 & 0 & 0 & 0 & \frac{C_{11}-C_{12}}{2} \end{pmatrix} \begin{pmatrix}\varepsilon_1\\ \varepsilon_2\\ \varepsilon_3\\ \varepsilon_4\\ \varepsilon_5\\ \varepsilon_6\end{pmatrix} \quad \text{(I-4)}$$

A couple of theoretical and experimental values of the elastic coefficients are given in Table I-3. According to the literature, there is a fairly high dispersion of these values.

Table I-3 : Experimental and theoretical elastic constant values for AlN and GaN in GPa, with "th" the notation for the theoretical data.

	References	C_{11}	C_{12}	C_{13}	C_{33}	C_{44}
AlN	**Wright (th) [15]**	396	137	108	373	116
	Kim(th)[16]	398	140	127	382	96
	Deger [17]	410	140	100	390	120
	Mc Neil [18]	411	149	99	389	125
GaN	**Wright (th) [15]**	367	135	103	405	95
	Kim (th) [16]	396	144	100	392	91
	Deger [17]	370	145	110	390	90
	Polian [19]	390	145	106	398	105

During the epitaxy along the polar axis [0001] (i.e. z axis), the epilayer undergoes a uniform stress only along the two perpendicular directions of the in plane (i.e. X and Y axis), which is called the biaxial stress state, and no stress is exerted along the c-axis (σ_3=0) nor shear stress (σ_4, σ_5, σ_6 = 0). Due to this uniform biaxial stress, the in-plane stress components are equal ($\sigma_1 = \sigma_2 = \sigma$).

In the following, the hook's law can be simplified to be:

$$\begin{pmatrix}\sigma\\ \sigma\\ 0\end{pmatrix}=\begin{pmatrix}C_{11} & C_{12} & C_{13}\\ C_{12} & C_{11} & C_{13}\\ C_{13} & C_{13} & C_{33}\end{pmatrix}\begin{pmatrix}\varepsilon_1\\ \varepsilon_2\\ \varepsilon_3\end{pmatrix} \quad \text{(I-5)}$$

And the lattice constants can be expressed in terms of the strain tensors as:

$$\varepsilon_1 = \varepsilon_2 = \varepsilon_{xx} = (a_{sub} - a_{epi}) \,/\, a_{epi} \quad \text{(I-6)}$$

$$\varepsilon_3 = \varepsilon_{zz} = (c_{sub} - c_{epi}) \,/\, c_{epi} \quad \text{(I-7)}$$

with a_{sub} and c_{sub} the lattice parameters of the substrate (or of a thick relaxed buffer epilayer in our heterostructures as described in chapter II) and a_{epi} and c_{epi} the relaxed lattice parameters of the epilayer grown above (i.e. the strained epilayer).

Finally, due to the in-plane biaxial strain, an out of plane strain (ε_3) is also induced. An out-of-plane and in-plane strain relation can also be given thanks to Hook's law as followed:

$$\sigma_3 = C_{13}.(\varepsilon_1 + \varepsilon_2) + C_{33}.\varepsilon_3 = 0 \quad \text{(I-8)}$$

Or $\varepsilon_1 = \varepsilon_2 = \varepsilon_{xx}$ which simplifies the equation to:

$$\varepsilon_3 = \varepsilon_{zz} = -2\left(\frac{C_{13}}{C_{33}}\right)\varepsilon_{xx} = \frac{(c_{sub}-c_{epi})}{c_{epi}} \quad \text{(I-9)}$$

I.1.2.2 Polarization and Stark effect

Most of the wurtzite III-nitride heterostructures are grown in the polar orientation. One of the specific aspects of this phase is the presence of a strong electric fields induced by polarization discontinuities at hetero-interfaces, which can strongly impact the optoelectronic properties of the devices. In wurtzite structures, polarization is intrinsic (spontaneous polarization) and strain induced (piezoelectric polarization).

Spontaneous polarization

The symmetry of the crystal structure of a material has important consequences on its polarization properties. For III-nitride elements, the crystal polarity (introduced in part I.1.1) and the deformation of the electron cloud, due to the electo-negativity difference between the metal-atom and the N-atom, creates electron dipoles. In other words, due to the electro-negativity of nitrogen compared to other III element atoms, negative charges are then present at the (0001) surface and positive charges on the $(000\bar{1})$ surface. A set of dipoles is then induced, which creates a macroscopic spontaneous polarization (P_{sp}) pointing from the (0001) surface (i.e. metal polar surface) towards the $(000\bar{1})$ axis (i.e. N polar surface), as presented on Figure I-6, which

creates a negative spontaneous polarization value. This value was calculated by Zoroddu et al. for III-nitride materials, obtaining P_{sp}= - 0.034 and - 0.090 C / m^2 for GaN and AlN, respectively [20]. For $Al_xGa_{1-x}N$ alloys, the spontaneous polarization can also be calculated as follows [21, 22]:

$$P_{sp}(Al_xGa_{1-x}N) = x.P_{sp}(AlN) + (1-x).P_{sp}(GaN) + b.x(1-x) \quad \text{(I-10)}$$

with b the bowing parameter for the spontaneous polarization in (Al,Ga)N equals to 0.019 C / m^2 [22].

Piezoelectric polarization

The piezoelectric polarization (P_{pz}) is an external type of polarization. It is due to the lattice mismatch between two given materials during the heteroepitaxial growth which induces a crystal deformation. In fact, under stress condition, the tetrahedrons of the wurtzite structure are deformed, inducing a displacement of the positive and negative charges barycenters from their usual location. This displacement changes the polarization. Moreover, the direction of this polarization depends on the type of strain. For compressive strain, the P_{pz} points along the [0001] direction and for tensile strain, P_{pz} points along the [000$\bar{1}$] direction (cf. Figure I-6).

The piezoelectric polarization can finally be expressed as a function of the strain tensor (ε):

$$P_{pz} = e_{ij}.\begin{pmatrix}\varepsilon_{xx}\\ \varepsilon_{yy}\\ \varepsilon_{zz}\\ \varepsilon_{yz}\\ \varepsilon_{xz}\\ \varepsilon_{xy}\end{pmatrix} \quad \text{(I-11)}$$

where e_{ij} are the piezoelectric coefficients [23, 24] and can be expressed as follows:

$$e_{ij} = \begin{pmatrix} 0 & 0 & 0 & 0 & e_{15} & 0\\ 0 & 0 & 0 & e_{15} & 0 & 0\\ e_{31} & e_{31} & e_{33} & 0 & 0 & 0\end{pmatrix} \quad \text{(I-12)}$$

The calculated piezoelectric coefficient values are given in Table I-4.

Table I-4 : Piezoelectric coefficients for GaN and AlN [23, 24]

	e_{15} (C / m^2)	e_{31} (C / m^2)	e_{33} (C / m^2)
AlN	- 0.48	- 0.60	- 1.46
GaN	- 0.30	- 0.49	- 0.73

The P_{pz} can then be expressed by the following equation for biaxial [0001] strain:

$$P_{pz} = e_{33}\varepsilon_{zz} + e_{31}(\varepsilon_{xx} + \varepsilon_{yy}) \quad \text{(I-13)}$$

Finally, by combining equations (I-9) and (I-13), the P_{pz}can be expressed as follows:

$$P_{pz} = 2.\varepsilon_{xx}(e_{31} - e_{33}\frac{C_{13}}{C_{33}}) \quad \text{(I-14)}$$

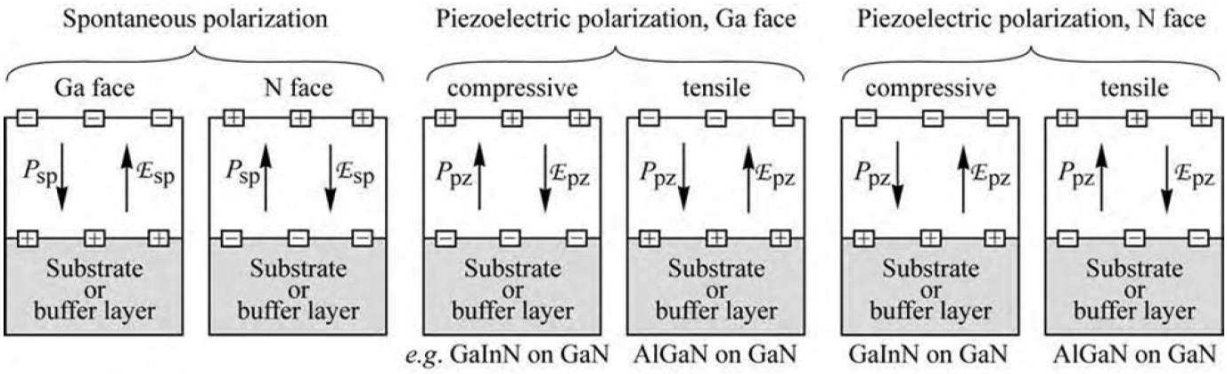

Figure I-6. Schematic representation of the polarization (P) and electric field (E) for spontaneous and piezoelectric polarizations for Ga- and N-face III-nitride materials [25].

Quantum confined Stark effect

In a wurtzite structure, the total polarization can finally be expressed as the sum of the spontaneous and piezoelectric polarizations:

$$\vec{P} = \vec{P}_{sp} + \vec{P}_{pz} \quad \text{(I-15)}$$

In the case of heterostructures, taking the example of GaN / (Al,Ga)N, the different total polarization in the two layers induces polarization discontinuities. This difference in polarization between the materials will be translated by the formation of charge densities (-σ and +σ) at each interface, which in turn generates an internal electric field in the heterostructure. This surface charge density (σ) at the interface between the two materials is:

$$\sigma = (\vec{P}_{(Al,Ga)N} - \vec{P}_{GaN}).\vec{n} \quad \text{(I-16)}$$

where $\vec{n}$ is the unit vector normal to the heterointerface plane and $\vec{P}_{(Al,Ga)N}$, $\vec{P}_{GaN}$ are the polarizations at both sides of the interface. This leads to the creation of an internal electric field created by the surface charge density:

$$\begin{cases} F_{AlGaN} = \dfrac{\sigma}{2\varepsilon_0\varepsilon_{(Al,Ga)N}} \\ F_{GaN} = -\dfrac{\sigma}{2\varepsilon_0\varepsilon_{GaN}} \end{cases} \quad \text{(I-17)}$$

where ε_0 is the vacuum dielectric permittivity and ε_{GaN}, $\varepsilon_{(Al,Ga)N}$ are the GaN and (Al,Ga)N relative permittivity respectively.

Inside the heterostructure the electric displacement vector ($\vec{D} = \varepsilon_0 \varepsilon \vec{F} + \vec{P}$) is conserved for each interface, between the GaN quantum well and (Al,Ga)N barrier, which makes it possible to write:

$$\vec{D}_{GaN} = \vec{D}_{(Al,Ga)N} \tag{I-18}$$

and give rise to the following equation:

$$\varepsilon_0 \varepsilon_{GaN} F_{GaN} + P_{GaN} = \varepsilon_0 \varepsilon_{(Al,Ga)N} F_{(Al,Ga)N} + P_{(Al,Ga)N} \tag{I-19}$$

By assuming that barriers and QD planes have a similar static dielectric constant ($\varepsilon_{(Al,Ga)N} = \varepsilon_{GaN} = \varepsilon$), the internal electric field discontinuity (ΔF) in the GaN layer equals to:

$$\Delta F = \frac{P_{(Al,Ga)N} - P_{GaN}}{\varepsilon_0 \varepsilon} = \frac{\sigma}{\varepsilon_0 \varepsilon} \tag{I-20}$$

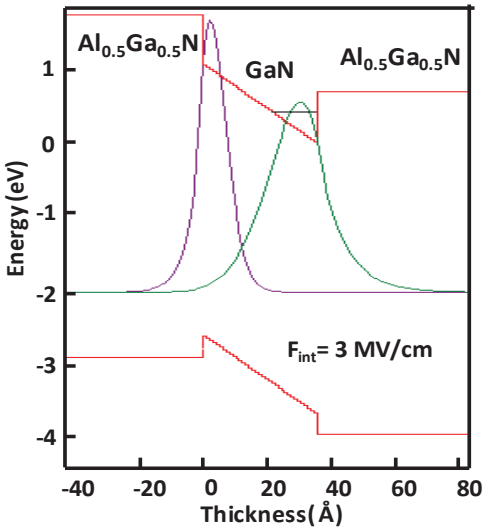

Figure I-7. Example of the band structure and the electron and hole wave functions overlap in GaN / $Al_{0.5}Ga_{0.5}N$ system with F_{int} = 3 MV / cm.

The generated internal electric field (F_{int}) tends to bend the band structure of the hetero-junction (Figure I-7) which induces a spatial separation of the electrons and holes wave functions and hence reduces the transition energy and the radiative recombination probability [23, 26]. This is known as the quantum confined Stark effect (QCSE).

The fundamental transition energy in the GaN quantum well (QW) can finally be calculated as a function of the internal electric field and the quantum well thickness (h_{QW}):

$$E_{e1-hh1} = E_g^{QW} + e_{11} + h_{11} - E_{Ry} - eF_{int}h_{QW} \tag{I-21}$$

where E_g^{QW} refers to the band gap energy of the QW, e_{11} and h_{11} are the quantum confinement energies of electrons and holes respectively, E_{Ry} is the Rydberg energy which corresponds to the excitonic binding energy and e is the electron charge.

I.1.3 Band structure

Like most conventional III-V elements (GaAs, InP,…), III-nitride materials are direct band gap semiconductors, with the maximum and minimum of the valence band and conduction band located at the Γ point, k = 0. Figure I-8 shows the band structures of GaN and AlN. Due to the asymmetry of the wurtzite structure and the spin-orbit coupling, the valence band is splitted into three energy subbands levels (Γ_7, Γ_9). Three transitions are then possible from the valence bands to the conduction band.

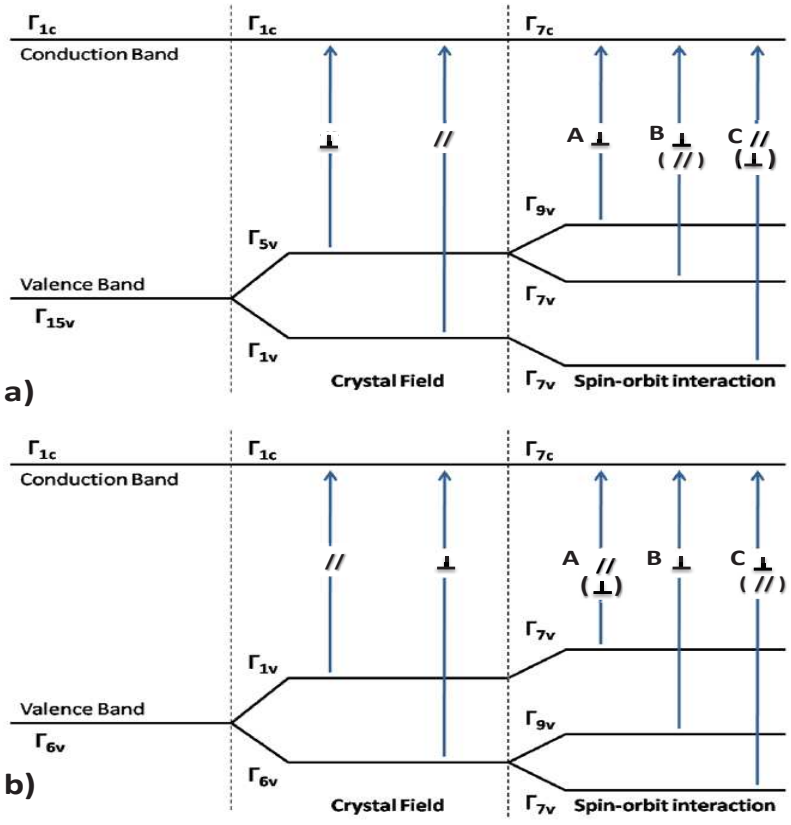

Figure I-8. Schematics presenting the band structure for a) GaN and b) AlN. The blue arrows represent the different optical transitions. The indication // and ⊥ correspond to the light polarization E parallel and perpendicular to the c-axis [27, 28].

The transitions give rise to an exciton with an energy slightly lower than that of the crystal band gap. More precisely, it is equal to the band gap energy minus the exciton binding energy (i.e. excitonic Rydberg). Depending from which valence band the hole originates, the associated

exciton is called A, B or C. The excitonic transition energies are also shown to be very sensitive to the strain in the layers [29].

For GaN, the crystal field term (Δ_{cr}) is weakly superior to 0 (Δ_{cr} = 10 meV [30]), resulting in the splitting of the subbands as presented in Figure I-8 (a), with the symmetry of the holes in the ground state Γ_9. For AlN, Δ_{cr} is strongly negative (Δ_{cr} = -169 meV [29]), which makes the symmetry of the holes in the base state Γ_7 (Figure I-8(b)). Both compounds share a common anion (N) and have a similar weak value of the spin-orbit coupling term. In GaN, the three valence bands are very near in energy.

The band gap energy of nitride alloys (Al,Ga,In)N covers a wide range of energies, ranging from 0.69 eV for InN, to 6.1 eV for AlN at low temperature (cf. table I-5). An approximated way to calculate the band gap energy of the alloys can be found using equation I-22, while taking into account a corrective term (bowing parameter "b") for the deviation from a linear interpolation between two binary compounds. For $Al_xGa_{1-x}N$ alloys, the bowing parameter was estimated at around 0.9 eV, typically for $x_{Al} \leq 0.3$ [31]. We recall that the upper valence band state in GaN has Γ_9 symmetry while for AlN it has Γ_7 symmetry. This means that in $Al_xGa_{1-x}N$ alloys a change of the hole ground state from Γ_9 to Γ_7 occur while increasing x_{Al} inducing a change of the symmetry of the top of the valence band. Indeed it was shown in previous study, that at low x_{Al}, both photoluminescence and reflectivity results can be described with a 0.9 eV bowing parameter, however for x > 0.3, the PL energies strongly deviate [31].

$$E_g^{Al_xGa_{1-x}N} = xE_g^{AlN} + (1-x)E_g^{GaN} - x(1-x)b \qquad \text{(I-22)}$$

Different parameters can also impact the band gap energy. One of them is the temperature due to the electron-lattice interaction and the lattice expansion. The variation of the band gap energy is well described by the empirical equation of Varshni [32]:

$$E_g(T) = E_g(0) - \frac{\alpha T^2}{\beta + T} \qquad \text{(I-23)}$$

where $E_g(0)$ is the band gap energy at T= 0 K and α and β are fitting parameters.

Table I-5: Band gap parameters of InN, GaN and AlN at low and room temperatures.

	E_g at 0 K (eV)	**E_g at 300 K (eV)**	**α (meV / K)**	**β (K)**	**References**
InN	0.69	0.642	0.414	454	[33]
GaN	3.47 3.492	3.411 3.426	0.59 0.531	600 432	[34] [35]
AlN	6.12 6.242	6.026 6.16	1.799 0.72	1462 500	[36] [37]

I.2 State of the art of III-nitride ultraviolet emitters

After the successful introduction of III-nitride semiconductors for visible emitters, LEDs started to attract a lot of attention as UV sources. Currently, the main UV emitters are mercury (Hg) vapour lamps, which have an emission spectrum composed of different emission energy lines, covering from deep UV to infrared regions. The energy conversion efficiency of those lamps is between 10 % and 40 % [38, 39, 40], but they suffer from different technical limitations as their large sizes and short lifetimes [41]. Moreover, the use of mercury is a main concern as it is a toxic material which induces environmental problems. As a consequence, the use of Hg is starting to be limited for the past years which makes the role of UV LEDs more important with an actual market growth rate of 34 % per year [42]. (Al,Ga)N alloys are promising materials for such replacement as they can cover a large part of the UV range by tuning the band gap emission from 3.4 eV (for GaN) to 6.1 eV (for AlN).

UV LEDs are motivated by a wide range of industrial applications, in the different UV ranges, such as:

- UV curing and 3D printing in the **UVA range (400-320 nm)**
- Phototherapy and plant growth in the **UVB range (320-280 nm)**
- Water and air purifications in the **UVC range (< 280 nm)**

Contrary to (In,Ga)N blue LEDs which already showed very high external quantum efficiencies (EQE) up to 84 % [43], UV LEDs suffer from a significant decrease of the EQE while going towards shorter wavelengths, typically below 10 % for wavelengths under 380 nm. Figure I-9 represents the state of the art of EQE for UV LEDs.

Three main terms are impacting the EQE:

1) The internal quantum efficiency (IQE) which is defined as: the ratio between the number of emitted photons in the active region and the number of generated electron-hole pairs in the active region.
2) The injection efficiency (IE) which is defined as: the ratio between the number of generated electron-hole pairs in the active region and the number of total injected carriers in the device.
3) The light extraction efficiency (LEE) which is defined as: the ratio between the number of extracted photons from the semiconductor and the number of emitted photons in the active region.

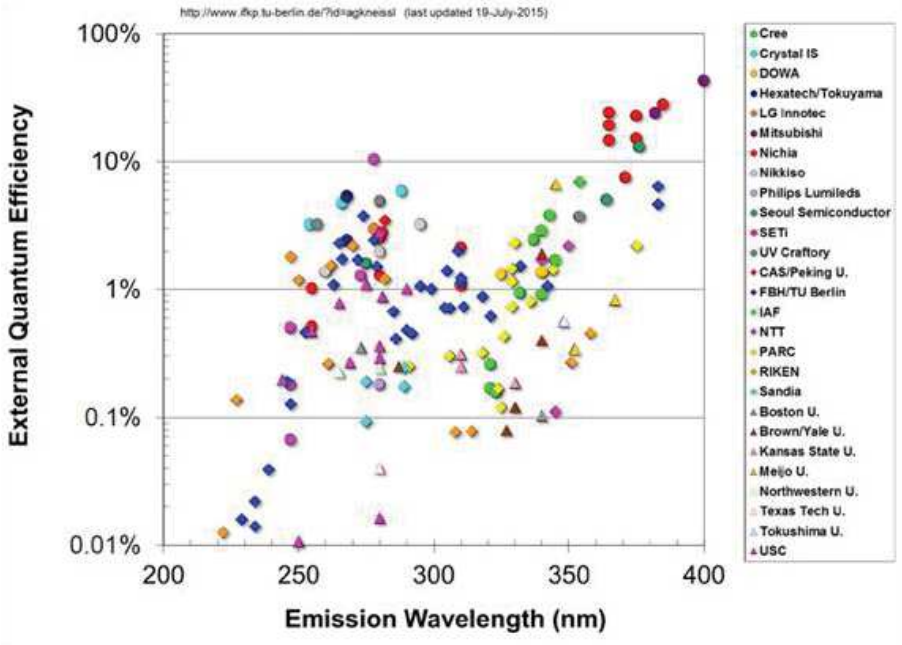

Figure I-9. State of the art of external quantum efficiencies for ultraviolet LEDs [44].

The EQE can then be expressed as the product of these three terms:

$$EQE = IQE.IE.LEE = \frac{P_{opt}}{h\gamma}.\frac{q}{I}$$

with P_{opt} is the optical output power, q the elementary charge, h Planck constant, γ the generated photons frequency and I the current.

Finally, the LED wall plug efficiency (WPE) or the power conversion efficiency can be calculated by the ratio of P_{opt} and the injected electric power (P_{inj}):

$$WPE = \frac{P_{opt}}{P_{inj}} = \frac{P_{opt}}{I.V} = \frac{h\gamma}{V.q}.EQE$$

The decrease of the EQE values, while going towards shorter wavelengths, is due in part to the intrinsic material properties of (Al,Ga)N. Figure I-10 describes a schematic of a typical (Al,Ga)N based LED structure. Each epilayer in the structure can induce different technical issues which impact the different efficiency terms. In the following, we will introduce the main challenges impacting each of the three efficiency terms with the different proposed solutions in the literature.

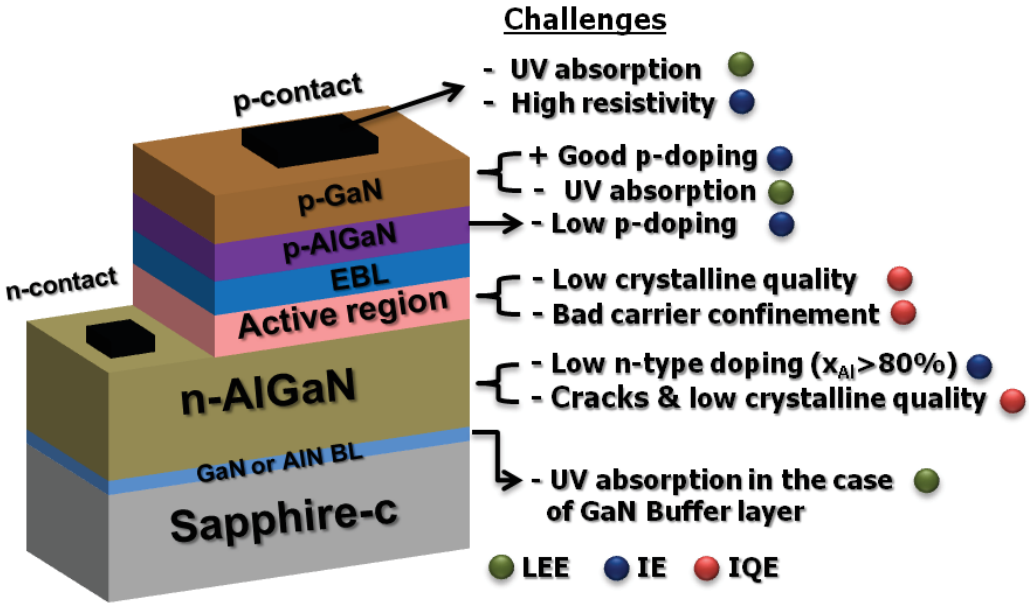

Figure I-10. Schematic of a conventional UV LED with the different remaining challenges and their influence on the different efficiency terms.

I.2.1 Internal quantum efficiency (IQE)

Improving the IQE is one of the main issues in UV LEDs, on which more and more groups are working, including us, and made a lot of progress in the last years. It mainly depends on the structural defects density found in (Al,Ga)N materials, as dislocations and point defects. Those defects act as non radiative recombination centers. Dislocations are mainly threading dislocations (TDs), originating from the heteroepitaxial growth, and the large lattice mismatch between the epilayers and the substrate. Also for (Al,Ga)N alloys, the low Al mobility, on the growth surface, results in a reduction of lateral mass transport and the formation of high density of small-area islands. TDs have been shown to originate at the coalescence interfaces of these islands [45]. Due to the reduction of the Al mobility as a function of the Al concentration (for identical growth conditions), TDs density also increases (typically in the 10^{10}-10^{11} cm^{-2} range compared to 10^{8} - 10^{9} cm^{-2} in GaN epilayers) inducing a decrease of the radiative efficiency (i.e. IQE). This was also confirmed by the calculation of the IQE as a function of the dislocation density in the case of an (Al,Ga)N quantum well based LED emitting at 280 nm (Figure I-11(a)) [46]. The second problem for the IQE reduction is the high internal electric field discontinuities in (Al,Ga)N structures (up to 9 - 10 MV / cm for the GaN / AlN system [47]) which can induce a significant separation of the electron and hole wavefunctions and a decrease of the radiative transition rate.

Solutions

Different approaches have been proposed to increase the IQE by improving the crystalline quality of (Al,Ga)N materials. At first, the AlN buffer layer growth on sapphire by migration enhanced epitaxy (MEE) using molecular beam epitaxy (MBE) [48, 49] or Metal Organic Chemical Vapor Deposition (MOCVD) [50] growth was shown to decrease the defect density and improve the surface morphology of (Al,Ga)N epilayers. The MEE technique consists in alternating the supply of the Al and N fluxes during the growth of AlN buffer layer [49]. Another way to fabricate low TD density AlN buffer is by growing AlN multilayers using a pulsed flow growth technique [51]. This technique consists in applying a continuous aluminum (TMAl) flow and NH_3 pulse flow sequence, which showed to be effective for obtaining high quality AlN. Another approach has also been studied to reduce the defect densities by doing a post-growth annealing of AlN layers at high temperature (1550°C) [52]. Further improvement can also be made by growing the LED structure on AlN substrates [53]. However, such substrates are very expensive and only available in small sizes. Another approach was also introduced by inserting an (Al,Ga)N / AlN superlattice before growing the n-doped (Al,Ga)N layer [54, 55]. This supperlattice was found to be an efficient way to filter dislocations, manage the strain and avoid the cracks formation as well. The growth of (Al,Ga)N QWs using plasma assisted MBE (PAMBE) under metal rich conditions (III/V >> 1) was also shown to increase the IQE up to 32 % at 275 nm [56]. This was attributed to the formation of strong potential fluctuations which induce excitons localization.

On the other hand, minimizing the negative influence of defects is also possible by growing three dimensional quantum dots (QDs) instead of a 2D quantum well (QW) as active region. Thanks to this, the carriers are trapped inside the QDs and thus the probability to recombine non radiatively with TDs is reduced (cf. part I.3.4). Two types of QDs have been investigated: (Al,Ga)N QDs [57, 58] and recently ultra thin GaN QDs (0.6 - 2 MLs), which showed the ability to emit in deep UV [59, 60]. Figure I-11(b) shows the state of the art of the IQE values obtained for UV emitters using all these different approaches. The IQE values are estimated from temperature dependent PL measurements to fairly compare the results from the different groups working on UV emitters.

In this thesis, we will mainly focus on the study of (Al,Ga)N QDs and their ability to enhance the IQE for ultraviolet emitters.

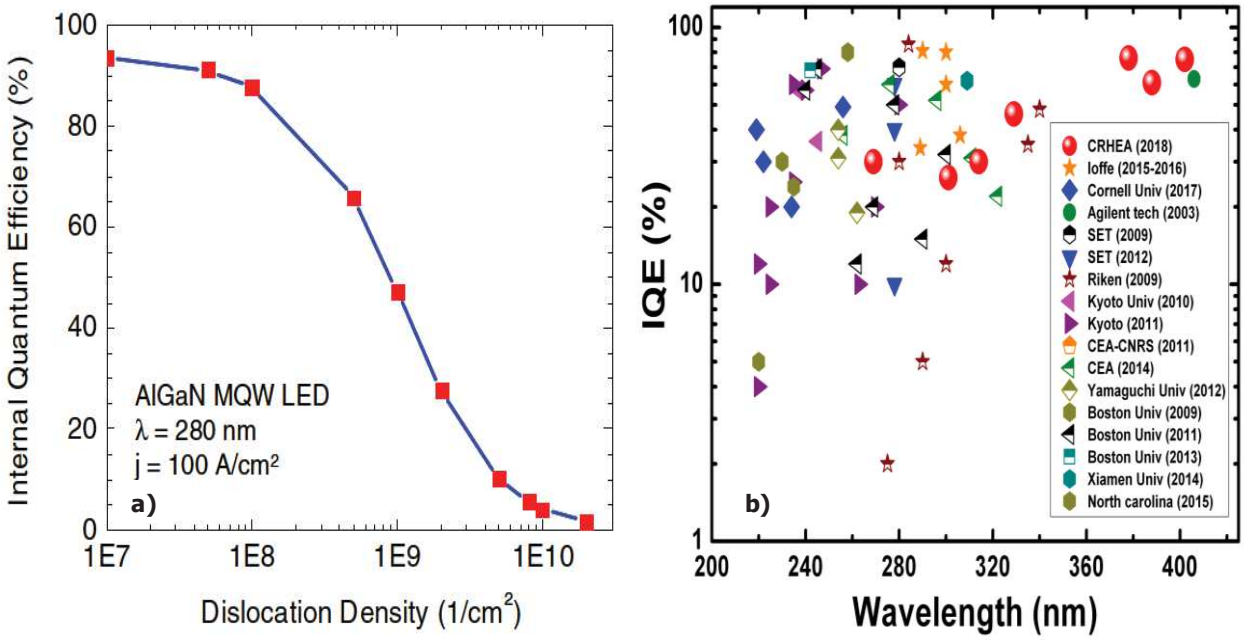

Figure I-11. a) Simulated IQE as a function of the dislocation density for a UV LED emitting at 280 nm [46]. b) State of the art of IQE values for UV sources. The IQE values are estimated from temperature dependent PL measurements to fairly compare the results from the different groups.

I.2.2 Injection efficiency (IE)

Poor injection efficiencies are mainly due to the low p-doping (using Mg) efficiencies for high Al concentrations due to the high acceptor ionization energy (≈ 160 meV and 630 meV for GaN: Mg and AlN:Mg, respectively) [61]. As a consequence, a high resistivity for the p-type layers is found. The high ohmic contact resistivity for Ni/Au contacts (generally used for blue LEDs) on (Al,Ga)N alloys is another problem.

Solutions

The main solution used is by adding a GaN:Mg contact layer on the top of the structure (Figure I-10) to enhance the hole injection. However, GaN is not adapted for UV technology as it absorbs a large part of the emitted light, which impacts the LEE. Other groups prefer to use transparent (Al,Ga)N:Mg layers, to minimize the absorption of GaN, combined with a rhodium (Rh) mirror electrode [62] in order to enhance the LEE. However, in this case, the IE is reduced compared to GaN:Mg. Another novel approach is by using Mg doped AlN nanowires which showed high hole concentrations, up to 6 x 10^{17}cm^{-3} versus ≈ 10^{10} cm^{-3} for a typical AlN:Mg epilayer [63].

Other ideas have also been proposed, as adding a 1 nm thin AlN interlayer between the active region and the electron blocking layer (EBL) in order to suppress the carrier overflow [64]. Also, replacing the usual single EBL by a multiquantum barrier (MQB) EBL showed an improvement of the IE, due to the suppression of electron leakage, which is blocked by the enhanced "effective" barrier height when using a MQB [65].

Finally, new ohmic contacts were also proposed to reduce the contact resistivity on n-doped Al rich (Al,Ga)N as vanadium alloys and Ti/Al based metals which showed contact resistivity down to 10^{-6} Ω.cm^2 and 10^{-3} Ω.cm^2, respectively [66, 67]. Concerning the p-type contacts, other materials such as indium-tin-oxide (ITO), Ni/Al electrode and graphene have also been proposed [64, 68, 69].

I.2.3 Light extraction efficiency (LEE)

The low LEE is mainly due to the p-GaN contact layer usually used on top of the epitaxial layers to improve the injection efficiency. **A solution** to this problem is to replace it by a transparent p-(Al,Ga)N layer, which will impact and degrade the IE. Also, different packaging materials suitable for UV photons are under investigation as the use of photonic crystals, shaping of LED dies, patterned sapphire substrates, encapsulation using sapphire lenses and suitable resins for UV [70, 71, 72].

An additional complication impacting the LEE is the change in the symmetry of the valence band structure for (Al,Ga)N alloys with high Al concentrations, which favours light emission perpendicular to the c-axis (edge emission), i.e. lowers the escape cone for [0001] grown LEDs [73].

Now by looking at the different research works on UV LEDs, we can see that improving the IQE is primordial and different approaches are being investigated as discussed before. Concerning the IE and LEE, different compromises are used. Some groups favour the enhancement of the IE by using a p-GaN contact layer (which impacts and degrades the LEE) while others prefer to enhance the LEE by using a transparent p-(Al,Ga)N contact layer (which then impacts and degrades the IE). Indeed, enhancing the LEE by using an (Al,Ga)N contact layer, Rh mirror electrodes, patterned sapphire substrates and encapsulating resins was shown to improve the EQE up to 20 % at 275 nm [62]. However, the WPE is two times lower (≈ 10 %). Otherwise, in the literature, typical values of EQE for UVC LEDs are found to be below 5 % (Figure I-9).

Another approach recently used, which shows promises for a good compromise between the IE and the LEE is by using a tunnel junction [74]. Using this technique, an n-AlGaN layer is

added on the top of a thin p-AlGaN layer which enables n-type contacts for both bottom and top contact layers of the LED and thus reduces both the absorption and the electrical losses. Using this approach, holes can be introduced through non-equilibrium injection across the tunnel junction. Finally, the replacement of electrical injection by electron-beam pumping has also been investigated showing the ability to reach a high power of 100 - 230 mW for an emission in the UVC range [75, 76].

I.3 Epitaxial growth

In the following subsections, we will introduce the different epitaxial growth modes and techniques. We will describe more specifically the molecular beam epitaxy growth technique via ammonia and plasma nitrogen sources. Then, we will introduce the growth procedure used for our samples and more specifically the growth mode of quantum dots.

I.3.1 General introduction on epitaxy

Epitaxy is a technique of material growth by depositing a given material on a crystalline substrate. We can find two types of epitaxy, the first is "homoepitaxy" for which the grown crystal film and the substrate have identical chemical nature (i.e. same material). The second is called "heteroepitaxy" for which the film and the substrate are of different chemical nature/crystal structure or lattice parameter.

The main techniques used for the growth of III-nitride materials are hybride vapor phase epitaxy (HVPE), metal organic chemical vapor deposition (MOCVD) and molecular beam epitaxy (MBE).

Thanks to the very high achievable growth rates (10 - 100 µm / h), HVPE is mainly used for the production of thick nitride layers (i.e. pseudo substrates). Today, MOCVD is the technique of choice in the industry as it can produce epitaxial layers having good crystalline quality with an acceptable growth rate (0.2 - 5 µm / h). MBE can also produce good crystalline quality of materials, especially for homo-epitaxial growth. Compared to the previous techniques, its main advantages are the in-situ surface characterization techniques (which are powerful tools in particular to study and better understand the formation mechanisms of the nanostructures) and the ability to work with low growth rate (< Angstrom / s) and lower growth temperature.

I.3.2 Molecular beam epitaxy

Molecular beam epitaxy is a thin film deposition technique carried out in an ultra-high vacuum reactor (typically 10^{-10} Torr for the residual pressure). The different III elements are contained in effusion cells in the form of solid sources of high chemical purity. These cells are

then heated and the elements are transferred in form of fluxes of atoms or molecules towards the surface of a substrate, heated at a certain temperature. Thanks to the ultrahigh vacuum, the atomic species can reach the substrate without interactions with other molecules. In other words, the mean free path of atoms is longer than the distance between the effusion cells and the substrate (few meters versus 30 cm). The substrate is fixed on a rotating molybdenum support equipped with a furnace, whose temperature is controlled by both a thermocouple and a pyrometer. The rotation is used to obtain a homogeneous layer deposition. The adatom kinetics, which is mainly affected by the substrate surface temperature and the growth rate, is very important for the growth process. A too low temperature limits the diffusion length of the atoms on the surface and a very high temperature favours the desorption of the atoms. Therefore, choosing the growth temperature is very important and is different from one material to another. Also, the growth rate has a strong influence on the growth kinetics, as it limits the diffusion length (i.e. it fixes the diffusion time as the one needed to grow a monolayer).

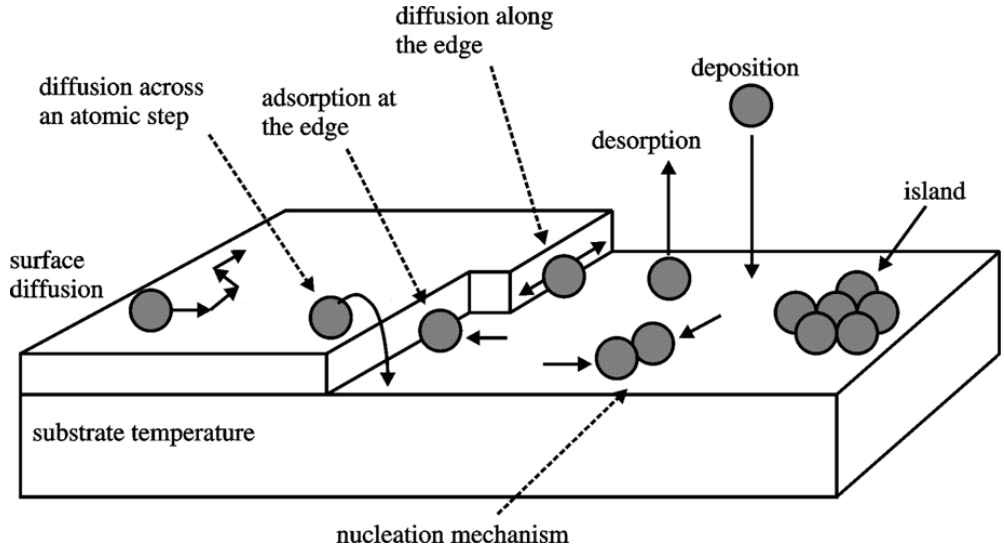

Figure I-12. Schematic presenting the different adatoms possible behaviours during the growth process [77].

During the growth of thin layers by MBE, several processes of physicochemical nature take place as illustrated in Figure I-12. First of all, the atoms begin to adsorb on the surface. Then, they start to diffuse on the surface until finding a site of lower energy where they can interact by nucleating with other atoms forming small islands and/or by incorporating on the surface steps. Atoms can also be desorbed after the diffusion on the surface.

The growth process in MBE is occurring outside thermodynamic equilibrium and so adatom kinetics play an important role, which mainly depends on the substrate temperature, the growth rate and the diffusion length.

One of the main advantages of MBE is that it can provide in-situ information on the surface morphology in real time by using reflection high energy electron diffraction (RHEED). Using this technique, we have access to different informations such as the variation of the in-plane lattice parameter, the growth rate and the surface reconstruction. This technique can only be used under vacuum to avoid any interactions between the electron beam and the molecules in the chamber.

I.3.2.1 Ammonia and plasma assisted molecular beam epitaxy for III-nitrides

In the case of nitrides, the active species of elements III (Ga, Al, and In) and doping elements (Si, Mg) are provided by sublimation of solid sources from the effusion cells. As for nitrogen, N_2 molecules have a high dissociation energy and cannot be thermally dissociated at the growth temperature.

Two methods are generally used to make possible the use of nitrogen atoms for the growth of nitrides. The first is a radio frequency plasma source in order to dissociate the N_2 molecule by breaking the bonds between the atoms of the molecule [78, 79, 80]. Such system is called plasma assisted MBE (PAMBE). The second method is by using ammonia (NH_3) as a precursor (i.e. NH_3-MBE) [81, 82, 83]. In this case, the bounds of nitrogen atoms with hydrogen are weaker and N species are obtained by the pyrolytic decomposition of the NH_3 molecule on the surface. Taking the example of GaN, Ga adatoms react with NH_3 through a surface decomposition to form GaN (equation I-24).

$$NH_3 + Ga \rightleftharpoons GaN + \frac{3}{2}H_2 \qquad \text{(I-24)}.$$

The different characteristics of the layers are comparable for both growth methods and nitrogen sources, but the growth conditions such as the V/III ratio and the temperature vary widely. For NH_3-MBE, the presence of NH_3 on the surface can prevent GaN from dissociating or evaporating. For this reason, in NH_3-MBE, GaN can be grown at higher temperatures compared to PAMBE (≈ 800°C versus 700°C).

In previous studies of NH_3-MBE, it has been shown that the decomposition of NH_3 on the surface is very low (around 4 % at 800°C and much lower, << 1 %, below 450°C) [84]. Therefore, to have a suitable growth rate and quality, a high flux of NH_3, typically 50 sccm, is injected. It was also shown that for nitride materials (e.g.: GaN), the crystalline quality is better for high V/III ratios [85]. For such a high gas flow, a liquid nitrogen cold panel is used to trap residual ammonia, and also a turbo-molecular pump is needed in order to maintain a sufficient vacuum in the chamber.

For PAMBE, it was shown that metal-rich conditions are needed to have a 2D growth [86, 87]. The growth under N-rich conditions leads to a rough and faceted surface. This is due to the low temperature of growth and also because the nitrogen activated species are highly reactive [88].

I.3.2.2 Reflection high energy electron diffraction (RHEED)

The RHEED is a very important in-situ characterization method which allows controlling the surface of the material during growth.

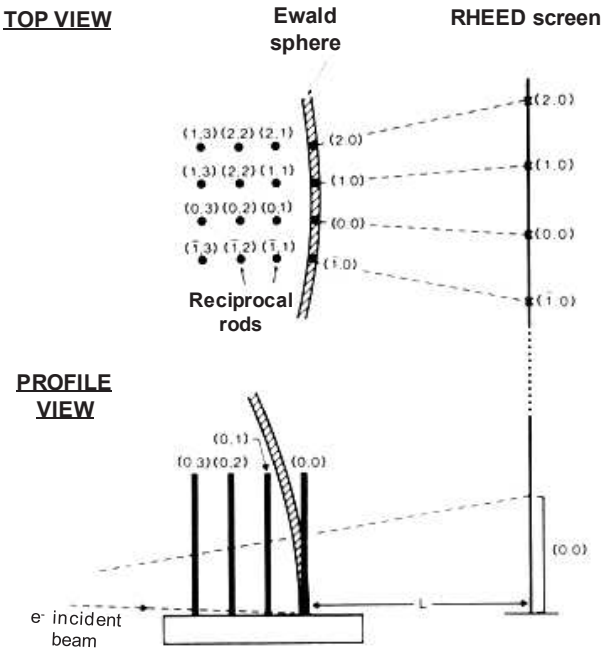

Figure I-13. 3D Schematic description representing the RHEED technique and the intersection of the Ewald sphere with the reciprocal space of the surface, made of reciprocal rods [89].

The principle of RHEED consists in sending electrons (via an electron gun) with an energy between 10 KeV and 30 KeV on the surface of the substrate at a grazing incidence angle ($0 < \theta < 2°$). In this configuration, the interaction of the electrons with the surface limits the penetration of the beam into the layer at a few atomic planes. Then, the diffracted and reflected beams from the surface are observed on a fluorescent screen and generate the interference pattern that corresponds to the reciprocal space view of the surface. A schematic description of the principle of the RHEED technique is presented in Figure I-13.

The accelerated electrons arriving on the surface can be assimilated to monochromatic plane waves, which will be diffracted from the surface. The diffraction of electrons by the atomic array will induce the formation of constructive interferences. These interferences will result in the visualization of the reciprocal space of the surface, made of reciprocal rods perpendicular to the

surface. The Ewald sphere is a geometrical construction used in the theoretical description of the diffraction by a solid, by constructing a sphere around a point in reciprocal space. In reciprocal space, and by using the Ewald sphere, an explanation of the diffraction pattern can be provided. In fact, every time a reciprocal lattice point (3D) or rod (2D) coincides with the sphere surface, a reflection pattern appears on the fluorescent screen.

In the case of a perfectly smooth surface (2D growth mode), the figure of diffraction is a series of parallel diffraction lines, called a ‘’streaky pattern’’. However, for a rough surface (3D growth mode), the figure of diffraction on the screen will consist of points, called a ‘’spotty pattern’’ (Figure I-14). The in-plane lattice constant (a) can finally be determined:

$$a = \frac{L\lambda}{t} \tag{I-25}$$

where L is the distance from the normal surface to the RHEED screen, t is the distance between two arrays of spots (two lines of the RHEED patterns) and λ is the electron wavelength.

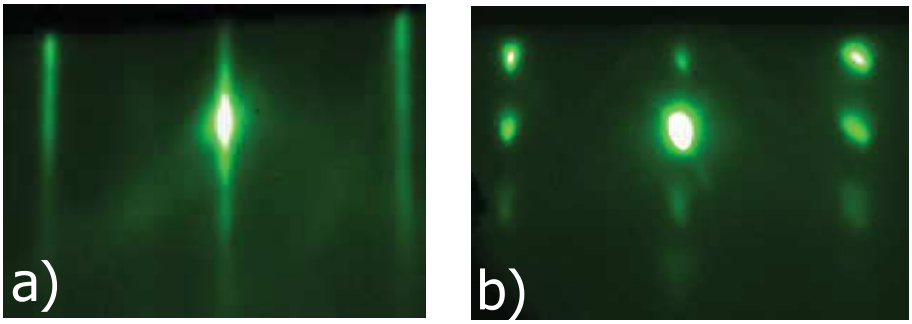

Figure I-14. Reflection high energy electron diffraction for a) 2D and b) 3D surface morphologies.

On the other hand, the growth rate can also be determined using RHEED. While growing a 2D layer, the surface changes periodically by the subsequent filling of the atomic monolayers (MLs, 1 ML corresponding to half the c lattice parameter). During growth, a change in the intensity of the reflected beam due to the variation of the roughness of the surface is taking place. The reflected intensity is directly related to the density of atomic steps on the surface. As presented in Figure I-15, this difference in roughness happens when going from a 2D layer, for which there is a full atomic coverage of the surface with a low roughness, to a state where there is the growth of a second atomic layer (high roughness). For a 2D surface, the RHEED intensity is maximum (θ = 0 ML) and decreases progressively till reaching a minimum level at θ = 0.5 ML (maximum roughness). The growth rate can then be determined from the coverage of one monolayer divided by the interval time spent between θ = 0 ML and θ = 1 ML.

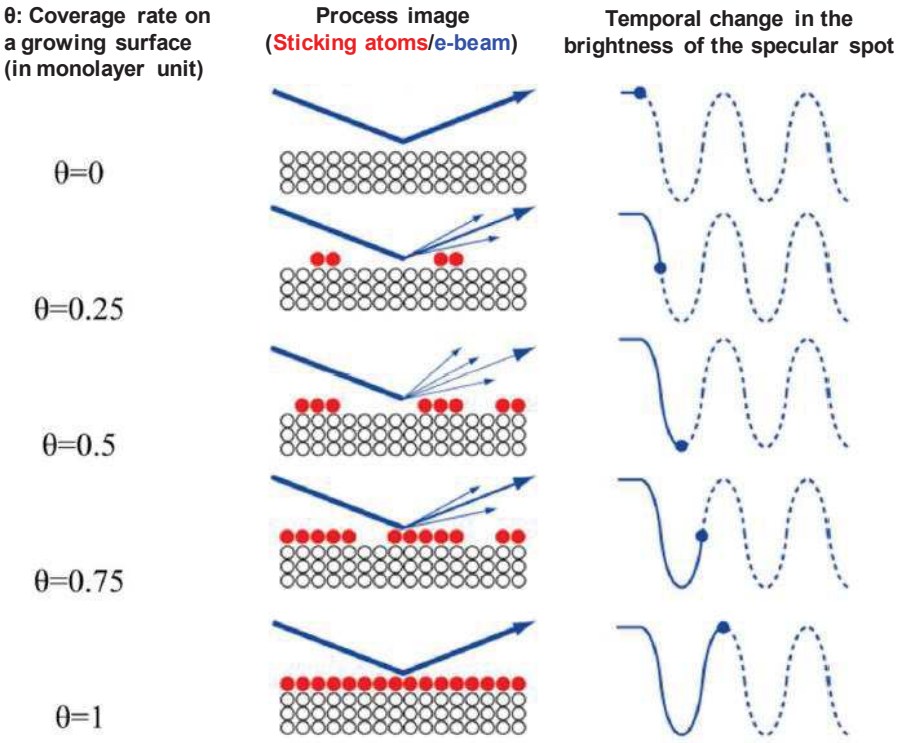

Figure I-15. Schematic description of the process to determine the growth rate using the variation of the RHEED intensity.

I.3.3 Growth modes

In crystal growth, three main growth modes exist (cf. Figure I-16):

1) Frank-Van der Merwe (FM) mode, which corresponds to a layer by layer growth (2D growth),
2) Volmer-Weber (VW) mode, which corresponds to a 3D growth of islands,
3) Stranski-Krastanov (SK), which starts with a 2D layer by layer growth, then after a critical deposited thickness continues with the formation of 3D islands (referred as a 2D-3D transition).

The key parameters impacting the growth mode are the surface energies of the different layers, known as γ_{sub}, γ_{film}, $\gamma_{interface}$ corresponding to the surface energy of the substrate, the film and the interface between the substrate and the film respectively. Finally, the surface energy cost ($\Delta\gamma$) between a 2D film ($\gamma^{2D} = \gamma_{interface} + \gamma_{film}$) and a 3D morphology covering half of the substrate ($\gamma^{3D} = 1/2(\gamma_{film} + \gamma_{sub} + \gamma_{interface}$) can be written as:

$$\Delta\gamma = \gamma^{3D} - \gamma^{2D} \approx \frac{1}{2}\left(\gamma_{sub} - \gamma_{film} - \gamma_{interface}\right) \quad \text{(I-26)}$$

It is therefore the difference $\gamma_{sub} - \gamma_{film} - \gamma_{interface}$ which will condition the growth mode at the initial nucleation stage (cf. Figure I-16).

For **Frank-van der Merwe growth mode** (2D): The substrate surface energy should be more important than both the film and the interface surface energies (i.e $\gamma_{sub} > \gamma_{film} + \gamma_{interface}$ or $\Delta\gamma > 0$).

For **Volmer-Weber growth mode** (3D): The substrate surface energy should be weaker than both the film and the interface surface energies (i.e: $\gamma_{sub} < \gamma_{film} + \gamma_{interface}$ or $\Delta\gamma < 0$).

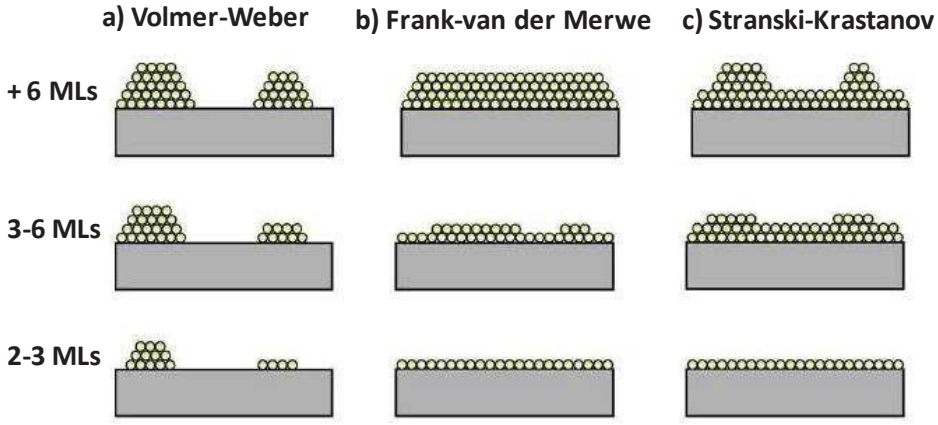

Figure I-16. The different growth modes: a) the 3D growth mode (Volmer-Weber), b) the layer by layer 2D growth mode (Frank-van der Merwe), and c) the 2D-3D growth mode (Stranski-Krastanov) [90].

In the absence of lattice mismatch (Δa/a = 0) between the layer and its substrate (homoepitaxy), the 2D or 3D coherent growth modes describe the only two morphologies that can be adopted at the initial growth of the epitaxial layer. However, in most cases, there is a lattice mismatch.

The growth of a stressed layer leads to an accumulation of energy, called elastic energy, in the layer. This energy increases as the thickness of the epitaxial film increases, which makes the system unstable. After a certain so-called critical thickness, the elastic stress becomes too high to be accommodated by the layer and must be relaxed. The layer can then be relaxed either plastically by forming dislocations (2D-MD) or elastically by forming 3D islands at the surface leading to a (**Stranski-Krastanov growth mode**). After a certain deposited thickness during the 3D growth, an SK-growth mode with misfit dislocations can also occurs (SK-MD). The different growth modes are presented in Figure I-17.

The free energies per unit area of a film can be written as a function of its height (with h > 1 monolayer) for the different growth modes [91, 92]:

$$E_{2D}(h) = M\left(\frac{\Delta a}{a}\right)^2 h + \gamma_{film} \quad \text{(I-27)}$$

$$E_{SK}(h) = (1-\alpha)M\left(\frac{\Delta a}{a}\right)^2 h + \gamma_{film} + \Delta\gamma \quad \text{(I-28)}$$

$$E_{2D-MD}(h,d) = \left(1-\frac{d_0}{d}\right)^2 M\left(\frac{\Delta a}{a}\right)^2 h + 2\frac{E_{MD}(h)}{d} + \gamma_{film} \quad \text{(I-29)}$$

$$E_{SK-MD}(h,d) = (1-\alpha)\left(1-\frac{d_0}{d}\right)^2 M\left(\frac{\Delta a}{a}\right)^2 h + 2\frac{E_{MD}(h)}{d} + \gamma_{film} + \Delta\gamma \quad \text{(I-30)}$$

with M the film biaxial modulus (rigidity of the layer), γ_{film} the surface energy of the epitaxial film, $\frac{\Delta a}{a}$ the lattice mismatch between the epilayer and the substrate, α the fraction of the elastic energy gain through the formation of partly relaxed SK islands, $\Delta\gamma$ the additional surface energy cost to form additional surfaces (i.e. island facets), d the average distance between dislocations at the film-substrate interface, d_0 the distance between dislocations for a fully relaxed epilayer, and E_{MD} the energy cost per unit length to form the dislocations.

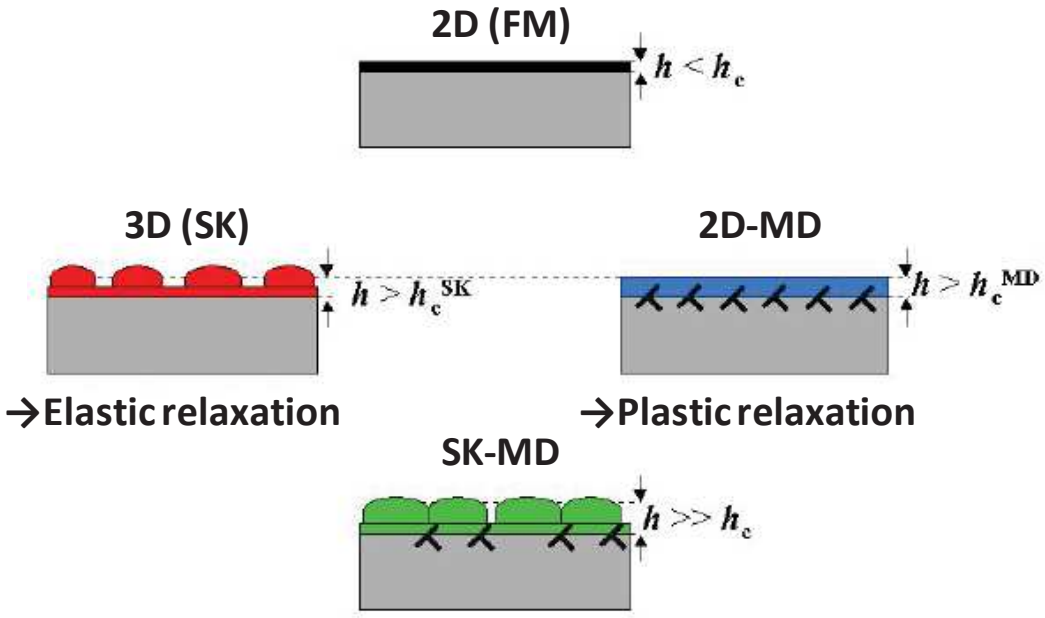

Figure I-17. Schematic illustrating the different growth modes: 2D, 2D with plastic relaxation (2D-MD), SK and SK-MD [93]. h_c is the critical thickness from which the accumulated elastic stress in the 2D layer is relaxed, h_c^{SK} is the critical thickness from which a 3D growth mode is favourable, and h_c^{MD} is the critical thickness where the layer is plastically relaxed with the formation of misfit dislocations.

The choice of the growth mode between SK or FM can be expressed by the energy balance (ΔE) between the additional surface energy cost ($\Delta E_{surf} = \gamma^{3D} - \gamma^{2D} = \Delta\gamma$) to form islands and the elastic energy gain ($\Delta E_{elastic} = E_{SK} - E_{2D}$) from the relaxation of a part of the epitaxial stress.

$$\Delta E = \Delta E_{elastic} + \Delta E_{surf} \quad \text{(I-31)}$$

Where $\Delta E_{elastic}$ is the elastic energy gain and ΔE_{surf} (= $\Delta\gamma$) is the surface energy cost to form the islands.

As long as ΔE is positive, the 2D-3D transition is unfavourable. This is the case at the beginning of the growth, when the quantity of deposited material is small (i.e. large surface to volume ratio) while the accumulated elastic energy ($E_{elastic}$), which is proportional to the deposited thickness h, is not high enough to trigger the 2D-3D transition.

As soon as ΔE becomes negative, the Stranski-Krastanov transition becomes possible. In this case, moving from a 2D stressed layer to a 3D partially relaxed surface decreases the total energy of the layer. In other words, using equation (I-28), the elastic energy $\alpha M \left(\frac{\Delta a}{a}\right)^2 h$ has to be greater than the additional surface energy cost ($\Delta\gamma = \Delta E_{surf}$) to observe a 2D-3D transition, which also means:

$$|\Delta E_{elastic}| > |\Delta\gamma| \tag{I-32}$$

It is thus possible to deduce the critical thickness (h_c^{SK}) from which a 3D growth mode becomes more favourable than a 2D growth mode:

$$h_c^{SK} = \frac{\Delta\gamma}{\alpha M \left(\frac{\Delta a}{a}\right)^2} \tag{I-33}$$

In the case of a truncated pyramidal island (cf. Figure I-18), $\Delta\gamma$ can be expressed as a function of γ_{film} and γ_{facet} (representing the facets' surface energy) [94]:

$$\Delta\gamma = A.\left(\frac{\gamma_{facet}}{sin\theta} - \frac{\gamma_{film}}{tan\theta}\right) \tag{I-34}$$

Where A is a coefficient, depending on both the 3D islands density and the 3D islands sizes and θ is the angle between the facets and the (0001) plane.

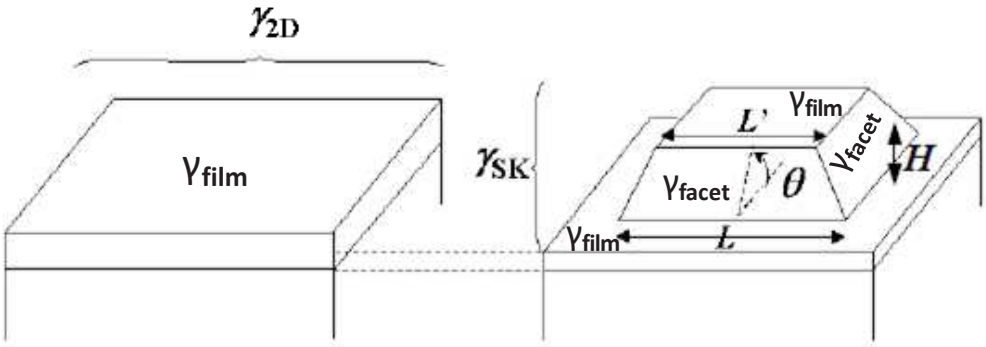

Figure I-18. A schematic showing the different surface energies and parameters in the case of a regular 2D film and a truncated pyramid [93].

We can also deduce the critical thickness h_c^{MD} from which the 2D-MD growth mode (using equation I-29) becomes more favourable than the 2D coherent mode, i.e. the plastically relaxed elastic energy, $\left(2\frac{d_0}{d}\right)M\left(\frac{\Delta a}{a}\right)^2 h$, becomes greater than the energy cost ($2\frac{E_{MD}(h)}{d}$) to create a network of dislocations at the interface:

$$h_c^{MD} = \frac{E_{MD}(h_c^{MD})}{d_0 M\left(\frac{\Delta a}{a}\right)^2} \quad \text{(I-35)}$$

We can also predict which growth mode will occur first by considering the ratio η between the two critical thicknesses (equation I-36), as presented in Figure I-19.

$$\eta = \frac{h_c^{MD}}{h_c^{SK}} \quad \text{(I-36)}$$

As shown on this figure, we can see that if η < 1 (i.e. $h_c^{MD} < h_c^{SK}$) the system favours plastic relaxation. However, if the surface energy cost ($\Delta\gamma$) can be decreased, h_c^{SK} will also be lowered and thus η can be greater than 1 which can induce a SK transition before the plastic one. This transition to a 3D mode instead of a 2D mode by changing the surface energy is presented by the red path in Figure I-19.

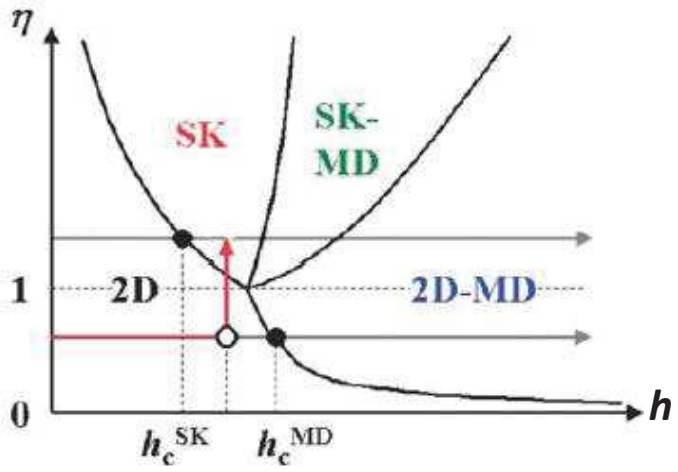

Figure I-19. Schematic diagram illustrating the different growth modes as a function of the deposited thickness (h) and the two critical thicknesses ratio (η) [92].

The formation of 3D islands, i.e. quantum dots, were studied for different materials: it was shown in the case of InAs / GaAs system that the large lattice mismatch (Δa/a ≈ 7 %) induces the SK transition [95] and the formation of QDs. However, in other systems such as the II-VI semiconductors CdTe / CdSe, although a large lattice mismatch (Δa/a ≈ 6 %), no SK transition was observed. For the GaN / (Al,Ga)N system, the lattice mismatch is much lower and the 2D-

3D transition was observed. Thus, it is obvious that the **growth mode depends also on the surface energy** and **not only on the lattice mismatch**, as discussed before.

I.3.4 Nitride quantum dots growth

As described in part I.2, UV LEDs suffer from a drop in the EQE efficiency while reaching shorter wavelengths. Part of this drop is due to the low structural quality of $Al_xGa_{1-x}N$ materials with high dislocation densities (typically > 10^9 cm^{-2}). These dislocations act as non radiative centers and induce a decrease of the IQE (Figure I-11). Quantum dots are 3D structures, by using these nanostructures as the active region of LEDs instead of 2D quantum wells (QWs), the excitons are confined in all three spatial directions (i.e. inside the QDs) and thus the probability to recombine non radiatively with surrounding TDs can be reduced (Figure I-20).

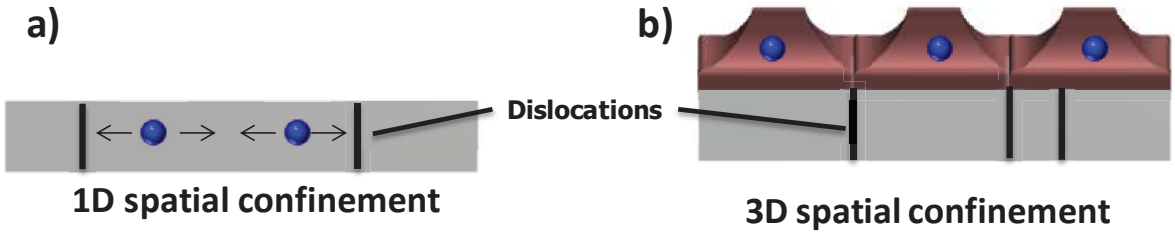

Figure I-20. Schematics presenting the excitons (blue circles) confinement in a) a quantum well and b) quantum dots.

As described in part I.3.3, the surface energy play an important role to obtain a 2D-3D transition (SK growth mode leading to the formation of QDs). The formation of QDs can be triggered by an increase of the (0001) film surface energy (γ_{film}; cf. Figure I-18) to favour the minimization of $\Delta\gamma$ and the stress relaxation by forming QDs with facets (which are parallel to {10-13} planes in the case of GaN-based QDs). Those facets will have a surface energy γ_{facet} (as described in part I.3.3). In equation I-34, the relation between γ_{film} (i.e. γ_{0001}), γ_{facet} (i.e. $\gamma_{10\text{-}13}$) and $\Delta\gamma$ was described. γ_{film} can be increased by adjusting the growth conditions whereas γ_{facet} remains constant or less affected. By enhancing γ_{film}, the surface energy cost ($\Delta\gamma$) will decrease until reaching a level where it will be lower than the elastic energy gain ($\Delta E_{elastic}$). In other words, the ratio γ_{film} / γ_{facet} have to be enhanced untill $\Delta\gamma$ will be lower than $\Delta E_{elastic}$. In this case, the condition of equation I-32 ($|\Delta E_{elastic}| > |\Delta\gamma|$) will be respected and the formation of QDs will occur.

For (Al,Ga)N QDs, two ways are possible in order to enhance the (0001) film surface energy (γ_{film}): growing under N-rich conditions or doing a growth interruption under vacuum. Indeed theoretical calculations have shown that the GaN (0001) surface energy (γ_{0001}) increases for N rich conditions [96]. Also, it was suggested that making a growth interruption under vacuum

increases the (0001) surface energy [92, 99]. Growing (Al,Ga)N QDs can be made using either an NH_3 source or an N_2 plasma source. However, the growth of QDs occurs in a different way using each source, as it will be described in the following. For example, when growing under N-rich conditions the 2D-3D transition does not occur when using NH_3.

Quantum dots using ammonia source

Ammonia is historically used as the nitrogen source in CRHEA. Using NH_3, a 2D growth mode is obtained under N-rich conditions with typically a V/III ratio of 4 in the case of GaN [97]. However, the growth under NH_3 flux has some consequences on the growth process of nitride QDs. Taking the example of GaN grown on AlN (0001), no 2D-3D transition is observed during growth contrary to the case of GaN / AlN using a nitrogen plasma source. In fact, the presence of ammonia prevents the SK transition, whatever the deposited GaN layer thickness. It was shown that for GaN QDs formation, performing a growth interruption of the GaN layer under vacuum by switching off the NH_3 flux is required [83]. This means that during growth, the condition of equation I-32 is not respected and that the elastic energy gain is lower than the surface energy cost for island formation ($|\Delta E_{elastic}| < |\Delta\gamma|$), which prevents the formation of QDs. Then, with a growth interruption, the surface energy cost is reduced under vacuum and the energy balance is in favour of a (0001) surface covered by elastically relaxed faceted islands (Figure I-21). This means that under vacuum γ_{film} is higher and/or γ_{facet} is lower (i.e. $\gamma_{film}/\gamma_{facet}$ increases under vaccum), and the condition $|\Delta E_{elastic}| > |\Delta\gamma|$ is respected to have the 2D-3D transition. Indeed, calculations indicate that under NH_3 flux, the GaN (0001) surfaces with NH_2+NH_3 or NH +NH_2 chemisorbed species are the most stable [98]. Also, it was shown that hydrogenated surfaces with a large number of N-H bonds have significantly lower γ_{film} energies, and consequently higher surface energy cost for the formation of 3D islands ($|\Delta\gamma|$), than bare surfaces (without H). Then, when going from N-rich (under NH_3) to vacuum conditions, the (0001) surface energy (γ_{film}) increases [99], which induces a decrease of the surface energy cost ($|\Delta\gamma|$) leading to $|\Delta E_{elastic}| > |\Delta\gamma|$ and the formation of QDs through a 2D-3D transition. Calculations also showed that the surface energy cost decreases from 17 meV / Å^2 under H-rich conditions (NH_3) to 4 meV / Å^2 under vacuum [92].

To summarize, using an NH_3 source has an important impact for the growth of nitrides QDs, due to the influence of the hydrogenated surfaces which decrease γ_{film} (i.e. the {0001} surface energy) and consequently increase the surface energy cost associated to 3D island formation ($|\Delta\gamma|$). As a consequence, under NH_3 flux, no 2D-3D transition is taking place as $|\Delta\gamma|$ is higher than $|\Delta E_{elastic}|$. Then, under vacuum, $\Delta\gamma$ is decreased and becomes lower than $\Delta E_{elastic}$, allowing

the 2D-3D transition of the GaN layer. As will be seen in the case of QDs grown using an N_2 source (no hydrogen), $\Delta E_{elastic}$ is predominant and the 2D-3D transition is taking place directly.

The second important condition to fulfil for a 2D-3D transition is that the deposited amount has to be higher than the SK critical thickness (e.g. 3 MLs for the GaN / AlN system [99]). This 2D-3D transition can be monitored in-situ using the RHEED intensity monitoring during the change of the diffraction pattern from a streaky pattern (2D surface) to Bragg spots (3D surface) as presented in Figure I-21. We can also observe the QD facets which are forming an angle of 30° on the (0001) surface.

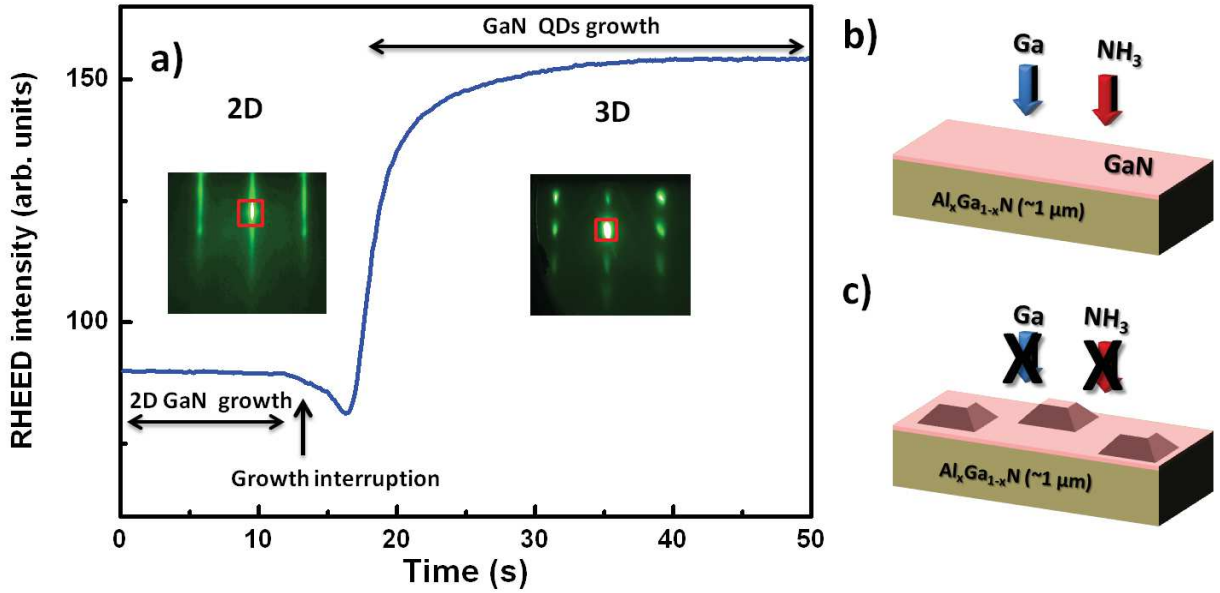

Figure I-21. a) Variation of the RHEED pattern intensity pattern recorded during the formation of GaN QDs using an ammonia source. The inset presents the RHEED figures for a 2D GaN layer and 3D GaN QDs with the red square presenting the postion where the intensity is measured. Schematics presenting the corresponding growth steps: a) deposition of a 2D GaN layer, b) QDs formation under vacuum.

Quantum dots using a plasma source

Growing GaN QDs using a plasma N_2 source can be achieved in a classical SK growth mode. This is possible by adjusting the growth conditions and more specifically when the growth is made under N-rich conditions (III/V < 1). As discussed before, N-rich conditions increase the (0001) surface energy (γ_{film})[96], then the growth favours the formation of 3D faceted structures. This surface energy increase is then associated to a decrease of the surface energy cost ($|\Delta\gamma|$) which is then lower than the elastic energy gain ($|\Delta\gamma| < |\Delta E_{elastic}|$) leading to a 2D-3D growth mode transition. This is different than NH_3 growth (performed under N-rich conditions) which requires a growth interruption to sufficiently decrease the surface energy cost. As discussed before, the presence of hydrogen, in the case of NH_3-QDs, has an important impact on the

surface energy and impact the 2D-3D transition [99]. Also as will be shown in chapter II, growing GaN QDs using an N_2 source results on the formation of higher QD densities compared to QDs grown using an NH_3 source, which is probably related to surface diffusion and the effect of hydrogen on the surface energy (as will discussed in chapter II). These results confirm that kinetics has an important role on the QD formation.

To summarize, when using a plasma N_2 source for GaN QDs, the 2D-3D transition process starts during growth in a classical Stranski-Krastanov mode contrary to the case of an NH_3 source where the transition happens during a growth interruption under vacuum after the 2D layer-by-layer deposition. This difference has been related to the surface energy contribution which strongly differs by using NH_3 or N_2 gas sources to fabricate the QDs. In the case of NH_3 growth, the 2D-3D transition has been associated with the desorption of NH_x species during the growth interruption and the vacuum annealing step [99].

References

[1] H. Morkoç Handbook of nitride semiconductor and devices Vol.1 page 2, (2009).

[2] F. Rol, PhD thesis " Etude optique de boîtes quantiques uniques non polaires de GaN/AlN", Université Joseph Fourrier Grenoble I (2007).

[3] B. Gil, Group III Nitride Semiconductor Compounds physics and Applications, (1998).

[4] H. Morkoç, S. Strite, G. B. Gao, M. E. Lin, B. Sverdlov, and M. Burns, J. Appl. Phys., vol. 76, no. 3, p. 1363, (1994).

[5] H. Amano, M. Iwaya, T. Kashima, M. Katsuragawa, I. Akasaki, J. Han, S. Hearne, J.A. Floro, E. Cheson, J. Fiegel, Jpn. J. Appl. Phys. 37, L1540 (1998).

[6] T. Kashima, R. Nakamura, M. Iwaya, H. Katoh, S.Yamaguchi, H. Amano, I. Akasaki, Jpn. J. Appl. Phys. 38, L1515 (1999).

[7] M. Iwaya, S. Terao, N. Hayashi, T. Kashima, H. Amano, I. Akasaki, Appl. Surf. Science 159-160, 405 (2000)

[8] L. Vegard. Z. Phys. 5, 17 (1921).

[9] M. Khoury, PhD thesis ”Metal Organic Phase Epitaxy of Semipolar GaN on Patterend Silicon Substrates” Université de Nice-Sophia Antipolis (2016).

[10] M. Kamp, C. Kirchner, V. Schwegler, A. Pelzmann, K.J. Ebeling, M. Leszczynski, I. Grzegory, T. Suskiand, and S. Porowski. Mat. Res. Soc. Symp.Proc. 537, G 10.2 (1999).

[11] B. Daudin, J. L. Rouvière, and M. Arlery. Appl. Phys. Lett. 69, 2480 (1996).

[12] S. K. Davidson, J. F. Falth, X. Y. Liu, H. Zirath, and T. G. Anderson, J. Appl. Phys. 98, 016109 (2005).

[13] O. Ambacher, J. Phys. D: Appl. Phys., 31, 2653 (1998).

[14] J. F. Nye, Physical Properties of Crystals, Oxford University Press, New York, (1985).

[15] A. F. Wright, Journal of Applied Physics 82, 2833 (1997).

[16] Kwiseon Kim, Walter R. L. Lambrecht, and Benjamin Segall, Physical Review B 53, 16310 (1996).

[17] C. Deger, E. Born, H. Angerer, O. Ambacher, M. Stutzmann, J. Hornsteiner, E. Riha, and G. Fischerauer, Applied Physics Letters 72, 2400 (1998).

[18] Laurie E. McNeil, Marcos Grimsditch, and Roger H. French, Journal of the American Ceramic Society 76, 1132 (1993).

[19] A. Polian, M. Grimsditch, and I. Grzegory, Journal of Applied Physics 79, 3343 (1996).

[20] A. Zoroddu, F. Bernardini, P. Ruggerone, and V. Fiorentini, Phys Rev B. 64, 045208 (2001).

[21] F. Bernardini and V. Fiorentini, Phys. Stat. Sol. (a), 190, 65 (2002).

[22] V. Fiorentini, F. Bernardini, and O. Ambacher, Appl. Phys. Lett. 80, 1204 (2002).

[23] F. Bernardini, V. Fiorentini, and D. Vanderbilt, Phys. Rev. B. 56, R10024 (1997).

[24] O. Ambacher, B. Foutz, J. Smart, J. R. Shealy, N. G. Weimann, K. Chu, M. Murphy, A. J. Sierakowski, W. J. Schaff, L. F. Eastman, R. Dimitrov, A. Mitchell, and M. Stutzmann, J. Appl. Phys. 87, 334 (2000).

[25] E. Fred Schubert, Light-emitting diodes. 2nd edition, Cambridge university press (2006).

[26] M. Leroux, N. Grandjean, M. Laugt, J. Massies, B. Gil, P. Lefebvre, and P. Bigenwald, Phys. Rev. B 58, R13371 (1998).

[27] R. Dingle, D. D. Sell, S. E. Stokowski and M. Ilegems, Phys. Rev. B, 4, 1211 (1971).

[28] T. Onuma, S. F. Chichibu, T. Sota, K. Asai, S. Sumiya, T. Shibata and M. Tanaka, Appl. Phys. Lett. 81, 652 (2002).

[29] B. Gil, O. Briot et R-L. Aulombard, Phys. Rev. B. 52, 17028 (1995).

[30] I. Vurgaftman and J.R. Meyer, J. Appl. Phys. 94, 3675 (2003)

[31] M. Leroux, S. Dalmasso, F. Natali, S. Helin, C. Touzi, S. Laugt, M. Passerel, F. Omnes, F. Semond, J. Massies, and P. Gibart. Phys. Stat. Sol. (b) 234, 887 (2002).

[32] Y. P. Varshni, Physica, 34, 149, (1967).

[33] J.Wu, W Walukiewicz, W. Shan, K. M. Yu, J.W Ager III, S. X. Li, E.E. Haller, Hai Lu and William J. Schaff, J. Appl. Phys., 94, 4457 (2003).

[34] Y. Li, Y. Lu, H. Shen, M. Wraback, M. G. Brown, M. Schurman, L. Koszi, and R. A. Stall, Appl. Phys. Lett., 70, 2458 (1997).

[35] S. Tripathy, R. K. Soni, H. Asahi, K. Iwata, R. Kuroiwa, K. Asami, and S. Gonda, J. Appl. Phys. 85, 8386 (1999).

[36] Q. Guo and A. Yoshida, Jpn. J. Appl. Phys. 33, 2453 (1994).

[37] T. Wethkamp, K. Wilmers, C. Cobet, N. Esser, W. Richter, O. Ambacher, M. Stutzmann, and M. Cardona, Phys. Rev. B 59, 1845 (1999).

[38] http://www.heliosquartz.com/wp-content/uploads/2016/01/Helios-Quartz_UV-LAMPS_eng.pdf

[39] https://www.techsil.co.uk/media/wysiwyg/pdf/UV_vs_LED.pdf

[40] G. Derra, H. Moench, E. Fischer, H. Giese, U. Hechtfischer, G. Heusler, A. Koerber, U. Niemann, F.-C. Noertemann, P. Pekarski, J. Pollmann-Retsch, A. Ritz, and U. Weichmann, J. Phys. Appl. Phys., 38, 2995 (2005).

[41] Y. Muramoto, M. Kimura, and S. Nouda, Semicond. Sci. Technol. 29, 084004 (2014).

[42] http://www.semiconductor-today.com/news_items/2017/jun/ledinside_150617.shtml

[43] Y. Narukawa, M. Ichikawa, D. Sanga, M. Sano, T. Mukai, J. Phys. D Appl. Phys. 43, 354002 (2010).

[44]M. Kneissl ``UV LED Efficiency 2015 (last update 19-July-2015)". http://www.researchgate.net/publication/280131929, (2015).

[45] S. Nitta, Y. Yukawa, Y. Watanabe, S. Kamiyama, H. Amano, I. Akasaki," Phys. Stat. Soli. (a) 194, 485 (2002).

[46] M. Kneissl, T. Kolbe, C. Chua, V. Kueller, N. Lobo, J. Stellmach, A. Knauer, H. Rodriguez, S. Einfeldt, Z. Yang, N. M. Johnson and M. Weyers, Semicond. Sci. Technol. 26 014036 (2011).

[47] M. Leroux, J. Brault, A. Kahouli, D. Elmaghraoui, B. Damilano, P. de Mierry, M. Korytov, J.-H. Kim, and Y.-H. Cho, J. Appl. Phys. 116, 034308 (2014).

[48] V. N. Jmerik, D. V. Nechaev, S. Rouvimov, V. V. Ratnikiv. P.S. Kopev, M. V. Rzheutski, E.V. Lutsenko, G. P. Yahlonskii, M. Aljohenii, A. Aljerwii and A. Alyamani, S. V. Ivanov J. Mater. Res. 30, 2871 (2015).

[49] D. V. Nechaev, P.A. Aseev, V.N. Jmerik, P.N. Brunkov, Y.V. Kuznetsova, A.A. Sitnikova, V.V. Ratnikov, S.V. Ivanov, J. Cryst. Growth 378, 319 (2013).

[50] J. Zhang , X. Hu , A. Lunev , J. Deng , Y. Bilenko, T. M. Katona, M.S. Shur, R. Gaska and M. A. Khan, Jpn. J. Appl. Phys. 44, 7250 (2005).

[51] H. Hirayama, T. Yatabe, N. Noguchi, T. Ohashi and N. Kamata, Appl. Phys. Lett. 91, 071901 (2007).

[52] M. Nemoz, R. Dagher, S. Matta, A. Michon, P. Vennéguès, J. Brault, J. Cryst. Growth, 461, 10 (2017).

[53] J. R. Grandusky, S. R. Gibb, M.C. Mendrick, C. Moe, M. Wraback and L.J. Schowalter, Appl. Phys. Express 4 082101 (2011).

[54] H. Wang, J-P. Zhang, C-Q. Chen, Q. Fareed, J-W. Yang, and M. Asif Khan, Appl. Phys. Lett., 81, 604 (2002).

[55] J. P. Zhang, H. M. Wang, M. E. Gaevski, C. Q. Chen, Q. Fareed, J. W. Yang, G. Simin, and M. A. Khan, Appl. Phys. Lett., 80, 3542 (2002).

[56] Y. Liao, C. Thomidis, C-K. Kao, and T.D. Moustakas, Appl. Phys. Lett. 98, 081110 (2011).

[57] J. Brault, S. Matta, T.-H. Ngo, M. Korytov, D. Rosales, B. Damilano, M. Leroux, P. Vennéguès, M. Al Khalifioui, A. Courville, O. Tottereau, J. Massies, and B. Gil, Jpn. J. Appl. Phys 55, 05FG06 (2016).

[58] C. Himwas, R. Songmuang, L. S. Dang, J. Bleuse, L. Rapenne, E. Sarigiannidou, and E. Monroy, Appl. Phys. Lett. 101, 241914 (2012).

[59] S. M. Islam, V. Protasenko, K. Lee, S. Rouvimov, J. Verma, H. Xing, and D. Jena, Appl. Phys. Lett. 111, 091104 (2017).

[60] V. N. Jmerik, E. V. Lutsenko, and S. V. Ivanov, Phys. Stat. Sol. (a) 210, 439 (2013).

[61] Y. Taniyasu, M. Kasu, and T. Makimoto, Nature 441, 325 (2006).

[62] T. Takano, T. Mino, J. Sakai, N. Noguchi, K.Tsubaki, and H. Hirayama, Appl. Phys. Express 10, 031002 (2017).

[63] N. H Tran, B.H Le, S. Zhao, Z. Mi, Appl. Phys. Lett. 110, 032102 (2017).

[64] A. Fujioka, T. Misaki, T. Murayama, Y. Narukawa and T. Mukai, Appl. Phys. Express 3, 041001 (2010).

[65] H. Hirayama, Y. Tsukada, T. Maeda, and N Kamata, Appl. Phys. Express 3, 031002 (2010).

[66] R. France, T. Xu, P. Chen, R. Chandrasekaran, and T.D. Moustakas, Appl. Phys. Lett. 90, 062115 (2007).

[67] B. Zhang, W. Lin, S. Li, Y. Zheng, X. Yang, D. Cai, and J. Kang, J. Appl. Phys., 111, 113710 (2012).

[68] N. Maeda and H. Hirayama, Phys. Stat. Sol. (c) 10, 1521 (2013).

[69] T. H. Seo, B. K. Kim, G. Shin, C. Lee, M. J. Kim, H. Kim, and E.-K. Suh, Appl. Phys. Lett. 103, 051105 (2013).

[70] T.N. Oder, K.H. Kim, J.Y. Lin, H.X. Jiang, Appl. Phys. Lett. 84, 466 (2004).

[71] M. Kneissl and J. Rass, "III Nitride ultraviolet emitters", Springer International Publishing, chapter I (2016).

[72] M. Ichikawa, A. Fujioka, T. Kosugi, S. Endo, H. Sagawa, H. Tamaki, T. Mukai, M. Uomoto, and T. Shimatsu, Appl. Phys. Express 9, 072101 (2016).

[73] K.B. Nam, J. Li, M.L. Nakarmi, J.Y. Lin, and H.X. Jiang, Appl. Phys. Lett. 84, 5264 (2004).

[74] Y. Zhang, S. Krishnamoorthy, F. Akyol, A. A. Allerman, M. W. Moseley, A. M. Armstrong, and S. Rajan Appl. Phys. Lett. 109, 121102 (2016).

[75] X. Rong, X. Wang, S. V. Ivanov, X. Jiang, G. Chen, P. Wang, W. Wang, C. He, T. Wang, T. Schulz, M. Albrecht, V. N. Jmerik, A. A. Toropov, V. V. Ratnikov, V. I. Kozlovsky, V. P. Martovitsky, P. Jin, F. Xu, X. Yang, Z. Qin, W. Ge, J. Shi, and B. Shen, Adv. Mater., 28, 7978-7983 (2016).

[76] F. Tabataba-Vakili, T. Wunderer, M. kneissl, Z. Yang, M. Teepe, M. Batres, M. Feneberg, B. Vancil and N. M. Johnson, Appl. Phys. Lett. 109, 181105 (2016).

[77] https://www.physik.uni-kl.de/en/hillebrands/research/methods/molecular-beam-epitaxy/

[78] D. Schikoraj, M. Hankelni, D. J. As, K. Lischka, T. Litz, A. Waag, T. Buhrow, and F. Henneberger. Phys. Rev. B.54, 8381 (1996).

[79] A. Botchkarev, A. Salvador, B. Sverdlov, J. Myoung, and H. Morkoc. J. Appl. Phys. 77, 4455 (1995).

[80] B. Daudin, F. Widmann, G. Feuillet, Y. Samson, M. Arlery, and J. L. Rouvière. Phys. Rev. B. 56, 7069 (1997).

[81] S. Yoshida, S. Misawa, and S. Gonda. Appl. Phys. Lett. 42, 427 (1983).

[82] Z. Yang, L. K. Li, and W. I. Wang. Appl. Phys. Lett. 67, 1686 (1995).

[83] B. Damilano, N. Grandjean, F. Semond, J. Massies, and M. Leroux., Appl. Phys. Lett. 75, 962 (1999).

[84] M. Mesrine, N. Grandjean, and J. Massie, Appl. Phys. Lett. 72, 350 (1998).

[85] N. Grandjean, J. Massies, P. Vennéguès, M. Leroux, F. Demangeot, M. Renucci and J. Frandon, J. Appl. Phys., Vol. 83, 1379 (1998).

[86] P. K. Kandaswamy, F. Guillot, E. Bellet-Amalric, E. Monroy, L. Nevou, M. Tchernycheva, A. Michon, F. H. Julien, E. Baumann, F. R. Giorgetta, D. Hofstetter, T. Remmele, M. Albrecht, S. Birner, and L. S. Dang, J. Appl. Phys. 104, 093501, (2008).

[87] E. Iliopoulos and T. D. Moustakas, Appl. Phys. Lett. 81, 295, (2002).

[88] T.D. Moustakas, MRS Communications, 6, 247 (2016).

[89] E.H.C Parker, "The technology and physics of molecular beam epitaxy" Springer US (1985).

[90] R. Dujardin, PhD thesis "Epitaxie par jets moléculaires de nanostructures isolées de germanium sur silicium", Université Joseph-Fourier Grenoble I, (2006).

[91] F. Tinjod and H. Mariette, Phys. Stat. Sol. (b) 241, 550 (2004).

[92] H. Mariette. C. R. Physique. 6, 23 (2005).

[93] F. Tinjod, PhD thesis "Mécanismes de formation des boîtes quantiques semiconductrices, application aux nanostructures II-VI et étude de leurs propriétés optiques" (2003).

[94] J. Tersoff and R.M. Tromp, Phys. Rev. Lett. 70, 2782 (1993).

[95] L. Goldstein, F. Glas, J. Y. Marzin, M. N. Charasse, and G. Le Roux. Appl. Phys. Lett. 47, 1099 (1985).

[96] J. Elsner, M. Haugk, G. Jungnickel, and Th. Frauenheim, Solid State Commun. 106, 739 (1998).

[97] N. Grandjean, M. Leroux, J. Massies, M. Mesrine and M. Laugt, Jpn. J. Appl. Phys. Vol. 38, 618 (1999).

[98] C. G. Van de Walle and J. Neugebauer, Phys. Rev. Lett. 88, 066103 (2002).

[99] B. Damilano, J. Brault, and J. Massies, J. Appl. Phys. 118, 024304 (2015).

Table of Contents

II. GaN quantum dots

In this chapter, GaN quantum dots (QDs) grown using plasma N_2 and ammonia (NH_3) sources will be presented. The difference between the two growth techniques will be discussed. The role of the epitaxial strain in the QD self-assembling process will also be studied by fabricating GaN QD planes on different $Al_xGa_{1-x}N$ templates with $0.5 \leq x \leq 0.7$. Photoluminescence (PL) measurements performed on the samples account for the main influence of the internal electric field (F_{int}) on the QD optical response. Time resolved photoluminescence measurements combined with temperature dependent PL measurements enabled the estimation of the QD internal quantum efficiencies at low and room temperatures. In addition, a PL integrated intensity ratio up to 75 % is shown between 9 K and 300 K.

II.1 Introduction and samples structure

As described in chapter I, an intense research activity is currently dedicated to the improvement of UV emitters efficiency. For blue (In,Ga)N / GaN LEDs, carrier localization in (In,Ga)N was shown to be one of the main mechanism to reach high efficiencies, (i.e. with external quantum efficiency (EQE) values up to 84 % [1]), although the presence of high defect densities in the active region, with dislocation densities (DDs) in the $10^7 - 10^9$ cm^{-2} range [2]. For UV emitters, (Al,Ga)N materials are used, for which the crystalline quality is found to be plagued with a significant increase of the dislocation densities compared to GaN, with DDs in the 10^9 - 10^{11} cm^{-2} ranges [3]. Therefore, the use of QDs is an attractive solution to improve the carrier localization and thus increase the internal quantum efficiency in (Al,Ga)N based heterostructures since they can provide a confinement of carriers along the three dimensions and, as a consequence, forbid their diffusion towards surrounding defects, which act as non radiative recombination centers.

The samples studied in this thesis were grown in a Riber 32P MBE reactor. Solid sources were used for the III-elements (Al, Ga) and two different sources were used for nitrogen, either ammonia (NH_3) or nitrogen (N_2) gas. In fact, NH_3 was mainly used for the growth of the heterostructures, except for the fabrication of QDs for which either NH_3 or N_2 were used.

For GaN QD active layers, NH_3 or N_2 sources can be used and the fundamental difference between the growth using both techniques was presented in chapter I.3.4. In this chapter, two series of GaN QDs grown using either an N_2 or an NH_3 source will be presented. The main

characteristics of the QD growth while using each technique will be presented in part II-2 and part II-3, respectively.

The basic sample structure and the growth procedure are presented on Figure II-1. All the samples were grown on sapphire substrates oriented along the c-axis, as followed:

1) First of all, a nitridation step of the sapphire substrate is performed under ammonia flux at high temperature (~ 900 - 950°C) in order to form ~ 1 MLs of AlN. This step was shown to improve the morphological and optical properties of the heterostructures [4].

2) A GaN buffer layer of 30 nm is then grown at low temperature (~ 450°C) [5], followed by

3) a 120 nm thick AlN layer, grown at around 900 - 950°C. The role of this layer is to exert a compressive strain on the above $Al_xGa_{1-x}N$ layer and hence avoid the formation of cracks [6].

4) Then, an $Al_xGa_{1-x}N$ layer (≈ 1 µm), used as a template, is grown at a temperature range between 850 - 880°C (depending on the x_{Al} composition of the layer, with higher temperatures used for higher x_{Al} compositions).

5) On such an $Al_xGa_{1-x}N$ template, a GaN QD plane is grown, using either an N_2 plasma source or an NH_3 source. This procedure is then followed by an annealing step under vacuum, which duration corresponds to the maximum intensity of Bragg spots observed by RHEED during the QD formation [7].

6) A cap of 30 nm of $Al_xGa_{1-x}N$ barrier is then grown on top of the QD plane at the same temperature as the template.

7) Finally, an uncapped QD plane on the surface is also grown to study the morphological properties of the QDs, using atomic force microscopy (AFM) and scanning electron microscopy (SEM).

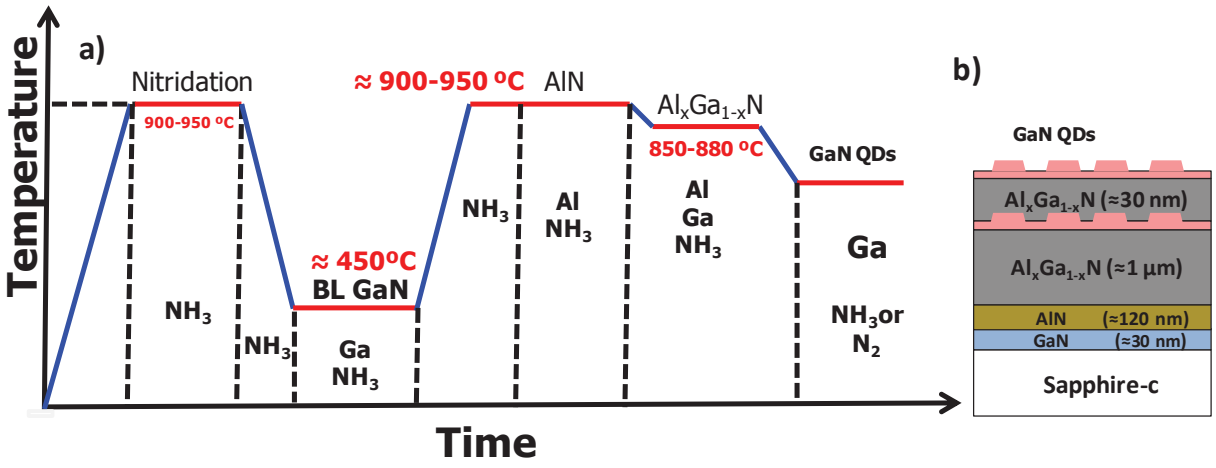

Figure II-1. Schematics presenting a) the growth procedure and b) the final structure designed to investigate the QD properties.

These two different growth techniques used for the fabrication of GaN QDs will be presented with the twofold aim to: 1) study the impact of carrier localization inside the QDs on the radiative efficiency, and 2) choose the best approach for UV emission.

The lattice mismatch $\left(\frac{\Delta a}{a} = \frac{a_{GaN} - a_{Al_xGa_{1-x}N}}{a_{Al_xGa_{1-x}N}}\right)$ is one of the main parameters at the origin of a change in the epitaxial layer morphology and can lead to the formation of QDs (as described in chapter I) as deeply investigated in the arsenides, phosphides, selenides [8] or SiGe [9] material systems. It is also at stake in the case of nitride QDs. An important difference with the previously quoted material systems comes from the strong values of the polarization induced electric field in nitride heterostructures (cf. chapter I.1.2.2), in particular for those oriented along the c axis of the wurtzite structure. This leads to the presence of an internal electric field discontinuity (ΔF) at interfaces equal to (as discussed in chapter I.1.2.2 equation I-20):

$$\Delta F = \frac{\sigma}{\varepsilon_0 \varepsilon} \qquad \text{(II-1)}$$

where σ is the interfacial charge density (σ = ΔP) and ε_0 is the vacuum dielectric permittivity. It is assumed that barriers and QD planes have a similar static dielectric constant ε.

In parts II.2 and II.3, both the influence of the epitaxial strain (determined by the lattice mismatch between the GaN QD layer and the $Al_xGa_{1-x}N$ matrix), and the influence of the polarization discontinuities at the GaN QD / $Al_xGa_{1-x}N$ interfaces (which lead to the quantum confined Stark effect (QCSE) [10]) will be studied. Also, the influence of kinetics, which plays an important role in the formation of QDs, will be studied by comparing the properties of GaN QDs grown using i) an N_2 plasma source, i.e. by so-called plasma assisted MBE (PAMBE), and ii) an NH_3 source, i.e. using ammonia MBE (NH_3-MBE) in part II.4.

II.2 Growth of GaN QDs using an N_2 source (PAMBE)

In this part, a series of three GaN QD / $Al_xGa_{1-x}N$ (0001) ($0.5 \leq x \leq 0.7$) samples were first designed to study the influence of the lattice and polarization mismatches by varying the Al concentration of the $Al_xGa_{1-x}N$ layers. This sample structure enabled us to modify the QD size and density as a function of the lattice-mismatch and to vary the strength of the Stark effect on the QD optical properties.

This series consists of three GaN QD samples grown on different $Al_xGa_{1-x}N$ matrices: GaN / $Al_{0.5}Ga_{0.5}N$, GaN / $Al_{0.6}Ga_{0.4}N$, and GaN / $Al_{0.7}Ga_{0.3}N$ QDs labeled sample A, B and C, and corresponding to lattice mismatch values (Δa/a) of 1.19 ± 0.06 %, 1.43 ± 0.06 % and 1.67 ± 0.06 % respectively. The Al concentration in the matrices (x_{Al}) is a nominal concentration determined, on 2D layers, by energy dispersive X-ray (EDX) spectroscopy with a typical error margin of ±

2.5 %. The lattice mismatch uncertainty is determined from the Al composition variation of the $Al_xGa_{1-x}N$ templates. GaN QDs were grown, in this part, using an N_2 source (i.e. by PAMBE). When using a plasma N_2 source, the 2D-3D transition process starts during growth in a classical Stranski-Krastanov mode [11], as described in chapter I.3.4. The growth conditions for QDs were held as much as possible the same, with a deposited amount of 6 ± 0.5 MLs, a III/V flux ratio of 0.7 and a growth temperature of 765°C ± 10°C. Figure II-2 shows an example of the RHEED intensity variation during the growth of GaN QDs. When using an N_2 plasma source, the 2D-3D transition process starts during growth in a classical Stranski-Krastanov mode.

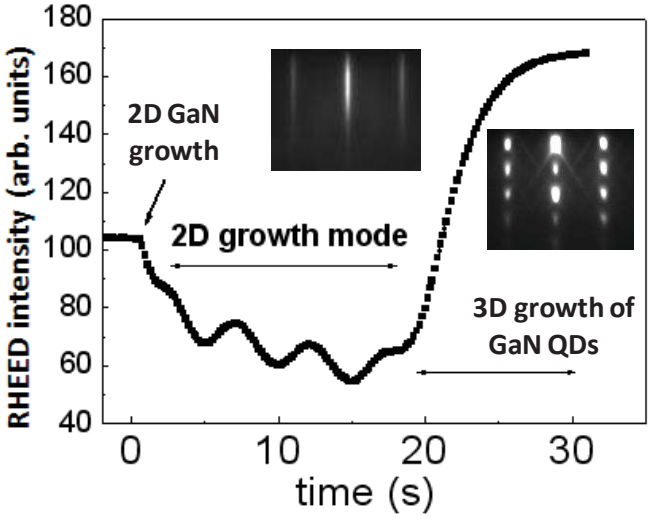

Figure II-2. Variation of the RHEED intensity during the growth of GaN quantum dots with an N_2 plasma source. The insets show RHEED images for 2D and 3D GaN surface morphologies.

II.2.1 Morphological properties

As a first step, the morphological properties of the three samples were studied by atomic force microscopy (AFM). Figure II-3 shows the impact of increasing the x_{Al} content in the $Al_xGa_{1-x}N$ matrix on the formation of GaN QDs. We can clearly see that while increasing the Al concentration (from 0.5 to 0.7), and hence the lattice mismatch value (Δa/a varying from 1.19 % to 1.67 %), higher QD densities (increasing from 2 x 10^{10} to 3 x 10^{11} cm^{-2}) and smaller QD dimensions (the average height (h_{QD}) decreasing from 5 nm to 3.5 nm and the average diameter (d_{QD}) from 45 nm to 23 nm) are obtained, as shown in Table II-1.

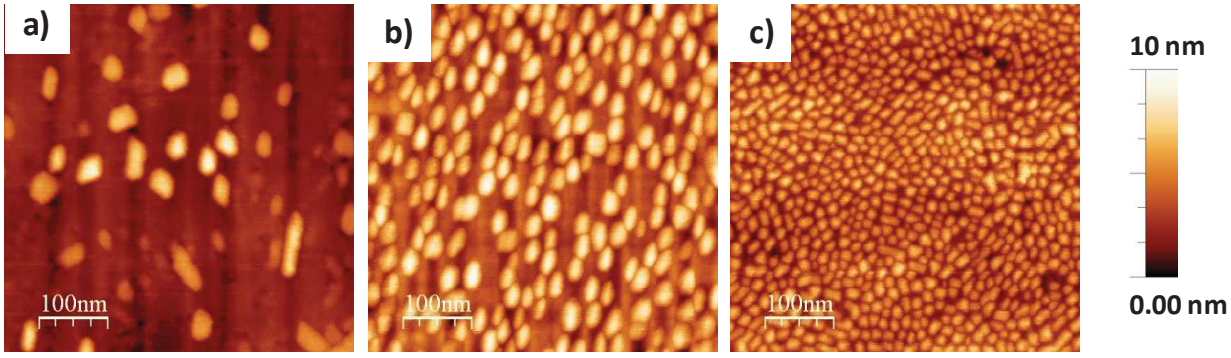

Figure II-3. AFM images of GaN QDs grown, using an N_2 plasma source, on $Al_xGa_{1-x}N$ (0001) with x equals to a) 0.5 (sample A), b) 0.6 (sample B) and c) 0.7 (sample C).

Scanning electron microscopy (SEM) complementary measurements (Figure II-4) were performed to have a more precise measure of the QD diameter. Average diameters were found to be (31 ± 9) nm, (20 ± 3) nm and (11 ± 1.5) nm for x = 0.5, 0.6 and 0.7. These lower lateral dimensions, compared with the AFM values, are attributed to the convolution effect between the AFM tip and the QDs. The QD density values are found to be close to the AFM ones with values varying between 2 x 10^{10} cm^{-2} for sample A, 1 x 10^{11} cm^{-2} for sample B and 5.5 x 10^{11} cm^{-2} for sample C (see Table II-1).

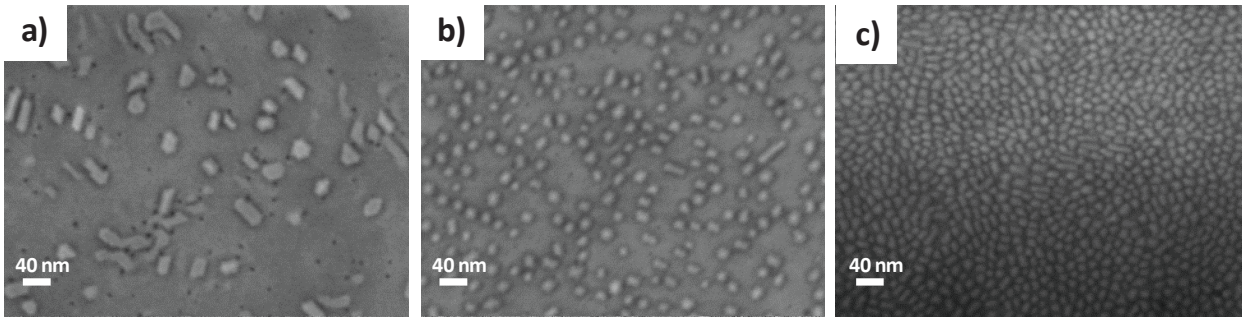

Figure II-4. SEM images of GaN QDs grown on $Al_xGa_{1-x}N$ (0001) with x equals to a) 0.5 (sample A), b) 0.6 (sample B) and c) 0.7 (sample C).

Finally, the morphological properties of the QDs were completed by cross sectional high-angle annular dark-field imaging in scanning transmission electron microscopy mode (HAADF - STEM). Figure II-5 shows the QD planes of sample B. The buried QDs have a pyramidal shape with a truncated top, and present an average height and diameter of (4.6 ± 0.8) nm and (22.6 ± 7.4) nm respectively. These values are in good agreement with the average height determined by AFM on surface QDs, and the average diameter determined by SEM. We can also observe the presence of a 2D GaN wetting layer (WL) connecting the QDs, with a thickness of 0.7 nm to 1 nm (3 MLs to 4 MLs), in agreement with previous studies [12, 13]. From these results, it appears that the average height of the buried QDs (measured by TEM), including the WL thickness, can

fairly be estimated from the average height of the QDs on surface measured by AFM (without taking the WL thickness into account).

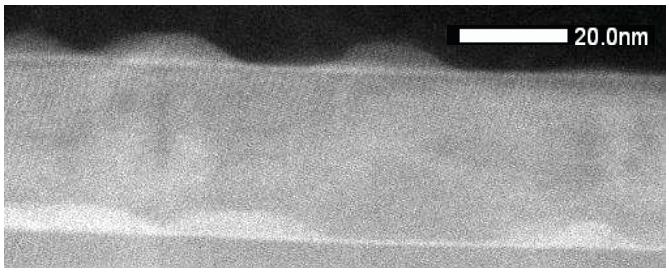

Figure II-5. Cross-sectional HAADF - STEM image of the GaN QD / $Al_{0.6}Ga_{0.4}N$ (0001) structure (sample B), consisting of a buried QD plane and a QD plane at the surface.

II.2.2 Optical properties

In a first stage, we studied the continuous wave photoluminescence (PL) characteristics of the samples at 9 K (Figure II-6) using a frequency-doubled argon (Ar) laser with an excitation wavelength of 244 nm (i.e. 5.08 eV), a laser spot diameter around 120 µm and an excitation power of 30 mW (corresponding to 2.6 x 10^{20} photons / sec.cm^2). Different transitions are observed: a high energy band varying from 4.43 eV (for x = 0.5) to 4.73 eV (for x = 0.7), which comes from the luminescence of the $Al_xGa_{1-x}N$ barriers; a band around 4 eV observed in Figure II-6 (a) and (b) which is attributed to the GaN wetting layer [14] and finally, a dominant band found between 3.22 eV and 2.95 eV (depending on the x_{Al} matrice composition), which originates from the QD emission. Noteworthy, the PL emission from the QDs is found at a lower energy than the energy of the GaN strained band gap (~ 3.5 eV for bulk GaN) [15]. This is related to the quantum confined Stark effect (QCSE) due to the large internal electric field (of the order of a few MV / cm) inside the heterostructures [10, 16].

Yet, since the quantum confinement is enhanced for smaller QDs, a shift toward shorter wavelengths could be expected [13] when going from GaN QDs grown on lower to higher Al content in $Al_xGa_{1-x}N$ layers, i.e. from sample A to sample C. Indeed, the PL properties of QDs can be deduced from the QD height as a first approximation since the QD base to height ratio is around or larger than 4. Indeed, due to the high effective mass in nitrides, lateral confinement effects are then minimized compared to confinement effects along the growth direction [17]. However, the PL measurements (Figure II-6) show a red shift, from 385 nm to 420 nm (i.e. 3.22 eV to 2.95 eV), when x_{Al} in the matrix increases. Figure II-7(a) also shows the PL red shift for the three samples at 300 K. This shift is due to the increase of the polarization induced electric field F_{int} inside the QDs with x_{Al}, leading to a stronger bending of the band structure (resulting from the QCSE) and consequently red-shifting the PL emission, which will be presented in further details in the next paragraph.

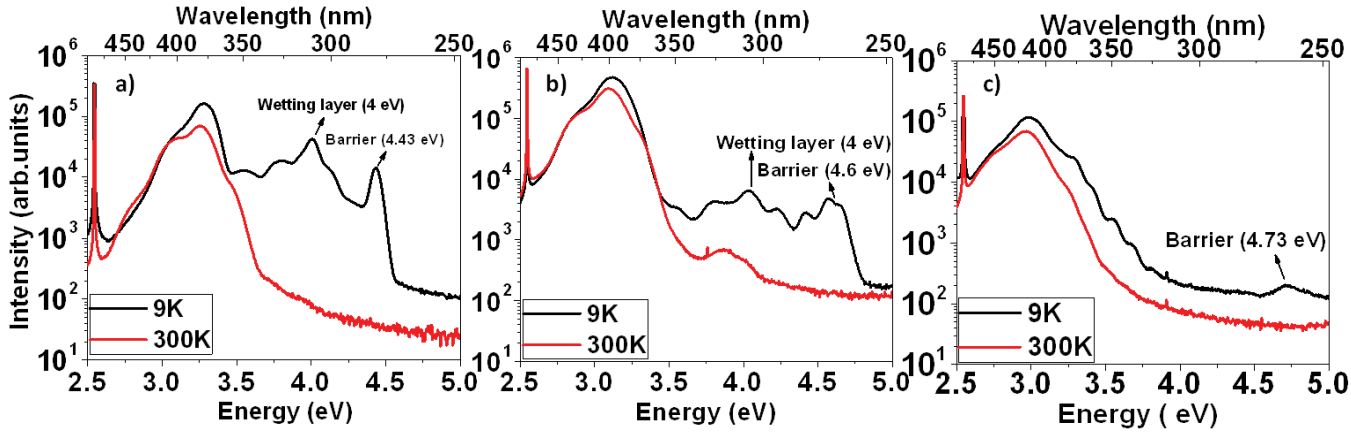

Figure II-6. Low temperature and room temperature PL spectra of a) GaN / $Al_{0.5}Ga_{0.5}N$ (sample A), b) GaN / $Al_{0.6}Ga_{0.4}N$ (sample B), and c) GaN / $Al_{0.7}Ga_{0.3}N$ (sample C). The peak at 488 nm is the excitation laser fundamental transition.

In order to further study the influence of F_{int}, power dependent PL measurements have been performed. A blue shift of the QD PL energy is observed while increasing the injected power. The origin of this shift is well-known as the result of the gradual screening of the Stark effect by the carriers injected in the QDs [17, 18]. Figure II-7(b) shows the energy shift for the three samples, for an excitation power varying between 9.5 µW and 30 mW. We can see an energy shift of 330 meV for sample A, i.e. with an average QD height (h_{QD}) of 5 nm, and a smaller shift of 250 meV for sample C, i.e. with a smaller average h_{QD} of 3.5 nm, the shift value for sample B falling in between these two extrema (320 meV). These characteristics are in good agreement with the previous studies in the GaN / $Al_{0.5}Ga_{0.5}N$ (0001) QD system [16, 19].

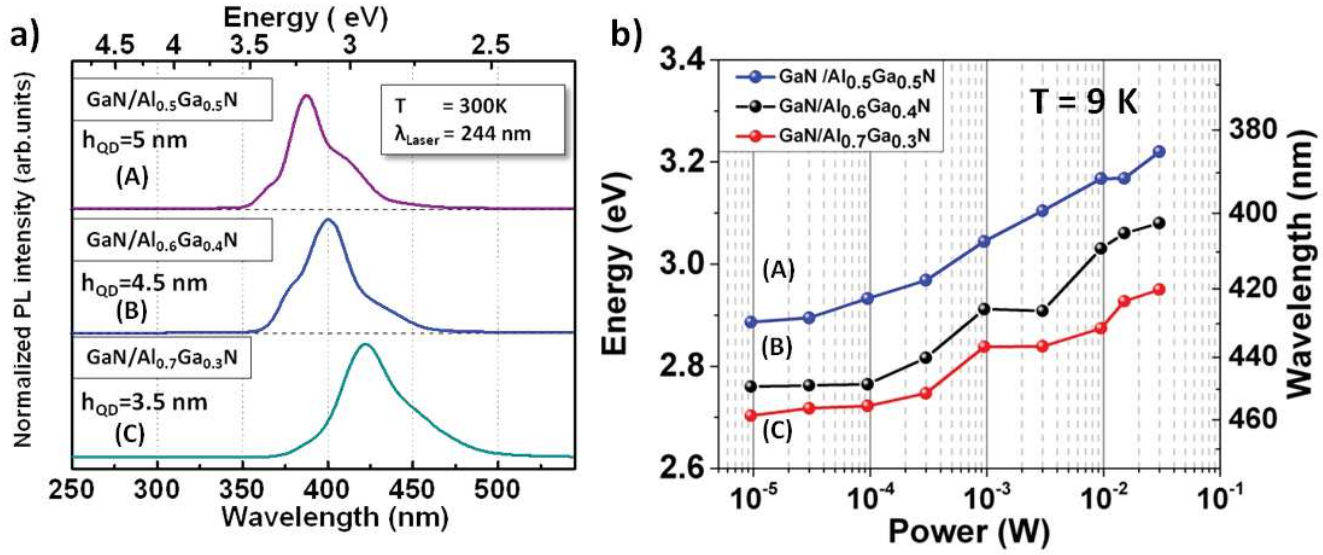

Figure II-7. a) PL spectra at room temperature and b) power dependence PL energy, at 9 K, for GaN / $Al_xGa_{1-x}N$ (0001) QDs with x_{Al} equals to 0.5 (sample A), 0.6 (sample B) and 0.7 (sample C).

Recalling that we assimilate our disk-shaped QDs to QWs (i.e. we neglect lateral confinement effects), the fundamental transition energy of a dot is:

$$E_{e1-hh1} = E_{QD} + E_g^{QD} - E_{Ry} - eF_{int}h_{QD} \quad \text{(II-2)}$$

where E_{QD} refers to the quantum confinement energy in the QD conduction and valence bands obtained by using the envelop function formalism, E_g^{QD} is the band gap energy of the dot material (strained GaN in this case), the Rydberg energy (E_{Ry}) corresponds to the excitonic binding energy, F_{int} is the electric field inside the dot and h_{QD} is the mean QD height. In order to verify the increase of F_{int} with increasing x_{Al} in the matrix, F_{int} and the total electric field discontinuity ΔF were estimated for the three samples using equation (II-2). We assume a near unity quantum efficiency at low temperature, as the spectrally integrated intensity is constant for $T \leq 80$ K, and use the mean QD height in each sample, as given in Table II-1. The PL energies under low excitation (i.e. with an almost unscreened electric field) are considered.

Figure II-8 compares our estimated values of the field discontinuity for the three samples (varying between 3, 3.8 and 5.3 MV / cm for sample A, B and C respectively) with that in other GaN / $Al_xGa_{1-x}N$ (0001) heterostructures as a function of x_{Al}. The data presented for $x < 0.3$ correspond to GaN / $Al_xGa_{1-x}N$ QWs [20, 21, 22], and for $x > 0.3$ to GaN / $Al_xGa_{1-x}N$ QDs [16, 17, 23].

There is a fair agreement with the expected variation with the barrier composition of ΔF, for structures grown on relaxed barriers, which is our case. Note that in view of the crudeness of the approximations made, we do not claim to give precise values of ΔF, but that the red shift observed for the PL of samples A to C is consistent with reasonable values of ΔF. Finally, it is clear that the photoluminescence optical properties of GaN / $Al_xGa_{1-x}N$ (0001) QDs are mainly determined by the Stark effect in this Al concentration range and for QD heights typically above 3 nm.

To complete the optical characterizations, low temperature PL measurements were compared to room temperature (T) ones (Figure II-6). The room T to low T intensity ratios obtained for samples A, B and C, are 61 %, 75 % and 57 %, respectively (see Table II-1). The radiative efficiency differences among the structures will be discussed in more details in the next paragraph. We can also see on Figure II-6 that the intensity of the barriers and the wetting layers luminescence at 9 K are at least one order of magnitude lower than the QD emission peak intensity, testifying of efficient capture of carriers by the dots. In addition, the PL peaks of the barriers and the wetting layers, which are 2D layers, are either unobservable or extremely weak at 300 K. These results clearly show the interest of using QDs (3D) instead of QWs (2D) to

confine the excitons and prevent them from recombining non radiatively with surrounding defects.

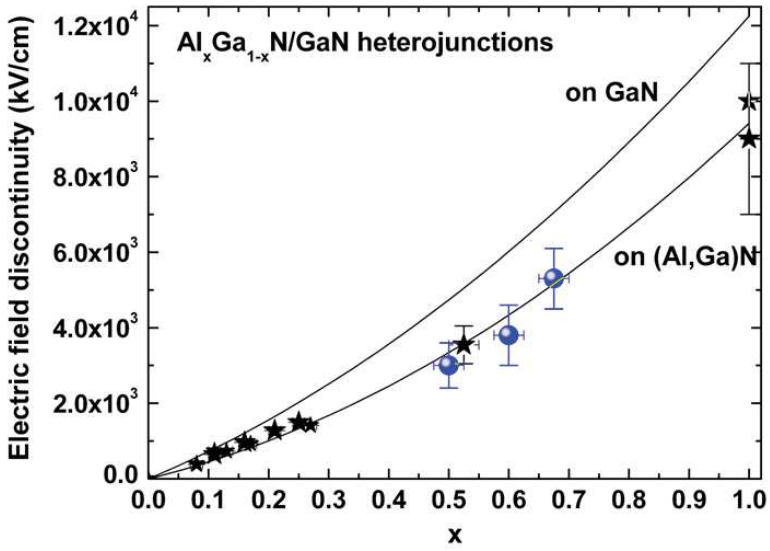

Figure II-8. Estimated electric field discontinuity for sample A, B, and C (bold blue dots), and comparison with values reported in the literature for GaN / $Al_xGa_{1-x}N$ QDs [16], (Al,Ga)N quantum wells [20, 21, 22], GaN / AlN QDs [17], and GaN / AlN superlattices [23].

To go a step further in the understanding of the origin of the better radiative properties of sample B, XRD measurements were performed. As given in Table II-1, the ω-scan full width at half maximum (FWHM) values of symmetric and asymmetric diffractions are minimum for sample B, accounting for a structural improvement of the $Al_xGa_{1-x}N$ layer, in particular a reduction of the threading dislocation density [24]. Dislocations being non radiative recombination centers, a decrease of non-radiative processes in sample B could be expected, either for directly injected carriers in the barriers and / or wetting layer or those thermally activated from the QDs to the barriers and wetting layer. However, the assumption of the non radiative recombination due to thermally activated QDs is not straightforward as it is difficult to have a precise information of the localization of the non radiative centers (dislocations, Shockley–Read–Hall centers, points defects), near the QDs or inside them. In fact, while increasing the temperature, several mechanisms can be at stake: the spreading of the electron and hole wavefunctions increases, which could lead to a delocalization of the carriers (excitons), or to the filling of excited states whose spatial extension also increases, enhancing the probability to encounter and recombine with non radiative centers. Consequently, such mechanisms imply that the barrier structural quality could potentially impact on the radiative efficiency of the QD layers. However, this influence is not always straightforward, and at least not the main parameter as will be discussed in part II.4.

Table II-1: Summary of the main structural and optical properties of GaN (6 MLs) QDs grown, using N_2 plasma source, on different $Al_xGa_{1-x}N$ (0001) templates.

Samples	QD height (nm) (AFM)	QD diameter (nm) (SEM)	X-Ray FWHM (°) 0002/30-32	QDs density (cm^{-2})	PL energy at 9 K / 300 K (eV)	I(300K) / I(9K) (%)
GaN(QDs)/ $Al_{0.5}Ga_{0.5}N$ (Sample A)	5 ± 1	31 ± 9	0.4/0.73	2×10^{10}(AFM) / 2×10^{10} (SEM)	3.22/3.19	61
GaN(QDs)/ $Al_{0.6}Ga_{0.4}N$ (Sample B)	4.5 ± 0.8 / 4.6 ± 0.8 (TEM buried plane)	20.3 ± 3 / 22.6 ± 7.4 (TEM buried plane)	0.34/0.73	9×10^{10} (AFM) / 1×10^{11} (SEM)	3.11/3.08	75
GaN(QDs)/ $Al_{0.7}Ga_{0.3}N$ (Sample C)	3.5 ± 0.6	11 ± 1.5	0.35/0.93	3×10^{11} (AFM) / 5.5×10^{11} (SEM)	2.95/2.93	57

II.3 Growth of GaN QDs using an ammonia source

In this part, GaN QDs were **grown using an ammonia source** (NH_3-MBE)**.** The deposited amounts were held the same as for QDs grown using an N_2 source (PAMBE), with a deposited amount of 6 ± 0.5 MLs, a growth temperature of 805°C ± 15°C and a III/V ratio around 0.1.

A series of three GaN QD / $Al_xGa_{1-x}N$ (0001) ($0.5 \leq x \leq 0.7$) samples were grown in order to compare them with the QDs series grown using PAMBE. Those samples are GaN / $Al_{0.5}Ga_{0.5}N$, GaN / $Al_{0.6}Ga_{0.4}N$ and GaN / $Al_{0.7}Ga_{0.3}N$ QDs, labeled as sample D, E and F in the following.

The use of ammonia has important consequences on the GaN QDs growth (cf. chapter I). This is observed experimentally as the 2D-3D transition is not a standard Stranski-Krastanov growth mode as observed while using an N_2 plasma source. A different growth procedure is required. In fact, no 2D-3D transition is happening during growth (i.e. during the deposition of Ga and NH_3). As presented on Figure II-9, the 2D GaN layer by layer is first deposited then a growth interruption under vacuum is required to trigger the 2D-3D transition [25].

This growth procedure difference, compared to PAMBE, is mainly due to the presence of NH_x species while using an ammonia source. Indeed, these species were shown to reduce the (0001) GaN surface energy and thus to increase the surface energy cost $\Delta\gamma$ when going from a 2D to a 3D morphology, inhibiting the 2D-3D transition [7]. Along this view, the 2D growth of GaN observed under NH_3 rich conditions, whereas the triggering of a 2D-3D transition by switching off the NH_3 flux (i.e. by performing a growth interruption as shown in figure II-9), is due to a strong decrease of the surface energy cost ($\Delta\gamma$) under vacuum compared to the surface energy cost under NH_3. Actually, the surface energy cost has been estimated to decrease from 17 meV / Å^2 under H-rich conditions ($\Delta\gamma_{(NH3)}$) to 4 meV / Å^2 under vacuum ($\Delta\gamma_{(vacuum)}$) [26].

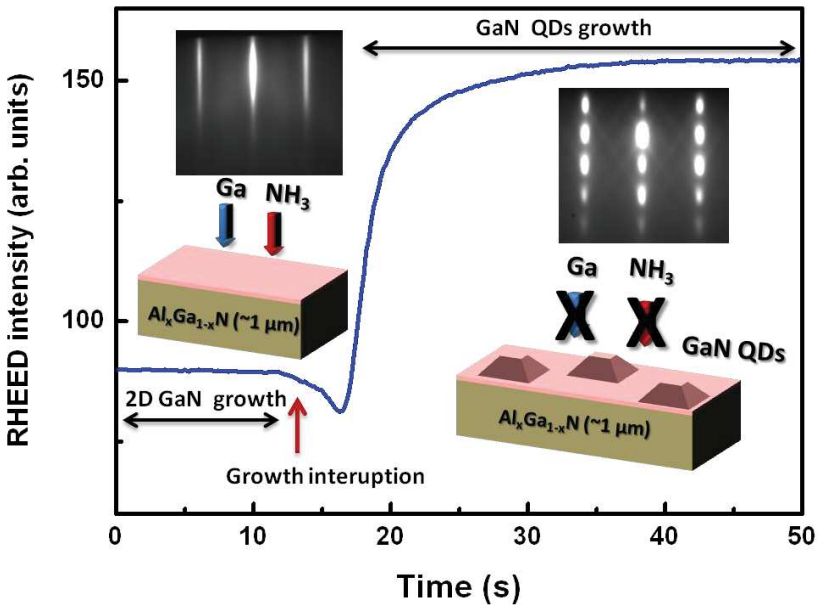

Figure II-9. Variation of the RHEED intensity during the growth of GaN QDs by NH_3-MBE. The inset shows a schematics of the 2D-3D morphology of GaN and RHEED images for 2D and 3D GaN surface morphologies.

II.3.1 Morphological properties

The three samples were first characterized by AFM (Figure II-10). As we can see, by increasing x_{Al} in the $Al_xGa_{1-x}N$ template from 0.5 to 0.7, and hence the lattice mismatch, the QD density increases, from 2.7 x 10^{10} cm^{-2} up to 1.2 x 10^{11} cm^{-2}, and their height decreases from 4.6 nm to 3.4 nm. This is in agreement with QDs grown by PAMBE which also showed an increase of the QD density and a decrease of their size while increasing x_{Al}. However, the main difference while using NH_3-MBE is the clear tendency of QDs to nucleate on the steps of the $Al_{0.5}Ga_{0.5}N$ surface. We can also see a modulation of the surface topography at a large scale on the AFM images. This specific feature originates from the growth of $Al_xGa_{1-x}N$ mounds (cf. Figure II-11). Those mounds are typically observed for GaN based layers grown by MBE using an NH_3 source, and it was shown that their formation is due to kinetic roughening [27]. A comparison between the QD properties resulting from both growth techniques will be presented in part II.4.

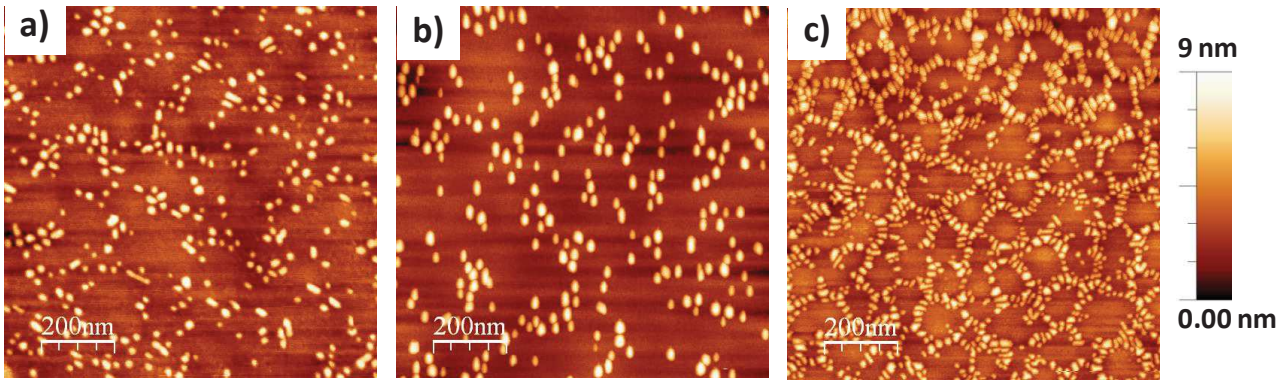

Figure II-10. AFM images of GaN QDs grown using an ammonia source on $Al_xGa_{1-x}N$ (0001) with x equals to a) 0.5 (sample D), b) 0.6 (sample E) and c) 0.7 (sample F).

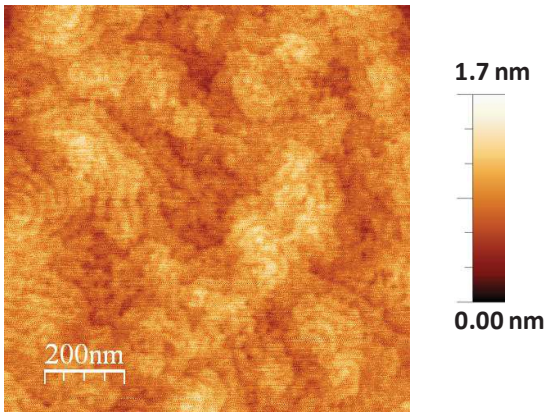

Figure II-11. AFM image of an $Al_{0.7}Ga_{0.3}N$ (0001) template grown using an ammonia source.

Cross-sectional HAADF-STEM characterization was also performed on sample E (GaN QDs / $Al_{0.6}Ga_{0.4}N$). A pyramidal shape with a truncated top was observed for buried QDs. The average QD height and diameter were determined to be (2.95 ± 0.4) nm and (21 ± 3.8) nm. Surprisingly, compared to results obtained for sample B (cf. paragraph II.2.1), the QD average height is much smaller than what was measured by AFM ((4.4 ± 0.7) nm). This is not in agreement with the case of GaN QDs grown by PAMBE (sample B), for which the average height of the buried plane (measured by TEM and including a wetting layer (WL)), was found to be equal to the average height of the QDs plane on the surface (measured by AFM; without taking into account the WL). In addition, on Figure II-12, no WL was observed whereas PL measurements show an emission around 4.1 eV (as will be shown in the next part), which is attributed to a WL. Obviously, the smaller QD sizes and the absence of the WL points out a difference in the growth conditions between the sample specimen investigated by AFM and PL and the sample specimen analyzed by TEM: most probably, in this latter case, the observed QDs were unintentionally grown at a higher temperature. Indeed, during the formation of the QDs under vacuum, some evaporation of GaN also takes place, which depends exponentially on the

growth temperature [29]. It was then shown that this evaporation, when increasing its time beyond the maximum RHEED intensity variation increase observed during the 2D – 3D growth mode transition (stage 2 in Figure II-13), can lead to the evaporation of the WL and the formation of isolated QDs (stage 3 in Figure II-13) [13], and eventually, to a complete evaporation of the GaN QDs (stage 4 in Figure II-13). Therefore, the QD morphological properties result in a balance between diffusion and evaporation processes: enhanced evaporation processes (due to a higher temperature) will then eventually lead to the formation of QDs without a WL as observed in the TEM sample specimen studied here.

Figure II-12. Cross-sectional HAADF-STEM image of the GaN QD / $Al_{0.6}Ga_{0.4}N$ structure (sample E).

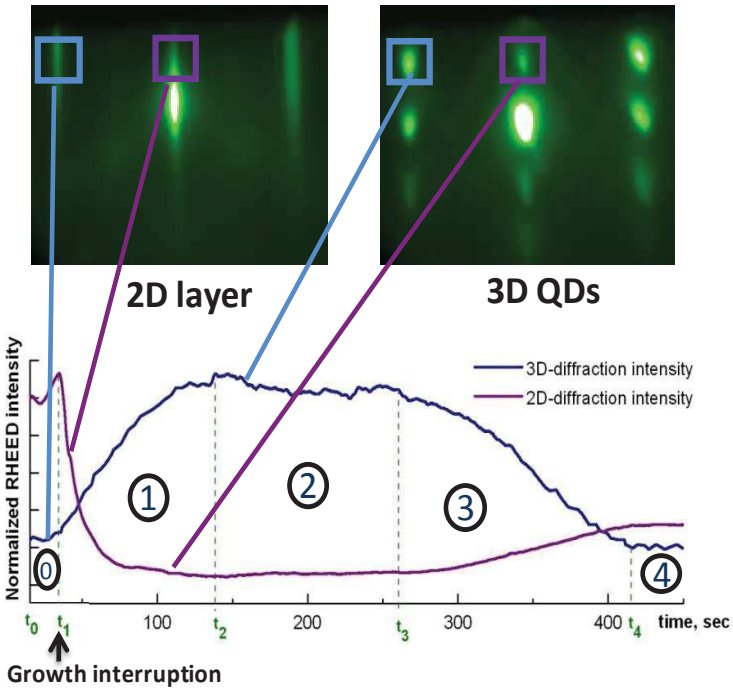

Figure II-13. Variation of the RHEED pattern intensity recorded on two zones during the formation / evaporation of GaN QDs grown using an ammonia source. The two squares are presenting the positions where the intensity is measured during the formation of QDs. The dashed lines indicate four main stages of the QDs evolution during the growth interruption. Stage 1: QD formation, stage 2: equilibrium QD formation / evaporation (constant RHEED intensity), stage 3: wetting layer and QD evaporation, 4) complete evaporation of the QDs [28].

Table II-2: Summary of the main structural and optical properties of GaN (6 MLs) QDs grown, using an ammonia source, on different $Al_xGa_{1-x}N$ (0001) templates.

Samples	QD Height (nm) (AFM)	QD diameter (nm) (SEM)	X-Ray FWHM (°) 0002/30-32	QDs density (cm^{-2})	PL Energy (eV) 9 K / 300 K	I (300K) / I(9K) (%)
GaN(QDs)/ $Al_{0.5}Ga_{0.5}N$ (Sample D)	4.6 ± 1.5	19 ± 5	0.39/0.9	2.7×10^{10}	3.36/3.28	76
GaN(QDs)/ $Al_{0.6}Ga_{0.4}N$ (Sample E)	4.4 ± 0.7 / 2.95 ± 0.4 (TEM buried plane; without WL)	15 ± 5 / 20.5 ± 4 (TEM buried plane)	0.35/0.86	2.5×10^{10}	3.23/3.21	38
GaN(QDs)/ $Al_{0.7}Ga_{0.3}N$ (Sample F)	3.4 ± 0.7	12 ± 4	0.35/1	1.2×10^{11}	2.97/2.89	30

II.3.2 Optical properties

The optical properties of the three samples were then studied at 9 K and 300 K (Figure II-14). As a general trend, by increasing x_{Al} in the $Al_xGa_{1-x}N$ matrix (from 0.5 to 0.7), a red shift of the PL energy emission (from 369 nm to 417 nm, i.e. from 3.36 eV to 2.97 eV, at 9 K) was observed. This shift is due to the increase of the polarization induced electric field (F_{int}) inside the QDs with increasing x_{Al}, although the formation of smaller QDs, as discussed in part II.2.2. An emission at 4.13 eV is also observed for sample E, this emission is due to the WL and is in close agreement to the WL emission observed from sample A and B (~ 4 eV).

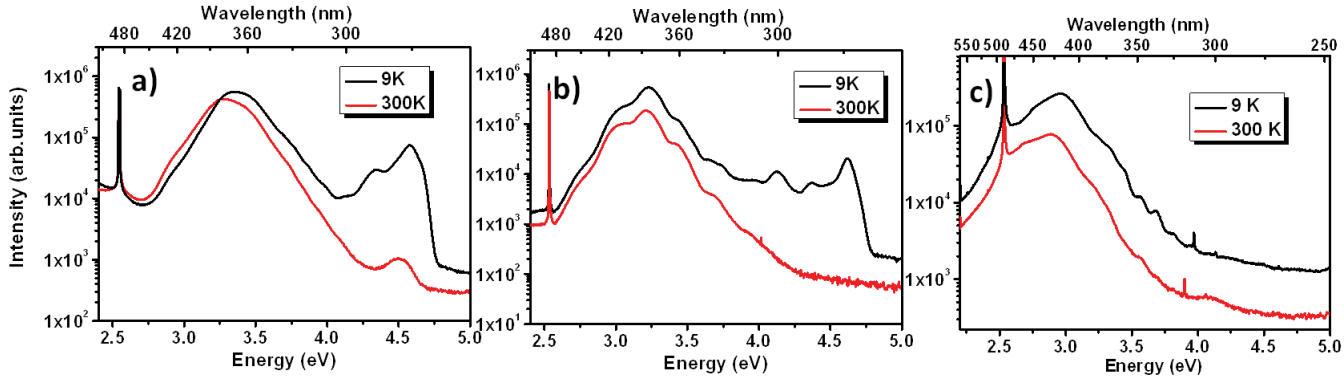

Figure II-14. Low and room temperatures PL spectra of: a) GaN QDs / $Al_{0.5}Ga_{0.5}N$ (sample D), b) GaN QDs / $Al_{0.6}Ga_{0.4}N$ (sample E), and c) GaN QDs / $Al_{0.7}Ga_{0.3}N$ (sample F), grown using ammonia source.

The PL intensity ratios of the room temperature over low temperature I(300K) / I(9K) were measured through our series of samples in order to estimate the radiative efficiency (i.e. proportional to the IQE). Ratios of 76 %, 38 % and 30 % were obtained for sample D, E and F,

respectively (cf. Table II-2). We remark that I(300K) / I(9K) ratios decrease while increasing x_{Al}. This result is seen as a direct manifestation of the increase of the internal electric field while increasing x_{Al} (cf. Figure II-8). Indeed, the increase of F_{int} (while increasing x_{Al}) induces a decrease of the electron and hole wavefunction overlap and thus an increase of the radiative recombination time which leads to a reduction of the radiative efficiency.

II.4 Comparison between the two growth processes (NH_3–MBE and PAMBE)

In this part, the morphological and optical properties of GaN QDs grown using either ammonia (NH_3-MBE) or plasma (PAMBE) source will be compared.

Based on the previous sections, our experimental results on the QD growth processes show that the main parameters controlling the 2D-3D transition are the lattice mismatch (i.e. the elastic strain) and the surface energy. Concerning the lattice mismatch, increasing $\Delta a/a$ (i.e. increasing the x_{Al} $Al_xGa_{1-x}N$ template composition) induces a decrease of the QD size and an increase of their density, for both NH_3-MBE and PAMBE. In the following study, a constant $\Delta a/a$ was chosen, i.e. a constant x_{Al} concentration was used to fabricate the different GaN / $Al_xGa_{1-x}N$ heterostructures, in order to investigate the influence of the nitrogen source on the QD formation.

From the previous results, it was shown that the QD formation mechanism is highly dependent on the nitrogen source used: when using a plasma N_2 source, the 2D-3D transition process starts during growth (in a classical Stranski-Krastanov growth mode) contrary to the case of an NH_3 source for which the 2D-3D transition only happens during a growth interruption under vacuum (the GaN growth following a layer by layer (2D) deposition).

Figure II-15 shows the AFM images for samples F and C (GaN QDs / $Al_{0.7}Ga_{0.3}N$ (0001) grown using NH_3–MBE and PAMBE, respectively). For those two samples, the lattice mismatch is identical and only the nitrogen source was changed. While using an NH_3 source, we clearly see the tendency of the QDs to nucleate on the edges of the $Al_{0.7}Ga_{0.3}N$ mounds. On the other hand, while using an N_2 source, we can see a more homogenous distribution of the QDs on the $Al_{0.7}Ga_{0.3}N$ surface with a higher density (i.e. a density of 3×10^{11} cm^{-2} versus 1.2×10^{11} cm^{-2} for sample C and F, respectively). Figure II-16 summarizes the variation of the QD density as a function of the lattice mismatch for the QDs grown by NH_3–MBE or PAMBE: as a general trend, an increase of the QD density is observed when the lattice mismatch increases.

From AFM images, the QDs average size was found to be roughly constant or slightly decreasing (cf. Table II-1 and Table II-2) while using NH_3-MBE. It is also important to note that the GaN deposited amount is identical for the different samples. A rough comparison of the

volume of the QDs over the GaN deposited amount (6 MLs) indicates that the amount of GaN in the QDs is larger for the samples grown by PAMBE. More precisely, the ratios are estimated at around (85 ± 5) % and (75 ± 5) % for PAMBE and NH_3-MBE grown QDs, respectively. This result implies that some evaporation process of GaN is taking place during the fabrication of the QDs, with a larger evaporation amount in the case of NH_3-MBE. In fact, QDs were grown at a higher temperature by NH_3-MBE compared to PAMBE (805°C versus 765°C). Since at higher temperature the GaN evaporation rate becomes more important following an Arrhenius law, with an activation energy of 3.6 eV for the thermal evaporation process [29], it can explain the lower conserved amount for NH_3-MBE fabrication process (with all other growth parameters being identical).

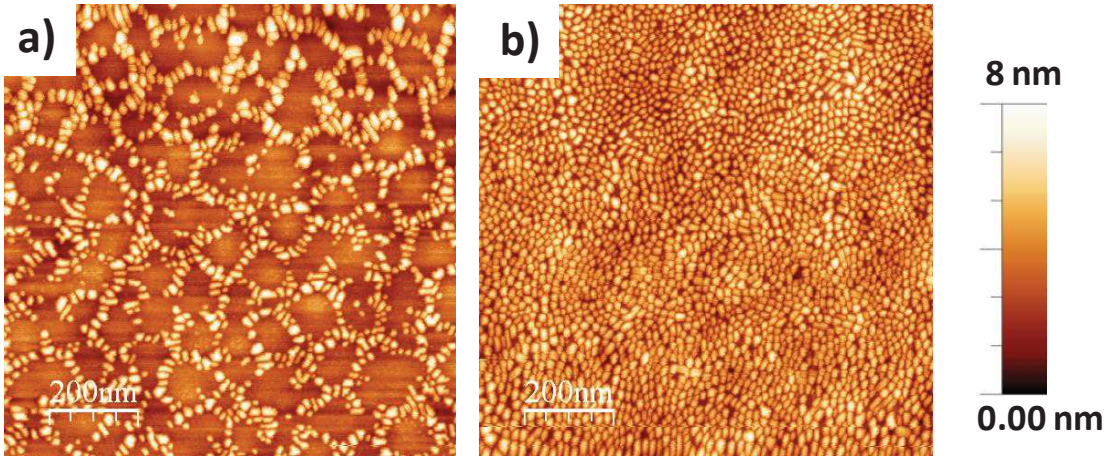

Figure II-15. AFM images of GaN QDs / $Al_{0.7}Ga_{0.3}N$ (0001) grown by: a) NH_3-MBE (sample F) and b) PAMBE (sample C).

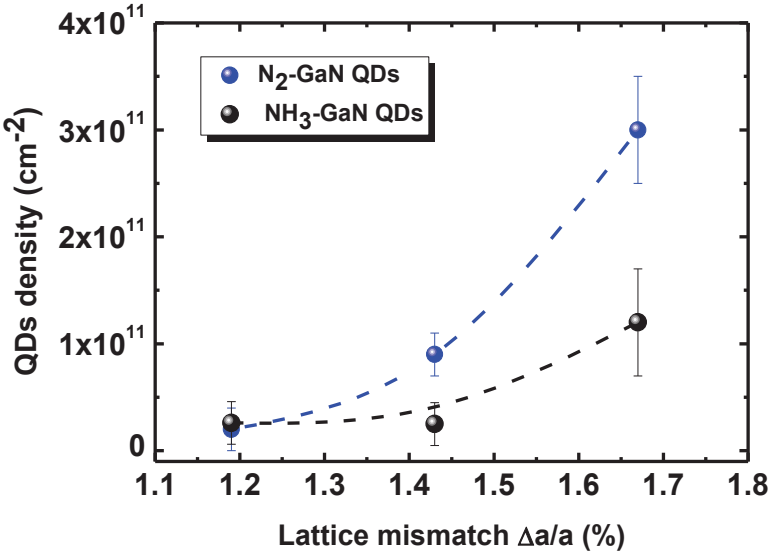

Figure II-16. QDs density as a function of the lattice mismatch between the GaN QDs layer and the $Al_xGa_{1-x}N$ (0001) template for NH_3-MBE and PAMBE fabrication processes.

In order to study the role of evaporation process on the QD fabrication, two samples, labeled sample F2 and C2, made of GaN (6 MLs) / $Al_{0.7}Ga_{0.3}N$ (0001) were grown at the same temperature (~ 730°C) using either NH_3–MBE or PAMBE respectively. This growth temperature was chosen to be lower than the ones used for the previous samples in order to minimize the evaporation effects during the QD formation under vacuum (i.e. in particular for NH_3-MBE). Figure II-17 presents the AFM images for both samples. We can see that the QD density increases (from 1.2 x 10^{11} cm^{-2} up to 3.1 x 10^{11} cm^{-2}) and their diameter decreases from (28 ± 5) nm down to (21 ± 4) nm while using an NH_3 source. Also, the QD average height was found to be almost constant or slightly smaller for NH_3-MBE grown QDs ((3.7 ± 0.9) nm and (3.8 ± 0.7) nm for NH_3-MBE and PAMBE, respectively). Finally, in this case, the volume of the QDs over the GaN deposited amount, calculated for both samples, were found to be roughly constant (values of (86 ± 4) % and (85 ± 5) % were found for samples C2 and F2, respectively).

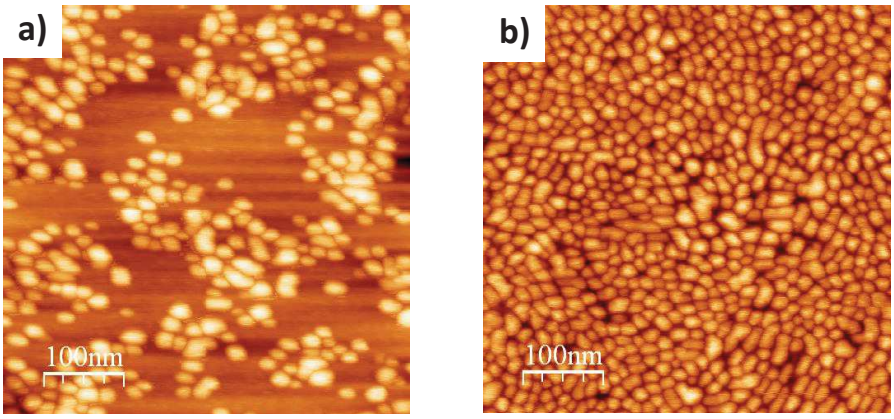

Figure II-17. AFM images for GaN QDs /$Al_{0.7}Ga_{0.3}N$ (0001) grown using: a) NH_3-MBE (sample F2) and b) PAMBE (sample C2).

To summarize the main differences in the QD formation for both sources, the 2D-3D transition is attributed to the minimization of the total energy ΔE ($\Delta E = \Delta\gamma + \Delta E_{elastic}$) between the surface energy variation ($\Delta\gamma$), and the elastic energy variation ($\Delta E_{elastic}$ which is originating from the lattice mismatch) between the 2D and the 3D layer morphology. Since in the case of samples C and F (and C2 and F2), the elastic energy is identical (with a lattice mismatch of 1.67 %), the morphological change is then directly related to the change of the surface energy, directly depending on the nitrogen source. Indeed, it was shown in a previous study [26], and in part II-3, that the presence of hydrogen, while using an ammonia source, induces an increase of the surface energy cost ($\Delta\gamma$) which prevents the QD formation. Therefore, a growth interruption under vacuum (i.e. without NH_3) is needed in order to reduce $\Delta\gamma$. This means that under H-rich conditions, $|\Delta\gamma|$ is always higher than $|\Delta_{Elastic}|$ for the GaN / $Al_xGa_{1-x}N$ system, which forbids the formation of QDs under NH_3. In the case of PAMBE, no hydrogen is present, leading to a

reduction of $|\Delta\gamma|$ and favouring the formation of QDs during growth (and with a higher surface density compared to NH_3-MBE grown QDs).

The PL properties of NH_3-MBE and PAMBE grown QDs were also compared. As a general trend, the PL intensity was found to be 2 to 3 times higher for QDs grown using an N_2 source (Figure II-18). This could be, partly, related to the higher QD density that was found for PAMBE grown QDs, which was also found to be 2 to 3 times higher for samples B and C compared to samples E and F. However, the QD density was found to be slightly higher for sample D (NH_3-MBE grown GaN QDs / $Al_{0.5}Ga_{0.5}N$) than for sample A (PAMBE grown GaN QDs / $Al_{0.5}Ga_{0.5}N$), although a lower PL intensity, which contradicts a direct relation between the QD density and the PL intensity. We can also point out from the PL spectrums that for NH_3-MBE grown QDs, the PL full width at half maximum (with values of 240 meV and 388 meV for samples E and F, respectively) is larger compared to PAMBE grown QDs (with values of 227 meV and 267 meV for samples B and C, respectively), indicating a better height homogeneity for PAMBE grown QDs.

By comparing the PL integrated intensity ratios between 300 K and 9 K, we can note that the radiative efficiency variation for PAMBE grown QD samples is more stable (ranging between 57 % and 75 %) than the one for NH_3-MBE grown QD samples which show a higher variation (ranging between 30 % and 76 %). Also, we can note that the best radiative efficiency using both techniques is obtained for sample B and D (with quasi-identical values of 75 % and 76 %). As presented in part II.2.2, the improvement of the crystalline quality of the $Al_xGa_{1-x}N$ template could be (in part) responsible for this improvement, accounting in a reduction of the threading dislocation density. However, this interpretation does not hold in the case for NH_3-MBE grown QDs, since roughly similar XRD results have been found for the whole sample series whereas one sample (D) shows significantly improved PL characteristics. Therefore, another significant parameter could be the size of the QDs. Indeed, by decreasing the QD height, an increase of the radiative efficiency could be expected due to an increase in the electron and hole wavefunction overlap. However, for the extreme case of very small QD heights (typically below 1.5 nm [13, 30]), a spreading of the wavefunctions takes place in the (defective) barriers, which can negatively impact on the radiative efficiency [13, 30]. To conclude, it is worth noting that we are dealing with samples presenting inhomogeneous distribution of defects and QDs, and different parameters can impact the QD radiative efficiency, requiring for a trade-off to be found in order to design the GaN / $Al_xGa_{1-x}N$ QD region.

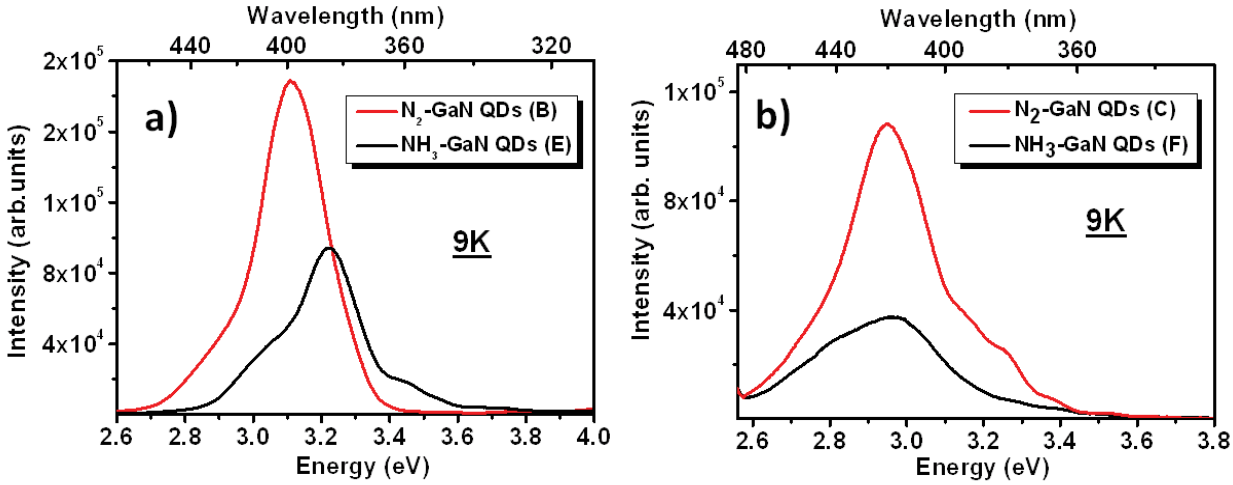

Figure II-18. PL comparison, at low temperature, between PAMBE grown GaN QDs and NH_3-MBE grown GaN QDs in a) $Al_{0.6}Ga_{0.4}N$ (0001) and b) $Al_{0.7}Ga_{0.3}N$ (0001) matrices.

To summarize, using an N_2 plasma source, QDs are grown in a classical SK growth mode and higher QD densities are observed than in the case of using an NH_3 source. In this latter case, a tendency to nucleate on the edges of the $Al_xGa_{1-x}N$ mounds is observed. In terms of optical properties, we saw that PAMBE-QDs have up to three times higher PL intensities and smaller full width at half maximum compared to NH_3-QDs. Also, we saw that more stable radiative efficiencies (from 9 K to 300 K) are obtained while using an N_2 plasma source, with values above 50 % (compared to 30 % in the case of NH_3-MBE grown QDs) and reaching 75 %. Finally, we can say that the growth process is better controlled using an N_2 plasma source compared to an NH_3 source. These differences between NH_3 and N_2 grown GaN QDs have been related to the surface energy contribution which strongly differs between the two growth processes.

II.5 Time resolved photoluminescence

Time resolved photoluminescence (TRPL) measurements were also performed at low temperature on GaN QDs grown on different $Al_xGa_{1-x}N$ templates ($0.5 \leq x \leq 0.7$) in order to study the PL kinetic processes and to investigate the different recombination processes dynamics of the samples. The third harmonic of a mode-locked titanium-sapphire ($Ti:Al_2O_3$) laser was used, with a wavelength of 266 nm, a pulse width of 100 fs and a repetition rate which can vary between 80 KHz (12 µs) and 82 MHz (12 ns). The choice of the repetition rate is mainly depending on the decay time of the sample, in the case of GaN QDs a repetition rate of 80 KHz (12 µs) is used. In fact, it is important to reduce the repetition rate (i.e. increase the repetition time) in the case of a slow decay time (e.g. GaN QDs), to ensure a complete decay of the PL and avoid the accumulation of electron-hole pairs from one pulse to another. On the other hand, a very long repetition time can lead to a red shift of the PL energy peaks.

In this part, the influence of the internal electric field (by changing the Al composition of the $Al_xGa_{1-x}N$ template) on the decay times will be discussed. Also, the IQE at low temperature will be estimated for the different samples using a model developed by Iwata et al [31].

Those experiments were performed by T. H. NGO and B. GIL (for whom the credit should be given) at Charles Coulomb laboratory (Montpellier University).

The optical properties using TRPL spectroscopy measurements were performed on GaN QDs samples grown on different $Al_xGa_{1-x}N$ templates, either grown by NH_3- or PAMBE. The main characteristics of the different samples are summarized in Table II-3.

The PL transients of all the samples are ruled by a double exponential decay, a fast decay component and a slower one. As we can see on Figure II-19 the spectrally integrated temporal intensity can be fitted with a double exponential using the following equation:

$$I(t) = A_{fast}\exp\left(-\frac{t}{\tau_{fast}}\right) + A_{slow}\exp\left(-\frac{t}{\tau_{slow}}\right) \qquad \text{(II-3)}$$

where τ_{slow} and τ_{fast} refer to the slow and fast decays and A_{slow} and A_{fast} represent the coefficients of slow and fast recombination processes, respectively.

The origin of this bi-exponential behaviour was studied by Iwata et al. [31] on (Al,Ga)N / AlN (0001) quantum wells. They developed a model which considers that the samples are composed of purely radiative regions while other regions are plagued by non radiative recombination centers. In this picture, **τ_{slow}** corresponds to the **radiative lifetime**, while **τ_{fast} contains both radiative and non radiative components.**

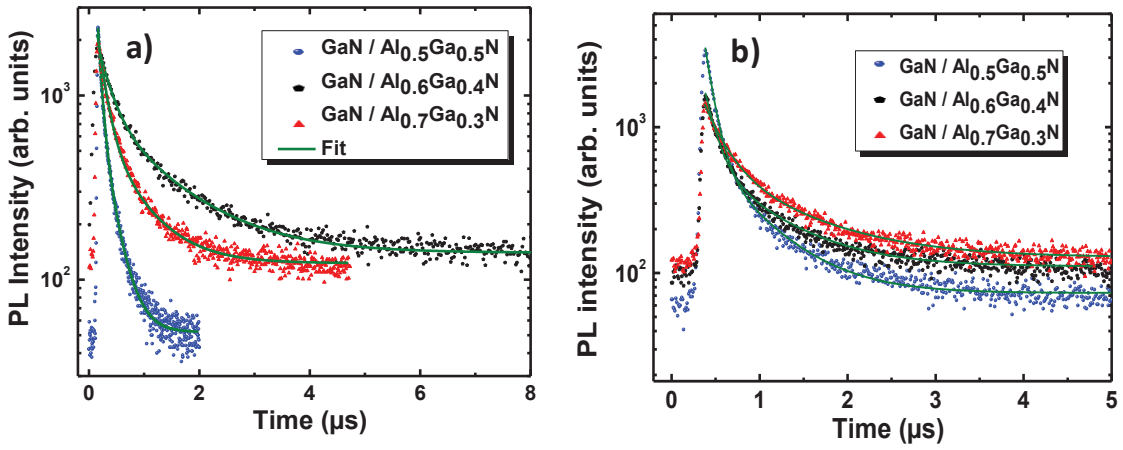

Figure II-19. Time resolved photoluminescence spectra at low temperature (18 K) for GaN QD / $Al_xGa_{1-x}N$ (0001) structures grown by a) PAMBE and b) NH_3-MBE with x_{Al} = 0.5, 0.6 and 0.7.

In general, it is supposed that at low temperature only radiative recombinations exist and that the internal quantum efficiency is 100 %. Using this assumption, the total PL intensity obtained by considering only the radiative contribution of both populations is:

$$I_{rad}(t) = A_{fast}\exp\left(-\frac{t}{\tau_{slow}}\right) + A_{slow}\exp\left(-\frac{t}{\tau_{slow}}\right) \quad \text{(II-4)}$$

Based on Iwata's model, radiative and non-radiative channels are taken into account at low temperature. The IQE at low temperature (IQE_{LT}) can then be defined (eq. II-5) as the ratio of the experimental decay curve fitted using equation II-3 and the time integrated intensity corresponding to pure radiative recombinations (eq. II-4):

$$IQE_{LT} = \frac{\int_0^\infty \left[A_{fast}\exp\left(-\frac{t}{\tau_{fast}}\right)+A_{slow}\exp\left(-\frac{t}{\tau_{slow}}\right)\right]}{\int_0^\infty \left[A_{fast}\exp\left(-\frac{t}{\tau_{slow}}\right)+A_{slow}\exp\left(-\frac{t}{\tau_{slow}}\right)\right]} = \frac{A_{fast}\tau_{fast}+A_{slow}\tau_{slow}}{(A_{fast}+A_{slow})\tau_{slow}} \quad \text{(II-5)}$$

Finally, τ_{fast} can also be expressed as:

$$\frac{1}{\tau_{fast}} = \frac{1}{\tau_{slow}} + \frac{1}{\tau_{nr}} \quad \text{(II-6)}$$

Table II-3: Summary of the main morphological and optical properties (energy emission, decay times and IQEs) of GaN QDs grown on different $Al_xGa_{1-x}N$ templates with ($0.5 \leq x \leq 0.7$), using PAMBE and NH_3-MBE.

	Samples	PL energy at LT (eV)	τ_{fast} (ns) (18K)	τ_{slow} (ns) (18K)	A_{fast}/A_{slow} (18K)	IQE_{LT} (%)	I_{RT}/I_{LT} (%)	IQE_{RT} (%)
N_2	GaN (QDs) /$Al_{0.5}Ga_{0.5}N$	3.22	65	231	2.18	51	61	31
	GaN (QDs) /$Al_{0.6}Ga_{0.4}N$	3.02	231	1156	1.7	49	75	37
	GaN (QDs) /$Al_{0.7}Ga_{0.3}N$	2.88	149	643	2.88	43	57	25
NH_3	GaN (QDs) /$Al_{0.5}Ga_{0.5}N$	3.35	5	20	2.7	45	76	34
	GaN (QDs) /$Al_{0.5}Ga_{0.5}N$	3.14	98	564	5.44	30	45	14
	GaN (QDs) /$Al_{0.6}Ga_{0.4}N$	3.06	126	694	2.75	40	37	15
	GaN (QDs) /$Al_{0.7}Ga_{0.3}N$	2.95	214	906	2.1	48	29	14

The slow and fast lifetime values for NH_3–MBE and PAMBE grown GaN QDs are summarized in Figure II-20. As a general trend, we can see that while going towards the UV range (i.e. by decreasing x_{Al} in the $Al_xGa_{1-x}N$ matrix as seen in the previous sections), the radiative decay time (τ_{slow}) decreases. This behaviour is due to the decrease of F_{int}, as a lower value leads to an increase of the electron and hole wavefunctions overlap, inducing a decrease of the radiative decay time.

However, a more detailed analysis of Table II-3 and Figure III-19 shows that the slow and fast lifetime values for the specific case of PAMBE grown GaN QDs do not vary monotonously

when going from GaN QDs grown on $Al_{0.5}Ga_{0.5}N$ (0001) to GaN QDs grown on $Al_{0.7}Ga_{0.3}N$ (0001) (i.e. while increasing the composition x_{Al} in the $Al_xGa_{1-x}N$ matrix from samples A to C). At the same time, the observed monotonous redshift of the PL emission should lead to a monotonous decrease of the radiative lifetime, in correlation with the electric field values estimated in section II.2.2 (cf. Figure II-8). Yet, the estimation of F_{int} was relying on the assumption of unity for the IQE at low temperature. This contradiction clearly indicates that we are dealing with samples presenting inhomogeneous distributions of defects and QDs (at the scale of the laser spot). The situation is then similar to the analogous of the situation in the samples described by Iwata et al.: at low temperature, the laser spot (with a total surface A) shines two regions of the sample which are named A_{fast} and A_{slow}. In the first region with fast recombination processes (A_{fast}), i.e. with high densities of non-radiative centers, the recombination dynamics is ruled by a typical decay time τ_{fast}; while in the second region of crystalline quality weakly affected or almost non-affected by such defects and corresponding to the surface region with slow recombination processes A_{slow}, the recombination dynamics is ruled by a decay time τ_{slow}. The resulting PL decay is ruled by two-component kinetics with proportions A_{fast} and its complementary A_{slow}. Changing the laser spot position, these proportions change while the values of τ_{fast} and τ_{slow} are not significantly modified. Iwata et al. suggested then to identify τ_{slow} as the value of the radiative decay time (or to a close representative of its value), while both radiative and non-radiative recombinations contribute to τ_{fast}. This model is valid when clear and unambiguous fitting of the decay time is achievable, that is to say, in defective enough samples so that A_{fast} is substantial enough, but not for too defective ones for which A_{slow} would be vanishingly decreasing. This is our case here, since the values of IQEs framed by this determination match very well with the time-integrated PL features. However, the major drawback of the model is its limitation to the low temperature range so that cross talking between both regions is not active, or the slow and fast decays are spatially isolated [31, 32]. Therefore, we cannot use it without including complementary interactions for the high temperature range, as presented in Table II-3. Finally, from the slow and fast lifetime values for NH_3–MBE and PAMBE grown GaN QDs, the IQEs obtained from equation II-5 for the different samples are summarized in Table II-3: they are around 50 % for PAMBE grown GaN QDs, whereas for NH_3–MBE grown GaN QDs, lower IQE_{LT} varying between 30 % and 45 % are obtained.

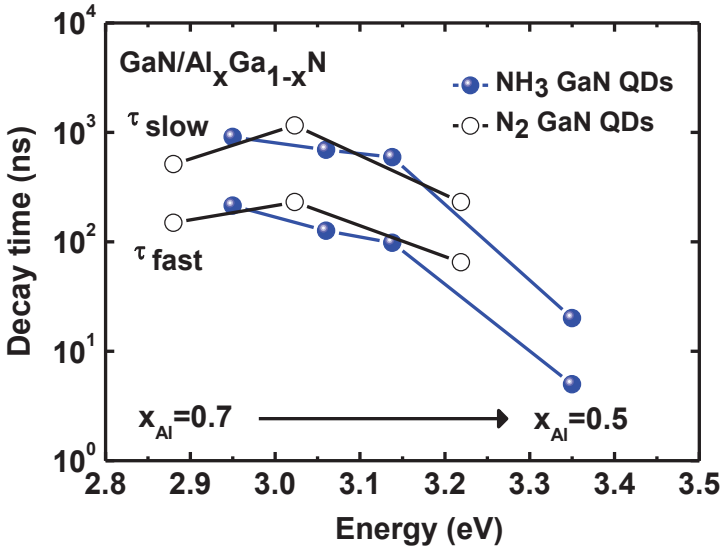

Figure II-20. Fast and slow decay times at low temperature as a function of the GaN QD emission energy. A blue (UV) shift is induced for lower x_{Al} in the $Al_xGa_{1-x}N$ matrix.

II.6 Conclusion

In this chapter, the morphological and optical properties of GaN quantum dots grown using either an N_2 or an NH_3 source, i.e. using plasma assisted molecular beam epitaxy (PAMBE) or ammonia assisted molecular beam epitaxy (NH_3-MBE), have been investigated and discussed.

By fabricating GaN QDs on different $Al_xGa_{1-x}N$ surfaces (with $0.5 \leq x \leq 0.7$), the influence of the epitaxial strain (with $1.2\ \% \leq \Delta a/a \leq 1.7\ \%$) on the QD self-assembling process and morphologies (size, density) was first studied. In this study, we showed that QDs with higher densities (increased by more than one decade) and smaller size are promoted by using a larger lattice-mismatch. However, photoluminescence (PL) measurements indicated a modification of the QD optical response by the internal electric field which induces a strong redshift in the emission energy as the Al content of the $Al_xGa_{1-x}N$ matrix increases: from 3.22 eV to 2.95 eV for PAMBE grown GaN QDs and from 3.36 eV to 2.97 eV for NH_3–MBE grown GaN QDs. This property results from the increase with x_{Al} of the total polarization differences between GaN and the surrounding $Al_xGa_{1-x}N$ matrix (varying between 3 and 5.3 MV / cm for x_{Al}= 0.5 and 0.7 respectively), leading to a larger value of F_{int}. In addition, power dependent PL measurements showed a correlation between the emission energy shift, which is due to the screening of F_{int} by the injected carriers in the QDs, and the height of the QDs. It was found that F_{int} has less influence on the optical properties of smaller QDs, implying a reduced shift in the PL energy compared to larger QDs.

The formation of GaN QDs using PAMBE or NH_3-MBE was also compared: using a plasma N_2 source, the 2D-3D transition process starts during growth in a classical Stranski-Krastanov mode while in the case of an NH_3 source, it happens during a growth interruption under vacuum after a 2D layer-by-layer deposition. This property was shown to be related to the surface energy cost contribution ($\Delta\gamma$) which strongly differs by using N_2 or NH_3. Also, it was shown that the growth process is better controlled using PAMBE, leading to the growth of GaN QDs with higher densities and a better size uniformity. NH_3-MBE grown GaN QDs show a tendency to nucleate on the edges of the $Al_{0.7}Ga_{0.3}N$ surface mounds. In terms of optical properties, PAMBE grown GaN QDs have up to three times higher PL intensities and smaller full width at half maximum compared to NH_3-MBE grown GaN QDs.

Finally, time resolved PL combined with temperature dependent PL measurements enabled us to determine the internal quantum efficiencies (IQE) of GaN QD / $Al_xGa_{1-x}N$ (0001) and values around 50 % were found at low temperature. Combined with the ability to reach a PL integrated intensity ratio up to 75 % between 300 K and 9 K, these results have confirmed the efficient carrier confinement in the GaN QDs.

References

[1] Y. Narukawa, M. Ichikawa, D. Sanga, M. Sano, T. Mukai, J. Phys. D Appl. Phys. 43, 354002 (2010).

[2] J. Xie, S. A. Chevtchenko, U. Ozgur, H. Morkoc. Appl. Phys. Let. 90, 262112 (2007).

[3] M. Kneissl, T. Kolbe, C. Chua, V. Kueller, N. Lobo, J. Stellmach, A. Knauer, H. Rodriguez, S. Einfeldt, Z. Yang, N.M. Johnson, M. Weyers, Semicond. Sci. Technol. 26, 014036 (2011).

[4] N. Grandjean, J. Massies and M. Leroux, Appl. Phys. Lett. 69, 2071 (1996).

[5] N. Grandjean, M. Leroux, M. Laugt, and J. Massies, Appl. Phys. Lett. 71, 240 (1997).

[6] J.-Y. Duboz, N. Grandjean, F. Omne`s, J.-L. Reverchon, and M. Mosca, Phys. Stat. Sol. (c) 2, 964 (2005).

[7] B. Damilano, J. Brault, and J. Massies, J. Appl. Phys. 118, 024304 (2015).

[8] J. Stangl, V. Hol_y, and G. Bauer, Rev. Mod. Phys. 76, 725 (2004).

[9] J.-N. Aqua, I. Berbezier, L. Favre, T. Frisch, and A. Ronda, Phys. Rep. 522, 59 (2013).

[10] M. Leroux, N. Grandjean, M. Laugt, J. Massies, B. Gil, P. Lefebvre, and P. Bigenwald, Phys. Rev. B 58, R13371 (1998).

[11] B. Daudin, F. Widmann, G. Feuillet, Y. Samson, M. Arlery, and J. L. Rouviere, Phys. Rev. B 56, R7069 (1997).

[12] M. Korytov, M. Benaissa, J. Brault, T. Huault, T. Neisius, and P. Vennéguès, Appl. Phys. Lett. 94, 143105 (2009).

[13] J. Brault, S. Matta, T.-H. Ngo, M. Korytov, D. Rosales, B. Damilano, M. Leroux, P. Vennéguès, M. Al Khalfioui, A. Courville, O. Tottereau, J. Massies, and B. Gil, Japanese. Journal. of Applied. Physics. 05FG06 (2016).

[14] T. Huault, J. Brault, F. Natali, B. Damilano, D. Lefebvre, L. Nguyen, M. Leroux, and J. Massies, Appl. Phys. Lett. 92, 051911 (2008).

[15] J. Brault, T. Huault, F. Natali, B. Damilano, D. Lefebvre, M. Leroux, M. Korytov, and J. Massies, J. Appl. Phys. 105, 033519 (2009).

[16] M. Leroux, J. Brault, A. Kahouli, D. Elmaghraoui, B. Damilano, P. de Mierry, M. Korytov, J.-H. Kim, and Y.-H. Cho, J. Appl. Phys. 116, 034308 (2014).

[17] T. Bretagnon, P. Lefebvre, P. Valvin, R. Bardoux, T. Guillet, T. Taliercio, B. Gil, N. Grandjean, F. Semond, B. Damilano, A. Dussaigne, and J. Massies, Phys. Rev. B 73, 113304 (2006).

[18] T. Bretagnon, S. Kalliakos, P. Lefebvre, P. Valvin, B. Gil, N. Grandjean, A. Dussaigne, B. Damilano, J. Massies, Phys. Rev. B 68, 205301 (2003).

[19] J. Brault, S. Matta, T. -H. Ngo, D. Rosales, M. Leroux, B. Damilano, M. Al Khalifioui, F. Tendille, S. Chenot, P. de Mierry, J. Massies, and B. Gil, Materials Science in Semiconductor Processing 55, 95 (2016).

[20] F. Natali, D. Byrne, M. Leroux, B. Damilano, F. Semond, A. Le Louarn, S. Vézian, N. Grandjean, and J. Massies, Phys. Rev. B 71, 075311 (2005).

[21] N. Grandjean, B. Damilano, S. Dalmasso, M. Leroux, M. Laugt, and J. Massies, J. Appl. Phys. 86, 3714 (1999).

[22] F. Natali, Y. Cordier, J. Massies, S. Vézian, B. Damilano, and M. Leroux, Phys. Rev. B 79, 035328 (2009).

[23] M. Tchernycheva, L. Nevou, L. Doyennette, F. H. Julien, E. Warde, F. Guillot, E. Monroy, E. Bellet-Amalric, T. Remmele, and M. Albrecht, Phys. Rev. B 73, 125347 (2006).

[24] M. Nemoz, R. Dagher, S. Matta, A. Michon, P. Vennéguès, J. Brault, J. Cryst. Growth, 461 (2016).

[25] B. Damilano, N. Grandjean, F. Semond, J. Massies, and M. Leroux, Appl. Phys. Lett. 75, 962 (1999).

[26] H. Mariette. C. R. Physique. 6, 23 (2005).

[27] S. Vezian, F. Natali, F. Semond, J. Massies, From spiral growth to kinetic roughening in molecular-beam epitaxy of GaN (0001), Phys. Rev. B 69, 125329 (2004).

[28] M. Korytov, PhD thesis "Quantitative Transmission Electron Microscopy Study of III-Nitride Semiconductor Nanostructures" Université de Nice-Sophia Antipolis (2010).

[29] N. Grandjean, J. Massies, F. Semond, S. Yu. Karpov, and R. A. Talalaev, Appl. Phys. Lett. 74, 1854 (1999).

[30] J. Brault, D. Rosales, B. Damilano, M. Leroux, A. Courville, M. Korytov, S. Chenot, P. Vennéguès, B. Vinter, P. de Mierry, A. Kahouli, J. Massies, T. Bretagnon, and B. Gil, Semicond. Sci. Technol. 29, 084001 (2014).

[31] Y. Iwata, R. G. Banal, S. Ichikawa, M. Funato, and Y. Kawakami, J. Appl. Phys. 117, 075701 (2015).

[32] T. H. Ngo, PhD thesis "Optimisation du rendement quantique des dispositifs à base de nitrures opérant le jaune au rouge". Université de Montpellier (2017).

Table of Contents

III. $Al_{0.1}Ga_{0.9}N$ quantum dots

This chapter will be dedicated to study the growth and the optical properties of $Al_{0.1}Ga_{0.9}N$ quantum dots (QDs). At the beginning, a brief introduction will be given. Then, different QD layer designs will be introduced. The growth challenges of $Al_{0.1}Ga_{0.9}N$ QDs will be discussed regarding the influence of growth conditions on the QD shapes and the ability to grow elongated or symmetric dots. The optical properties of the QDs will then be presented, showing in particular the ability to cover a large part of the UVA range. Finally, the influence of the QD design on the optical properties will be discussed.

III.1 Introduction

As discussed before, (Al,Ga)N alloys suffer from high defect densities, typically threading dislocations (TDs), in the 10^9 - 10^{10} cm^{-2} ranges. This dislocation density was found to increase as a function of the Al concentration due to a large lattice mismatch with the host substrate (i.e. generally sapphire) and the low surface mobility of Al adatoms resulting in a reduction of the lateral mass transport and the formation of a high density of nanometer-sized islands whose coalescence is responsible for the formation of TDs [1, 2]. TDs are structural defects that act as non-radiative recombination centers. Due to these high TD densities, an important droop in the efficiency is observed while going towards shorter wavelengths (i.e. using (Al,Ga)N alloys with higher Al concentrations). Using GaN quantum dots, instead of quantum wells (QWs) in an (Al,Ga)N matrix, was shown to improve the photoluminescence efficiencies in the near UVA-blue range by trapping the carriers inside the QDs and thus decreasing the probability to recombine non radiatively with TDs (chapter II, [3]). (Al,Ga)N QDs were also successfully grown on AlN [4, 5] thanks to the high compressive strain induced by the large lattice mismatch ($\Delta a/a \approx 2.3$ %) between both layers. However, the use of AlN matrices for the fabrication of LED devices is a huge challenge because of the difficulty to p-dope AlN, due to the very high acceptor activation energy (≈ 0.6 eV) [6].

We would like to underline that in (Al,Ga)N alloys, a composition modulation and phase separation could also be expected. Indeed, it was shown in previous studies [7, 8, 9] that (Al,Ga)N epilayers present pronounced phase separation mechanisms for low Al concentrations (< 0.5). As we are dealing with $Al_yGa_{1-y}N$ QDs with Al nominal concentrations (n.c.) below 0.5, a composition fluctuation inside the QDs and / or the formation of different QD families with concentrations different than the nominal one may be expected.

In this chapter, we will show the possibility to grow $Al_{0.1}Ga_{0.9}N$ QDs on $Al_{0.5}Ga_{0.5}N$ templates. The main interest of using $Al_{0.5}Ga_{0.5}N$ templates is the possibility to get n and p type layers and thus to be able to fabricate LED structures [10, 11, 12, 13].

The samples structure studied have a similar design than the structures presented in chapter II.1, except for the active layer design. In this chapter, $Al_{0.1}Ga_{0.9}N$ / $Al_{0.5}Ga_{0.5}N$ QD layers with different deposited amounts of $Al_{0.1}Ga_{0.9}N$ (n.c.), varying between 6 and 10.5 monolayers (MLs, 1 ML corresponding to half the c lattice parameter), are investigated. The 2D-3D morphological transition was followed in-situ using RHEED, through the change of the diffraction pattern from streaky lines to Bragg spots. A two-step process was used for the QD growth:

1) The growth of the $Al_{0.1}Ga_{0.9}N$ (n.c.) layer with a specific deposited amount.
2) A growth interruption and an annealing step under vacuum, typically of 6 minutes.

We have investigated the QD morphological and optical properties while varying: i) their height, i.e. by changing the $Al_{0.1}Ga_{0.9}N$ deposited amount, and ii) their shape (elongated versus symmetric QDs), by changing the annealing conditions during their formation. All the QD planes were grown using an N_2 plasma source under N-rich conditions with a III/V flux ratio of 0.7 and a growth rate around 0.3 ± 0.05 ML / s.

III.2 Elongated quantum dots (1st generation)

III.2.1 Active layer design and morphological properties

A series of four samples with different $Al_{0.1}Ga_{0.9}N$ (n.c.) deposited amounts was first designed: 6, 7.5, 9.5, 10.5 MLs were deposited at 740°C, followed by an annealing step of 6 minutes at the same temperature. These samples will be referred in the following as A6, A7, A9, A10.

As a first step, the formation of the QDs was followed in-situ by RHEED. The modification of the QD morphology is characterized by an increase of the diffraction line intensity. Figure III-1 illustrates the change of the RHEED pattern from a streaky pattern to a slightly spotty one. The increase of a spot intensity was recorded in-situ as a function of time. The 2D-3D transition was observed during growth after depositing 5 ± 1 MLs. During the annealing step, the RHEED pattern is unchanged and the intensity remains constant.

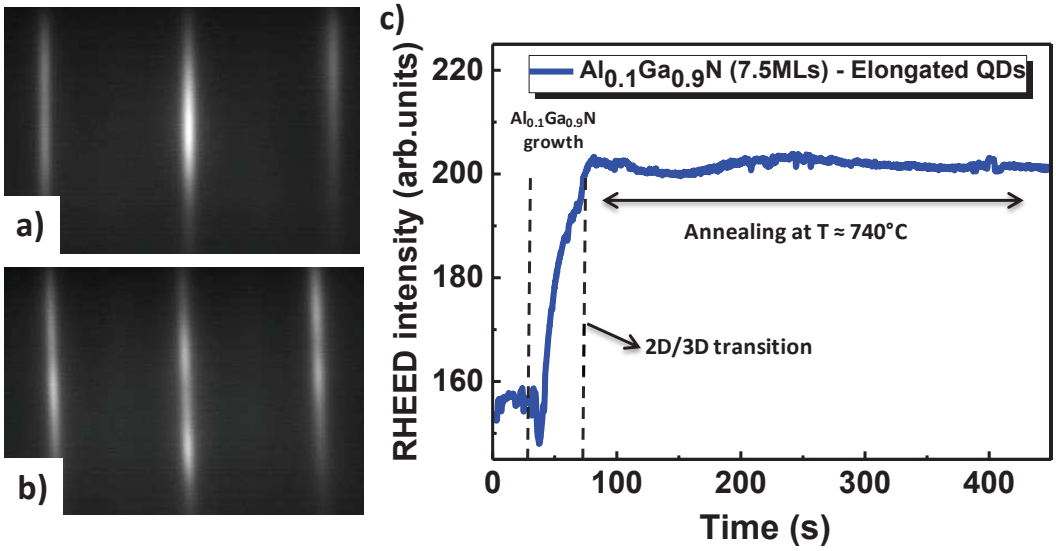

Figure III-1. Reflection high–energy electron diffraction patterns along the <11-20> azimuth of a) an $Al_{0.5}Ga_{0.5}N$ (0001) template before the QD growth, b) after the formation of $Al_{0.1}Ga_{0.9}N$ QDs with a deposited amount of 7.5 MLs (sample A7). c) RHEED intensity recorded during the formation of elongated $Al_{0.1}Ga_{0.9}N$ QDs.

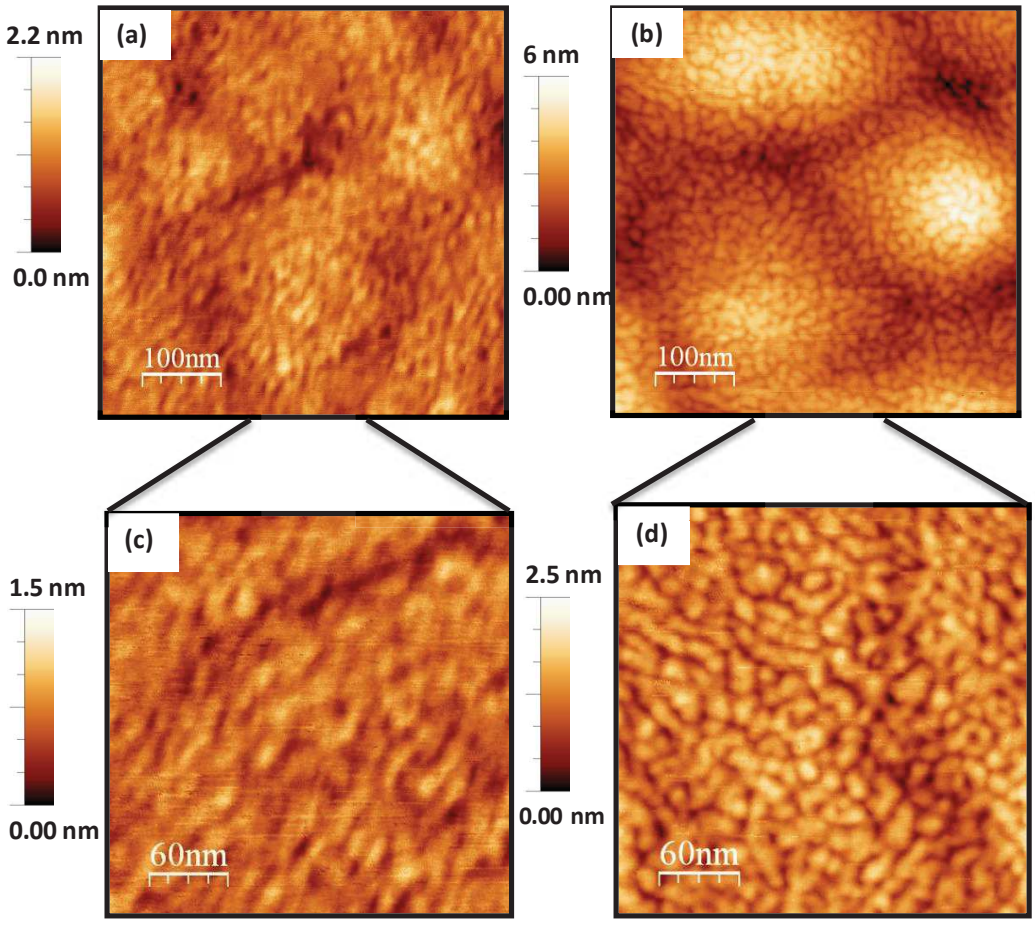

Figure III-2. AFM images of $Al_{0.1}Ga_{0.9}N$ nanostructures with a deposited thickness of a) 7.5 MLs and b) 10.5 MLs. c) and d) are zooms of images a) and b) respectively.

The samples were then characterized by AFM to study their morphological properties. At first, we observe a modulation of the surface topography at a large scale on the AFM images [Figure III-2(a) and (b)]: this specific feature originates from the growth of $Al_{0.5}Ga_{0.5}N$ mounds. Those mounds are typically observed for GaN layers grown by MBE using NH_3, and it was found that their formation is due to kinetic roughening [14]. We can also note the successful growth of QDs on an $Al_{0.5}Ga_{0.5}N$ (0001) template with a low lattice mismatch of 1 % between the two layers.

These QD dimensions are also found smaller and with higher densities compared to GaN QDs / $Al_{0.5}Ga_{0.5}N$ (0001) (studied in chapter II) although a higher lattice mismatch in the latter case (i.e. $\Delta a/a \approx 1.2$ % compared to $\Delta a/a \approx 1$ %). This may be due to the lower Al adatoms mobility compared to the Ga ones, inducing an increase of the QD nucleation centers and thus leading to higher QD densities with smaller dimensions compared to GaN QDs.

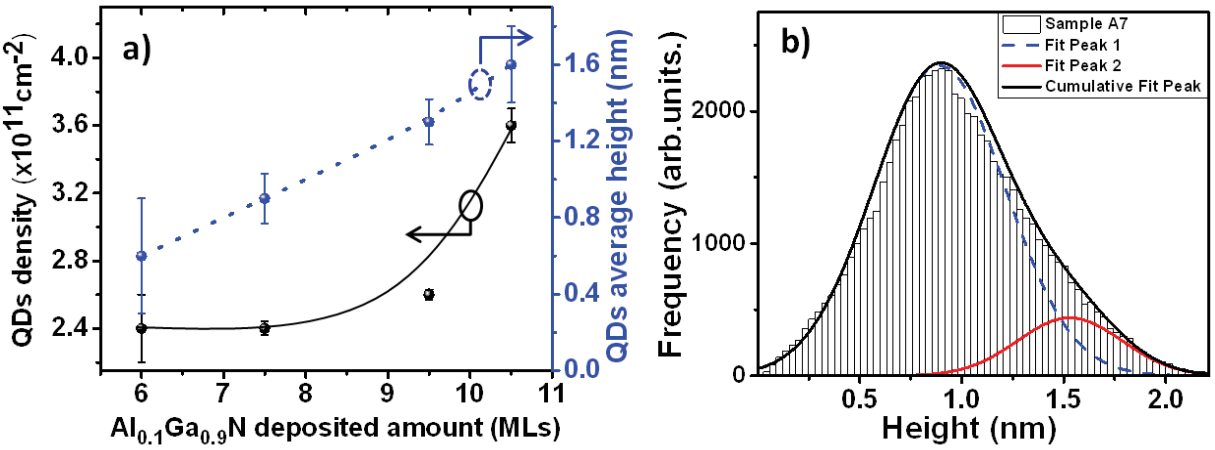

Figure III-3. a) Nanostructures average height and density variation as a function of the deposited amount. b) Height distribution of $Al_{0.1}Ga_{0.9}N$ nanostructures determined by AFM (sample A7), and fitting with two Gaussian functions.

The nanostructure height distribution was also measured on the different samples, using WSxM program [15], showing an asymmetric distribution, i.e. the nanostructure height distribution can be defined with two main components. As an example, a histogram of the nanostructure heights distribution is presented in the case of sample A7 (Figure III-3(b)). The histogram can be well fitted by two Gaussians, accounting for the presence of an asymmetric distribution of heights. Two average height values, corresponding to the center value of each Gaussian, were then determined with h* = 0.9 nm and h** = 1.5 nm. The asymmetrical height distribution is then attributed to two QD distributions (centered at h* and h**), as discussed in the following. For the whole sample series, a roughly constant difference value between the centers of both Gaussians is found (≈ 0.6 nm).

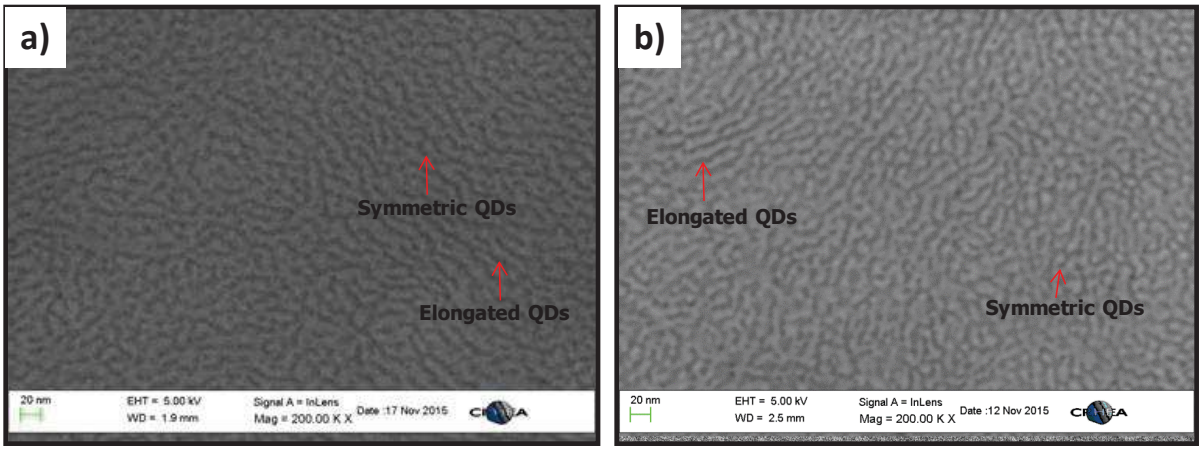

Figure III-4. Scanning electron microscopy images of sample a) A10 and b) A9. The red arrows point out examples of elongated and symmetric QDs.

SEM measurements were also performed (Figure III-4) on the different samples in order to extract more precise QD diameter values. We can also observe on the different AFM and SEM measurements the presence of different nanostructure shapes: either elongated QDs (with a lateral size reaching 60 nm) and/or symmetric QDs with an average diameter around 10 nm. Elongated QDs have also been observed in the GaN / $Al_{0.5}Ga_{0.5}N$ (0001) system, and can even lead to the formation of self-assembled GaN quantum dashes (QDashes) [16]. It was shown that the ammonia pressure has an effective impact on the shape of GaN QDs and the fabrication of QDashes as well as QDs is possible. In fact, as the $Al_{0.5}Ga_{0.5}N$ barriers are grown with an NH_3 source, some residual NH_3 could be present in the growth chamber while growing the QD plane. This residual NH_3 can induce some changes in the surface energy and thus impacts the QD shape, favouring the formation of elongated QDs (i.e. with a lower surface/volume (S/V) ratio compared to QDs). In the case of GaN QDashes, it was shown that they are preferentially nucleating along the $Al_{0.5}Ga_{0.5}N$ steps. However, in the case of $Al_yGa_{1-y}N$ QDs, it is difficult to confirm if they are preferentially nucleating along steps due to their very high densities.

III.2.2 Optical properties

Effect of the QD thickness

To assess the QD optical properties, photoluminescence (PL) measurements were done at 9 K using a frequency-doubled argon (Ar) laser with an excitation power of 30 mW. By looking at Figure III-5 and Figure III-7, different transitions are observed. A high energy band around 4.55 eV comes from the luminescence of the $Al_{0.5}Ga_{0.5}N$ barrier, in close agreement with previous studies [17, 18]. A dominant band found between 3.65 eV and 3.83 eV is originating from the

QD emission and finally an additional broad band emission at lower energy, between 3.2 eV and 3.5 eV, is also observed (whose origin will be discussed in the following).

As a first step, we will focus on the main PL emission peak. By looking at the A sample series spectrums, it is noted that decreasing the $Al_{0.1}Ga_{0.9}N$ deposited amount from 10.5 MLs down to 6 MLs leads to a UV shift from 340 nm (3.65 eV) to 324 nm (3.83 eV) due to the decrease of the QDs height, as presented in Figure III-3(a). Therefore, the deep UVA range can be covered.

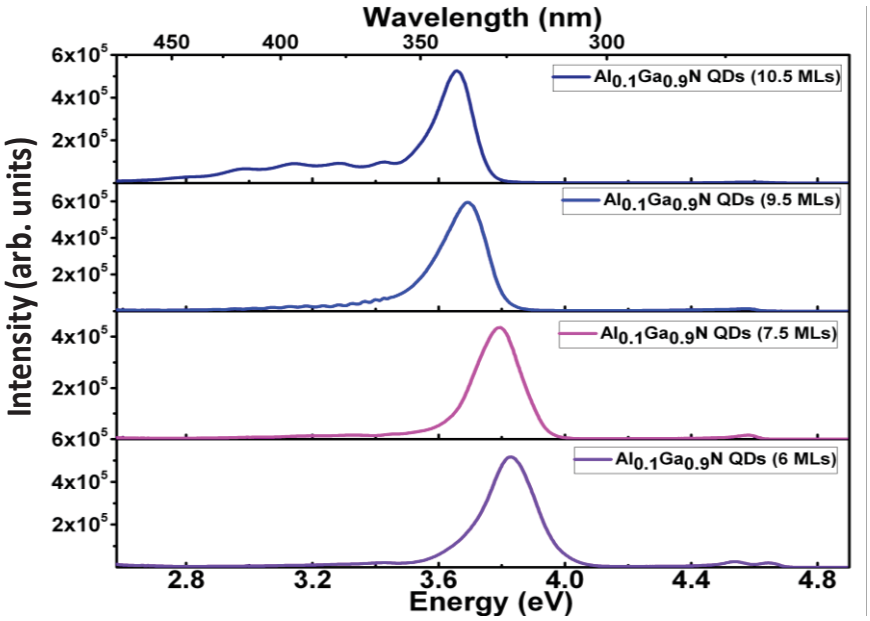

Figure III-5. PL spectra at 9 K of $Al_{0.1}Ga_{0.9}N$ QDs / $Al_{0.5}Ga_{0.5}N$ (0001) as a function of the deposited amount.

Internal electric field estimation

The experimental PL energy values of the different samples were then compared to the calculated fundamental energy transition (E_{e1-hh1}), using equation III-1, for different internal electric field values (F_{int}) and QD heights. In fact, due to the large effective mass values and since the QD base to height ratio is larger than 4, the lateral confinement can be neglected, and we can consider the confinement to be principally along the QD height [19]. On the other hand, as mentioned before, the exact height (h) values of the QDs are hard to extract from the AFM images. For this reason, an average height value H_1 was directly deduced from the $Al_{0.1}Ga_{0.9}N$ deposited amount following two principal results: 1) cross-sectional TEM measurements have shown that the average height of $Al_{0.1}Ga_{0.9}N$ QDs fairly corresponds to the $Al_{0.1}Ga_{0.9}N$ deposited amount [20, 21] (in agreement with TEM results presented in part III.4); 2) Also, AFM measurements show that the relative average QD heights variation between the samples is

identical to the relative variation of $Al_{0.1}Ga_{0.9}N$ deposited amounts. Finally, the fundamental transition energy can be calculated as follows:

$$E_{e1-hh1} = E_{QD} + E_g^{QD} - E_{Ry} - eF_{int}h \quad \text{(III-1)}$$

Where E_{QD} refers to the quantum confinement energy in the QD conduction and valence bands obtained by using the envelop function formalism, E_g^{QD} is the strained $Al_{0.1}Ga_{0.9}N$ band gap energy, and E_{Ry} is the Rydberg energy which corresponds to the excitonic binding energy.

The $Al_{0.1}Ga_{0.9}N$ strained band gap (E_g^{QD}) can be calculated as follows:

$$E_g^{QD} = E_g - a.\varepsilon_{xx} \quad \text{(III-2)}$$

with E_g the relaxed $Al_{0.1}Ga_{0.9}N$ band gap, a the biaxial deformation potential (estimated at -8.5 eV as for GaN) [22], and ε_{xx} the in-plane strain tensor (presented in paragraph I.1.2.1).

The results of the calculated energy transition were then compared to the experimental PL peak energies as a function of the QD height and for different F_{int} values. As presented in Figure III-6, the best fit with the experimental points is obtained for $F_{int} \approx 2 \pm 0.5$ MV / cm. This value is lower than the one estimated for GaN / $Al_{0.5}Ga_{0.5}N$ (0001) system (≈ 3 MV / cm as shown in chapter II), as expected. Also, if we compare this value with the value obtained in the GaN / $Al_{0.4}Ga_{0.6}N$ system (i.e. for a similar chemical contrast as for the $Al_{0.1}Ga_{0.9}N$ / $Al_{0.5}Ga_{0.5}N$ system), an electric field between 2 and 2.5 MV / cm was determined [23], which is very similar to the results obtained here. We can also see that the PL emission energies from the smallest QD layers (A6 and A7 samples) are found slightly above the estimated strained band gap energy of $Al_{0.1}Ga_{0.9}N$, which indicates a minimized influence of F_{int} on the PL energy emission for QD heights below 2 nm. Indeed, the internal electric field induces a red shift (i.e. an emission at energies below the strained band gap), as discussed in chapter I.1.2.2. The large error bars in the field estimation in Figure III-6 is related to the full width at half maximum (FWHM) of the QD PL peaks together with the QD height distribution which give uncertainties in the field calculations.

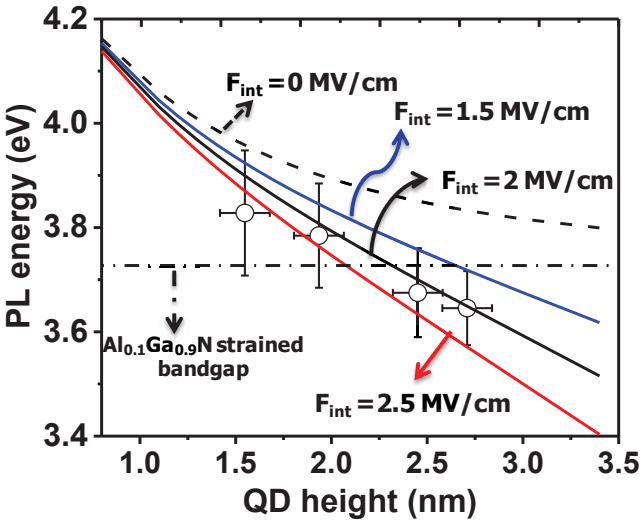

Figure III-6. Calculated transition energies at 9 K as a function of the $Al_{0.1}Ga_{0.9}N$ QD height for different values of F_{int}. The empty circles represent the main experimental PL energies for the four samples series.

The origin of the additional band emission at lower energy

In addition to the main PL peak, we can observe a broad band emission at lower energies, i.e. between 3.2 eV and 3.5 eV (Figure III-7). As will be discussed in the following, this band at lower energy can be the consequence of three features:

⇒ the presence of deep levels emitting in the near UV-blue range in the $Al_{0.5}Ga_{0.5}N$ (0001) template;

⇒ the asymmetric height distribution of the QDs (Figure III-3(b));

⇒ a fluctuation of the QD Al concentration (y_{Al}).

As a first step in order to verify if this emission band at lower energy comes from deep levels in the $Al_{0.5}Ga_{0.5}N$ matrix, the PL spectra of the $Al_{0.1}Ga_{0.9}N$ QDs were compared to the spectrum of a typical $Al_{0.5}Ga_{0.5}N$ template grown on sapphire (Figure III-7). As we can see, there is almost no emission coming from the $Al_{0.5}Ga_{0.5}N$ template in the energy range between 2.84 eV and 3.4 eV, which indicates that this additional band at lower energy originates from the QD layers and not from deep levels in the template. Concerning the second point, as shown on the histogram (Figure III-3(b)), the asymmetric height distribution can also be one of the explanations of this additional band, with higher nanostructures corresponding to the low energy band emission; however this result alone cannot explain the measured PL characteristics, as it will be discussed in the following.

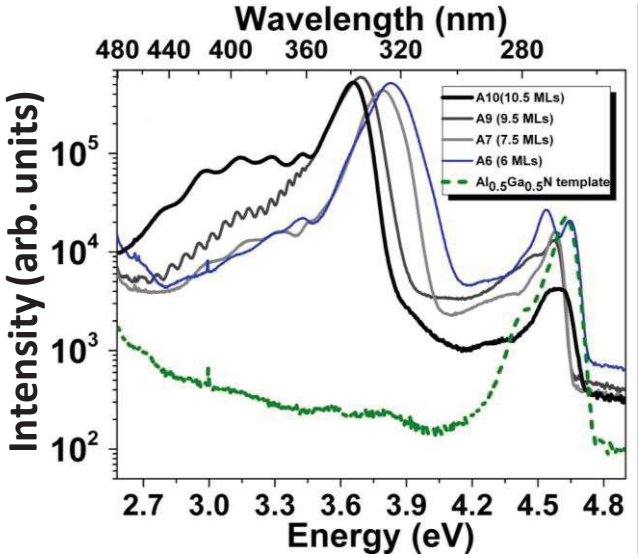

Figure III-7. PL spectra in semi-log scale of $Al_{0.1}Ga_{0.9}N$ (n.c.) QDs for different deposited amounts of $Al_{0.1}Ga_{0.9}N$ at 9 K and comparison with an $Al_{0.5}Ga_{0.5}N$ (0001) template (green dashed line).

In order to further analyze the QD PL spectra and more specifically the origin of this additional emission band at lower energies, we deconvoluted the two PL peak components by fitting each spectrum of the sample series with two Gaussians, at 9 K and 300 K (Figure III-8), to analyze the behaviour of each band separately. By taking the centered energy values obtained from the Gaussian fits for the complete sample series, a similar behaviour is observed with a blue (UV) shift (i.e. towards higher energies) as the $Al_{0.1}Ga_{0.9}N$ deposited amount decreases (Figure III-9(a)).

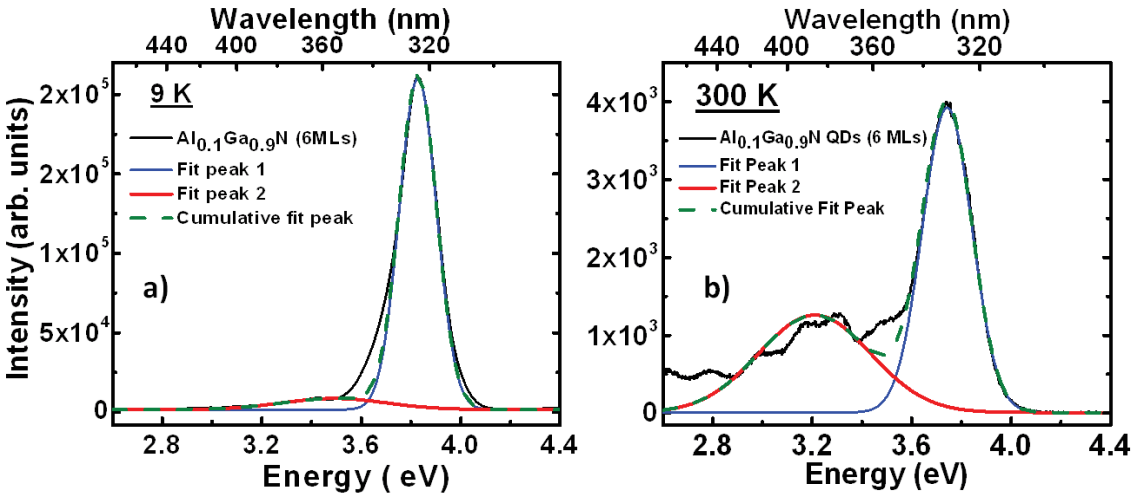

Figure III-8. PL spectrum of $Al_{0.1}Ga_{0.9}N$ (n.c.) QDs with a deposited amount of 6 MLs (sample A6) at a) 9 K and b) 300 K. Two fitting Gaussian curves have been defined to fit each PL spectrum.

Using equation III-1, the calculated energy transitions were compared with the two peak emissions for the whole sample series (Figure III-9(a)). For the second QD family (supposed to be responsible for the low energy PL band, as discussed before), an average height value H_2 was

estimated to be equal to the sum of H_1 (average height of the main QD family corresponding to the deposited amount) plus the relative height difference ($\Delta h = h^{**} - h^{*}$) between the average heights of the two QD distributions determined from Gaussian fits of the AFM height histograms of the samples (Figure III-3(b)). Δh was deduced from the histogram fitting curves and was found to be roughly constant and equal to 0.6 nm for the four samples. This behaviour implies that in average the nanostructure height decreases when the deposited amount decreases as shown in Figure III-9(a).

As discussed before, the main PL peaks can be fitted with $F_{int} \approx 2 \pm 0.5$ MV / cm. For the additional band emission at lower energy, we can clearly see that it cannot be fitted with the same F_{int} value. A larger F_{int} estimated at 3 MV / cm is needed to fit the experimental emission of these additional bands. Such a large value would imply a modification of the QD composition. Consequently, we tried to fit the experimental values of this additional band using different active region compositions (with an Al composition ranging from $0 \leq y_{Al} \leq 0.1$). The best fit was obtained for a value of $F_{int} \approx 3 \pm 0.5$ MV / cm using GaN as an active region (Figure III-9(a)). This seems to indicate the presence of a composition fluctuation in the $Al_yGa_{1-y}N$ QD layers: more precisely, a decrease of the Al composition for this second $Al_yGa_{1-y}N$ QD family, compared to the nominal composition of $Al_{0.1}Ga_{0.9}N$ corresponding to the first (main) QD family, leading to an emission at lower energies.

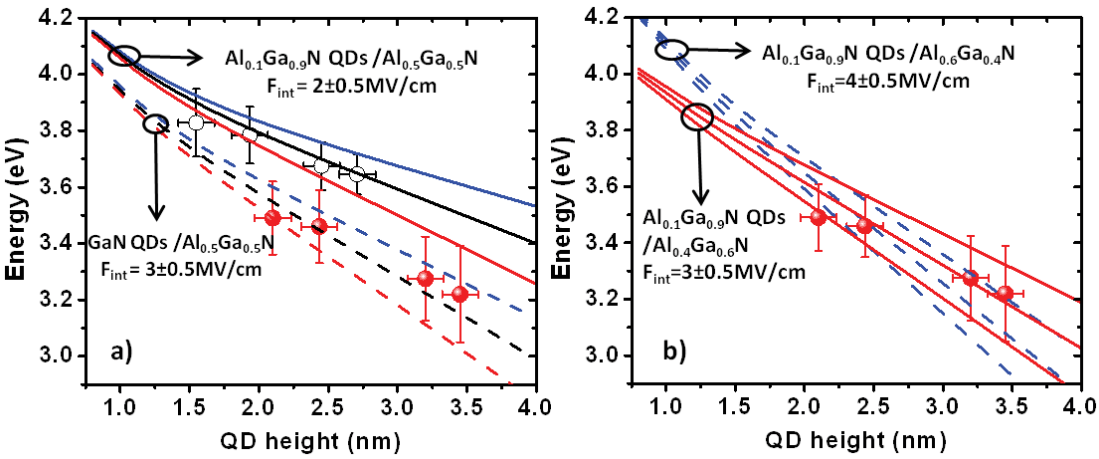

Figure III-9. Calculated transition energies as a function of the QD heights at 9 K, using different electric field values (F_{int}) for: a) $Al_{0.1}Ga_{0.9}N$ QD / $Al_{0.5}Ga_{0.5}N$ (0001) (full lines) and GaN QD / $Al_{0.5}Ga_{0.5}N$ (0001) (broken lines) and for b) $Al_{0.1}Ga_{0.9}N$ QD / $Al_{0.6}Ga_{0.4}N$ (0001) (broken blue lines) and $Al_{0.1}Ga_{0.9}N$ QD / $Al_{0.4}Ga_{0.6}N$ (0001) (full red lines), and compared to the PL peak energies found for the whole sample series (empty and full dots).

Another possibility is to have an Al fluctuation in the composition of the $Al_xGa_{1-x}N$ barrier and not in the dots. To evaluate such hypothesis, the same calculations were performed by maintaining constant the QD composition ($y_{Al} = 0.1$) while changing the barrier composition

between $0.4 \leq x_{Al} \leq 0.6$ (Figure III-9(b)). Different interpretations can be discussed from these results:

- As a first case, if we suppose that the x_{Al} in the matrix decreases (e.g: $Al_{0.4}Ga_{0.6}N$) a value of $F_{int} \approx 3$ MV / cm will be needed to fit the experimental data (red lines Figure III-9(b)). This value is obviously too large as the value of F_{int} should decrease while decreasing the Al composition of the matrix (x_{Al}), which is not the case here, as we already determined a value of $F_{int} \approx 2$ MV / cm for the $Al_{0.1}Ga_{0.9}N$ / $Al_{0.5}Ga_{0.5}N$ (0001) system.
- Now, if we calculate the transitions in the case of an increase of x_{Al} in the matrix, i.e. with the case of $Al_{0.6}Ga_{0.4}N$ system, the experimental results can be -very roughly- fitted with $F_{int} \approx 4 \pm 0.5$ MV / cm (blue dashed lines, Figure III-9(b)). This is indeed a reasonable value, however, as it will be discussed in the following points, it is not in agreement with our experimental results. Also, by comparing those fits with the fits presented for the GaN QDs / $Al_{0.5}Ga_{0.5}N$ (0001) system (dashed lines in Figure III-9(a)), better fits are observed for the last case.
- If we suppose that the additional band emission at lower energy is due to an increase of the Al concentration in the template (i.e. corresponding to the $Al_{0.1}Ga_{0.9}N$ / $Al_{0.6}Ga_{0.4}N$ system), it would imply that: 1) the main peak emission at higher energy is due to $Al_{0.1}Ga_{0.9}N$ QDs / $Al_{0.5}Ga_{0.5}N$ matrix and that 2) the additional band emission at lower energy is the consequence of: i) a local increase of F_{int} by an increasing x_{Al} concentration in localized regions in the matrix, which induces an emission at lower energy, and ii) associated with an increase of the QD height. However, as presented in chapter II, an increase of x_{Al} concentration in the $Al_xGa_{1-x}N$ template (i.e. leading to a lattice mismatch increase with the QD layer) typically induces the formation of QDs with smaller size, which is not in agreement with the measured height histograms from the AFM measurements (Figure III-3(a)).
- In addition, as it will be presented in chapter IV, growing $Al_{0.1}Ga_{0.9}N$ QDs on different $Al_xGa_{1-x}N$ (0001) templates (with $x \geq 0.5$) induces a PL energy shift toward higher energies, when the Al composition in the matrix increases, and not towards lower energy, as for the additional band emission observed here.

To summarize this part, if we suppose a fluctuation of the Al composition in the $Al_xGa_{1-x}N$ templates, a formation of smaller dots would be expected, leading to a weaker influence of F_{int} and an emission towards higher energies. This feature could not explain the PL band emission observed at lower energy, and therefore supports the hypothesis that this band emission is due to a fluctuation in the Al composition (i.e. a reduction of y_{Al}) in the QD layer.

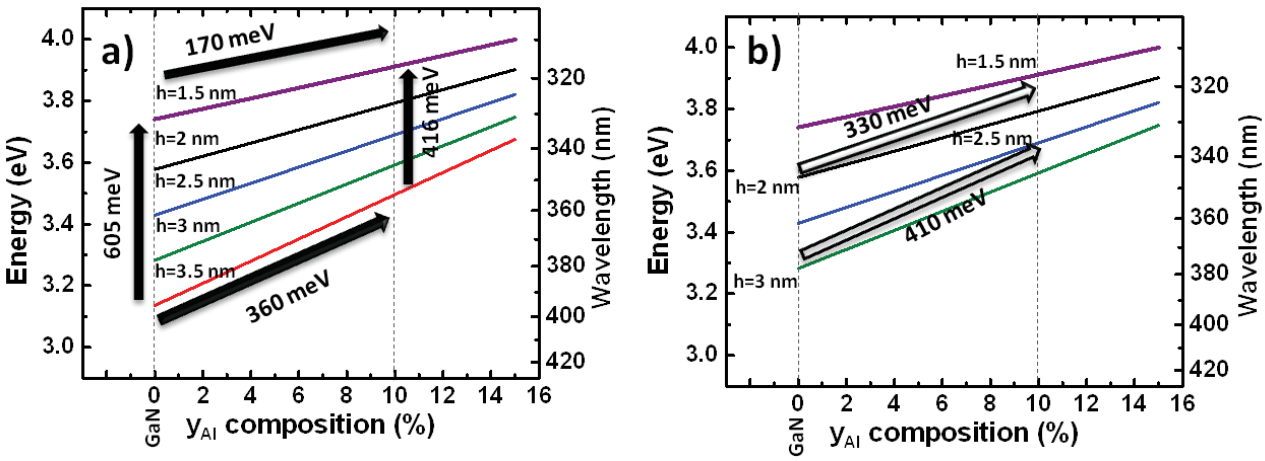

Figure III-10. a) Calculated transition energies variation as a function of y_{Al}, for different QD heights. A linear variation of F_{int}, between 2 MV / cm for $Al_{0.1}Ga_{0.9}N$ and 3 MV / cm for GaN was considered for active regions with y_{Al} varying between 0 and 0.1. The solid arrows show the trends in the transition energy differences between different points. b) Same figure with different solid arrows.

To continue the above discussion, Figure III-10 presents the calculated energy transitions as a function of the QD composition (y_{Al}) and height (h). From these calculations, we can notice two important features on the fundamental transition energy within the QD height variation observed experimentally (i.e. from 1.5 nm to 3.5 nm):

1) **A shift towards higher energies as the y_{Al} concentration in the $Al_yGa_{1-y}N$ QDs increases**. **This shift is observed to increase as the QD height increases**. Typically, for a constant QD height of 1.5 nm, an energy shift of 170 meV (i.e. from 3.74 eV to 3.91 eV) is obtained and for a height of 3.5 nm, a stronger energy shift of 360 meV (i.e. from 3.14 eV to 3.5 eV) is observed (while increasing y_{Al} from 0 to 10 %). This result shows the stronger influence of F_{int} for higher QDs height.
2) **It is also noted that a larger energy shift as a function of the $Al_yGa_{1-y}N$ QD height is observed while decreasing y_{Al}** (i.e. 416 meV for $Al_{0.1}Ga_{0.9}N$ QDs, while going from 1.5 nm to 3.5 nm, versus 605 meV for GaN, while going from 1.5 nm to 3.5 nm)**.**

Therefore, from the calculations, we can conclude that an enhancement of the shift in the $Al_yGa_{1-y}N$ QD fundamental energy transition is observed while combining a decrease of the y_{Al} concentration with an increase of the QD height: in other words, an **enhancement of the shift from 330 meV (for 1.5 nm $Al_{0.1}Ga_{0.9}N$ to 2 nm GaN QDs) to 410 meV (for 2.5 nm $Al_{0.1}Ga_{0.9}N$ to 3 nm GaN)** is calculated, as presented by the arrows in Figure III-10(b). These results show that fluctuations of the QD height and/or composition have a strong impact on the PL emission energy. Finally, this leads us to attribute this PL band at lower energy, which corresponds to an energy shift between 320 meV and 430 meV compared to the PL emission at

high energy, to a variation of the $Al_yGa_{1-y}N$ QD composition (lower y_{Al}) and height distribution (higher height) in the structures.

To further analyse the QD properties, power dependent PL measurements were performed (between 30 mW and 9.5 µW) at 9 K to search for any screening effects on both PL bands (Figure III-11). An example for sample A7 is shown in Figure III-11. We can see that for a similar excitation power variation, over more than 3 decades, no PL energy shift is observed for the QD family emitting at higher energy (above 3.6 eV), however a shift is observed for QDs emitting at lower energy. These results agree with the presence of an asymmetric distribution of QDs with the smaller $Al_{0.1}Ga_{0.9}N$ QDs being insensitive to the injected carrier density, whereas the higher $Al_yGa_{1-y}N$ QDs with a reduced y_{Al} concentration show a shift of more than 180 meV due to the partial screening of F_{int} by the injected carriers [24]. Also, by comparing the full samples series, this shift tends to increase as the deposited amount used to fabricate the QDs increases (Table III-1).

It is also important to say that fitting such a large band, composed of multi peak emissions, is difficult, and complicates the estimation of the exact energy position. For this reason, important error bars are added. Also, we could think that the variation of the relative intensities of peak 1 and peak 2 (Figure III-11(a)) can mislead our interpretation. To analyze this, on Figure III-11(b), we are showing a zoom on the low energy band for two different excitation powers (30 mW and 0.3 mW). We have multiplied the spectra measured at an excitation power of 0.3 mW by 100 to clarify the presence of an energy shift for the low energy band. As shown by the dashed lines on a specific single peak in this band, a shift towards higher energies is observed while increasing the excitation power. However, it would be very difficult to make an interpretation of each single peak in the band at lower energy, due to the presence of interference fringes: therefore, we have averaged the spectra by only two fitting Gaussians. Once again, the fitting shows only an estimation of the low energy peak position.

Table III-1: Summary of the main optical properties of the asymmetric A sample series.

$Al_{0.1}Ga_{0.9}N$ QDs Samples	PL emission at 9 K		Energy shift between 9.5 µW and 30 mW (meV) (Low energy peak)	Integrated intensity ratio between 300 K and 9 K	
	High energy peak (eV)	Low energy peak (eV)		High energy peak (%)	Low energy peak (%)
A (6 MLs)	3.83	3.49	200 ± 40	2	15
B (7.5 MLs)	3.78	3.46	180 ± 40	2	14
C (9.5 MLs)	3.68	3.28	250 ± 50	3	28
D (10.5 MLs)	3.65	3.22	260 ± 50	1	11

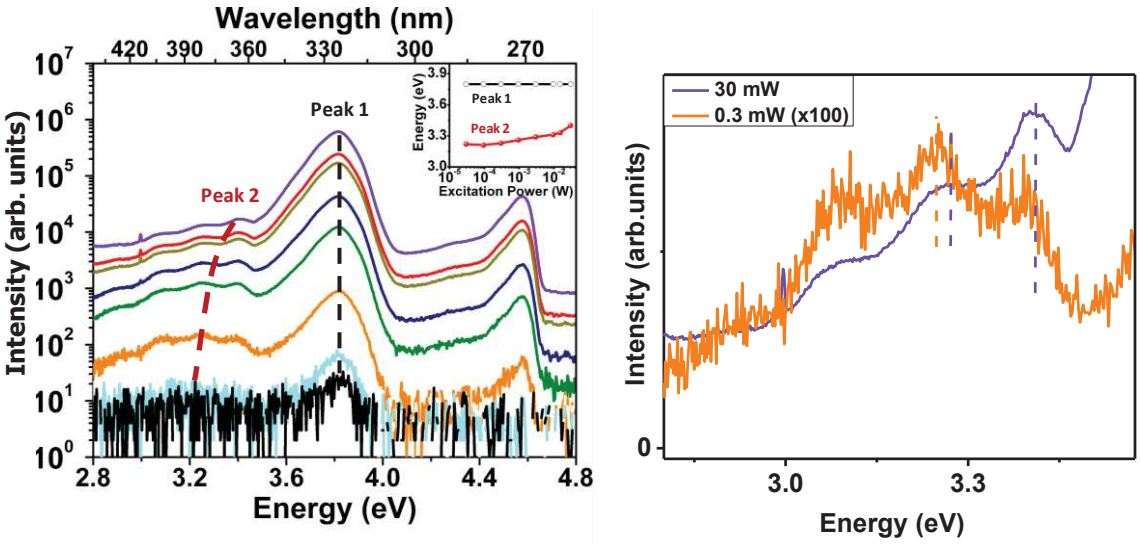

Figure III-11. Low temperature power dependent PL spectra, for $Al_{0.1}Ga_{0.9}N$ (n.c.) QDs with 7.5 MLs (sample A7): a) between 30 mW and 9.5 µW, and b) by zooming on the additional low energy band emission for excitation powers of 30 mW and 0.3 mW. The inset in Figure III-11(a) shows the variation of the PL energy as function of the incident power.

To have a step forward into the optical properties of these samples, room temperature measurements were compared to low temperature ones to estimate their radiative efficiency. An example for samples A6 and A7 are presented on Figure III-8 and Figure III-12 respectively. By studying the two QD emission peaks, two different quenching behaviours were observed:

- **For the peaks at higher energy**, an important PL integrated intensity reduction was observed with an intensity ratio, between 300 K and 9 K [I(300K) / I(9K)], around 1 % to 3 %.
- **For the energy bands at lower energy**, better I(300K) / I(9K) ratios are observed, varying between 11 % and 30 %.

These characteristics indicate a stronger carrier confinement in higher QDs, as previously observed [20]. Also, the weak radiative recombination efficiency values can be correlated with the QDs morphology observed on the AFM and SEM images (Figure III-2 and Figure III-4), due to the presence of elongated QDs. Indeed, as elongated QDs present a larger surface area compared to isotropic QDs (three times higher surface area), carriers are less confined (i.e. localized), and the probability to have non radiative recombinations on surrounding defects (or within them) is higher; i.e. in particular the presence of a threading dislocation propagating through an elongated QD. It is worth noting that the radiative efficiency was also compared between QDashes and QDs in the GaN / $Al_{0.5}Ga_{0.5}N$ (0001) system and a lower radiative efficiency was observed for QDashes [25]. It was also shown that the ammonia pressure has an effective impact on the shape of GaN nanostructures and the fabrication of QDashes or QDs. In

fact, as the $Al_{0.5}Ga_{0.5}N$ layers are grown with an NH_3 source, residual NH_3 could be present in the growth chamber while growing the QD plane. As discussed in chapter II, the presence of NH_3 induces some changes in the surface energy and thus impacts the QD shape, favouring the growth of elongated QDs [16].

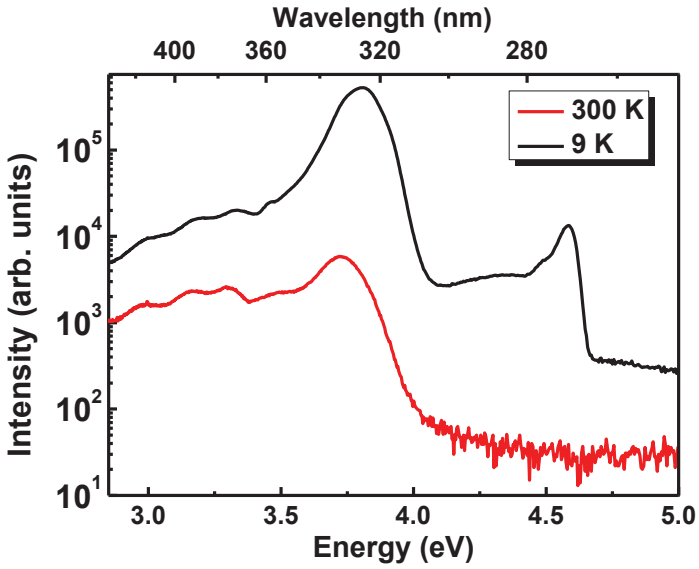

Figure III-12. PL spectrum of $Al_{0.1}Ga_{0.9}N$ (n.c.) QDs grown on $Al_{0.5}Ga_{0.5}N$ (0001) with 7.5 MLs (sample A7) at 9 K and 300 K.

III.3 Symmetric QDs (2nd generation) versus elongated QDs

In this part, we have modified the QD growth conditions to better control their shape. From the last part, we observed the formation of elongated QDs which has an important impact on the optical properties. This elongated QD shape is seen as the consequence of two mechanisms: 1) the presence of residual ammonia in the chamber while growing the QDs planes, which plays a role on the surface energy and the 2D-3D growth mode transition [16] and 2) the limited adatom mobility (at 740°C) which favours the creation of a high density of nucleation centers which can then coalesce to form larger and elongated QDs. Different growth conditions were studied to better control and optimize the QD shape and the optical properties. In this part, an $Al_{0.1}Ga_{0.9}N$ / $Al_{0.5}Ga_{0.5}N$ (0001) QD sample was grown with 7.5 MLs of $Al_{0.1}Ga_{0.9}N$ deposited amount (similar to sample A7 studied in the last part) which will be referred to as B7. After the growth of the $Al_{0.5}Ga_{0.5}N$ template, the QDs were grown using the following procedure:

1) A growth interruption under vacuum, before the growth of the QD layer, is performed to decrease residual ammonia in the chamber.

2) The deposition of $Al_{0.1}Ga_{0.9}N$ QDs was then realized around 740°C.

3) An annealing under vacuum for 6 min, associated to an increase of the temperature up to 830°C ± 10°C (Figure III-13(c))[26].

III.3.1 Morphological properties

The 2D/3D transition was also followed and recorded in-situ using the RHEED diagram. As we can see on Figure III-13(c), after the 2D-3D transition, the RHEED intensity remains constant at low annealing temperature (≈ 740°C). Then, an increase of the Bragg spot intensity is observed while annealing at higher temperature (≥ 800°C). Indeed, at higher temperature, the adatom mobility is enhanced which induces a QD rearrangement and explains the increase of the Bragg spot intensity. At higher temperature, QDs growth was also shown to be kinetically favoured [27]. Also, by looking at the RHEED images of the QDs (Figure III-13(a) and (b)), we can see that the Bragg spots are better defined for sample B7 (Figure III-13(b) compared to sample A7 (Figure III-13(a)). This could also be verified by comparing the RHEED intensity relative variation between the minimum and maximum intensities ($\Delta I_{RHEED}/I_{RHEED}$) for samples B7 and A7 (Figure III-13(c). We can see that this relative variation is two times higher for sample B7.

As we can see on the SEM and AFM images (Figure III-14 (a) and (b)), a significant improvement in the QD shape uniformity is found. More precisely, a symmetric shape is observed for sample B7 compared to the elongated QDs studied in the previous part. Indeed, QDs morphological changes (i.e. size, shape and density) could be expected under vacuum, due to the thermal enhancement of the adatoms mobility, as a function of time and temperature. Also, a change of the surface energy cost could be induced (as presented in chapter II). Finally, this modification during the annealing step at higher temperature could be the consequence of different mechanisms: i) a higher adatom mobility and ii) evaporation processes, since it has already been shown that GaN evaporate under vacuum with a significant evaporation rates at temperatures higher than 780°C, which will be further discussed in section III-4.

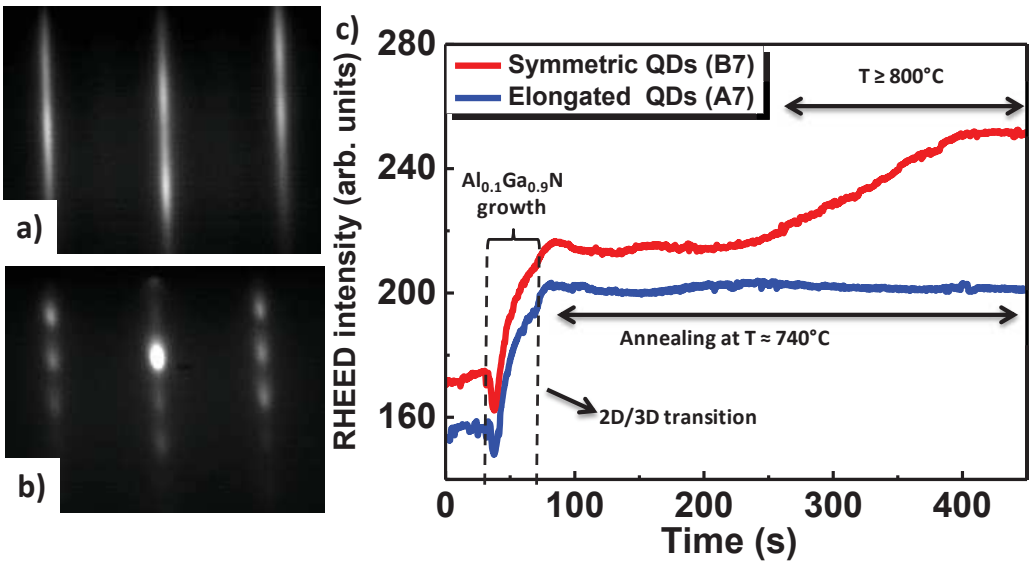

Figure III-13. Reflection high – energy electron diffraction patterns along the <11-20> azimuth for $Al_{0.1}Ga_{0.9}N$ QDs using two different annealing temperatures: a) sample A7 (annealing at 740°C), b) sample B7 (annealing ≥ 800°C). c) RHEED intensity recorded during the formation of $Al_{0.1}Ga_{0.9}N$ QDs for samples B7 and A7.

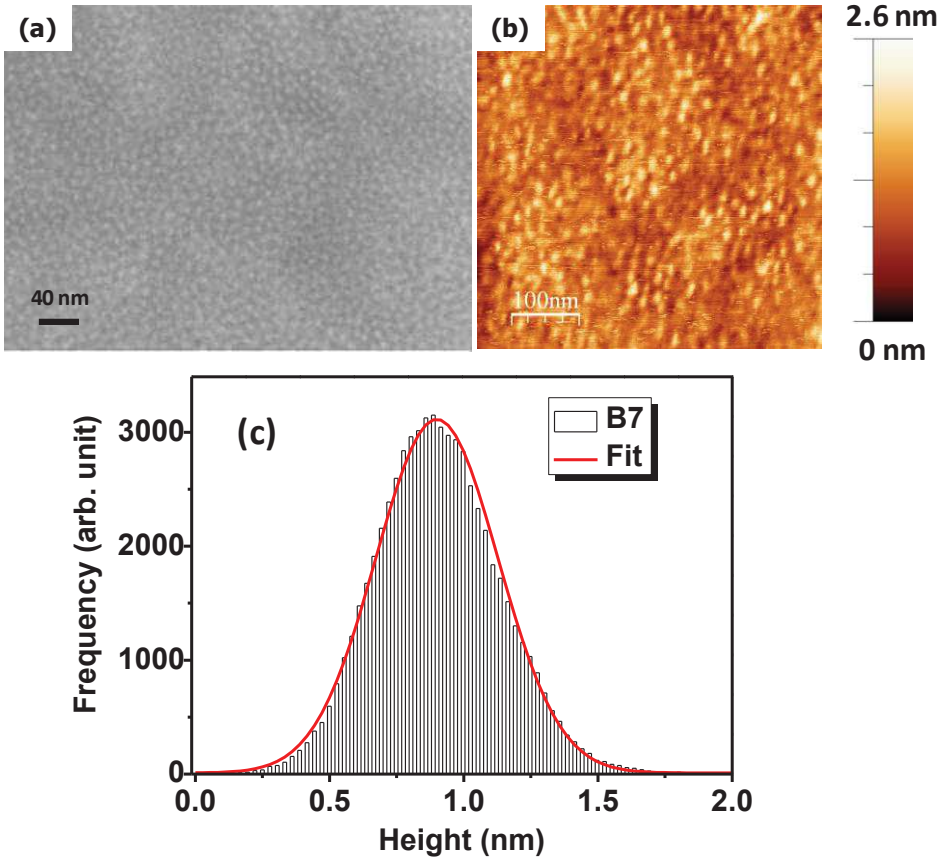

Figure III-14. Sample B7 (symmetric QDs): a) scanning electron microscopy image, b) atomic force microscopy image and c) height distribution histogram determined by AFM, and fitting with one Gaussian function.

By looking at the height distribution of sample B7 (Figure III-14 (c)), we can clearly see that the histogram can be well fitted using a single Gaussian, contrary to the case of sample A7 (Figure III-3(b)). The fact that adding an annealing step at higher temperature changes the shape of the height distribution (i.e. from asymmetric to symmetric) agrees well with the hypothesis that the second QD family present in the A sample series is due to the formation of Ga-rich $Al_yGa_{1-y}N$ QDs with a composition approaching to GaN (i.e. a low y_{Al} (<< 0.1) concentration leading to (Al)GaN QDs). Indeed, the annealing procedure (above 800°C) could lead to a redistribution and/or evaporation of GaN, whereas AlN bonds remains stable at these temperatures. We can also note that the QD density is around 1.5 x 10^{11} cm^{-2} with an average QD height around 0.9 nm. Finally, an average QD diameter of 8 ± 3 nm was determined from the SEM characterization.

III.3.2 Comparison of the optical properties between symmetric and elongated QDs

Concerning the PL properties, different behaviours were observed for sample B7 (symmetric QDs) compared to the A sample series (elongated QDs). The PL emission energy is found around 3.73 eV, at 300 K, which is in good agreement with the PL energy found for sample A7 (3.7 eV). The additional PL band at lower energy, observed for the A sample series, is found to have a much weaker intensity (the PL integrated intensity of the emission between 2.8 eV and 3.4 eV is found to be 7 to 10 times weaker) for sample B7 (Figure III-15(a)).

Temperature dependent PL measurements were also performed for sample B7 and compared with sample A7 in Figure III-15(b). It is worth noting that the PL spectrally integrated intensity ratio between 300 K and 9 K is around 10 % for symmetric QDs (B7) which is more than three times higher compared to elongated QDs (≤ 3 %). GaN / $Al_{0.5}Ga_{0.5}N$ (0001) QDashes integrated intensity ratios were also compared with QDs and about three times lower ratio values were also obtained for QDashes [25]. This better PL efficiency for symmetric QDs compared to elongated QDs is attributed to the reduction of their lateral size and thus a lower probability to recombine non radiatively on surrounding defects.

In stationary conditions (continuous excitation of the sample), the variation of the PL integrated intensity as a function of temperature can be described by:

$$I(T) = \frac{I_0}{1+A.\exp(\frac{-Ea}{K_bT})} \quad \text{(III-3)}$$

where I_0 is the intensity at low temperature, E_a is the needed activation energy for a non radiative process and A is a coefficient related to the radiative (τ_r) and non-radiative (τ_{nr}) lifetimes [i.e. $\tau_{nr} = \tau_0 \exp\left(\frac{E_a}{K_b T}\right)$ and $A = \frac{\tau_r}{\tau_0}$][28].

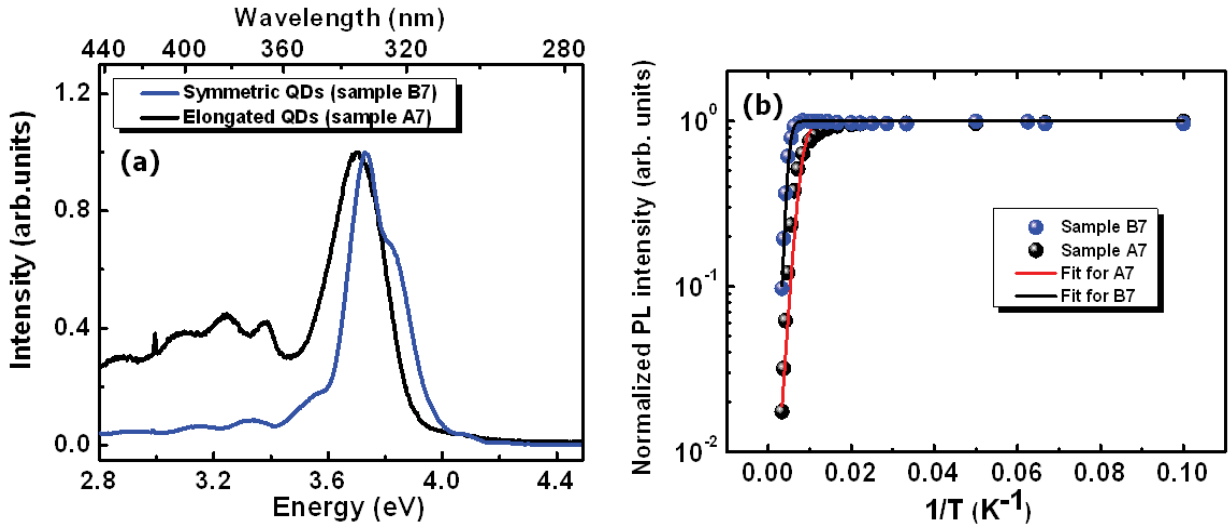

Figure III-15. a) PL spectrum of samples B7 (symmetric QDs) and A7 (elongated QDs) at 300 K. b) Temperature dependence of the integrated PL intensity for samples B7 and A7. The solid lines represent the fitting curves.

On Figure III-15(b), the experimental values were fitted using equation III-3 for samples B7 and A7. The values of E_a and A are summarized in Table III-2. We can note that E_a increases from 76 meV (for elongated QDs) to 140 meV (for symmetric QDs). This activation energy can be related to the potential barrier that the carriers have to overcome to reach non radiative recombination centers. E_a was also found to increase while going from QW to QDs (i.e. from 41 meV to 126 meV for GaN QW and QDs respectively [29]), thanks to the 3D carrier confinement. In our case, we found that E_a also increases while going from elongated (A7) to symmetric (B7) QDs which also confirms the better spatial confinement for symmetric QDs.

Table III-2. Summary of the main PL properties for sample B7 and A7.

	PL Energy emission (eV) at 9 K / 300 K	**I(300K) / I(9K) (%)**	**E_a (meV)**	**A**
Symmetric QDs (B7)	3.8/3.73	10	140	2000
Elongated QDs (A7)	3.78/3.71	2	76	980

III.4 Study of the annealing effect by TEM

To get more insight on the annealing effect, at different temperatures, on the QD formation and heights, a sample dedicated to transmission electron microscopy (TEM) was grown with two planes of $Al_{0.1}Ga_{0.9}N$ QDs (10 MLs) grown on an $Al_{0.7}Ga_{0.3}N$ (0001) template. The first plane of QDs, **annealed at 740°C,** and the second one, **annealed above 800°C,** are labelled **LA-plane and HA-plane** respectively, in the following. Cross-sectional high-angle annular dark-field imaging in scanning transmission electron microscopy mode (HAADF -STEM) was realized using a JEOL 2010F (200 KV) microscope. For the high atomic resolution characterization (Figure III-19), a TITAN ULTIMATE 300 KV (MINATEC) microscope was used. Figure III-16 shows the HAADF-STEM images taken along the [14-50] zone axis for the LA-plane (Figure III-16(a)) and the HA-plane (Figure III-16 (b) and (c)). In general, $Al_{0.1}Ga_{0.9}N$ QDs composed of heavier material appear brighter than the $Al_{0.7}Ga_{0.3}N$ matrix. We can also note that for the LA-plane a continuous 2D layer is observed (Figure III-16(a)), contrary to the HA-plane for which QDs with a truncated pyramidal shape (Figure III-16(b) and(c)) are observed. As seen before, on the AFM and SEM images, elongated QDs are formed when annealed at 740°C (A sample series; cf. Figure III-2 and Figure III-4) while symmetric ones are formed when annealed above 800°C (sample B7; cf. Figure III-14). Noteworthy, in cross section, TEM images of QDs can originate from the projection and the superposition of several QDs along the thickness of the TEM sample specimen due to the nm-size lateral dimensions of the QDs. This feature complicates the observation of a precise QD shape, and thus the exact determination of the QD dimensions. As the surface area of elongated QDs is three times higher than that of symmetric ones, the probability of projection and superposition of several QDs along the thickness of the sample is higher. Consequently, the observation of high density nm-sized elongated QDs on cross sectional TEM images are even more difficult than in the case of symmetric ones. Nevertheless, the average height of the QDs can still be estimated. For LA-plane, a height varying between 3.3 nm and 4.5 nm, giving an average height of 3.9 ± 0.5 nm was determined. For HA-plane, a smaller average QD height of 2.8 nm ± 0.4 nm was measured. This last value for HA-plane is in close agreement with the deposited amount of 10 MLs (~ 2.6 nm), as introduced in part III.2.2. It is important to remember that the QD samples with annealing at 740°C showed an asymmetric height distribution with a QD family having higher heights (cf. Figure III-17). The presence of QDs with higher heights could impact on the average estimation of the height from the STEM images obtained for LA-plane, which could clarify the higher average QD height measured in this case compared to HA-plane. As discussed before, **those QDs with higher heights are presumably $Al_yGa_{1-y}N$ QDs with y_{Al} concentration close to 0** (as discussed in part III.2.2) and which will be **labelled Ga-rich QDs** in the following, for

simplicity. Therefore, the QD height reduction for HA-plane is attributed to the evaporation of these Ga-rich QDs, with higher heights, by annealing at higher temperature. Actually, this hypothesis is confirmed by comparing the QD height histograms for samples A7 and B7 (QDs annealed at low and high temperature, respectively). We can clearly see that the height distribution is modified from an asymmetric to a symmetric distribution and the QD family at higher heights (Ga-rich QDs) is suppressed (Figure III-17(a)). Also, the main QD family is found to be at the same average height for sample B7 and A7, around 0.9 nm (AFM height estimation). It is important to note that this height value (0.9 nm) is not an accurate estimation for the average QD heights. As discussed before, in the case of $Al_{0.1}Ga_{0.9}N$ QDs, the height estimation from AFM measurements is not precise due to their small size and very high densities. Also, on AFM images the wetting layer cannot be measured. Therefore, the AFM histograms **underline** the modification of the height distribution when going from asymmetric to symmetric QDs, which is in agreement with the suppression of the QD family with higher heights (Ga-rich), by GaN evaporation while the main $Al_{0.1}Ga_{0.9}N$ (n.c.) QD family is found to be at the same average height, which is equal to the $Al_{0.1}Ga_{0.9}N$ deposited amount of 10 MLs (~ 2.6 nm).

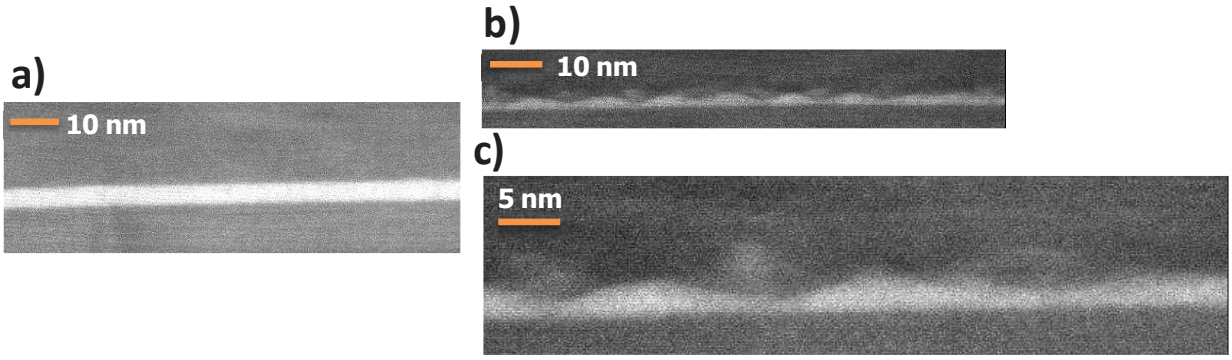

Figure III-16. Cross – section high angle annular dark-field imaging in scanning transmission electron microscopy mode (HAADF-STEM) of $Al_{0.1}Ga_{0.9}N$ QDs with a) an annealing at low temperature (740°C), and b) an annealing at high temperature (above 800°C). c) High magnification of image b).

We would like to underline that the formation of Ga-rich QDs, while depositing the $Al_{0.1}Ga_{0.9}N$ (n.c.) layers, together with the growth of the main $Al_{0.1}Ga_{0.9}N$ (n.c.) QDs family (with h_{QD} equals to the $Al_{0.1}Ga_{0.9}N$ deposited amount), may lead to a composition fluctuation inside the $Al_{0.1}Ga_{0.9}N$ (n.c.) QDs and / or the presence of another QD family with Al concentrations higher than the nominal one (named $Al_{0.1}Ga_{0.9}N$ (n.c.) QDs with an Al-rich top) (cf. Figure III-18).

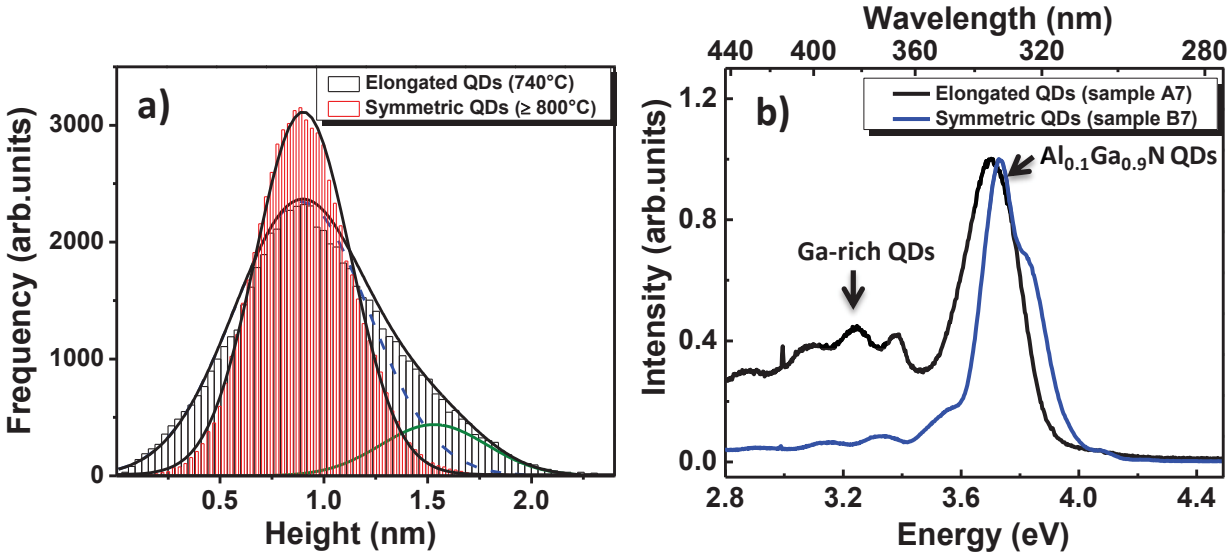

Figure III-17. a) Height distribution of $Al_{0.1}Ga_{0.9}N$ QDs determined by AFM for symmetric QDs (annealed above 800°C (HA-plane) and presented by red and white bars) and elongated QDs (annealed at 740°C (LT-plane) and presented by black and white bars). Elongated QDs were fitted using two Gaussians curves and symmetric QDs were fitted using one Gaussian curve. b) PL spectrum for symmetric and elongated QDs samples at 300 K.

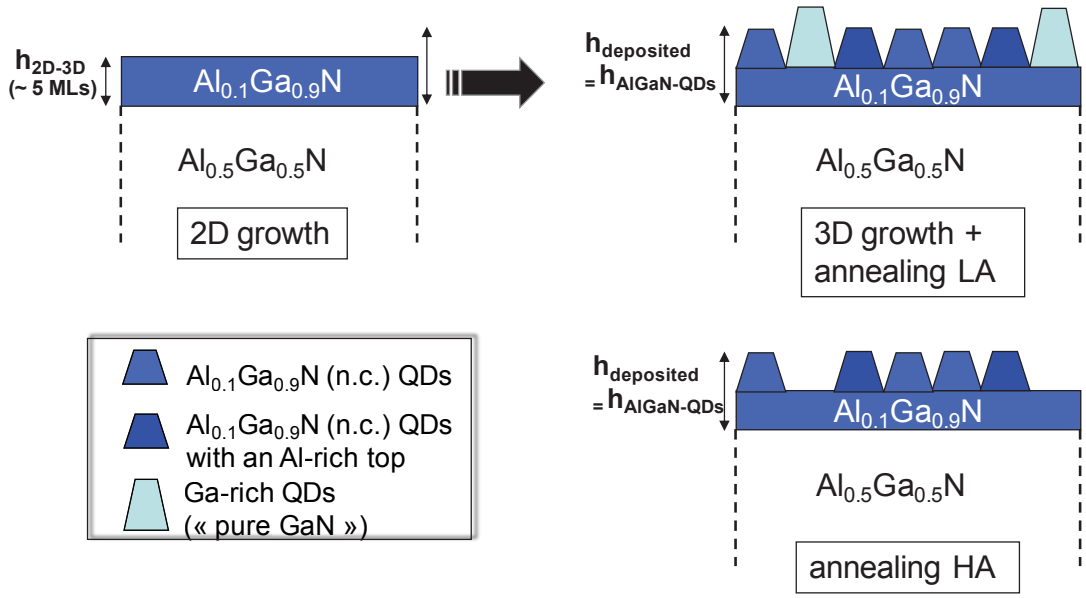

Figure III-18. Schematics presenting the different steps of $Al_{0.1}Ga_{0.9}N$ QDs (10 MLs) growth with the different annealing processes: a) initial growth of an $Al_{0.1}Ga_{0.9}N$ 2D layer (before the 2D-3D transition); b) QDs formed at low annealing (LA) temperature (≈ 740°C); c) QDs formed at high annealing (HA) temperatures (≥ 800°C).

Also, from PL measurements in part III.2.2, the additional band emission at lower energy was estimated to be due to Ga-rich (Al,Ga)N QDs with higher heights. Yet, by annealing above 800°C, the relative intensity of this band emission is found to be importantly decreasing (Figure III-17 (b)). In fact, the evaporation rate of GaN is strongly enhanced above 800°C [30]. Clearly, the annealing steps under vacuum induce some evaporation of GaN [31], i.e. the Ga-rich

(Al,Ga)N QDs emitting at lower energy. Along this view, a fluctuation of the composition of the main QD family (with an $Al_{0.1}Ga_{0.9}N$ (n.c.) composition) is also expected, i.e. with a higher Al concentration compared to the nominal value of 0.1. However, since the main PL peaks are found at a similar energy for samples A7 and B7 (Figure III-17 (b)), the average QD composition is not expected to be strongly modified compared to the nominal value. A tentative explanation for the preservation of the $Al_{0.1}Ga_{0.9}N$ QDs height and composition integrity during the annealing procedure at high temperature is attributed to the formation of a thin AlN shell surrounding the QDs during the initial stage of the annealing process related to growth mechanisms associated to the modification of the QD morphology by adatom diffusion and GaN evaporation. Such an AlN layer would then prevent the $Al_{0.1}Ga_{0.9}N$ QDs "core" from any possible evaporation mechanism during the final annealing steps at higher temperature, keeping the same QD nominal composition before and after the annealing step. However, at this stage the presence of such an AlN layer remains to be clarified.

In order to confirm the possible presence of such an AlN layer and get more insight on the evaporation process under vacuum for (Al,Ga)N alloys, a sample was grown with three $Al_{0.5}Ga_{0.5}N$ (0001) layers of 10 nm (i.e. 39 MLs). After the growth of each layer, an annealing step under vacuum at 800°C was performed. Different annealing times were applied for the three layers: **28 min, 5 min and 30 sec for layer #1, #2 and #3 respectively**. 8 MLs of GaN were deposited between the different $Al_{0.5}Ga_{0.5}N$ layers in order to separate them. This sample was then characterized by HAADF-STEM in cross section (Figure III-19(a)). After analysing different images, we can see that the $Al_{0.5}Ga_{0.5}N$ thickness measured after annealing is independent of the annealing time within a one ML uncertainty (Table III-3). A thickness around 36 MLs is measured for the three different layers. This means that at a very early stage of annealing (i.e. within the first 30 seconds at a temperature ~ 800°C) only the composition of the first 3 to 4 MLs from the surface is modified. In other words, the evaporation process is taking place only in the first 3 to 4 MLs. This is the result of the formation of an AlN layer which acts as a protecting layer from any further evaporation process in the under-layers. This AlN layer can be clearly seen in Figure III-19(a) and (c) (presented by the red arrows) and its thickness was estimated to be around 3 ± 1 MLs.

Table III-3. Summary of the measured thickness, using TEM, of a stacking of three $Al_{0.5}Ga_{0.5}N$ / GaN layers after different annealing times: 28 min, 5 min and 30 sec performed on the $Al_{0.5}Ga_{0.5}N$ layers #1, #2 and #3, respectively. The $Al_{0.5}Ga_{0.5}N$ deposited amount is identical for the three layers and corresponds to 10 nm (39 MLs).

	Layer #1 (Annealing 28 min)	**Layer #2 (Annealing 5 min)**	**Layer #3 (Annealing 30 sec)**
Layer thickness (MLs)	35 ± 1MLs	36 ± 1MLs	36 ± 1MLs

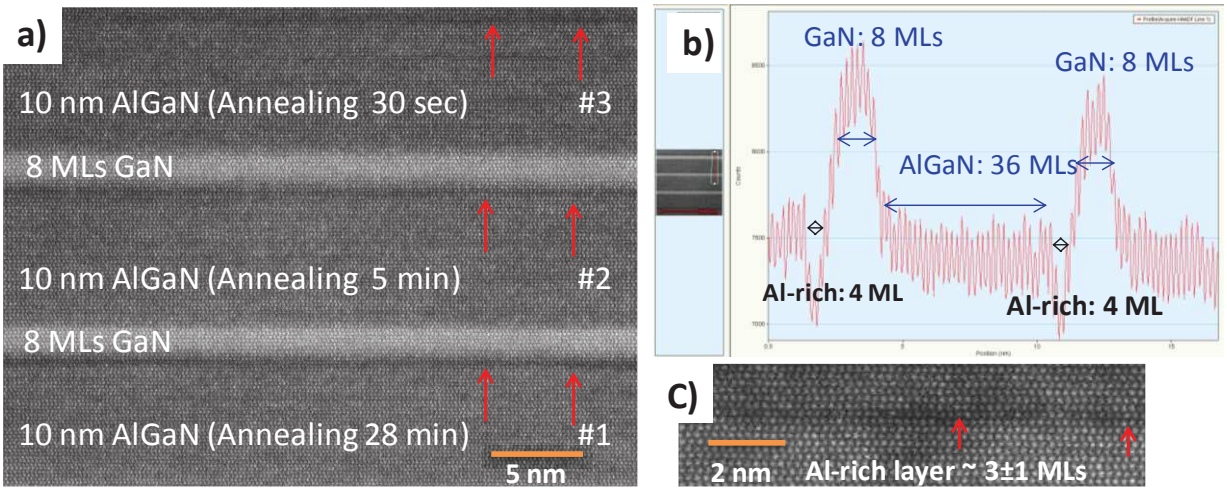

Figure III-19. a) High resolution HAADF-TEM image along the [11-20] zone axis for a sample grown with a stacking of three $Al_{0.5}Ga_{0.5}N$ / GaN layers having a thickness of (10 nm / 2 nm) . The three $Al_{0.5}Ga_{0.5}N$ layers were annealed at 800°C using different annealing times: 28 min, 5 min and 30 sec for layer #1, #2 and #3, respectively. The $Al_{0.5}Ga_{0.5}N$ layers are separated by 2 nm (8 MLs) of GaN used as a marker layers. b) A profile of figure (a) along the growth direction. c) High magnification of image a), showing the AlN layer pointed out by the red arrows.

In the following, we proposed a model in order to further explain the formation of the AlN layer and how the evaporation process is taking place. Figure III-20 presents a schematic model of the possible evaporation process steps for the $Al_{0.5}Ga_{0.5}N$ layer. At the first moments of the annealing, the (Al,Ga)N surface contains 50 % of Ga atoms and 50 % of Al atoms (cf. Figure III-20(a)). Since the GaN chemical bond energy is lower than that of AlN, the Ga evaporates more rapidly. The evaporated GaN reveals the underlying layers of $Al_{0.5}Ga_{0.5}N$, allowing them to also evaporate (Figure III-20(b)). The GaN evaporation from the different under-layers leads to the gradual formation of an AlN layer on the surface. Once a monolayer of AlN is formed (cf. Figure III-20(c), green circles), it prevents further evaporation of GaN and stabilizes the $Al_{0.5}Ga_{0.5}N$ surface. In addition, even low, Al adatoms mobility should allow to recover a flat surface.

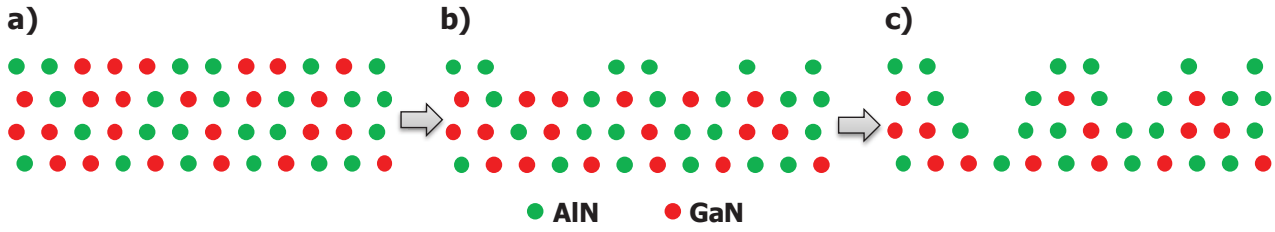

Figure III-20. A possible atomic structure of an $Al_{0.5}Ga_{0.5}N$ layer at different annealing stages: a) initial layer, b) first evaporation steps and c) stabilization of the surface due to the formation of an AlN layer. Green and red circles represent AlN and GaN, respectively.

In $Al_{0.1}Ga_{0.9}N$ QDs, the evaporation process is probably not following the exact same scheme, but the formation of a thin AlN shell surrounding the QDs for an annealing at 800°C or (above) may also be expected. The presence of such a layer would then prevent the $Al_{0.1}Ga_{0.9}N$ QDs "core" from any evaporation effect that would induce a fluctuation of the nominal $Al_{0.1}Ga_{0.9}N$ concentration. This is also confirmed by the PL characterization which showed the same PL energy emission for both low temperature and high temperature annealing (Figure III-15 (a)).

The presence of a thin AlN layer is clearly observed on the $Al_{0.5}Ga_{0.5}N$ layer, however for $Al_{0.1}Ga_{0.9}N$ QDs the presence of such a layer remains a hypothesis.

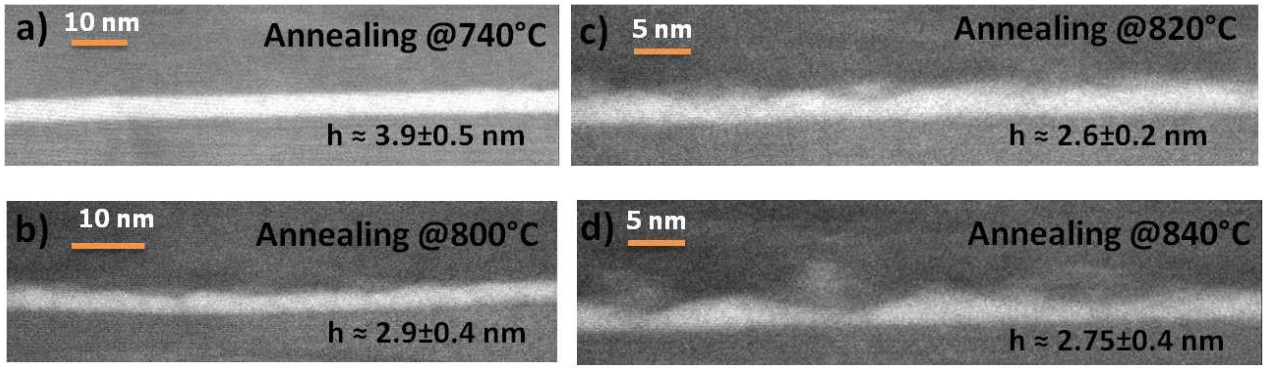

Figure III-21. Cross –section HAADF-STEM images of $Al_{0.1}Ga_{0.9}N$ QDs with an annealing at a) 740°C, b) 800°C, c) 820°C, and d) 840°C.

Finally, TEM characterizations were also performed on different $Al_{0.1}Ga_{0.9}N$ QD (10 MLs) layers grown at 740°C and annealed at different temperatures: 740°C, 800°C, 820°C and 840°C. Figure III-21 presents the different QD planes. As discussed before, a clear difference is observed while annealing at low temperature (~ 740°C) and at higher temperature (≥ 800°C). Going from an annealing at 740°C to 800°C, the average QD height is observed to decrease, from 3.9 nm ± 0.5 nm down to 2.9 nm ± 0.4 nm, due to the evaporation of the second QD family with higher heights ((Ga-rich QDs), as explained before). For annealing temperatures above 800°C (i.e. 820°C and 840°C), the evaporation rate of the higher Ga-rich QDs is enhanced which permit to only observe the "main" $Al_{0.1}Ga_{0.9}N$ (n.c.) QDs family with an average QDs height around 2.6 nm ± 0.2 nm (equal to the deposited amount ~ 2.6 nm). Also, while annealing at 820°C and 840°C the QDs average height seems to be unchanged confirming that no evaporation process is taking place, inside the QDs, while increasing the annealing temperature. **This result confirms that a mechanism protecting the $Al_{0.1}Ga_{0.9}N$ QDs "core" from any possible evaporation mechanism is present**. This mechanism is tentatively attributed to the formation of an AlN layer protecting the $Al_{0.1}Ga_{0.9}N$ QDs as explained before.

III.5 Discussion on the different growth procedures

As discussed in this chapter, the shape of the QDs has a drastic impact on the QD optical properties. It was shown that by performing a growth interruption under vacuum before growing the QDs, together with the use of an annealing step at high temperature (≥ 800°C), symmetric QDs are formed. Importantly, this growth process leads to the suppression of an additional emission band at low energy. Such a feature involves a redistribution of the surface atomic arrangement including adatom diffusion and evaporation mechanisms which modify the QD shape. By in-situ RHEED measurements, it is found to be triggered at around 800°C, as followed by the increase in the RHEED intensity related to the QD. Importantly, it has been shown that the evaporation rate of GaN becomes significant in this temperature range. This indicates that such an annealing step under vacuum also induces some evaporation of GaN. To verify this point, we have calculated the average volume of a QD and multiplied it by the QD density. This value was then roughly compared to the $Al_{0.1}Ga_{0.9}N$ deposited amounts. Such a rough comparison shows that the deposited amount is not strictly conserved and that some evaporation takes place. However, it is important to note, that due to the very small dimensions of $Al_{0.1}Ga_{0.9}N$ QDs and the difficulties to determine their precise dimensions, it is quite complicated to have a high precision in the calculation. Yet, in average, the estimated QD volume was found to decrease by a factor 2 or 3 from comparing different samples with QDs annealing at low or high temperature, respectively. This feature could also mean that a fluctuation of the main QD family with an $Al_{0.1}Ga_{0.9}N$ (n.c.) composition could occur. However, since the main PL peaks are found at a similar energy for samples A7 (elongated QDs) and B7 (symmetric QDs), annealed at low and high temperatures, respectively, the average QD nominal composition is not expected to be strongly modified between the two different growth procedures. In fact, as pointed out from the TEM study (cf. part III.4), a thin AlN layer could be possibly formed, surrounding the QDs, which acts as a protecting layer preventing any further evaporation process in the $Al_{0.1}Ga_{0.9}N$ QDs.

Along this view, the additional PL band emission observed on the A sample series is almost suppressed by using an annealing step at higher temperature. This additional band emission was found to be due to fluctuations in the composition and height of the $Al_yGa_{1-y}N$ QDs plane, implying the formation of a second QD family (together with the formation of a main QD family with a near nominal $Al_{0.1}Ga_{0.9}N$ composition). This second QD family is characterized by a reduction of the y_{Al} composition ($Al_yGa_{1-y}N$ QDs with a composition approaching to GaN "Ga-rich QDs") and an increase of the QD height. Also, it is found from the different morphological characterizations that a high temperature annealing (above 800°C) leads to the formation of a symmetric QD height distribution together with a symmetric shape (sample B7).

Putting all these arguments together, we can conclude that by performing an annealing step at higher temperatures, the QDs with a lower Al concentration (Ga-rich QDs) have a tendency to be dissolved by the evaporation of GaN. Also thanks to the symmetric QD shape leading to a reduction of their lateral dimensions, an improvement of the radiative efficiency is also observed.

III.6 Conclusion

The growth of $Al_{0.1}Ga_{0.9}N$ QDs on (0001) oriented $Al_{0.5}Ga_{0.5}N$ templates, with a lattice mismatch of 1 %, has been studied. Changing the growth procedure, especially the annealing step, has shown to modify the QD shape from elongated QDs, formed with an annealing at 740°C, to symmetric QDs, formed with an annealing at a temperature around or above 800°C. The variation of the QD deposited amounts from 10.5 MLs down to 6 MLs showed the ability to cover the deep UVA range, by going from 340 nm (i.e. 3.65 eV) down to 324 nm (i.e. 3.83 eV). An additional band emission at lower energies was also observed for the whole sample series grown with a lower annealing temperature of 740°C. By combining morphological and optical characterizations, this band was attributed to a composition fluctuation in the QD active region inducing the formation of QDs with a reduced Al composition (less than 10 %), estimated to be close to "pure" GaN QDs. These QDs were also found to have higher heights compared to the main $Al_{0.1}Ga_{0.9}N$ QDs family. The formation of different QD characteristics within a QD active layer was also confirmed by power dependent PL results, showing a blue shift of the PL emission of more than 180 meV with increasing the excitation power for the QDs emitting at low energy, whereas no PL energy shift for the emission of the $Al_{0.1}Ga_{0.9}N$ QDs emitting at higher energy was observed. Calculations of the ground state transition energies as a function of the QD height and composition were compared to the experimental PL emission energies of the two peaks. The main peak emissions coming from the $Al_{0.1}Ga_{0.9}N$ QDs were fitted with $F_{int} \approx 2$ MV / cm and the additional low energy emissions were fitted with $F_{int} \approx 3$ MV / cm.

Finally, the influence of the annealing step performed at higher temperature on the additional low energy PL band (assumed to correspond to Ga-rich (Al)GaN QDs) has been shown, with a strong decrease (by about a factor 10) of their PL intensity. This feature is attributed to an adatom rearrangement process including some evaporation of GaN material, leading to the formation of an array of symmetric QDs with a nominal composition of $Al_{0.1}Ga_{0.9}N$. Also, the influence of the QD shape on the radiative efficiency showed an improvement of the confinement for symmetric QDs, characterized by a three times increase of the radiative efficiency.

References

[1] M. Kneissl, T. Kolbe, C. Chua, V. Kueller, N. Lobo, J. Stellmach, A. Knauer, H. Rodriguez, S. Einfeldt, Z. Yang, N. M. Johnson and M. Weyers, Semicond. Sci. Technol. 26 014036 (2011).

[2] S. Nitta, Y. Yukawa, Y. Watanabe, S. Kamiyama, H. Amano, I. Akasaki, Phys. Stat. Sol. (a) 194, 485 (2002).

[3] J. Brault, D. Rosales, B. Damilano, M. Leroux, A. Courville, M. Korytov, S. Chenot, P. Vennéguès, B. Vinter, P. de Mierry, A. Kahouli, J. Massies, T. Bretagnon, and B. Gil, Semicond. Sci. Technol. 29, 084001 (2014).

[4] C. Himwas, R. Songmuang, L. S. Dang, J. Bleuse, L. Rapenne, E. Sarigiannidou, and E. Monroy, Appl. Phys. Lett. 101, 241914 (2012).

[5] C. Himwas, PhD thesis "Nanostructures à base de semi-conducteurs nitrures pour l'émission ultraviolette", Université Joseph-Fourier Grenoble I, (2006).

[6] Y. Taniyasu, M. Kasu, T. Makimoto, Nature (London) 441, 325 (2006).

[7] V. N. Jmerik, E. V. Lutsenko, and S. V. Ivanov, Phys. Stat. Sol. (a) 210, 439 (2013)

[8] C. J. Collins, A. V. Sampath, G. A. Garrett, W. L. Sarney, H. Shen, M. Wraback, A. Yu Nikiforov, G. S. Cargill III, and V. Dierolf, Appl. Phys. Lett. 86, 031916 (2005).

[9] M. Gao, S. T. Bradley, Y. Cao, D. Jena, Y. Lin, S. A. Ringel, J. Hwang, W. J. Schaff, and L. J. Brillson, J. Appl. Phys. 100, 103512 (2006).

[10] J. Brault, B. Damilano, A. Kahouli, S. Chenot, M. Leroux, B. Vinter, and J. Massies, J. Cryst. Growth 363, 282 (2013).

[11] T. Kinoshita, T. Obata, H. Yanagi, and S. Inoue, Appl. Phys. Lett. 102, 012105 (2013).

[12] S. R. Jeon, Z. Ren, G. Cui, J. Su, M. Gherimova, J. Hana, H. K. Cho, and L. Zhou, Appl. Phys. Lett. 86, 082107 (2005).

[13] J. Brault, S. Matta, T.-H. Ngo, D. Rosales, M. Leroux, B. Damilano, M. Al Khalifioui, F. Tendille, S. Chenot, P. de Mierry, J. Massies, and B. Gil, Materials Science in Semiconductor Processing 55, 95 (2016).

[14] S. Vézian, F. Natali, F. Semond, and J. Massies, Phys. Rev. B 69, 125329 (2004).

[15] I. Horcas, R. Fernández, J. M. Gómez-Rodríguez, J. Colchero, J. Gómez-Herrero, and A. M. Baro, Rev. Sci. Instrum., 78, 013705 (2007).

[16] J. Brault, T. Huault, F. Natali, B. Damilano, D. Lefebvre, M. Leroux, M.Korytov, and J. Massies, J. Appl. Phys. 105, 033519 (2009).

[17] T. Huault, J. Brault, F. Natali, B. Damilano, D. Lefebvre, L. Nguyen, M. Leroux, and J. Massies, Appl. Phys. Lett. 92, 051911 (2008).

[18] M. Leroux, S. Dalmasso, F. Natali, S. Helin, C. Touzi, S. Laügt, M. Passerel, F. Omnes, F. Semond, J. Massies, and P. Gibart, Phys. Stat. Sol. (b) 234, 887 (2002).

[19] T. Bretagnon, P. Lefebvre, P. Valvin, R. Bardoux, T. Guillet, T. Taliercio, B. Gil, N. Grandjean, F. Semond, B. Damilano, A. Dussaigne, and J. Massies, Phys. Rev. B 73, 113304 (2006).

[20] J. Brault, S. Matta, T.-H. Ngo, M. Korytov, D. Rosales, B. Damilano, M. Leroux, P. Vennéguès, M. Al Khalifioui, A. Courville, O. Tottereau, J. Massies, and B. Gil, Jpn. J. Appl. Phys. 55, 05FG06 (2016).

[21] C. Himwas, M. den Hertog, E. Bellet-Amalric, R. Songmuang, F. Donatini, L. S. Dang, and E. Monroy, J. Appl. Phys. 116, 023502 (2014).

[22] M. Leroux, H. Lahrèche, F. Semond, M. Laügt, E. Feltin, N. Schnell, B. Beaumont, P. Gibart and J, Massies, Materials Science Forum, 353, 795 (2001).

[23] M. Leroux, J. Brault, A. Kahouli, D. Elmaghraoui, B. Damilano, P. de Mierry, M. Korytov, J.-H. Kim, and Y.-H. Cho, J. Appl. Phys. 116, 034308 (2014).

[24] T. Bretagnon, S. Kalliakos, P. Lefebvre, P. Valvin, B. Gil, N. Grandjean, A. Dussaigne, B. Damilano, J. Massies, Phys. Rev. B 68, 205301 (2003).

[25] T. Huault, J. Brault, F. Natali, B. Damilano, D. Lefebvre, R. Tauk, M. Leroux, and J. Massies, Phys. Status Solidi B 246(4), 842–845 (2009).

[26] S. Matta, J. Brault, T. H. Ngo, B.Damilano, M. Korytov, P. Vennéguès, M. Nemoz, J. Massies, M.Leroux and B. Gil, J. Appl. Phys. 122, 085706 (2017).

[27] B. Damilano, J. Brault, and J. Massies, J. Appl. Phys. 118, 024304 (2015).

[28] M. Leroux, N. Grandjean, B. Beaumont, G. Nataf, F. Semond, J. Massies, and P. Gibart , J. Appl. Phys. 86, 3721 (1999).

[29] Y. H. Cho, H. S. Kwack, B.J. Kwon, J. Barjon, J. Brault, B. Daudin, Le Si Dang, Appl. Phys. Lett. 89, 251914 (2006).

[30] N. Grandjean, J. Massies, F. Semond, S. Yu. Karpov, and R. A. Talalaev, Appl. Phys. Lett. 74, 1854 (1999).

[31] M. Mesrine, N. Grandjean, and J. Massies, Appl. Phys. Lett. 72, 350 (1998).

Table of Contents

IV. $Al_yGa_{1-y}N$ quantum dots ($0 \leq y \leq 0.4$) on $Al_xGa_{1-x}N$ (0001) ($0.5 \leq x \leq 0.7$)

After studying and optimizing the growth conditions of $Al_{0.1}Ga_{0.9}N$ / $Al_{0.5}Ga_{0.5}N$ (0001) nanostructures in chapter III, this chapter will be dedicated to the study of $Al_yGa_{1-y}N$ QDs ($0 \leq y \leq 0.4$) grown on $Al_xGa_{1-x}N$ (0001) ($0.5 \leq x \leq 0.7$) templates with the aim to go deeper in the UV range. In a first part, the impact of changing x_{Al} (i.e. the epitaxial strain and the electric field) on the formation of $Al_{0.1}Ga_{0.9}N$ QDs will be studied. Then, $Al_yGa_{1-y}N$ QDs composition as well as the deposited amount will be varied in order to study the range of accessible wavelengths emission. As a result, the possibility to tune the emission wavelength from the blue down to the UVC range will be presented. Finally, time resolved photoluminescence measurements were also performed to investigate the different recombination processes dynamics in $Al_yGa_{1-y}N$ QD samples and to estimate the internal quantum efficiency at low temperature.

IV.1 $Al_{0.1}Ga_{0.9}N$ QD properties grown on different $Al_xGa_{1-x}N$ (0001) templates

In chapter III, $Al_{0.1}Ga_{0.9}N$ QDs (nominal concentration (n.c.)) grown on $Al_{0.5}Ga_{0.5}N$ (0001) templates were presented. The growth conditions for the QDs were studied showing in particular an important impact of the QD annealing process on the morphological and optical properties. In this part, the influence of the $Al_xGa_{1-x}N$ template Al concentration on the formation and physical properties of $Al_{0.1}Ga_{0.9}N$ QDs will be studied as a first step. For this purpose, $Al_{0.1}Ga_{0.9}N$ QDs, with 10 MLs deposited amount, were grown, using the optimized growth conditions (presented in chapter III), on $Al_xGa_{1-x}N$ (0001) templates with an Al composition varying between $0.5 \leq x \leq 0.7$. The $Al_{0.1}Ga_{0.9}N$ QDs were grown at 720°C followed by an annealing step at higher temperature (≥ 800°C). All the QD planes were grown under N-rich conditions with a III/V flux ratio of 0.7 and a growth rate around (0.3 ± 0.05) ML / s.

As a first step, the QD formation was studied by using RHEED measurements. Figure IV-1, shows a comparison of the 2D-3D transition of $Al_{0.1}Ga_{0.9}N$ (n.c.) QDs grown on $Al_xGa_{1-x}N$ (0001) templates with $x_{Al} = 0.5$ and 0.7. As we can see, by increasing x_{Al}, the RHEED intensity starts to increase, and oscillations disappear, after a shorter deposition time. The critical thickness for the 2D-3D transition (h_c^{2D-3D}) can then be deduced showing a decrease of h_c^{2D-3D} from (5 ± 0.5) MLs down to (3 ± 0.5) MLs while going from $x_{Al} = 0.5$ to 0.7. Indeed, the lattice

mismatch between the QD layer ($Al_{0.1}Ga_{0.9}N$) and the template ($Al_xGa_{1-x}N$) increases from $\Delta a/a$ = 1 % to 1.5 % for x_{Al} = 0.5 and 0.7, respectively.

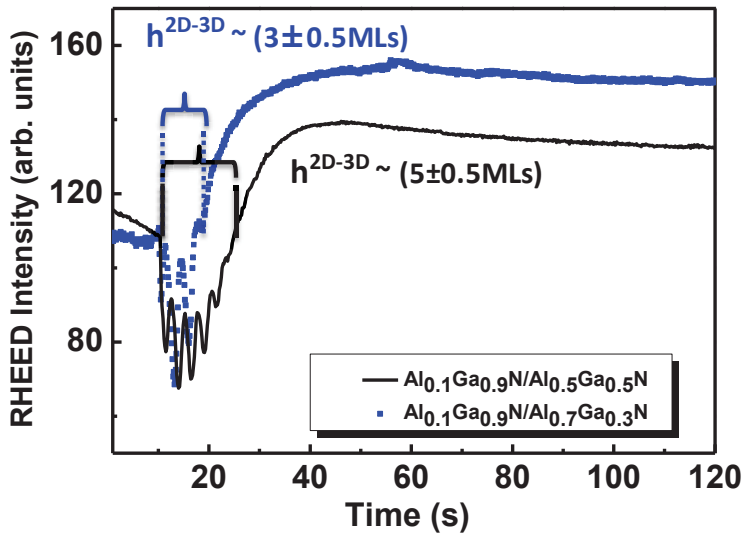

Figure IV-1. Reflection high-energy electron diffraction intensity recorded during the formation of $Al_{0.1}Ga_{0.9}N$ QDs grown on $Al_{0.5}Ga_{0.5}N$ (0001) and $Al_{0.7}Ga_{0.3}N$ (0001) templates.

AFM characterizations were then performed for different samples grown on $Al_{0.5}Ga_{0.5}N$ and $Al_{0.7}Ga_{0.3}N$ templates. The observation of small (Al,Ga)N QDs (with lateral dimensions below 10 nm and heights below 2.5 nm) is at the resolution limit of our AFM equipment, and the determination of their precise morphology is difficult. However, after characterizing different samples, we found that, as a general trend, by increasing x_{Al} in the template, the QD density slightly increases from 3 x 10^{11} cm^{-2} up to 5 x 10^{11} cm^{-2} and the QD diameter decreases from (20 ± 4) nm to (14 ± 2) nm. Figure IV-2 shows an example of AFM images of $Al_{0.1}Ga_{0.9}N$ QDs grown on $Al_xGa_{1-x}N$ (0001) with x equals to 0.5 and 0.7.

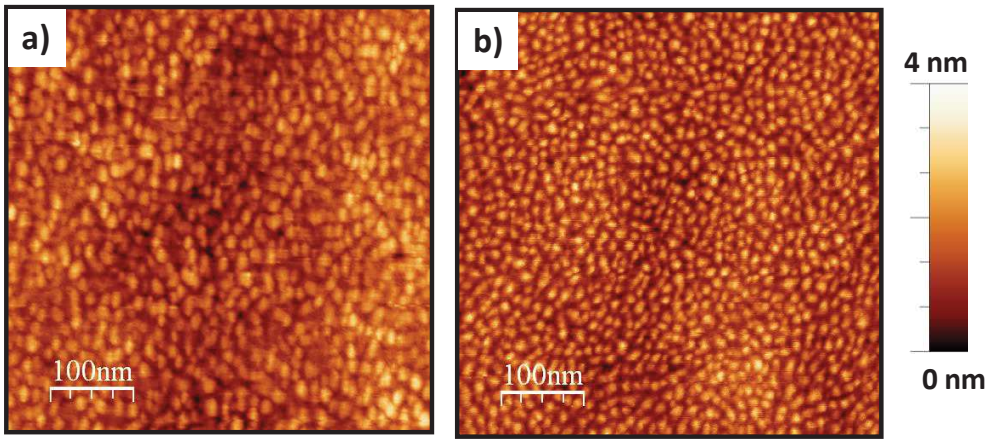

Figure IV-2. AFM images of (0001) $Al_{0.1}Ga_{0.9}N$ QDs grown on a) $Al_{0.5}Ga_{0.5}N$ and b) $Al_{0.7}Ga_{0.3}N$ templates.

Photoluminescence measurements were also performed at 9 K for three $Al_{0.1}Ga_{0.9}N$ (10 MLs) / $Al_xGa_{1-x}N$ (0001) samples, with x_{Al} equal to 0.5, 0.6 and 0.7, in order to access the QD optical properties and study the impact of increasing the Al concentration of the template. In chapter II, increasing x_{Al} in the template was shown to have an important impact on the optical properties of GaN QDs, showing a red shift towards lower energies for higher x_{Al} (although the formation of QDs with smaller heights). This behaviour was shown to be due to the increase of the internal electric field (F_{int}) in the structure for higher x_{Al} [1, 2]. For $Al_{0.1}Ga_{0.9}N$ (n.c.) QDs, a different behaviour was observed. As shown in Figure IV-3, by increasing x_{Al} from 0.5 to 0.7, no PL red shift was observed. In the opposite, we can observe a blue (UV) shift of the QD PL emission (from 3.66 eV to 3.76 eV at 9 K while going from $x_{Al} = 0.5$ to $x_{Al} = 0.6$). On the other hand, no significant PL energy shift is observed while going from x_{Al} equal to 0.6 to x_{Al} equal to 0.7. Having a shift towards higher energies, by increasing x_{Al}, would be the consequence of the formation of QDs with smaller heights. However, as it is hard to extract a precise QD height estimation, it is thus hard to confirm experimentally such assumption (in addition that the variation of the height would be very small as the PL shift is limited to several tens of meV only). In order to confirm this point, the fundamental transition energies (E_{e1-hh1}), were calculated for $Al_{0.1}Ga_{0.9}N$ (n.c.) QDs grown on $Al_xGa_{1-x}N$ with x_{Al} equals to 0.5, 0.6 and 0.7 (similar to the calculation performed in chapter III), the internal electric field values used in the calculation were estimated around 2, 3 and 3.5 MV / cm, respectively. These values were estimated based on the values obtained for $Al_{0.1}Ga_{0.9}N$ QDs / $Al_{0.5}Ga_{0.5}N$ (cf. chapter III) and for GaN QDs / $Al_{0.5}Ga_{0.5}N$ and GaN QDs / $Al_{0.6}Ga_{0.4}N$ with the same chemical contrast as for $Al_{0.1}Ga_{0.9}N$ / $Al_{0.6}Ga_{0.4}N$ and $Al_{0.1}Ga_{0.9}N$ / $Al_{0.7}Ga_{0.3}N$ (cf. chapter II). If we consider a constant QD height of 2.5 nm (~ 10 MLs), the calculations indicate an energy red shift of 90 meV, while going from x_{Al} = 0.5 to 0.6 and a smaller shift of 20 meV, while going from x_{Al} = 0.6 to 0.7. These calculations confirm that for a similar QD height (~ 2.5 nm) a red shift should be expected while increasing $x_{Al,}$, however as shown on the PL results a blue shift is observed while increasing x_{Al}, indicating the formation of QDs with smaller heights, for higher x_{Al}, and which are less sensitive to F_{int}. To conclude, it is observed that no redshift is taking place while increasing x_{Al} (i.e. while increasing the internal electric field). This characteristic is presumably due to the small average height of the QDs. Indeed for such small dimensions, the PL properties are less sensitive to the internal electric field since the quantum confined levels are not or at least only weakly affected by F_{int}: typically, for QDs with a height equal to or below 2 nm, the influence of F_{int} is negligible (cf. Figure IV-4). This feature is also correlated to the absence of a PL shift in power dependent PL measurements, which showed no PL energy shift for $Al_{0.1}Ga_{0.9}N$ QDs (cf. chapter III-2.2).

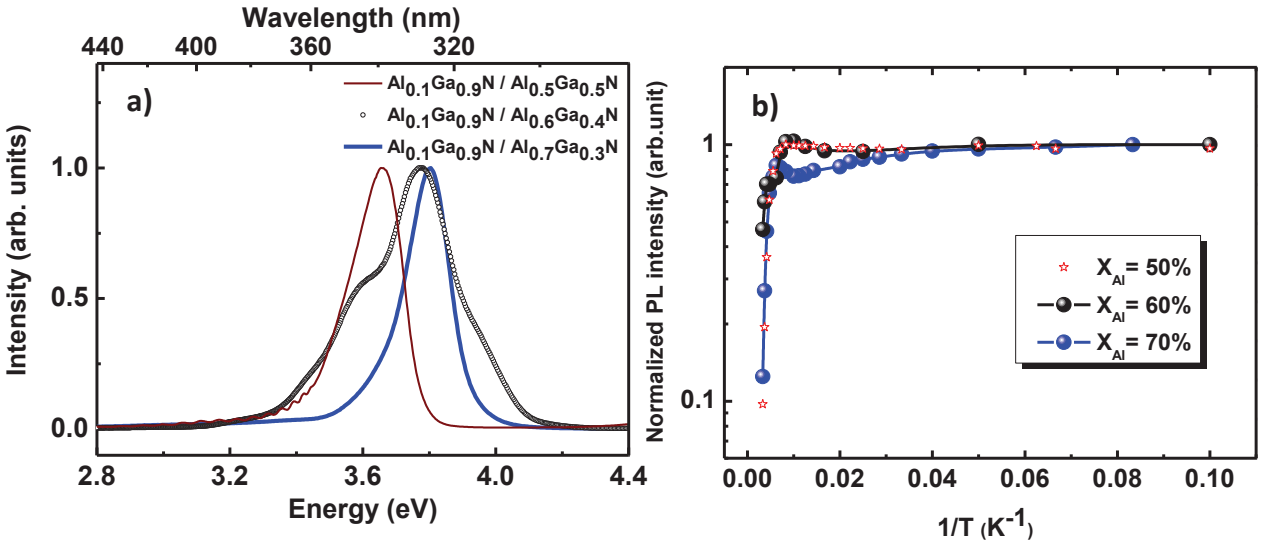

Figure IV-3. a) PL spectrum at 9 K and b) temperature dependence of the integrated PL intensity for $Al_{0.1}Ga_{0.9}N$ QDs (10MLs) grown on $Al_xGa_{1-x}N$ (0001) ($0.5 \leq x \leq 0.7$).

Temperature dependent PL measurements were also performed, for the three samples, to have insights on the radiative efficiencies and thus on the internal quantum efficiency (IQE). As shown in Figure IV-3, the PL intensity remains stable at low temperature (up to 120 K), then a decrease is obtained while reaching higher temperatures. As discussed before, this decrease is mainly attributed to the escape of excitons from the QDs through the wetting layer, which increases the probability to recombine none radiatively with dislocations. However, different behaviours are observed between 80 K and 160 K among the three samples. We can see that by increasing the Al content in the template, the intensity, which remains constant at low temperature, tends to slightly increase between 80 K and 160 K before decreasing again at higher temperatures. This behaviour is similar to the one observed for GaN QDs on $Al_xGa_{1-x}N$ (0001) ($0.5 \leq x \leq 0.7$). As discussed in the case of GaN / $Al_xGa_{1-x}N$ QDs (cf. Appendix A), this could be due to a crossover of the Γ_9 - Γ_7 valence band maxima in the hole ground state of $Al_{0.1}Ga_{0.9}N$ QDs together with a redistribution of the carriers, leading to a redistribution of the emission cones. This crossover is amplified while increasing the chemical contrast between $Al_{0.1}Ga_{0.9}N$ QD layer and the $Al_xGa_{1-x}N$ template due to the increase of the biaxial compressive strain and of the internal electric field. Indeed, it was shown in a previous study on GaN / $Al_xGa_{1-x}N$ QWs a change of the hole ground state from Γ_9 to Γ_7 by increasing the QW width (i.e. equivalent to the QD height in our case) at different x_{Al} compositions [3]. It was also shown that the higher the electric field value in the QW (i.e. higher x_{Al} in the barrier), the larger the Γ_7 domain (i.e. the hole base state becomes Γ_7) [3].

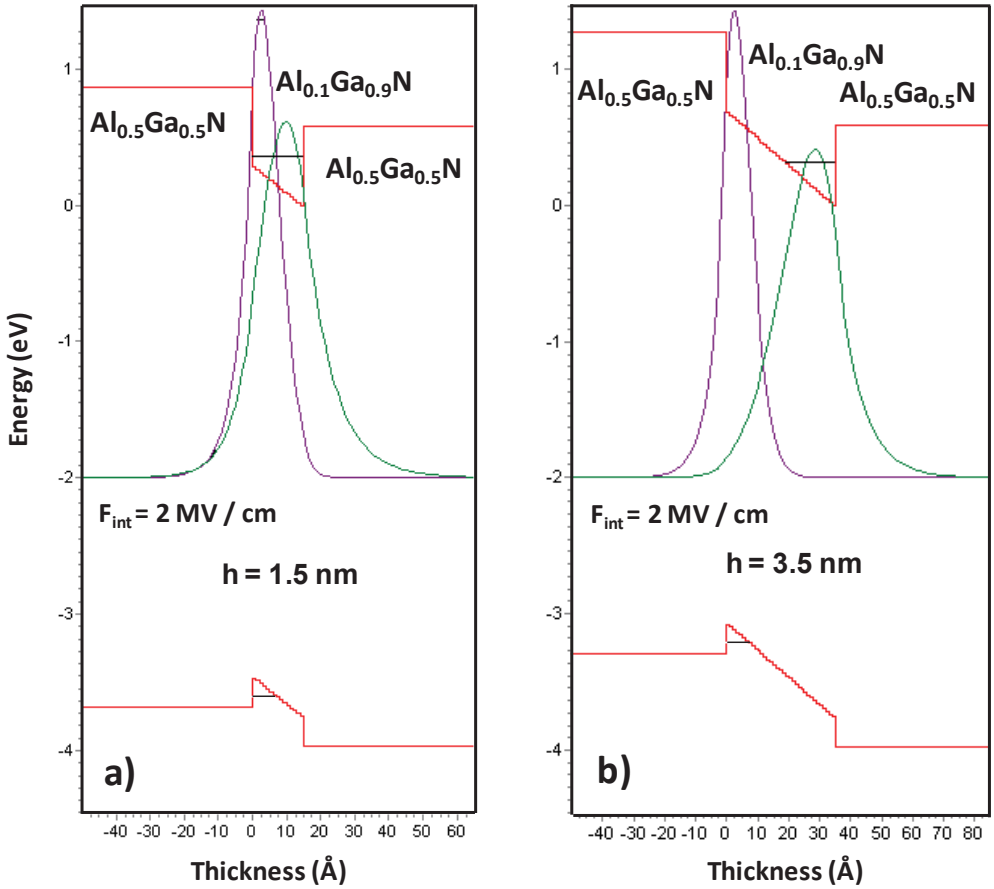

Figure IV-4. Band structures with the electron and hole wave functions and the first energy levels in $Al_{0.1}Ga_{0.9}N$ QW / $Al_{0.5}Ga_{0.5}N$ (0001) system with F_{int} = 2 MV / cm and QW height equal to a) 1.5 nm and b) 3.5 nm.

The integrated intensity ratios between 300 K and 9 K were measured: ratios of 10 %, 46 % and 13 % were obtained for x_{Al} = 50 %, 60 % and 70 %, respectively. At this stage, an improvement for QDs grown on $Al_{0.6}Ga_{0.4}N$ compared with QDs grown on templates with x_{Al} equal to 50 % and 70 % is found, which origin is not clear. However, as will be discussed in the following parts, we believe that there is a competition between two mechanisms leading to opposite behaviours while increasing x_{Al} of the $Al_xGa_{1-x}N$ template:

1) **The increase of F_{int} while increasing x_{Al}**, which causes a decrease of the electron and hole wavefunctions overlap and thus an increase of the radiative lifetime and a decrease of the radiative efficiency (for similar non radiative lifetimes).
2) **The decrease of the QD size (their diameters and possibly their height as discussed before and as shown for GaN QDs (cf. Chapter II)) while increasing x_{Al}**, which decreases the probability to have a dislocation inside the QD and also increase the electron and hole wavefunctions overlap (for QDs with smaller heights). As a consequence, an increase of the radiative efficiency can be expected. However, if the QD size becomes

"ultra" small, large parts of the electron and hole wavefunctions spread in the barrier or any wetting layer, which negatively impacts the radiative efficiency due to the very high dislocation densities.

To summarize, based on AFM and PL measurements, we can determine that by increasing x_{Al} from 50 % to 70 % in the $Al_xGa_{1-x}N$ template, the QD size (height and diameter) decreases, which improves the radiative efficiency, and their density increases. However, the internal electric field also becomes more important, which induces an electron-hole wavefunctions separation and can favour a decrease of the radiative efficiency. Finally, a compromise between the size of the QDs and F_{int} is important to improve the radiative efficiency (i.e. the IQE). In other words, **moderated QD size embedded in a barrier with a moderated chemical contrast is necessary to improve the IQE**. In our case, this compromise is found to be in the $Al_{0.1}Ga_{0.9}N$ / $Al_{0.6}Ga_{0.4}N$ system (i.e. a chemical contrast, between the QD layer and the barrier, of 0.5), which showed a room temperature internal radiative efficiency of 46 %. This assumption will be further discussed and confirmed in parts IV.2.1 and IV.2.2.

Finally, if we assume a near unity quantum efficiency at low temperature (as the PL intensity remains stable at low temperature), the integrated intensity ratio between 300 K and 9 K can be seen as a realistic approach for the estimation of the internal quantum efficiency (IQE) at 300 K.

IV.2 Wavelength tunability (from blue to UVC range)

IV.2.1 Impact of increasing y_{Al} in the QD composition (from 10 % to 20 %)

In this part, we will study the effect of the Al concentration in the $Al_yGa_{1-y}N$ QDs on their morphological and optical properties. As a first step, $Al_yGa_{1-y}N$ QDs / $Al_{0.7}Ga_{0.3}N$ (0001) samples with 10 MLs deposited amount and y_{Al} of 0.1 and 0.2 (n.c.) were studied and compared.

Figure IV-5(a) and (b) present typical AFM images for $Al_{0.1}Ga_{0.9}N$ QDs and $Al_{0.2}Ga_{0.8}N$ QDs. By analyzing different samples, high QD densities are observed, between 2 x 10^{11} cm^{-2} and 5 x 10^{11} cm^{-2}, with a tendency to get higher densities for $Al_{0.2}Ga_{0.8}N$ QDs. Also, the QD diameters were found to vary between 10 nm and 20 nm, and the QD heights between 1 nm and 2.5 nm with a tendency to get smaller QDs for $Al_{0.2}Ga_{0.8}N$ composition. In fact, as the Al adatom mobility is lower than the Ga one, we can expect that increasing the Al concentration leads to an increase of the QD nucleation centers and therefore to a rise in their densities and a reduction of their size. Indeed, it has been shown that kinetics play an important role in the formation mechanisms of GaN QDs, strongly influenced by surface diffusion [4]. To have more insight on

the QD height, HAADF - STEM characterizations were performed (Figure IV-5 (c and d)). As a general trend, a variation of the QD height between 1.5 and 3 nm was determined with an average QD height around (2.5 ± 0.4) nm (close to the $Al_yGa_{1-y}N$ deposited amount of 10 MLs ~ 2.6 nm). In the next part (part IV.2.2.1), HAADF - STEM characterization for different QD layers with y_{Al} varying between 0.1 and 0.4 will also be compared.

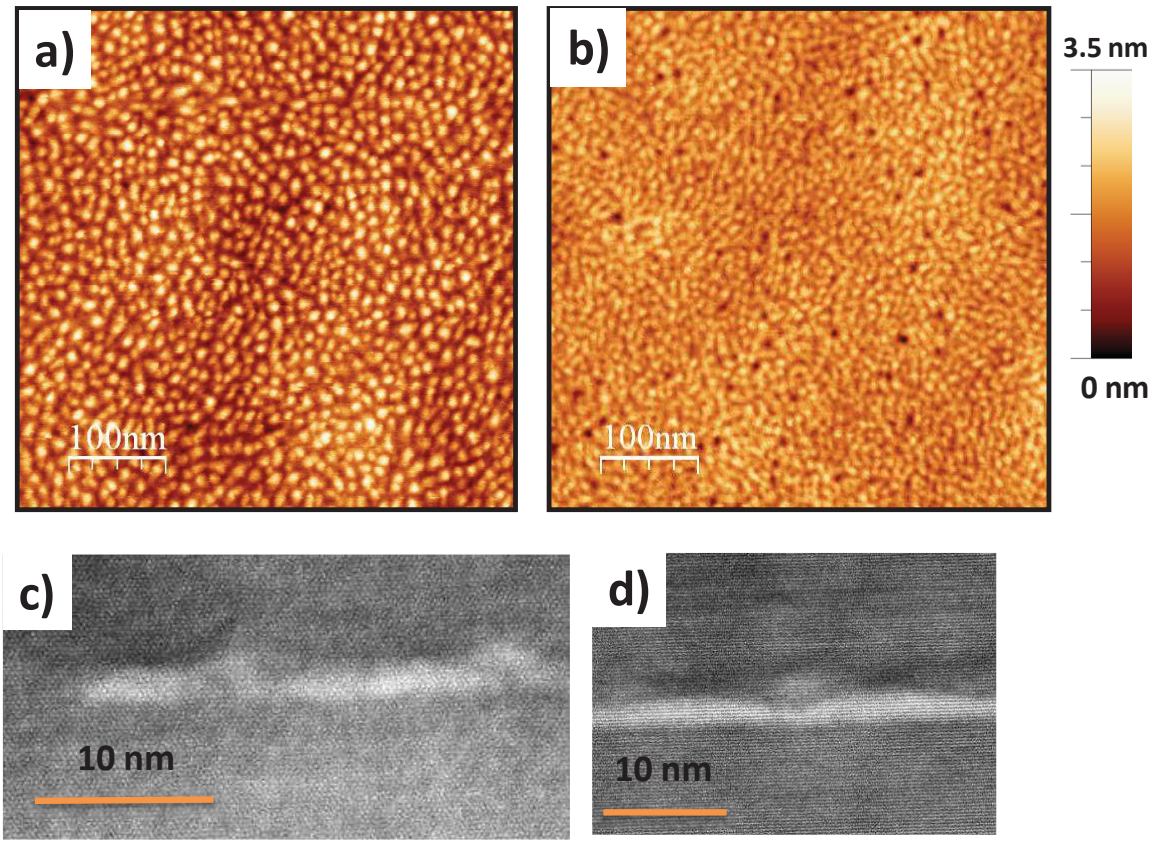

Figure IV-5. AFM and cross sectional TEM images of $Al_{0.1}Ga_{0.9}N$ QDs (a and c, respectively), and $Al_{0.2}Ga_{0.8}N$ QDs (b and d, respectively).

PL measurements of the samples were first characterized at room temperature. Figure IV-6(a) shows a shift from 3.72 eV (333 nm) to 3.95 eV (314 nm) while increasing the $Al_yGa_{1-y}N$ QD Al nominal concentration from 10 % to 20 %. Temperature dependent measurements also showed an integrated intensity ratio between 300 K and 9 K of 12 % and 30 % for y_{Al} equal to 10 % and 20 %, respectively. This difference indicates a better confinement in $Al_{0.2}Ga_{0.8}N$ QDs / $Al_{0.7}Ga_{0.3}N$ (0001) system, with lower chemical contrast between the two layers. As the chemical contrast in $Al_{0.2}Ga_{0.8}N$ / $Al_{0.7}Ga_{0.3}N$ (0001) system is lower compared to the $Al_{0.1}Ga_{0.9}N$ QDs / $Al_{0.7}Ga_{0.3}N$ one, a lower value of F_{int} is also expected, which favours a better electron and hole wavefunctions overlap (for similar QD heights). It is important to note that in part IV.1, the best integrated intensity ratio was obtained in the case of $Al_{0.1}Ga_{0.9}N$ (n.c.) QDs / $Al_{0.6}Ga_{0.4}N$ (0001) system (Figure IV-3 (b)), which contains a similar difference in the Al concentration as for

$Al_{0.2}Ga_{0.8}N$ (n.c.) QDs / $Al_{0.7}Ga_{0.3}N$ system (i.e. a similar chemical contrast in the Al concentration difference and a lattice mismatch of 1.2 %). This confirms that a moderated chemical contrast (i.e a moderated F_{int}) should be favoured to improve the radiative efficiency.

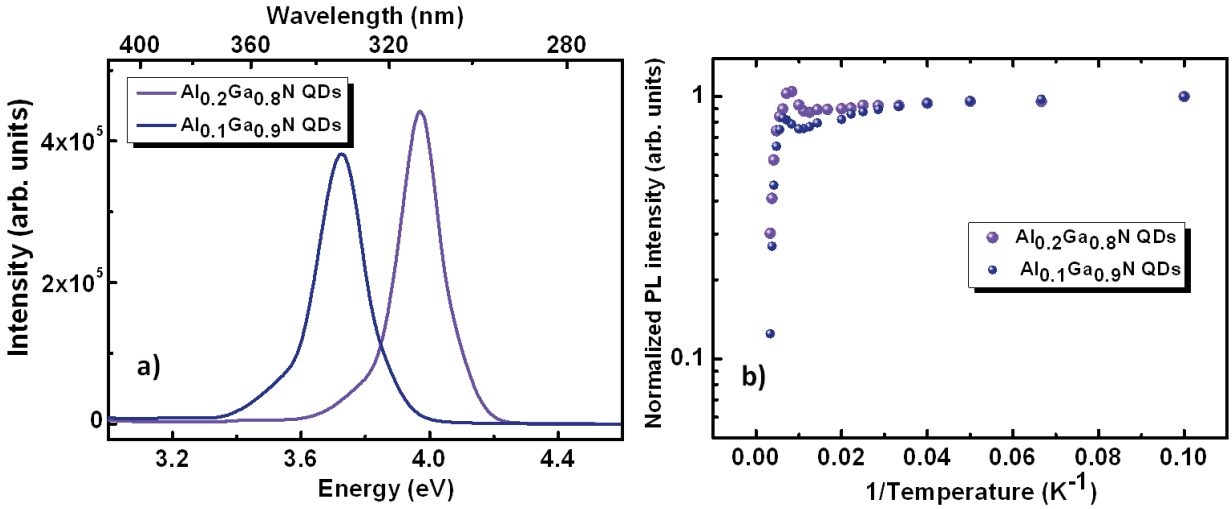

Figure IV-6. a) Room temperature PL spectra and b) temperature dependence of the integrated PL intensity for $Al_{0.1}Ga_{0.9}N$ and $Al_{0.2}Ga_{0.8}N$ QDs grown on $Al_{0.7}Ga_{0.3}N$ (0001).

To conclude the last parts (IV.1 and IV.2.1), it was shown that increasing the Al content in the barrier induces a slight UV shift of the QD emission (attributed to the formation of smaller QD heights). It was also shown that by increasing y_{Al} (n.c.) in the $Al_yGa_{1-y}N$ QD layer from 0.1 to 0.2, a blue (UV) shift (from 333 nm down to 314 nm) is obtained. Finally, I(300K) / I(9K) ratios varying between 10 % and 46 % were found, with the higher values obtained in $Al_yGa_{1-y}N$ / $Al_xGa_{1-x}N$ (0001) system with an Al concentration difference of 0.5 (i.e. $Al_{0.1}Ga_{0.9}N$ / $Al_{0.6}Ga_{0.4}N$ (0001) and $Al_{0.2}Ga_{0.8}N$ / $Al_{0.7}Ga_{0.3}N$ (0001); corresponding to a lattice mismatch ~ 1.2 %). These results point at a compromise between the size (height) of the QDs and the value of the internal electric field that is necessary to improve the radiative efficiency.

IV.2.2 $Al_yGa_{1-y}N$ QDs with an Al composition variation from 10 % to 40 %

IV.2.2.1 Morphological properties

In this part, the $Al_yGa_{1-y}N$ QDs composition as well as the deposited amount will be varied in order to assess the range of emission energies accessible, with the aim to go deeper in the UV range. **In order to compare the different QD samples, the mainly used $Al_xGa_{1-x}N$ template in this section will be $Al_{0.7}Ga_{0.3}N$ (0001)**. The Al concentration of the template was chosen to get a good compromise between a sufficient strain (to allow the 2D-3D transition; $\Delta a/a \geq 0.7$ %)

and a minimized Al concentration (to allow efficient n-type doping in a complete LED structure).

As a first step, the growth of $Al_yGa_{1-y}N$ QDs on $Al_{0.7}Ga_{0.3}N$ (0001) systems with y_{Al} (n.c.) equals to 0.1, 0.2, 0.3 and 0.4 was studied in-situ using RHEED measurements. As we know, increasing y_{Al} from 0.1 to 0.4 induces a decrease of the lattice mismatch (Δa/a) with the $Al_{0.7}Ga_{0.3}N$ template, from Δa/a equals to 1.5 % down to 0.75 %. This change impacts the formation of the QDs. For this reason, the critical thickness for the 2D-3D transition (h_c^{2D-3D}) was first studied for the four QD systems (Figure IV-7) showing an increase of h_c^{2D-3D} from (3 ± 0.5) MLs to (4 ± 0.5) MLs while going from $Al_{0.1}Ga_{0.9}N$ to $Al_{0.4}Ga_{0.6}N$ (n.c.) QDs.

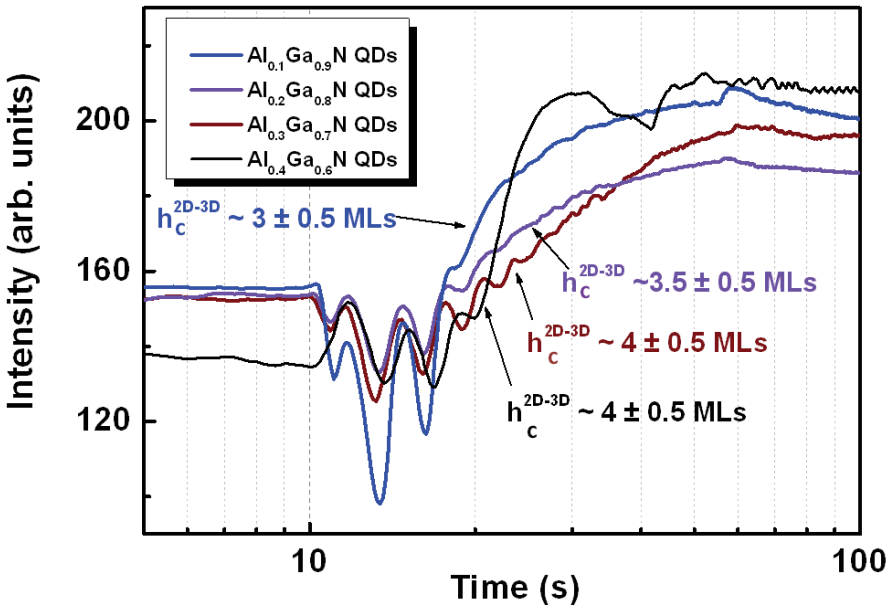

Figure IV-7. Reflection high-energy electron diffraction intensity recorded during the formation of $Al_yGa_{1-y}N$ QDs with $0.1 \leq y_{Al} \leq 0.4$ on $Al_{0.7}Ga_{0.3}N$, with an estimation of the critical thickness for the 2D-3D transition (h_c^{2D-3D}).

AFM measurements were also performed on $Al_{0.3}Ga_{0.7}N$ QDs and $Al_{0.4}Ga_{0.6}N$ QDs (Figure IV-8). By analyzing different images, high QD densities are observed between 3 x 10^{11} cm^{-2} and up to 9 x 10^{11} cm^{-2} with a slight tendency to get higher densities for $Al_{0.4}Ga_{0.6}N$ QDs. It is important to note that the QD density also increases as a function of the deposited amount (as observed in chapter III). However, we can also note that by increasing y_{Al}, the observation and the characterization of such small QDs with high densities become complicated as we get closer to the limits of the AFM resolution. In fact, as the QDs density increases and their lateral dimensions decreases (~ 10 nm which is comparable to the tip radius (~ 7nm)), it leads to important convolution effects which affect the apparent shape of the QDs.

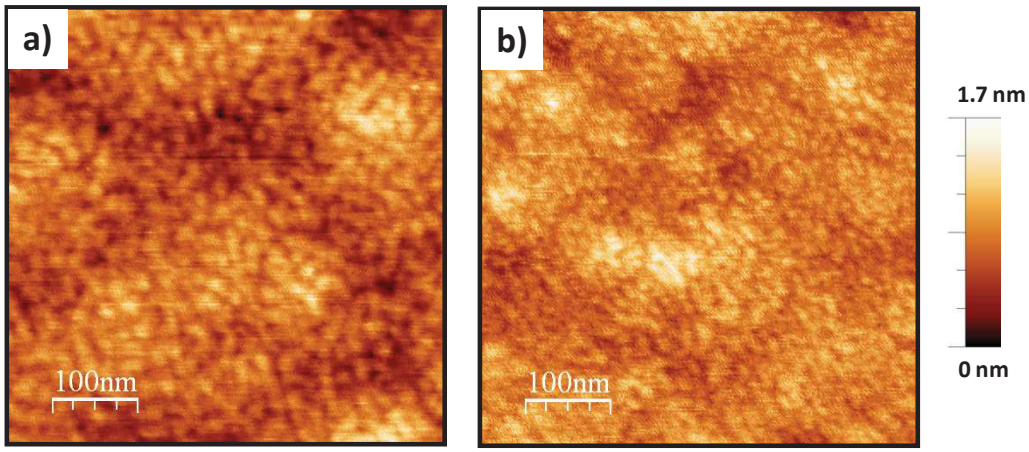

Figure IV-8. AFM images of (0001) a) $Al_{0.3}Ga_{0.7}N$ QDs and b) $Al_{0.4}Ga_{0.6}N$ QDs.

To have more insight on the QD size for the different y_{Al} compositions, a sample dedicated to TEM studies was grown. This sample contains four layers of $Al_yGa_{1-y}N$ QDs with y_{Al} equals to 0.1, 0.2, 0.3 and 0.4 for layer 1, 2, 3 and 4 respectively. The same deposited amount of 10 MLs was used for the different layers. They were grown using the optimized growth conditions presented in chapter III.3.

Figure IV-9 presents a high-angle annular dark-field imaging in scanning transmission electron microscopy mode (HAADF-STEM) for the four layers. From the different images, average QD heights of (2.6 ± 0.27) nm, (2.5 ± 0.24) nm, (2.44 ± 0.23) nm and (2.4 ± 0.4) nm for y_{Al} equals to 0.1, 0.2, 0.3 and 0.4 were extracted, respectively. From these QD height distributions, no significant variation in the QD height is observed between the different layers. Therefore, we can conclude that the average $Al_yGa_{1-y}N$ QD height is in close agreement with the $Al_yGa_{1-y}N$ deposited amount of 10 MLs (~ 2.5 nm).

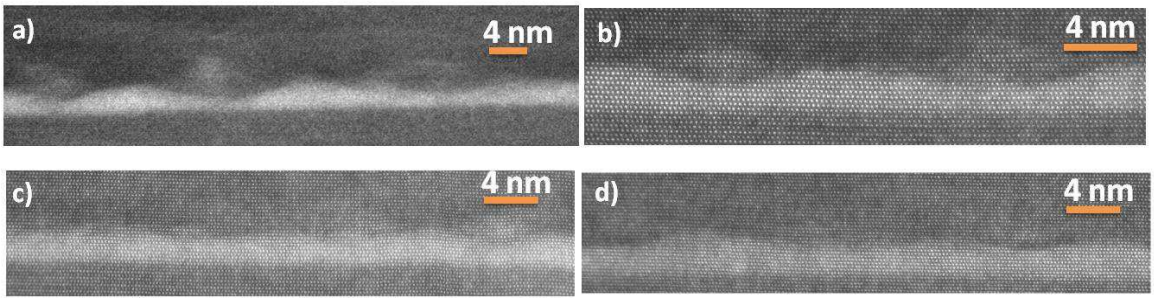

Figure IV-9. HAADF-STEM images for a) $Al_{0.1}Ga_{0.9}N$ QDs (layer 1), b) $Al_{0.2}Ga_{0.8}N$ QDs (layer 2), c) $Al_{0.3}Ga_{0.7}N$ QDs (layer 3) and d) $Al_{0.4}Ga_{0.6}N$ QDs (layer 4), grown on $Al_{0.7}Ga_{0.3}N$ (0001).

IV.2.2.1 Optical properties

Different samples were then grown with different $Al_yGa_{1-y}N$ QD nominal deposited amounts (from 5 MLs up to 12 MLs) and nominal Al compositions (y_{Al} ranging from 0.1 and up to 0.4) in

order to assess the range of emission energies accessible by $Al_yGa_{1-y}N$ QDs. Figure IV-10 summarizes the emission of the different samples at low temperature. We can see that by varying the growth conditions (i.e. the QD composition and size), the wavelength emission can be tuned from the UVA down to the UVC range (~ 270 - 280 nm). As expected, the wavelength emission decreases as a function of y_{Al} and while decreasing the QD deposited amount. We can also note that the blue (UV) shift is enhanced as a function of the QD deposited amount for higher y_{Al} concentrations (Figure IV-10). As we can see for $Al_{0.1}Ga_{0.9}N$ (n.c) QDs, a UV shift around 90 meV (i.e. from 332 nm down to 324 nm at 9 K) is observed while going from 8 MLs down to 6 MLs. On the other hand, for $Al_{0.4}Ga_{0.6}N$ (n.c.) QDs, a blue (UV) shift of 390 meV (from 294 nm down to 269 nm at 9 K) is observed while going from 8 MLs down to 6 MLs. As the deposited amount is nearly equal to the average QDs height (as observed from TEM images in the last part), we would expect a smaller energy shift as a function of the QD height while increasing y_{Al}. Indeed, as the lattice mismatch between the template and the QD layer is lower than for $Al_{0.1}Ga_{0.9}N$ (n.c.) QDs (i.e. F_{int} is expected to be reduced in the $Al_{0.4}Ga_{0.6}N$ (n.c) QDs / $Al_{0.7}Ga_{0.3}N$ system compared to the $Al_{0.1}Ga_{0.9}N$ (n.c) QDs / $Al_{0.7}Ga_{0.3}N$ and $Al_{0.1}Ga_{0.9}N$ (n.c) QDs / $Al_{0.5}Ga_{0.5}N$ systems) we could then expect a smaller energy shift, as a function of the QD height, while increasing $y_{Al.}$. However, as seen on Figure IV-10, the energy shift, as a function of the deposited amount is enhanced while increasing y_{Al}. Interestingly, such a behaviour was also observed in other studies on $Al_yGa_{1-y}N$ QDs / AlN systems [5, 6]. The origin of this behaviour is not clear yet. However one possible interpretation could be as follows: as the compressive strain (i.e. the lattice mismatch), between the $Al_yGa_{1-y}N$ QD layer and the $Al_xGa_{1-x}N$ matrix, decreases while increasing the value of y_{Al}, the QD height could also be impacted and slightly vary, implying that for $Al_yGa_{1-y}N$ QDs with higher Al concentration, the average height would be lower than the deposited amount. However, based on the TEM images, this variation would be very small (an average QD height difference of 0.2 nm between y_{Al} equals to 0.1 and 0.4 (cf. Figure IV-9)) and difficult to be confirmed due to the QD height distribution. Also, it is important to note that different features can play a role on the PL energy emission as the value of the internal electric field and possible enhancement of localization effects for QDs with higher y_{Al} (Al-rich QDs).

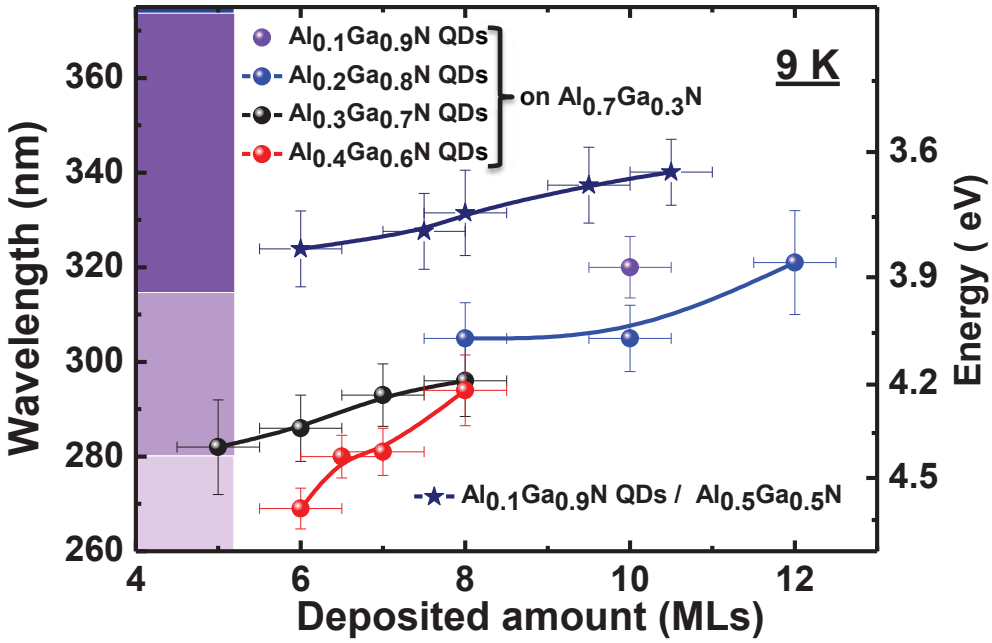

Figure IV-10. Variation of the emission wavelength (i.e. energy) as a function of the QD deposited amount and composition. All the samples presented here were grown on $Al_{0.7}Ga_{0.3}N$ (0001) templates <u>except $Al_{0.1}Ga_{0.9}N$ QDs which were grown on both $Al_{0.5}Ga_{0.5}N$ and $Al_{0.7}Ga_{0.3}N$ (0001) templates</u>.

To have more insights on the radiative efficiency and thus the internal quantum efficiency (IQE) of $Al_yGa_{1-y}N$ QDs, room temperature PL measurements were compared to low temperature ones, through our series of samples. The different values are summarized in table IV.1. We can note that, for the same QD deposited amount, increasing y_{Al} induces an increase of I(300K) / I(9K) ratio (i.e. going from y_{Al} equals to 0.1 to 0.2, with 10 MLs QD deposited amount, I(300K) / I(9K) increases from 13 % to 30 %. Also, while going from y_{Al} equals to 0.3 to 0.4, with 6 MLs deposited amount, I(300K) / I(9K) increases from 11 % to 30 %. The PL temperature dependent spectrums for the last two samples are presented in Figure IV-11. This behaviour can be seen as a direct manifestation of F_{int} on the electron and hole wavefunctions overlap and thus the radiative efficiency. Indeed, while increasing the value of $y_{Al,}$ the lattice mismatch between the QD layer and the template decreases and thus F_{int} also decreases, which induces a better electron and hole wavefunctions overlap and increases the radiative efficiency. However, at others deposited amounts (while going from y_{Al} equals 0.3 to y_{Al} equals 0.4, with 7 MLs and 8 MLs deposited amount), an opposite behaviour can be observed indicating that the internal electric field is not the only parameter which modifies the radiative efficiency. For instance, the structural quality of the $Al_xGa_{1-x}N$ matrix could also play a role in the PL intensity ratio as shown in the GaN / $Al_xGa_{1-x}N$ system, grown using a plasma N_2 source (cf. chapter II).

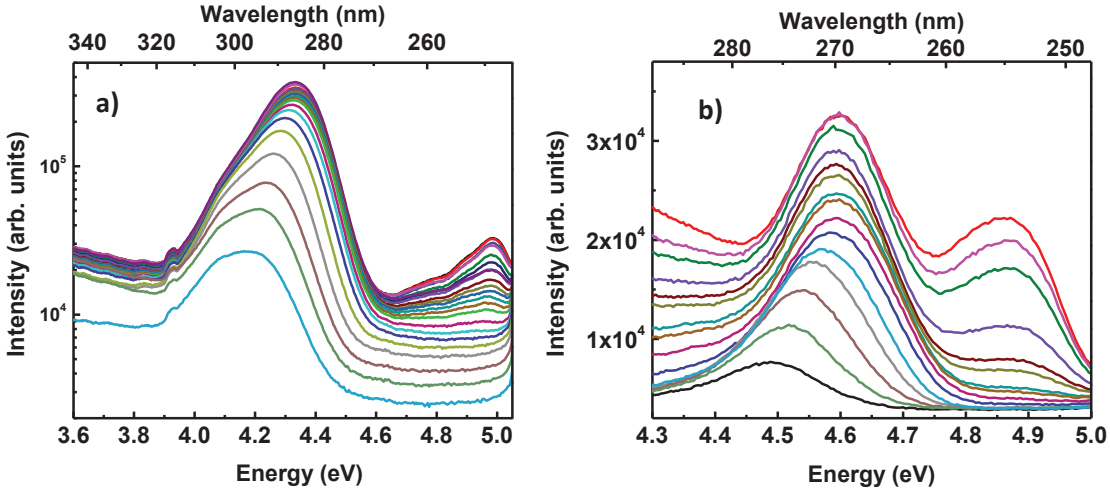

Figure IV-11. Temperature dependent PL spectrums between 9 K and 300 K for a) $Al_{0.3}Ga_{0.7}N$ QDs and b) $Al_{0.4}Ga_{0.6}N$ QDs grown in an $Al_{0.7}Ga_{0.3}N$ (0001) matrix. The PL emission at high energy (~ 4.9 eV) is originating from the $Al_{0.7}Ga_{0.3}N$ barrier.

We can also note that for each $Al_yGa_{1-y}N$ QD nominal composition, the I(300K) / I(9K) ratios vary between ≈ 10 % and 30 % as a function of the QD deposited amount (cf. Table IV-1). This behaviour could be related to the impact of the QD size on the radiative efficiency. In fact, decreasing the QD height increases the electron and hole wavefunctions overlap. However, if the QDs are very thin and small, the overlap of the carrier wave functions with the surrounding (defective) barrier layers could also increase. Therefore, a weaker confinement of the excitons inside the QDs can be expected, similarly to the case of $Al_{0.1}Ga_{0.9}N$ QDs / $Al_{0.5}Ga_{0.5}N$ [7] and thin and small $(11\bar{2}2)$ oriented GaN QDs / $Al_{0.5}Ga_{0.5}N$ [8]. In agreement with what we observed before, we can conclude that a compromise between the size of the QDs and the value of F_{int} is important to improve the radiative efficiency (i.e. IQE) of the samples. The maximum efficiency of $Al_yGa_{1-y}N$ QDs was found to be for a deposited amount of 10 MLs, 7 MLs and 6 MLs for y_{Al} (nominal concentration) equals 0.2, 0.3 and 0.4, respectively (c.f. Table IV-1). Figure IV-12 summarizes the PL emission spectral range, at 300 K, for the different $Al_yGa_{1-y}N$ QD samples ($0 \leq y \leq 0.4$), showing the possibility to tune the wavelength emission from 423 nm (using GaN QDs) down to 275 nm (using $Al_{0.4}Ga_{0.6}N$ QDs).

Finally, $Al_{0.4}Ga_{0.6}N$ QDs emitting at 275 nm, at 300 K, were compared to a sample with an $Al_{0.4}Ga_{0.6}N$ quantum well (QW) emitting at the same wavelength. We can clearly see on the temperature dependent measurements (Figure IV-13), that using QDs improve the radiative efficiency of UVC emitters, thanks to the 3D confinement of excitons, inside the QDs, with I(300K) / I(9K) up to 30 % compared to 0.5 % for the QW.

Table IV-1: Description of the different $Al_yGa_{1-y}N$ QDs samples grown on $Al_{0.7}Ga_{0.3}N$ (0001) templates, studied in this section including: lattice mismatch between the QD layer and the template, the $Al_yGa_{1-y}N$ deposited amount, the emission wavelength at room temperature and the integrated PL intensity I(300K) / I(9K) ratios.

QD samples	Lattice mismatch (%)	Deposited amount (MLs)	Emission wavelength (nm)	I(300K) / I(9K) (%)
$Al_{0.1}Ga_{0.9}N$ (QD-1)	1.5	10	333	13
$Al_{0.2}Ga_{0.8}N$ (QD-2)	1.2	8	314	5
$Al_{0.2}Ga_{0.8}N$ (QD-3)	1.2	10	314	30
$Al_{0.2}Ga_{0.8}N$ (QD-4)	1.2	12	329	-
$Al_{0.3}Ga_{0.7}N$ (QD-5)	1	5	293	17
$Al_{0.3}Ga_{0.7}N$ (QD-6)	1	6	298	11
$Al_{0.3}Ga_{0.7}N$ (QD-7)	1	7	301	26
$Al_{0.3}Ga_{0.7}N$ (QD-8)	1	8	304	20
$Al_{0.3}Ga_{0.7}N$ (QD-9)	1	12	328	-
$Al_{0.4}Ga_{0.6}N$ (QD-10)	0.75	6	275	30
$Al_{0.4}Ga_{0.6}N$ (QD-11)	0.75	6.5	288	9
$Al_{0.4}Ga_{0.6}N$ (QD-12)	0.75	7	286	7
$Al_{0.4}Ga_{0.6}N$ (QD-13)	0.75	8	301	10

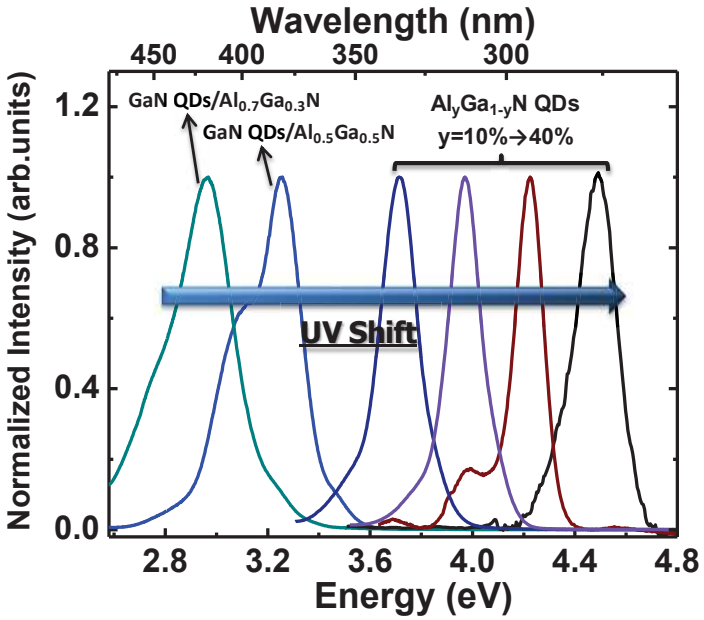

Figure IV-12. Room temperature PL spectra for $Al_yGa_{1-y}N$ QDs (with $0.1 \leq y \leq 0.4$) and comparison with GaN QDs (studied in chapter II). The samples with $y_{Al} > 0$ are grown on $Al_{0.7}Ga_{0.3}N$ (0001) templates.

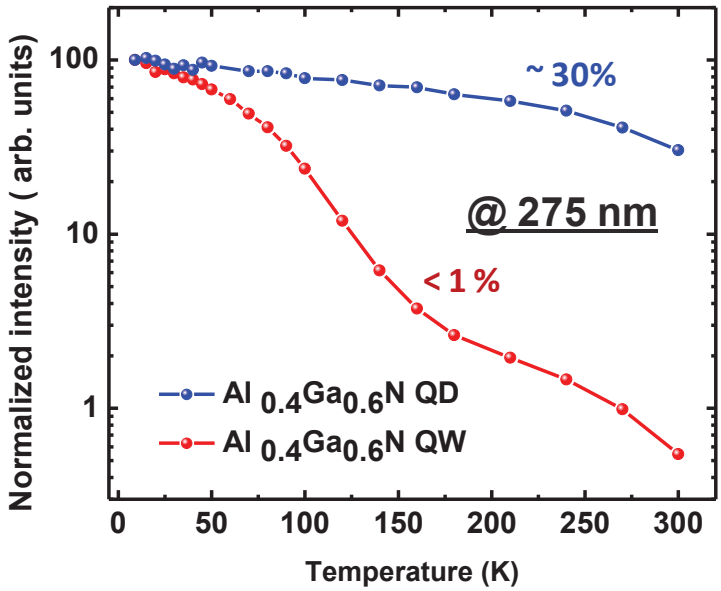

Figure IV-13. Temperature dependence of the integrated PL intensity for $Al_{0.4}Ga_{0.6}N$ QDs versus an $Al_{0.4}Ga_{0.6}N$ QW emitting at 275 nm.

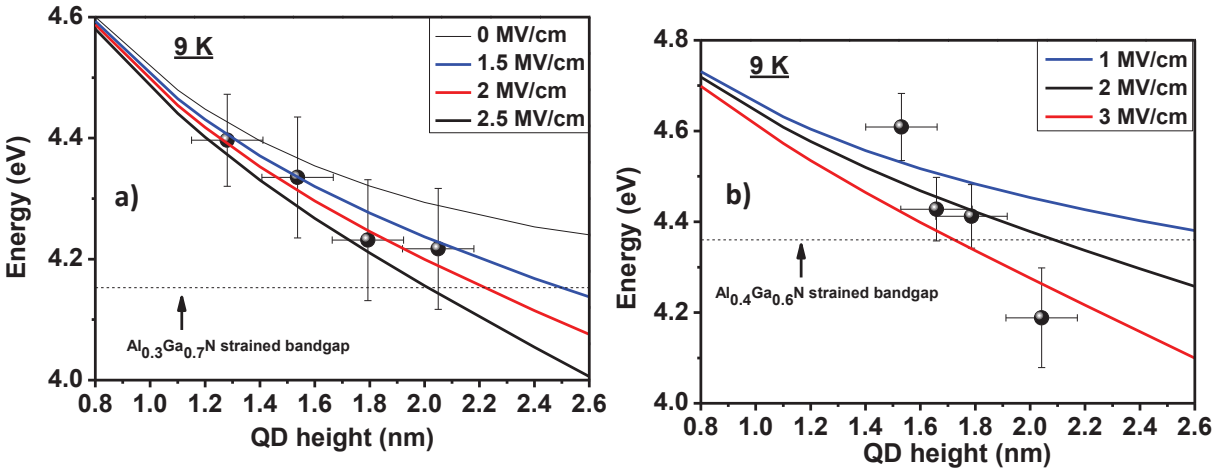

Figure IV-14. Calculated transition energies at 9 K as a function of the $Al_yGa_{1-y}N$ QD height using different F_{int} values for: a) $Al_{0.3}Ga_{0.7}N$ / $Al_{0.7}Ga_{0.3}N$ (0001) and b) $Al_{0.4}Ga_{0.6}N$ / $Al_{0.7}Ga_{0.3}N$ (0001) systems. The full circles represent the main experimental PL energies.

In order to get more insights on the internal electric field values in $Al_{0.4}Ga_{0.6}N$ / $Al_{0.7}Ga_{0.3}N$ and $Al_{0.3}Ga_{0.7}N$ / $Al_{0.7}Ga_{0.3}N$ systems, the experimental PL energy values of the different samples were then compared to the calculated fundamental energy transition (E_{e1-hh1}), for different internal electric field values (F_{int}) and QD heights (similar to the calculation performed in chapter III on the $Al_{0.1}Ga_{0.9}N$ (n.c.) QDs / $Al_{0.5}Ga_{0.5}N$ (0001) system). For $Al_{0.3}Ga_{0.7}N$ (n.c.) QDs / $Al_{0.7}Ga_{0.3}N$, the best fit with the experimental points is obtained for $F_{int} \approx 2 \pm 0.5$ MV / cm (cf. Figure IV-14(a)). This value is similar to the value obtained for the $Al_{0.1}Ga_{0.9}N$ (n.c.) QDs / $Al_{0.5}Ga_{0.5}N$ system (studied in chapter III), with a similar chemical contrast between the QD

layer and the matrix. We can also see that the PL emission energies for the different $Al_{0.3}Ga_{0.7}N$ QD samples are found above the strained band gap energy of $Al_{0.3}Ga_{0.7}N$, which confirms that for small QD heights (typically ≤ 2nm), F_{int} has a minimized influence on the PL energy emission, in agreement with our previous results in chapter III. On the other hand, surprisingly, for the $Al_{0.4}Ga_{0.6}N$ (n.c.) QDs / $Al_{0.7}Ga_{0.3}N$ system, we can see that the experimental points cannot be well fitted with any F_{int} values (cf. Figure IV-14(b)), accounting for possible fluctuation in the QD sizes and/or Al composition as a function of the $Al_yGa_{1-y}N$ deposited amount.

IV.3 Study of the PL decay time and IQE estimation from time resolved photoluminescence

Time resolved photoluminescence (TRPL) measurements were also performed at low temperature on $Al_yGa_{1-y}N$ QD samples ($0.1 \leq y \leq 0.4$) in order to study the PL kinetic processes and to reveal the different recombination processes dynamics of the samples as performed on GaN QDs (cf. Chapter II). The third and fourth harmonic of a mode-locked titanium-sapphire ($Ti:Al_2O_3$) laser were used, with a wavelength of 266 nm and 196 nm, respectively, a pulse width of 100 fs and a repetition rate which can vary between 80 KHz (12 µs) and 82 MHz (12 ns). As discussed in chapter II, GaN QDs showed slow decay times (~ µs range), and for this reason a weak repetition rate of 80 KHz (12 µs) was used to ensure a complete decay of the PL and avoid the accumulation of electron-hole pairs from one pulse to another. For $Al_yGa_{1-y}N$ QDs ($y > 0$), the decay times are much slower (in the ns range, as will be shown in this part), so the repetition rate was adjusted at higher frequencies (i.e. shorter repetition times) than the one used for GaN QDs. In fact, a very long repetition time can lead to a red shift of the PL energy peaks. In this part, the repetition rate is adjusted between 800 KHz (1.25 µs) and 82 MHz (12 ns).

Here, we will indirectly study the influence of the internal electric field (by changing the $Al_yGa_{1-y}N$ QDs composition) and the QD size (height) on the decay times. Also, the IQE at low temperature will be estimated for the samples using a model developed by Iwata et al. [9].

The experiments were performed by T. H. NGO, T. Q. P. Vuong, P. Valvin and B. GIL (for whom the credit should be given) at Charles Coulomb laboratory.

IV.3.1 $Al_yGa_{1-y}N$ QDs emitting in the blue-UVA range ($0 \leq y \leq 0.2$)

As a first step, TRPL measurements were performed using the third laser harmonic on $Al_{0.1}Ga_{0.9}N$ and $Al_{0.2}Ga_{0.8}N$ QDs grown on $Al_{0.7}Ga_{0.3}N$ (0001) template, with 10 MLs (≈ 2.6 nm)

deposited amount, (sample A and B, respectively) and compared with GaN QDs / $Al_{0.7}Ga_{0.3}N$ (0001) (presented in chapter II). As we can see on Figure IV-15(a), the PL transients of the samples are also ruled by a double exponential decay, a fast decay component and a longer one. The spectrally integrated temporal intensity for the different samples was fitted with a double exponential using equation IV-1:

$$I(t) = A_{fast}\exp\left(-\frac{t}{\tau_{fast}}\right) + A_{slow}\exp\left(-\frac{t}{\tau_{slow}}\right) \quad \text{(IV-1)}$$

where τ_{slow} and τ_{fast} refer to the slow and fast decays and A_{slow} and A_{fast} represent the coefficients of slow and fast recombination processes, respectively.

As explained in chapter II, the origin of this bi-exponential behaviour was studied by Iwata et al. [9] on (Al,Ga)N / AlN (0001) quantum wells. They developed a model which considers that the samples are composed of purely radiative regions while other regions are plagued by non radiative recombination centers. In this picture, τ_{slow} corresponds to the radiative lifetime, while τ_{fast} contains both radiative and non radiative components. This last one can be expressed as:

$$\frac{1}{\tau_{fast}} = \frac{1}{\tau_{slow}} + \frac{1}{\tau_{nr}} \quad \text{(IV-2)}$$

Based on Iwata's model, radiative and non-radiative channels are taken into account at low temperature and the IQE at low temperature (LT) can then be calculated using:

$$IQE = \frac{A_{fast}\tau_{fast} + A_{slow}\tau_{slow}}{(A_{fast} + A_{slow})\tau_{slow}} \quad \text{(IV-3)}$$

As presented in Figure IV-15(b), we can clearly see that going from GaN to $Al_yGa_{1-y}N$ QDs , the radiative decay time ($\tau_r \approx \tau_{slow}$) is found to strongly decrease to the ns range compared to the µs range for GaN QDs (Figure IV-15(b)). This behaviour is mainly seen as the consequence of the reduction of QD heights and of F_{int} in the case of $Al_yGa_{1-y}N$ QDs compared to GaN QDs, which induces a better wavefunction overlap. In the same way, the non radiative decay time values (τ_{nr}) are observed to decrease when going deeper in the UV range (i.e. going from GaN to $Al_{0.2}Ga_{0.8}N$ QDs and decreasing the QD height; with an average height around 3.5 nm for GaN QDs and around 2.5 nm for $Al_{0.2}Ga_{0.8}N$ QDs), which means that non radiative processes are more significant in active regions with smaller QDs or higher Al concentration ($Al_yGa_{1-y}N$ with $y > 0$). The IQE values at low temperature were also calculated and lower values were observed for $Al_yGa_{1-y}N$ QDs (with $y = 0.1$ and 0.2), with IQE values around 30 %, compared to GaN QDs, with IQE values around 50 %. These behaviours can be seen as a consequence of an increasing overlap of the carrier wave functions with the surrounding defective barrier layers and therefore a weaker confinement of the excitons inside the QDs. This was also observed in the case of small $(11\bar{2}2)$ oriented GaN QDs [8].

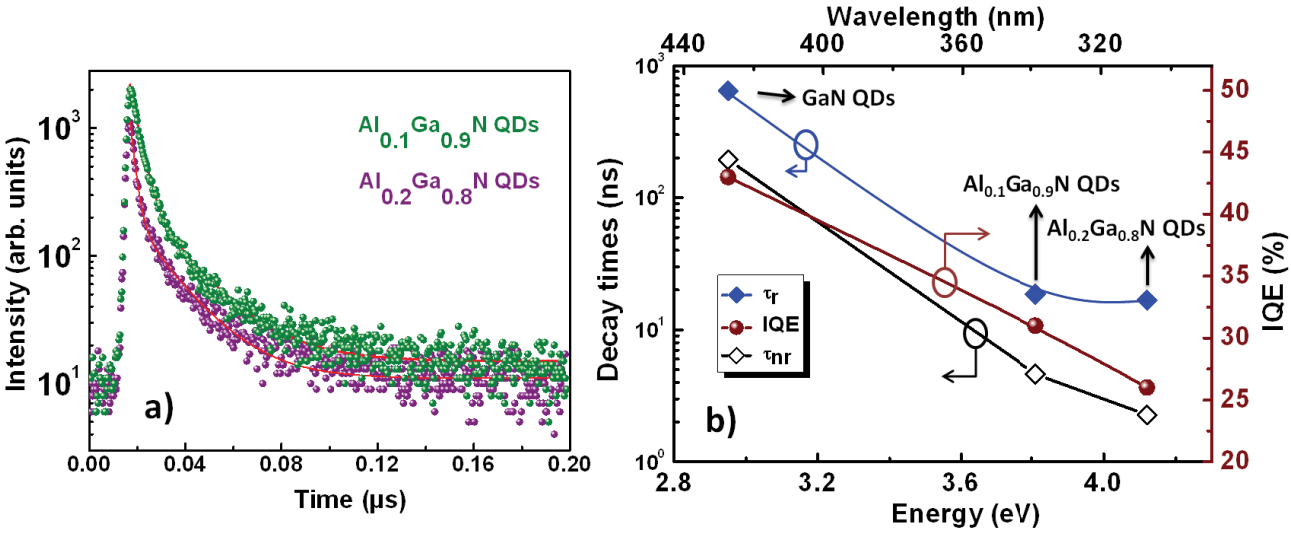

Figure IV-15: TRPL spectra at low temperature for $Al_{0.1}Ga_{0.9}N$ and $Al_{0.2}Ga_{0.8}N$ QDs grown on $Al_{0.7}Ga_{0.3}N$ (0001) template. b) Internal quantum efficiency (IQE) (deduced using eq. IV-3), radiative (equal to τ_{slow}) and non radiative (deduced using eq. IV-2) decay times for $Al_yGa_{1-y}N$ ($0 \leq y \leq 0.2$) QDs.

IV.3.2 $Al_yGa_{1-y}N$ QDs emitting in the UVB-UVC range ($0.3 \leq y \leq 0.4$)

In this part, three $Al_yGa_{1-y}N$ / $Al_{0.7}Ga_{0.3}N$ (0001) samples emitting in the UVB - UVC range were studied. For this series of samples, the fourth harmonic of the Ti: Sapphire laser (196 nm) was used in order to have a high enough excitation energy compared to the QD emission energy. The three samples are: $Al_{0.4}Ga_{0.6}N$ QDs with 8 MLs (sample C) and 6 MLs (sample D) deposited amount and $Al_{0.3}Ga_{0.7}N$ QDs with 6 MLs (sample E). The impact of the heights of the $Al_yGa_{1-y}N$ QDs at a given chemical contrast as well as the variation of the chemical contrast at constant QD height on the decay times will be studied.

In Figure IV-16 are plotted the evolution of radiative and non-radiative decay times against the average value of the PL energy at 8 K. The impact of the heights of the QDs at a given chemical contrast between the QD layer and the $Al_{0.7}Ga_{0.3}N$ barrier is indicated by an oblique arrow as well as the influence of the variation of the chemical contrast at constant QD height.

We can clearly see that decreasing the height of $Al_{0.4}Ga_{0.6}N$ QDs (from 8 MLs to 6 MLs) induces a decrease of the decay times. Similarly, decreasing F_{int} (i.e. going from y_{Al} equal to 0.3 to y_{Al} equal to 0.4 and so decreasing the chemical contrast (Δ_{x-y}) with the $Al_{0.7}Ga_{0.3}N$ (0001) barrier) also leads to a reduction of the decay times. Obviously, the observed trend is the signature of the Quantum Confined Stark Effect, inducing a better wavefunction overlap for thinner QDs and smaller F_{int}.

We have to emphasize that at the repetition rate of the laser (82 MHz), the decay time of sample C with 8 MLs of $Al_{0.4}Ga_{0.6}N$ deposited amount is not accurately measured and that a lower repetition rate could give slightly longer values. Unfortunately, pulse-peaking the 196 nm radiation of the laser did not deliver high enough power to deal with a signal to noise ratio adapted to the experimental measurement.

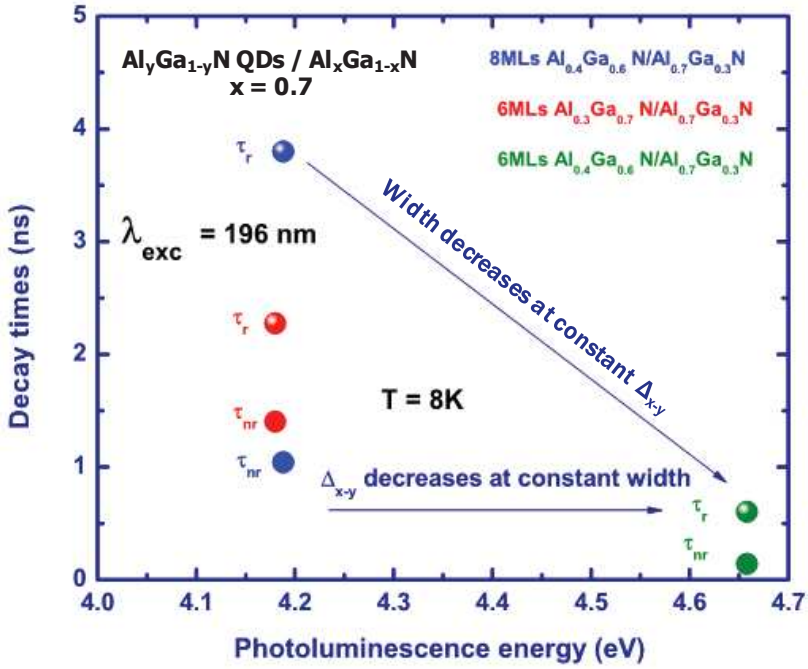

Figure IV-16. Radiative and non radiative decay times at 8 K of different $Al_yGa_{1-y}N$ QD active regions as a function of the emission energy.

Finally, in Figure IV-17 are reported the 2D representations of the temporal dependence of the photoluminescence wavelength at low and room temperature for $Al_{0.4}Ga_{0.6}N$ QDs (sample C) and $Al_{0.3}Ga_{0.7}N$ QDs (sample E). The upper (respectively lower) row corresponds to measurements at 8 K (respectively 300 K) of the time-resolved photoluminescence intensity. Note that decays at room temperature are plotted in the 0 to 5 ns range for 300 K and in the 0 to 10 ns range at low temperature.

From the left side to the right side figures, the decay time decreases as the average height of the quantum dots decreases (cf. Figure IV-17 and Table IV-2). In Figure IV-17(c) and (d) are reported the temporal dependence of the photoluminescence energy at room temperature. Compared with the situation at low temperature, both the decay times decrease as well as the intensities decrease when increasing the temperature as an evidence of the existence of non-radiative recombination channels.

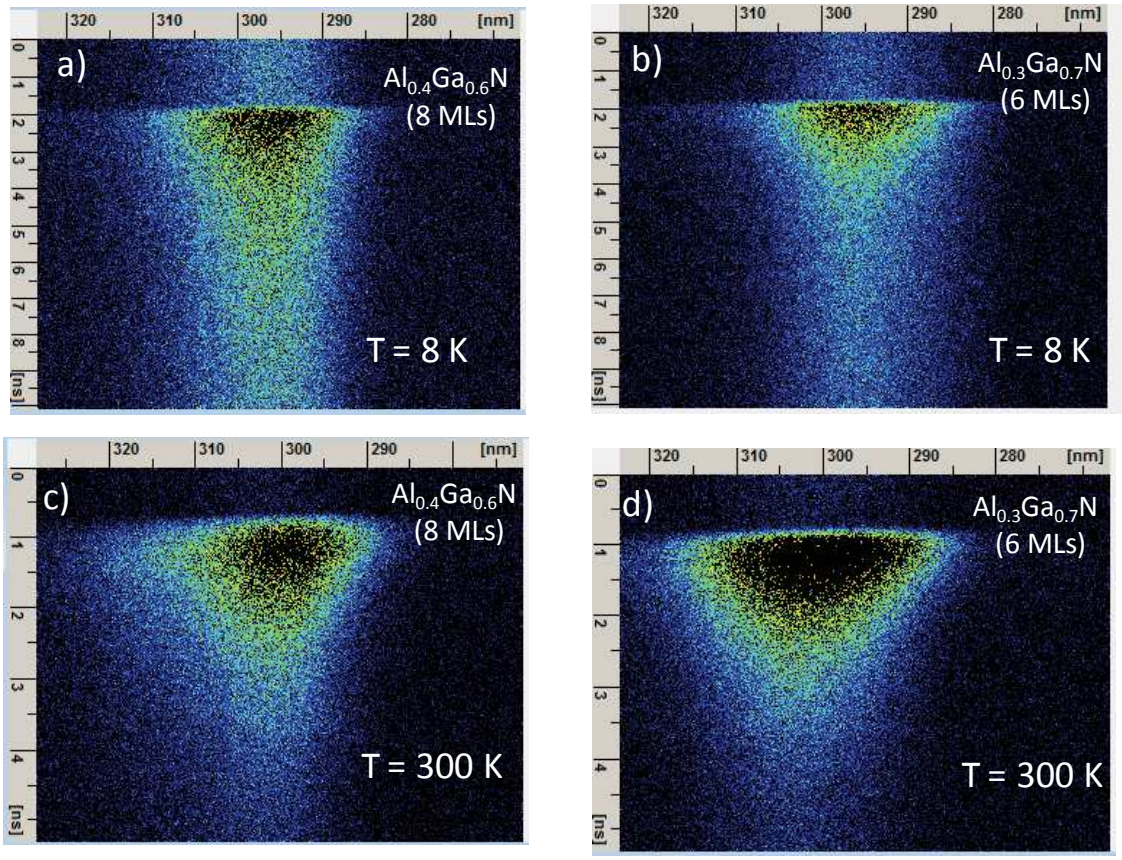

Figure IV-17. 2D representations of the temporal dependence of the photoluminescence wavelength at 8 K and 300 K for $Al_{0.4}Ga_{0.6}N$ (sample C) and $Al_{0.3}Ga_{0.7}N$ (sample E) QDs.

IQE values at low temperature were also calculated using equation IV-3, and the different values are summarized in Table IV-2. We remark that the higher IQE (66 %) is obtained by using **QDs embedded in a barrier with a moderate chemical contrast (6 MLs deposited amount $Al_{0.4}Ga_{0.6}N$ QDs / $Al_{0.7}Ga_{0.7}N$ with $\Delta_{x-y} = 0.3$)**. In that case, both the lattice mismatch and the QD height are reduced which limits the impact of the Quantum Confined Stark Effect. It appears that this is a text-book behaviour as increasing the alloy composition increases the carrier localization that is to say the proportion of radiative recombination relatively to the non-radiative recombination; but the departure of the IQE of our best sample from 100 % indicates that optimization of the quality of these aluminium rich $Al_{0.7}Ga_{0.3}N$ barrier layers is still to be reached.

Table IV-2 : Summary of the main optical properties (energy emission, decay times and IQEs) for $Al_{0.4}Ga_{0.6}N$ QDs (8 MLs and 6 MLs) and $Al_{0.3}Ga_{0.7}N$ QDs (6 MLs) grown on $Al_{0.7}Ga_{0.3}N$ (0001).

Sample design	PL energy at 8 K (eV)	τ_r at 8 K (ns)	τ_{nr} at 8 K (ns)	IQE at 8 K (%)	I(300K) / I(8K) (%)
8 MLs $Al_{0.4}Ga_{0.6}N$ (Sample C)	4.18	4	1	52	10
6 MLs $Al_{0.4}Ga_{0.6}N$ (Sample D)	4.66	0.60	0.15	66	30
6 MLs $Al_{0.3}Ga_{0.7}N$ (Sample E)	4.18	2.27	1.4	50	11

IV.4 Conclusion

This chapter was divided into three parts. In the first one, the influence of the Al composition, in the $Al_xGa_{1-x}N$ template, on the $Al_{0.1}Ga_{0.9}N$ QDs formation was studied. It was shown that by increasing x_{Al} (i.e. increasing F_{int}), no red shift of the PL emission was observed (contrary to GaN QDs, cf. chapter II). However, a slight blue (UV) shift is observed (attributed to the formation of slightly smaller QDs). This result confirms that for small $Al_{0.1}Ga_{0.9}N$ QDs, the PL energy emission is mainly insensitive to F_{int}. Temperature dependent PL measurements showed that growing a moderated QD size (h ~ 2 - 2.5 nm) embedded in a barrier with a moderated chemical contrast (Δ_{x-y}) is necessary to improve the radiative efficiency, with I(300K) / I(9K) ratio **reaching 46 %** in the $Al_{0.1}Ga_{0.9}N$ / $Al_{0.6}Ga_{0.4}N$ (0001) system.

In the second part, the $Al_yGa_{1-y}N$ QD compositions as well as the deposited amount were varied in order to assess the range of emission energies accessible, with the aim to go deeper in the UV range. By tuning these growth conditions, the wavelength emission was shifted from the UVA down to the UVC range, reaching the targeted wavelength emission of **270 - 275 nm** with a radiative efficiency of **30 % versus 0.5 % in a similar QW** structure.

In the third part, the different recombination process dynamics were studied using time resolved photoluminescence measurements (TRPL). The radiative decay time was found to strongly decrease from the µs range down to the ns range while going from GaN to $Al_yGa_{1-y}N$ QDs in part as a consequence of the strong reduction of F_{int}. IQE values at low temperature were also estimated, using TRPL measurements, reaching values between 50 % and 66 %.

References

[1] M. Leroux, J. Brault, A. Kahouli, D. Elmaghraoui, B. Damilano, P. de Mierry, M. Korytov, J.-H. Kim, and Y.-H. Cho, J. Appl. Phys. 116, 034308 (2014).

[2] S. Matta, J. Brault, S. Matta, T. H. Ngo, B.Damilano, M. Korytov, P. Vennéguès, M. Nemoz, J. Massies, M.Leroux and B. Gil, J. Appl. Phys. 122, 085706 (2017).

[3] M. Leroux, F. Semond, F. Natali, D. Byrne, F. Cadoret, B. Damilano, A. Dussaigne, N. Grandjean, A.Le Louarn, S. Vézian, J. Massies, Superlattices and Microstructures 36, 659–674 (2004).

[4] B. Damilano, J. Brault, and J. Massies, J. Appl. Phys. 118, 024304 (2015).

[5] C. Himwas, PhD thesis «Nanostructures à base de semi-conducteurs nitrures pour l'émission ultraviolette». Université Joseph-Fourier Grenoble I, (2006).

[6] C. Himwas, R. Songmuang, L. S. Dang, J. Bleuse, L. Rapenne, E. Sarigiannidou, and E. Monroy, Appl. Phys. Lett. 101, 241914 (2012).

[7] J. Brault, S. Matta, T.-H. Ngo, M. Korytov, D. Rosales, B. Damilano, M. Leroux, P. Vennéguès, M. Al Khalifioui, A. Courville, O. Tottereau, J. Massies, and B. Gil, Jpn. J. Appl. Phys. 55, 05FG06 (2016).

[8] J. Brault, D. Rosales, B. Damilano, M. Leroux, A. Courville, M. Korytov, S. Chenot, P. Vennéguès, B. Vinter, P. de Mierry, A. Kahouli, J. Massies, T. Bretagnon, and B. Gil, Semicond. Sci. Technol. 29, 084001 (2014).

[9] Y. Iwata, R. G. Banal, S. Ichikawa, M. Funato, and Y. Kawakami, J. Appl. Phys. 117, 075701 (2015).

Table of Contents

V. Prototype demonstration of $Al_yGa_{1-y}N$ quantum dots based UV LEDs

In the last chapter, the performances of $Al_yGa_{1-y}N$ QDs to emit down to the UVC range with better PL radiative efficiencies compared to QWs was shown. In this chapter, we will show the ability to fabricate electrically injected $Al_yGa_{1-y}N$ QDs-based UV LEDs. First of all, the different growth and fabrication steps for QDs-based LEDs will be presented. LEDs with GaN QDs (as an active region) are first studied, showing an EL emission in the near blue-UVA range (from 415 nm down to 360 nm). In a second part, prototypes of $Al_yGa_{1-y}N$ (y_{Al} = 0.1 and 0.2) QDs based UV LEDs emitting down to the UVB range (~ from 335 nm down to 305 nm) will be presented. The electrical and electro-optical characteristics for the different LEDs will be shown, along with the electroluminescence characteristics and the light output variation as a function of the current density, giving insights on the carrier injection and recombination mechanisms in these LEDs.

V.1 Introduction

In the previous chapters, we have shown the interest of using $Al_yGa_{1-y}N$ QDs in order to improve the photoluminescence radiative efficiency in the UV range by minimizing the negative influence of non-radiative defects. These results are promising for $Al_yGa_{1-y}N$ QDs as potentially good candidates for active regions of UV light emitting diodes (LEDs) in order to improve their internal quantum efficiencies (IQE). However, for electrically pumped UV-LED devices, additional limitations are present, as discussed in chapter I.2. In particular, the poor injection efficiency in $Al_xGa_{1-x}N$:Mg layers and the low light extraction efficiency are detrimental for the LED performances. This means that in order to reach an electroluminescent (EL) device with high wall-plug efficiencies, different elements have to be combined and optimized: 1) the epitaxial growth of (Al,Ga)N materials and specially the active region, 2) the control of efficient n and p type $Al_xGa_{1-x}N$ doped layers and 3) the device fabrication process. All those factors induce a limitation of the UV-LED performance (as presented in chapter I.2). In the literature, the external quantum efficiencies (EQE) of UV-LEDs is typically below 10 % (cf. Figure V-1).

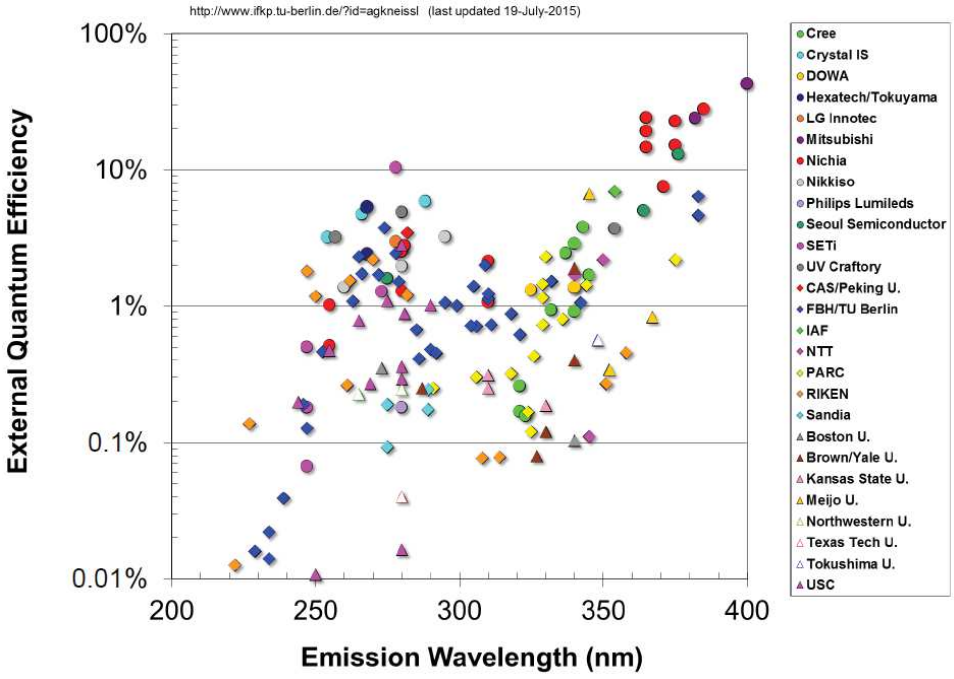

Figure V-1. State of the art of the external quantum efficiencies for ultraviolet LEDs [1].

Different approaches can be used to fabricate UV-LEDs, most of them being based on quantum wells as the active region. Only a few publications concern (Al,Ga)N QD based UV LEDs. Tanaka et al. have first demonstrated the fabrication of GaN QD based UV LEDs by metal organic chemical vapour deposition (MOCVD) emitting in the UVA range (~ 360 nm). GaN QDs were grown on an $Al_{0.1}Ga_{0.9}N$ (0001) surface using Si as an anti-surfactant [2]. Ultra-thin GaN QDs based UV LEDs grown on AlN (0001) by molecular beam epitaxy (MBE) were also demonstrated using tunnel assisted carrier injection. Electroluminescence emission peaks at 261 nm and 340 nm were found, those two peaks being attributed to the presence of two GaN QDs families with height of 2 MLs and 4 MLs [3]. Recently, EL emission down to 234 nm was shown using 1 to 3 MLs of GaN [4]. Also, electron-beam pumped UV sources based on quasi-2D ultra-thin (~ 0.6 ML) GaN quantum structure has been investigated showing high output power (~ 160 mW) [5]. In our group, GaN QD-based LEDs grown on $Al_{0.5}Ga_{0.5}N$ (0001) and (11-22) templates were demonstrated with an emission wavelength down to 360 nm and 320 nm for the polar and semipolar orientations, respectively [6, 7, 8]. As we can see very few works were performed to fabricate QD based UV LED and all of them use GaN QDs as emitters with a typical emission in the UVA range. In this chapter, we will present the demonstration of $Al_yGa_{1-y}N$ QDs based UV LEDs with y_{Al} nominal concentration (n.c.) up to 20 %.

In a first part of this chapter, the general epitaxial growth and the LED fabrication process will be presented. Then, the main optical and electrical properties of GaN QDs and $Al_yGa_{1-y}N$ QDs (with y_{Al} equal to 0.1 and 0.2 nominal concentration) based LEDs will be discussed.

V.2 Epitaxial growth and LED fabrication procedure

The QD based LED structures were entirely grown by MBE on (0001) c-plane sapphire substrates. The basic sample structure is presented on Figure V-2. The heterostructure growth begins with a 30 nm GaN buffer layer on which 120 nm of AlN is grown, as described in details in chapter II.1. Then, an n-doped $Al_xGa_{1-x}N$:Si layer is grown at around 850°C. The Si atoms concentration is typically in the order of 10^{19} cm^{-3}, as determined by secondary ion mass spectrometry (SIMS) on reference samples. The active region is composed of three $Al_yGa_{1-y}N$ QD plane ($0 \leq y_{Al} \leq 0.2$) separated by 10 nm of n.i.d $Al_xGa_{1-x}N$ barrier layers with x_{Al} equals to 0.5 or 0.6 (depending on the QD composition) for GaN and $Al_yGa_{1-y}N$ ($y_{Al} = 0.1$ or 0.2) QDs, respectively. The last QD plane is buried by 20 nm of $Al_xGa_{1-x}N$. $Al_yGa_{1-y}N$ QDs (with y_{Al} n.c. equals to 0.1 or 0.2) were grown, using the optimized growth conditions, as presented in chapter III.3. Next, the p-type region is grown. This region is composed of 10 nm Mg doped $Al_{x2}Ga_{1-x2}N$:Mg electron blocking layer (EBL) which serves to block the electrons in the active zone, with x2 > x (typically a 15 % higher Al concentration). Then, 10 nm of $Al_xGa_{1-x}N$:Mg layer is grown at 820°C followed by a 30 nm GaN:Mg contact layer in order to improve the electrical injection. The Mg doping concentration is typically around 1 - 5 x 10^{19} atoms.cm^{-3} in the $Al_xGa_{1-x}N$ layers and [Mg] ~ 1 x 10^{20} atoms.cm^{-3} in the GaN layer, as determined by SIMS on reference samples.

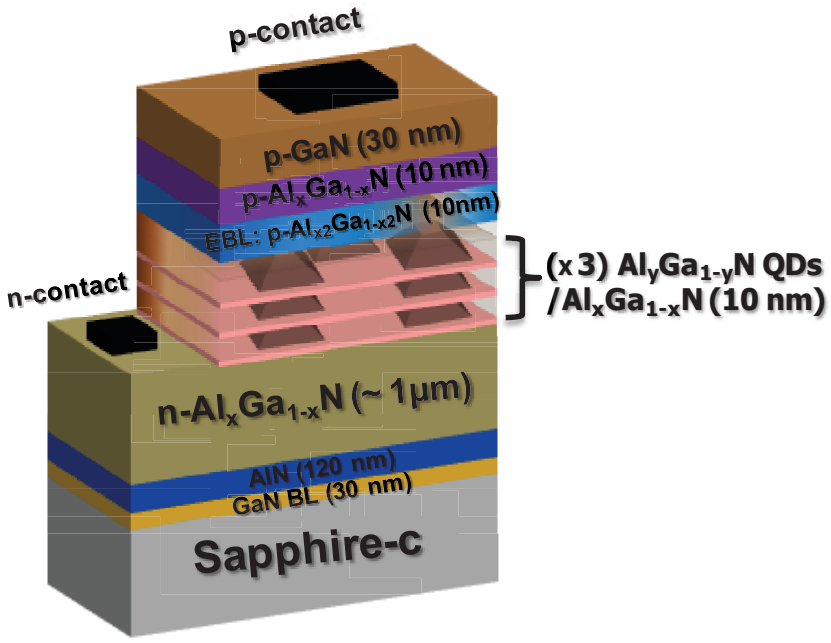

Figure V-2. Schematics presenting the main structure of an (Al,Ga)N QD-based UV LED.

After the epitaxial growth, a device fabrication process is performed. The standard technological processes used to fabricate the LED squared mesa patterns, defining variable LED

surface areas ranging between (x 140) μm^2 and (x 460) μm^2, are made by photolithography, metallization and reactive ion etching (RIE). First of all, a thin Ni (5 nm) / Au (5 nm) layer is deposited (covering the mesas) which serves as a semi-transparent electrode and favours a homogenous distribution of the current on the p-GaN layer surface. Ni (20 nm) / Au (200 nm) is then deposited as a p-contact top electrode. The n-contact, deposited on the $Al_xGa_{1-x}N$:Si layer, consists of a stacking of Ti (30 nm) / Al (180 nm) / Ni (40 nm) / Au (200 nm).

V.3 GaN QD based LEDs

V.3.1 Introduction

In this part, GaN / $Al_xGa_{1-x}N$ QD based LEDs were fabricated with x_{Al} equals to 0.5. Three structures were grown with GaN deposited amounts varying between 1.5 and 2 nm (i.e. 6 and 8 MLs). The LED characteristics were measured at room temperature by collecting the output light using an optical fibre and then converted into an electrical signal by a CCD detector. The LEDs mesa size characterized in this part have a surface area around 32000 μm^2.

V.3.2 Electroluminescence and electrical properties

Figure V-3 shows the electroluminescence (EL) measurements performed at room temperature for three devices with an injected current density ~ 30 A / cm^2. As we can see, an EL emission band is observed in the near UVA range. It is also observed that while decreasing the QD deposited amounts from 8 MLs down to 6 MLs (i.e. going from higher to smaller QD heights) the EL energy increases from 3.26 eV to 3.44 eV (i.e. blue shift is observed from 380 nm down to 360 nm). Those EL energies are in the same energy range as the photoluminescence emission observed for GaN / $Al_{0.5}Ga_{0.5}N$ QDs (~ 3.3 eV; cf. chapter II). However, as discussed in chapter II, the GaN QD emission energy strongly depends on the injected carrier density, especially in the case of QDs with higher heights (above 2 nm).

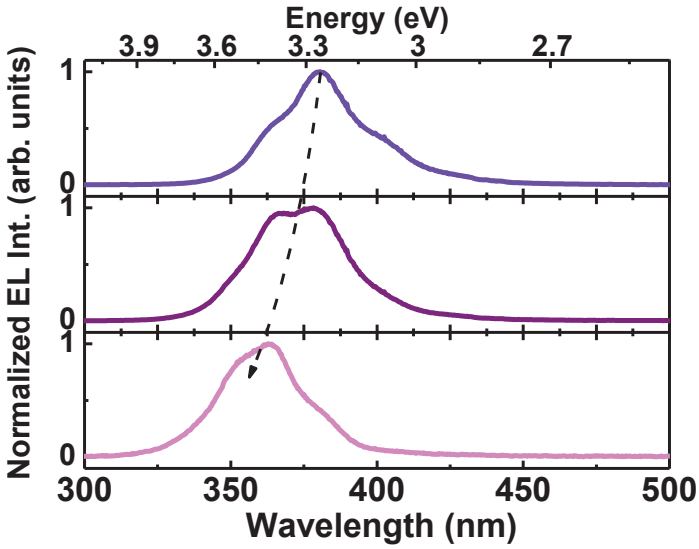

Figure V-3. Room temperature electroluminescence spectra for GaN / $Al_{0.5}Ga_{0.5}N$ QD-based LEDs (for an injection current density of ~ 30 A / cm^2) for different QD active regions (with a deposited amount between 6 and 8 MLs): going from higher QD height (top spectrum) to smaller QD height (bottom spectrum)

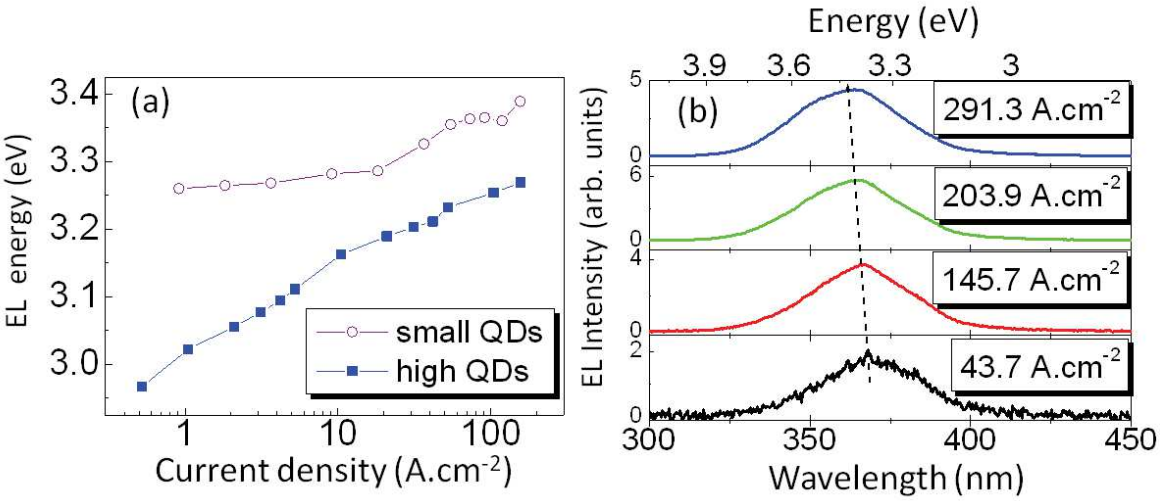

Figure V-4. (a) Variation of the electroluminescence energy of GaN / $Al_{0.5}Ga_{0.5}N$ (0001) QD-based UV LEDs, with different QD height active regions, as a function of the current density. (b) Electroluminescence spectra of a GaN / $Al_{0.5}Ga_{0.5}N$ (0001) QD based LED with small QD heights for different current densities.

To investigate this property in the case of LEDs, the EL emission energy measured as a function of the injected current density for two specific LEDs with different QD heights, referred as high and small QDs as presented in Figure V-4(a). By increasing the injected current density, a blue shift towards higher energies is observed for both devices. This shift is a result of the gradual screening of the internal electric field (F_{int}) by the injected carriers in the QDs [9, 10]. Noteworthy, this effect is reduced for smaller QDs. We can clearly see that for a similar current density range, a shift of 130 meV is observed (i.e. from 3.26 eV up to 3.39 eV) for small QDs, whereas a larger shift of 240 meV (i.e. 3.02 eV up to 3.26 eV) is found for higher QDs. Indeed,

for smaller QD height the influence of F_{int} on the QD fundamental energy transition is reduced. This is in agreement with previous results [10] and similar to the case of GaN / (Al,Ga)N quantum well structures [11].

J-V measurements were also performed. Figure V-5 presents an example of the typical J-V characteristics observed for a GaN QDs based LED. A turn on voltage of 6 V is found for 20 mA (~ 62 A / cm^2) with a series resistance (R_s) around 40 Ω. Those values are comparable with the values reported for $Al_{0.5}Ga_{0.5}N$ based LEDs [12]. However, they are not as good as standard blue InGaN / GaN LEDs. This is mainly due to the higher resistivity for (Al,Ga)N layers compared to GaN layers (typically ≈ 1 Ω.cm for GaN:Mg and above 30 Ω.cm for $Al_{0.5}Ga_{0.5}N$:Mg layers).

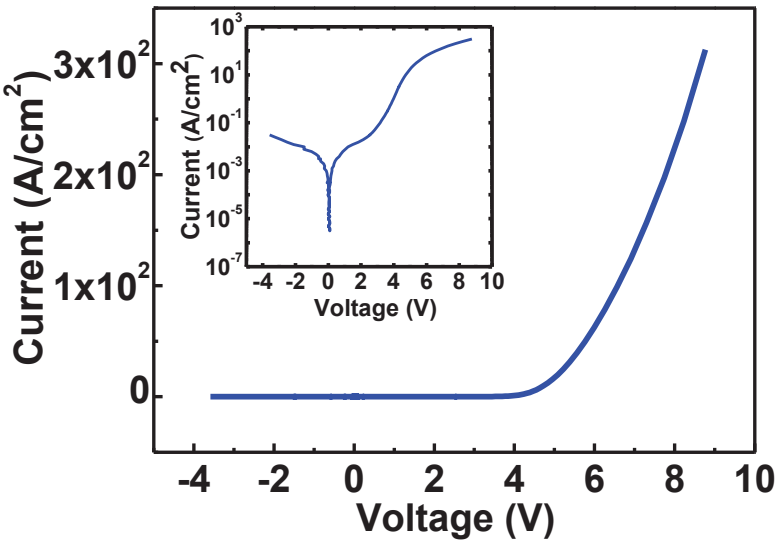

Figure V-5. Current-Voltage characteristics for a typical GaN / $Al_{0.5}Ga_{0.5}N$ (0001) QD-based LED. The inset represents the characteristic on a semi-log scale.

To conclude this part, (0001) GaN QD-based LEDs were successfully grown. The EL characteristics showed a strong dependence of the EL emission peak as a function of the injected current density with an emission in the near blue-UVA range. Changing the GaN deposited amount also showed the possibility to blue shift the wavelength emission from 380 nm down to 360 nm, using the same current injected density.

V.4 $Al_yGa_{1-y}N$ QD based UV LEDs

Using GaN QDs has resulted in the fabrication of (0001) LEDs emitting down to around 360 nm [6]. This minimum wavelength emission value is not strictly limited by the material intrinsic properties (i.e. the GaN strained band gap) but also the consequence of the strong F_{int} in polar structures (cf. chapter II)[13, 14], which induces a red shift of the wavelength emission due to the quantum confined Stark effect (QCSE). Indeed, semipolar GaN QDs (for which the influence

of F_{int} is reduced) have also been grown showing an emission down to 325 nm [6]. As described during this thesis, growing (0001) QDs with reduced heights (typically below 3 nm) can also limit the influence of F_{int} and thus permit to reach shorter wavelengths. Also, increasing the band gap energy, by increasing the value of y_{Al}, should push forward the emission into the UV range for our structures. Interestingly, both ways can be obtained by using $Al_yGa_{1-y}N$ QDs ($y_{Al} > 0$).

For this reason, $Al_yGa_{1-y}N$ QD / $Al_{0.6}Ga_{0.4}N$ based LEDs were fabricated with a value of y_{Al} (nominal concentration) equals to 0.1 and 0.2, and refereed as LED-A and LED-B, respectively, in the following. Except for the QD Al concentration, the rest of the LED structures were fabricated following identical growth conditions and structure design as described in part V.2 (cf. Figure V-6 (a)).

It is worth noting that in order to follow the 2D – 3D growth mode transition, the rotation of the samples was stopped during the growth of these layers. Therefore, the growth conditions have been chosen to obtain QDs with an Al nominal concentration (n.c.) of 0.1 and 0.2 for the QDs at the centre of the wafers. From the centre to the edge of the wafers, an Al variation of ± 20 % is estimated based on energy dispersive X-ray spectroscopy measurements in a scanning electron microscope performed on thick (0.5 µm) $Al_xGa_{1-x}N$ layers also fabricated without rotation of the samples: this characteristic implies an estimated variation of the Al n.c. of the QDs from 0.08 to 0.12 for LED-A, and from 0.16 to 0.24 for LED-B. The LEDs mesa size characterized in this part are of (x 310) μm^2, corresponding to an area of ~ 96000 μm^2 for the light emission.

V.4.1 Electrical properties

The electrical property of the LEDs was first evaluated by measuring the current density as a function of the voltage (J-V) characteristic. No significant differences were observed between the two LEDs (LED-A and LED-B). Figure V-6(b) presents a typical J-V curve obtained between a reverse bias of 8 V and forward bias of 14.5 V.

The LEDs turn-on voltage is found around 7 (± 1) V and a value of 8.5(± 1) V is measured at 20 mA (~ 23 A / cm^2). The typical R_s values are around 150 (± 50) Ω. These values are higher than the values obtained for GaN QDs / $Al_{0.5}Ga_{0.5}N$ based LEDs (~ 40 Ω; cf. part V.3), mainly due to the higher contact resistivity for $Al_xGa_{1-x}N$ layers with higher Al concentration, as a strong deepening of the acceptor and donor levels is observed, in particular in the case of p-type $Al_xGa_{1-x}N$ layers [15]. A high R_s value can lead to an important self-heating (Joule heating) and thus a rapid degradation of the device performance. It can also induce an important increase of the LED junction temperature and so a decrease of the $Al_yGa_{1-y}N$ band gap energy, as will be discussed in the next part.

The inset of Figure V-6(b) shows the Log (J -V), which allows to see much more details. In particular, low levels of injection (V < turn on voltage (~ 7 V)) can be characterized and the leakage current estimated, which is found in the 50 - 100 µA range at -4 V (i.e. 0.06 - 0.12 A / cm^2). We can also calculate the shunt resistance (R_p) which is around 1 MΩ. The significant leakage current and the low shunt resistance values point out important leakage paths in the devices. This leakage can be due to the high defects density in the epitaxial layers (TDs > 10^{10} cm^{-2}) [16].

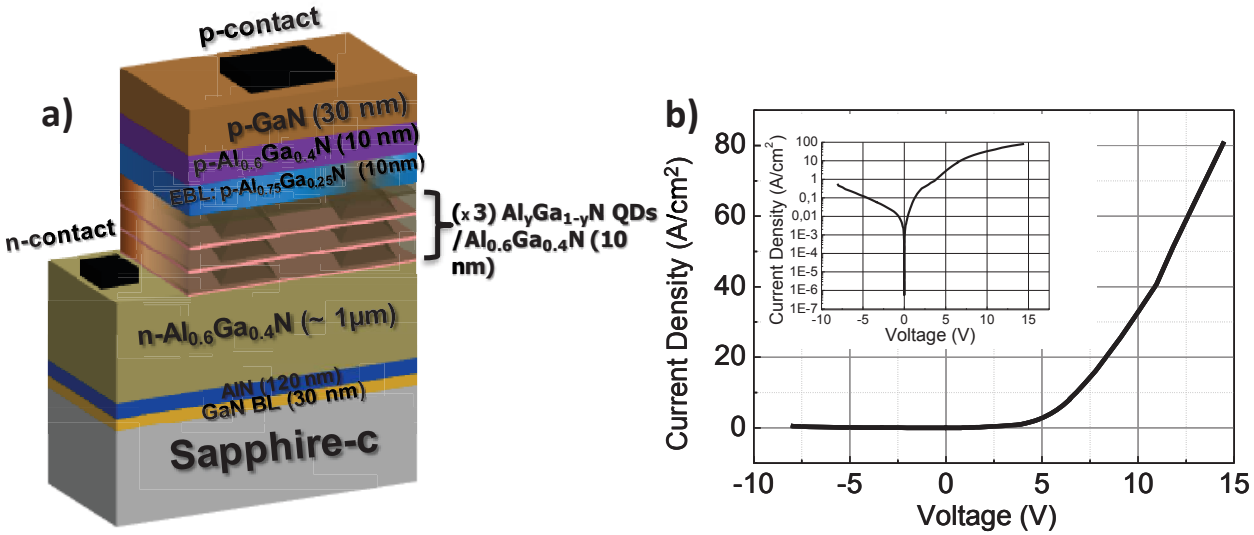

Figure V-6. a) Schematics presenting the main structure of an $Al_yGa_{1-y}N$ / $Al_{0.6}Ga_{0.4}N$ QD-based UV LED (with y = 0.1 or 0.2). b) Current-Voltage characteristic of an $Al_yGa_{1-y}N$ / $Al_{0.6}Ga_{0.4}N$ (0001)QD-based LED. The inset represents the semi-log scale characteristic.

V.4.1 Electroluminescence properties

As already pointed out, the rotation of the samples was stopped during the growth of the different QD planes, which induces a fluctuation of the QD Al nominal concentration. EL measurements were performed at room temperature for different LEDs across the wafers. An emission wavelength range in the 325 nm - 335 nm range (i.e. from 3.81 eV to 3.70 eV) and in the 305 nm - 320 nm range (i.e. 4.06 eV to 3.88 eV) has been observed for LED-A and LED-B, respectively. As expected a lower wavelength emission is observed for LED-B, i.e. with an $Al_yGa_{1-y}N$ QD active region with higher y_{Al}. In the following, we present an in-depth characterization of two typical LEDs made of $Al_{0.1}Ga_{0.9}N$ (n.c.) QDs and $Al_{0.2}Ga_{0.8}N$ (n.c.) QDs, referred as A1 and B1. Figure V-7 shows the EL spectrum for the two LEDs, measured on a spectral range between 200 nm and 600 nm, using an injected current density of 5.7 A / cm^2 (i.e. 5 mA). A main EL peak emission originating from the QD planes was observed at 326 nm (3.80 eV) and 305 nm (4.06 eV) for sample A1 and B1, respectively.

As discussed in this manuscript, the presence of F_{int} in the QD active region (around 2 - 3 MV / cm) could induce a red shift of the EL emission (QCSE). This negative influence of F_{int} could be reduced by growing QDs with small height (typically h < 2 nm). A way to estimate the influence of the QCSE on the QD emission is to compare the EL energy with the strained band gap energy of $Al_yGa_{1-y}N$ (E_g^{QD}) (for an Al concentration equals to 0.1 and 0.2). The $Al_{0.1}Ga_{0.9}N$ strained band gap (E_g^{QD}) is estimated as follows:

$$E_g^{QD} \approx E_g - a.\varepsilon_{xx}$$

with E_g is the relaxed $Al_yGa_{1-y}N$ band gap value (as determined in ref [17]), a the deformation potential (estimated at -8.5 eV as for GaN)[18], and ε_{xx} the in-plane strain tensor.

For the $Al_{0.1}Ga_{0.9}N$ and $Al_{0.2}Ga_{0.8}N$ strained band gaps, values of 3.72 eV and 3.89 eV are estimated. As we can see, those values are lower than the emission energy for both types of QD based LEDs (3.8 eV and 4.06 eV for A1 and B1, respectively) indicating a minimized influence of the QCSE in the band structure. This is contrary to the case of GaN QD-based LEDs where the EL emission is found at lower energies compared to the strained GaN band gap energy (~ 3.53 eV) (cf. Part V.3) [6, 7]. This difference is mainly due to the smaller height of $Al_yGa_{1-y}N$ QDs compared to GaN QDs, as discussed in chapter III.2. The full width at half maximum (FWHM) for both samples A1 and B1 were measured with values of 190 meV (16 nm) and 280 meV (22 nm), respectively.

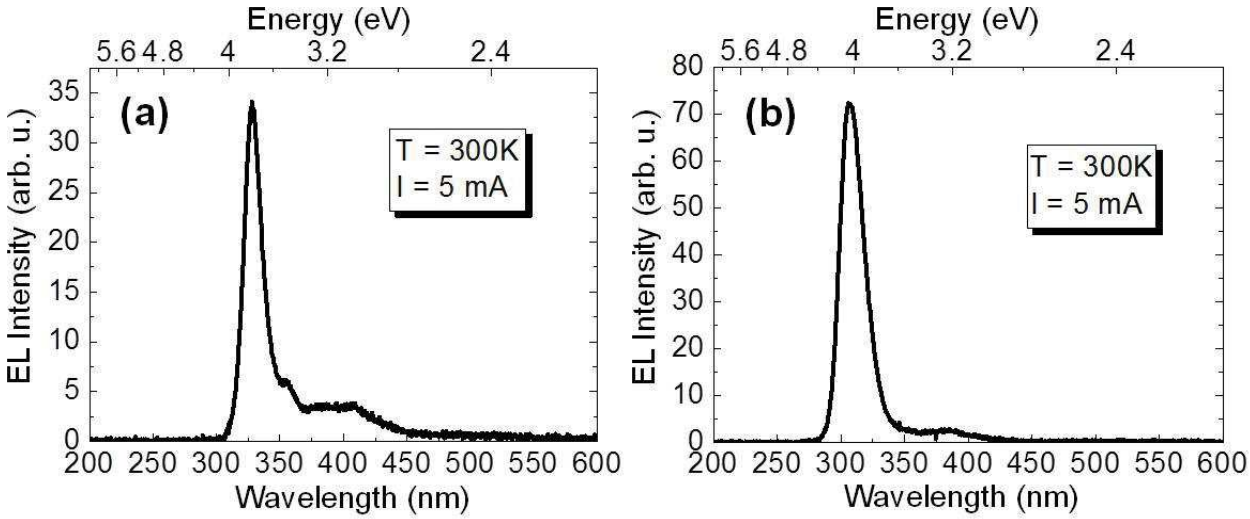

Figure V-7. Electroluminescence spectra over a broad spectral range for a) $Al_{0.1}Ga_{0.9}N$ / $Al_{0.6}Ga_{0.4}N$ (A1) and b) $Al_{0.2}Ga_{0.8}N$ / $Al_{0.6}Ga_{0.4}N$ (B1) active regions of QD-based LEDs. An injection current of 5 mA (i.e. 5.7 A / cm^2) was used.

It is worth noting that going from $Al_{0.1}Ga_{0.9}N$ (n.c.) to $Al_{0.2}Ga_{0.8}N$ (n.c.) QDs grown on a similar $Al_{0.6}Ga_{0.4}N$ (0001) barrier should lead to a lower F_{int} due to the lower chemical contrast

between the layers and a decrease of the polarization discontinuities, and consequently a reduction of the EL peak FWHM. However, as mentioned before, an opposite behaviour is observed with an increase of the FWHM for $Al_{0.2}Ga_{0.8}N$ QDs compared to $Al_{0.1}Ga_{0.9}N$ QDs, indicating that F_{int} is not the principal parameter accounting for the EL broadening. These phenomena can be attributed to a higher dispersion of the QD height when increasing the Al nominal concentration in the QDs. In addition, we can also observe an additional emission band at higher wavelength between 350 nm and 420 nm (Figure V-7). This is similarly to what we observed in photoluminescence measurements on $Al_{0.1}Ga_{0.9}N$ QDs samples grown with not fully optimized growth conditions. As discussed in chapter III, this band was attributed to an asymmetric distribution of QD heights and Al composition fluctuation in the QDs [19].

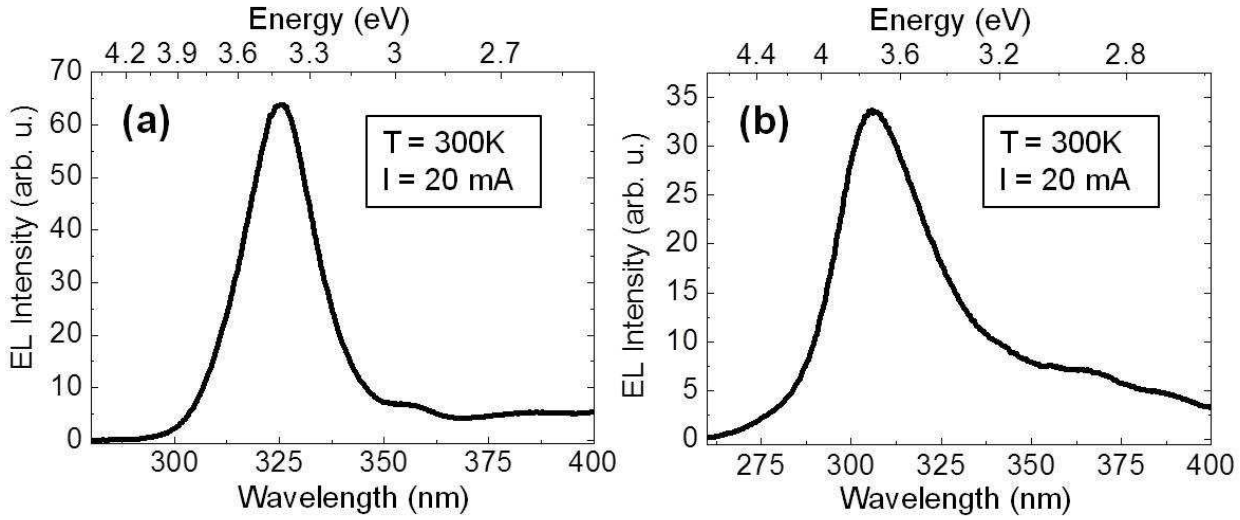

Figure V-8. Electroluminescence spetra of $Al_yGa_{1-y}N$ / $Al_{0.6}Ga_{0.4}N$ QD-based UV LEDs for an injection current of 20 mA (i.e. 23 A / cm^2) with y_{Al} equals to a) 0.1 (A1) and b) 0.2 (B1).

Figure V-8 presents the EL spectra of the two LEDs (A1 and B1) using a higher injected current density (~ 23 A / cm^2) compared to Figure V-7. Similar emission wavelengths were found while increasing the injected current density, typically at 326 nm and 305 nm for A1 and B1, respectively. However, a clear increase in the FWHM is observed for higher injected current density (Figure V-8) with values of 230 meV (20 nm) for A1 and 425 meV (32 nm) for B1. This increase of the FWHM while increasing the injected current density can be attributed to state filling effects in the QDs and/or the QD height and composition dispersion. In particular, while increasing the injected current a progressive increase of the injected carriers into the different QD planes is also expected (in particular holes which are mainly injected into the plane next to the p-type layers at low current density due to their low mobility and concentration); therefore, the larger EL peak FWHM would then account for a broadening of the QD size distribution from plane to plane. For instance, depending on the spacer layer thickness between the QD planes, a

variation of the QD sizes has been already observed in other QD material systems, and should be potentially optimized by adjusting the spacer layer thickness [20, 21].

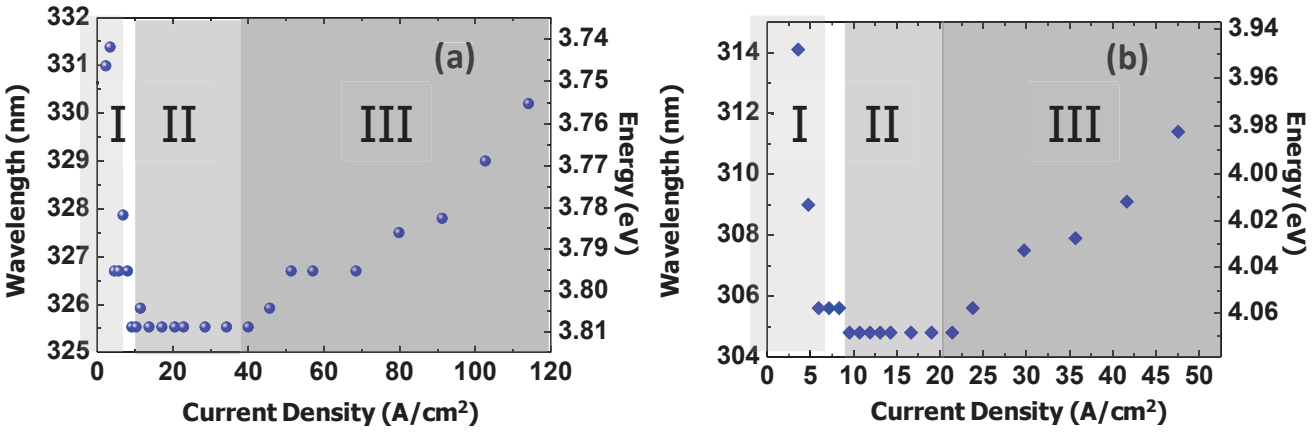

Figure V-9. Variation of the electroluminescence energy of $Al_yGa_{1-y}N$ / $Al_{0.6}Ga_{0.4}N$ (0001) QD-based LEDs as a function of the injected current density for a) $Al_{0.1}Ga_{0.9}N$ (A1) and b) $Al_{0.2}Ga_{0.8}N$ (B1) QD active regions.

To get more insight into the $Al_yGa_{1-y}N$ based QD-LED properties, the EL emission energy was measured as a function of the injected current density for both LEDs (cf. Figure V-9(a) and (b) for LED A1 and B1, respectively). As shown on both figures, three different regimes can be distinguished: **1)** at lower current densities (region I), a blueshift of the EL peak energy is observed when the current density increases, with the emitted wavelength varying from 331 nm to 325 nm for A1 and from 314 nm to 305 nm for B1. This shift corresponds to an energy variation around 70 meV and 120 meV for A1 and B1, respectively. This shift is attributed to a partial screening of F_{int} by the increase of the injected carrier density in the QDs, as for GaN QD-based LEDs [7, 22]. **2)** In region II (intermediate injected current densities), no wavelength shift is observed. This is the consequence of two opposite behaviours which are counterbalancing each other: a weak screening of F_{int} and a self-heating of the LED junction (Joule heating) by increasing the injected current. **3)** Finally, in region III (for a higher injected density) an opposite behaviour is observed compared to region I, with a progressive red shift of the EL peak wavelength from 325 nm to 330 nm and from 305 nm to 311 nm for A1 and B1, respectively. This effect is mainly due to the high series resistance value of the LEDs and the high resistivity of the p-$Al_xGa_{1-x}N$ layers leading to an important increase of the LED junction temperature and thus a decrease of the $Al_yGa_{1-y}N$ QD band gap energy (i.e. inducing a red shifted emission energy).

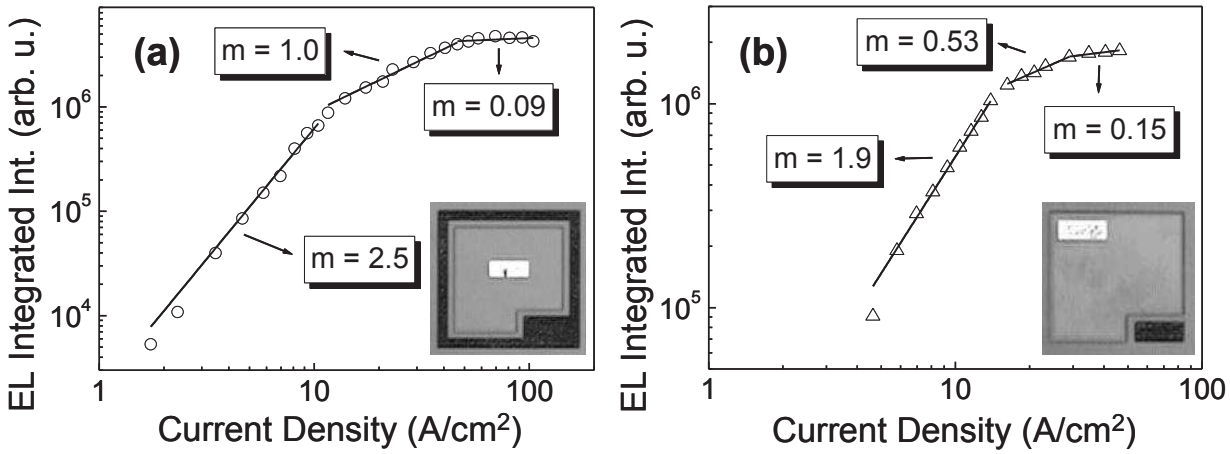

Figure V-10. Variation of the integrated electroluminescence intensity (i.e. output light) of $Al_yGa_{1-y}N$ / $Al_{0.6}Ga_{0.4}N$ (0001) QD-based LEDs as a function of the injected current density for different LED designs: a) an n-type contact surrounding the entire mesa and b) an isolated n-type contact at the right side of the mesa. The insets represent pictures of the different LED designs.

The three regimes discussed before were further analyzed by plotting the light output (i.e. the integrated intensity of the EL spectra between 280 nm and 400 nm) as a function of the injected current density (L-J) (cf. Figure V-10). In fact, two different types of LED designs were investigated with identical mesa area (~ 96000 µm^2). The main difference is the design of the n-contact. In the first case, the contact is surrounding the entire mesa (Figure V-10(a)) and for the second case, the contact is isolated at one side of the LED (Figure V-10(b)). As we can see on both figures, the output light varies as a function of the injected current density at a constant power m. In other words, L is proportional to J^m with m ranging between 0.09 and 2.5 for different injected current density ranges. In fact, this m parameter is related to the recombination mechanisms that take place in the LEDs [23, 24]. As we can see on Figure V-10, for low injection current density, typically between 1 - 10 A / cm^2, a linear dependence (m > 1) of L is observed, with a variation of the EL integrated intensity emission (L) proportional to the square of J: such behaviour is characteristic of LEDs dominated by non-radiative mechanisms. This behaviour was attributed either to tunnelling processes of carriers into defect states localized in the cladding layers or band gap states in the QD active layers. For intermediate injected current density between 10 - 40 A / cm^2, different behaviours are observed depending on the LED design. For the LED design presented in Figure V-10(a), a linear variation of L is found with m equals to 1, however for the LED design presented on Figure V-10(b) a sublinear variation of L is found with m below 1. The linear variation case, with m equals to 1, is obtained for the LED design with n contact surrounding the entire mesa and implies that the deep-level states are saturated with a constant LED internal quantum efficiency. On the other hand, when m is below 1, this means that the LED output power progressively starts to saturate with the injected current

density. This means that for m values approaching zero, L is independent of the injected current density and that the LEDs IQE is strongly decreasing. This behaviour is also observed at higher injected currents (more than 40 A / cm^2) for both types of LED designs. This regime coincides with the red shifted wavelength emission presented in regime III (cf. Figure V-9), pointing out that important thermal effects are at stake in the junction of the LED. As mentioned before, this behaviour is related to the low injection efficiencies and the poor current spreading. Finally, we can conclude that using an n-contact surrounding the entire mesa enables to improve the injection efficiency and the current spreading with the ability to reach higher injected current density and increase the output light of the LED, compared to the LED design with isolated n-contact at one side of the LED mesa.

V.5 Conclusion

In this chapter, we have shown the possibility to fabricate (Al,Ga)N QD-based LED covering from the blue down to the UVB range. In the first part, GaN / $Al_{0.5}Ga_{0.5}N$ QD-based LEDs were grown. The EL characteristics showed a strong dependence of the EL emission peak (blue shift) as a function of the injected current density with an emission in the near blue-UVA region (from 415 nm down to 360 nm). The difficulties to get an emission deeper in the UV range, while using GaN (0001) QDs, is related to the influence of the internal electric field and the QD height which is limited by the minimum deposited amount required (~ 6 MLs) to fabricate GaN QDs. Next, $Al_{0.1}Ga_{0.9}N$ and $Al_{0.2}Ga_{0.8}N$ QD-based UV LEDs were successfully fabricated for the first time, showing the ability to go deeper in the UV range. For $Al_{0.1}Ga_{0.9}N$ QD-based LEDs, an emission in the UVA range (between 325 nm and 335 nm) was shown, whereas for $Al_{0.2}Ga_{0.8}N$ QD based LEDs, a deeper UV emission down to the UVB range (between 305 nm and 320 nm) was shown.

The influence of the LED design on the output light was also studied. In general, the L-J characteristics of the two LEDs design showed three distinct operating regimes. The recombination mechanisms and thermal effects have been studied pointing out the importance of the LED design on the injection efficiency and current spreading, which are seen as severe issues in $Al_xGa_{1-x}N$ based LEDs.

The electrical characteristics of the different $Al_yGa_{1-y}N$ LEDs were also measured. At this stage, the performance of these LEDs is still modest but the important result is that these devices show the possibility to use QDs as an active region for electrically injected devices emitting in the deep UV range. Therefore, these first results will serve as a solid base for further development and optimization of electrically injected QD-based UV LEDs.

References

[1] M. kneissl "UV LED efficiency (last update 19-july-2015)" www. Researchgate.net/ publication/280131929, 6 Oct (2015).

[2] S. Tanaka, J.-S. Lee, P. Ramvall, H. Okagawa, Jpn. J. Appl. Phys. 42, L885 (2003).

[3] J. Verma, P.K. Kandaswamy, V. Protasenko, A. Verma, H.G. Xing, D. Jena, Appl. Phys. Lett. 102, 041103 (2013).

[4] C. Liu, Y. K. Ooi, S. M. Islam, H. Xing, D. Jena and J. Zhang, Appl. Phys. Lett. 112, 011101 (2018).

[5] X. Rong, X. Wang, S. V. Ivanov, X. Jiang, G. Chen, P. Wang, W. Wang, C. He, T. Wang, T. Schulz, M. Albrecht, V. N. Jmerik, A. A. Toropov, V. V. Ratnikov, V. I. Kozlovsky, V. P. Martovitsky, P. Jin, F. Xu, X. Yang, Z. Qin, W. Ge, J. Shi, and B. Shen, Adv. Mater., 28, 7978-7983 (2016).

[6] J. Brault, S. Matta, T.-H. Ngo, D. Rosales, M. Leroux, B. Damilano, M. AlKhalifioui, F. Tendille, S. Chenot, P. de Mierry, J. Massies, and B. Gil, Mater. Sci. Semicond. Process. 55, 95 (2016).

[7] J. Brault, D. Rosales, B. Damilano, M. Leroux, A. Courville, M. Korytov, S. Chenot, P. Vennéguès, B. Vinter, P. De Mierry, A. Kahouli, J. Massies, T. Bretagnon and B. Gil, Semicond. Sci. Technol. 084001 (2014).

[8] J. Brault, B. Damilano, A. Kahouli, S. Chenot, M. Leroux, B. Vinter and J. Massies "Ultra-violet GaN/Al0.5Ga0.5N quantum dot based light emitting diodes" J. Cryst. Growth 363, 282 (2013).

[9] T. Bretagnon, S. Kalliakos, P. Lefebvre, P. Valvin, B. Gil, N. Grandjean, A. Dussaigne, B. Damilano, and J. Massies, Phys. Rev. B 68, 205301 (2003).

[10] M. Leroux, J. Brault, A. Kahouli, D. Elmaghraoui, B. Damilano, P. de Mierry, M. Korytov, J.-H. Kim, and Y.-H. Cho, J. Appl. Phys. 116, 034308 (2014).

[11] N. Grandjean, B. Damilano, S. Dalmasso, M. Leroux, M. Laügt, J. Massies, J. Appl. Phys. 86, 3714 (1999).

[12] V. Adivarahan, A. Heidari, B. Zhang, Q. Fareed, M. Islam, S. Hwang, Krishnan Balakrishnan, Asif Khan, Appl. Phys. Express 2, 092102 (2009).

[13] M. Leroux, J. Brault, A. Kahouli, D. Maghraoui, B. Damilano, P. de Mierry, M. Korytov, J. H. Kim and Y. H Cho, J. Appl. Phys. 116 034308 (2014)

[14] S. Matta, J. Brault, T. H. Ngo, B. Damilano, M. Korytov, P. Vennéguès, M. Nemoz, J. Massies, M. Leroux, and B. Gil, J. Appl. Phys. 122, 085706 (2017).

[15] M. Kneissl and J. Rass, "III-Nitride Ultraviolet Emitters" Springer Series in Materials Science 227 (2016).

[16] S. W. Lee, D. C. Oh, H. Goto, J. S. Ha, H. J. Lee, T. Hanada, M. W. Cho, S. K. Hong, H. Y. Lee, S. R. Cho, J. W. Choi, J. H. Choi, J. H. Jang, J. E. Shin and J. S. Lee, Appl. Phys. Lett. 89, 132117 (2006).

[17] N. Nepal, J. Li, M. L. Nakarmi, J. Y. Lin and H. X. Jiang, Appl. Phys. Lett. 87, 242104 (2005).

[18] M. Leroux, H. Lahrèche, F. Semond, M. Laügt, E. Feltin, N. Schnell, B. Beaumont, P. Gibart and J, Massies, Materials Science Forum, 353, 795 (2001).

[19] S. Matta, J. Brault, T. H. Ngo, B. Damilano, M. Leroux, J. Massies and B. Gil, Superlattices and Microstructures 114, 161 (2018).

[20] J. Stangl, V. Holý and G. Bauer, Rev. Mod. Phys. 76 725 (2004).

[21] J. Brault, M. Gendry, O. Marty, M. Pitaval, J. Olivares, G. Grenet, G. Hollinger, Appl. Surf. Sci. 162, 584 (2000).

[22] J. Brault, B. Damilano, B. Vinter, P. Vennéguès, M. Leroux, A. Kahouli and J. Massies, Jpn. J. Appl. Phys. 52 08JG01 (2013).

[23] S. Dalmasso, B. Damilano, C. Pernot, A. Dussaigne, D. Byrne, N. Grandjean, M. Leroux and J. Massies, phys. stat. sol. (a) 192, 139 (2002).

[24] X. A. Cao, K. Topol, F. Shahedipour-Sandvik, J. Teetsov, P. M. Sandvik, S. F. LeBoeuf, A. Ebong, J. Kretchmer, E. B. Stokes, S. Arthur, A. E. Kaloyeros and D. Walker, Proceedings of SPIE 4776, 105 (2002).

General conclusions and perspectives

This PhD thesis was set out to investigate the growth mechanisms, the structural and optical properties of $Al_yGa_{1-y}N$ QDs / $Al_xGa_{1-x}N$ grown along the polar (0001) orientation. This study was carried out with the aim to develop QD growth processes by molecular beam epitaxy (MBE) and study the potential of (Al,Ga)N QDs as a novel route for efficient ultraviolet (UV) emitters, and more specifically for UV light emitting diodes (LEDs).

The primary objective of this PhD was to grow efficient (Al,Ga)N QDs: in a first part, GaN QDs were grown using either plasma MBE (PAMBE) or ammonia MBE (NH_3-MBE) with the aim to study the best nitrogen source approach for UV emission. First, **the influence of the epitaxial strain** on the QD self-assembling process and morphologies (size, density) was studied by fabricating GaN QDs on different $Al_xGa_{1-x}N$ surfaces (with $0.5 \leq x \leq 0.7$; i.e. a lattice mismatch $1.2\ \% \leq \Delta a/a \leq 1.7\ \%$). In this study, we showed that smaller QDs with higher densities (increased by more than one decade) and narrower size distributions are promoted by using a larger lattice-mismatch. However, photoluminescence (PL) measurements indicated a modification of the QD optical response by the internal electric field (F_{int}) which induces a strong redshift in the emission energy as the Al content of the $Al_xGa_{1-x}N$ matrix increases (a shift from 3.22 eV to 2.95 eV for PAMBE grown GaN QDs and from 3.36 eV to 2.97 eV for NH_3–MBE grown GaN QDs while increasing x_{Al} from 0.5 to 0.7). Indeed, we showed that the total polarization differences between GaN and the surrounding $Al_xGa_{1-x}N$ matrix increases from 3 to 5.3 MV / cm while increasing x_{Al} from 0.5 to 0.7. In addition, power dependent PL measurements showed that F_{int} has less influence on the optical properties of smaller QDs, implying a reduced shift in the PL energy compared to QDs with higher height. On the other hand, the formation of GaN QDs using PAMBE or NH_3-MBE was also compared showing **an influence of the growth method on the surface energy cost contribution ($\Delta\gamma$) which strongly differs by using N_2 or NH_3 sources**. It was shown that the growth process is better controlled using PAMBE, leading to the growth of GaN QDs with higher densities and a better size uniformity. In terms of optical properties, PAMBE grown GaN QDs have up to three times higher PL intensities and smaller full width at half maximum compared to NH_3-MBE grown GaN QDs. Finally, time resolved photoluminescence (TRPL) combined with temperature dependent PL measurements enabled us to determine the internal quantum efficiencies (IQE) of GaN QDs / $Al_xGa_{1-x}N$ (0001) and values around 50 % were found at low temperature. Combined

with the ability to reach a **PL integrated intensity ratio up to 75 %** between 300 K and 9 K, these results have confirmed the efficient carrier confinement in GaN QDs.

Next, in-depth investigations of the growth conditions and optical properties of $Al_{0.1}Ga_{0.9}N$ QDs / $Al_{0.5}Ga_{0.5}N$ were presented showing the different challenges to grow efficient QDs. Changing the growth procedure, especially the annealing step, has shown to modify the QD shape from elongated QDs, formed with an annealing at 740°C, to symmetric QDs, formed with an annealing at a temperature around or above 800°C. The variation of the QD deposited amounts from 10.5 MLs down to 6 MLs showed the ability to cover the deep UVA range, by going from 340 nm (i.e. 3.65 eV) down to 324 nm (i.e. 3.83 eV). An additional band emission at lower energies was also observed for QDs grown with a lower annealing temperature of 740°C. By combining morphological and optical characterizations, this band was attributed to a composition fluctuation in the QD active region inducing the formation of QDs with a reduced Al composition less than 10 %, estimated to be close to "pure" GaN QDs, and higher heights compared to the nominal $Al_{0.1}Ga_{0.9}N$ QDs. Also, an internal electric field around 2 MV / cm was estimated for $Al_{0.1}Ga_{0.9}N$ / $Al_{0.5}Ga_{0.5}N$ system. **Finally, the influence of the annealing step performed at higher temperature has been shown to strongly decrease the PL emission from this additional QD family (Ga-rich (Al)GaN QDs). In addition, this annealing step strongly impacted the QD shape and lead to an improvement of the QD radiative efficiency by a factor 3.**

After defining the optimized growth conditions for $Al_{0.1}Ga_{0.9}N$ / $Al_{0.5}Ga_{0.5}N$ (0001) nanostructures, $Al_yGa_{1-y}N$ QDs ($0 \leq y \leq 0.4$) grown on $Al_xGa_{1-x}N$ (0001) ($0.5 \leq x \leq 0.7$) templates were studied with the aim to go deeper in the UV range. The influence of the Al composition, in the $Al_xGa_{1-x}N$ template, on the $Al_{0.1}Ga_{0.9}N$ QDs formation was studied. It was shown that by increasing x_{Al} (i.e. increasing F_{int}), no red shift of the PL emission was observed (contrary to GaN QDs). On the contrary, a slight blue (UV) shift is observed (attributed to the formation of slightly lower QDs). This result shows that for small $Al_{0.1}Ga_{0.9}N$ QDs, the PL energy emission is almost insensitive to F_{int}. Temperature dependent PL measurements showed that a moderated QD size embedded in a barrier with a moderated chemical contrast (Δ_{x-y}) is necessary to improve the radiative efficiency, with I(300K) / I(9K) ratios **reaching 46 %** in $Al_{0.1}Ga_{0.9}N$ / $Al_{0.6}Ga_{0.4}N$ (0001) system. Then, the $Al_yGa_{1-y}N$ QD composition as well as the deposited amount were varied in order to assess the range of emission energies accessible. By tuning these growth conditions, the QD wavelength emission was shifted from the UVA down to the UVC range, reaching the targeted wavelength emission of **270 - 275 nm** (for water and air purification applications) with a radiative efficiency of **30 %, versus 0.5 % in a similar QW** structure. The different recombination process dynamics were also studied using time resolved

photoluminescence measurements. The radiative decay time was found to strongly decrease from the µs range down to the ns range while going from GaN to $Al_yGa_{1-y}N$ QDs with higher Al concentrations. IQE values at low temperature were also estimated, using TRPL measurements, reaching values between **50 % and 66 %.**

In the last part of this work, we have shown the possibility to fabricate electrically injected (Al,Ga)N QD-based LEDs covering the near blue down to the UVB range (from 415 nm down to 300 nm). The EL characteristics of GaN / $Al_{0.5}Ga_{0.5}N$ QDs showed an emission in the near blue-UVA region (from 415 nm down to 360 nm). The difficulties to get an emission deeper in the UV range, while using GaN (0001) QDs, was related to the influence of the internal electric field and the QD height which is limited by the minimum deposited amount required (~ 6 MLs) to fabricate GaN QDs. Next, $Al_{0.1}Ga_{0.9}N$ and $Al_{0.2}Ga_{0.8}N$ QD-based UV LEDs were successfully fabricated for the first time, showing the ability to go deeper in the UV range. For $Al_{0.1}Ga_{0.9}N$ QD-based LEDs, an emission in the UVA range (between 325 nm and 335 nm) was shown, whereas for $Al_{0.2}Ga_{0.8}N$ QD based LEDs, a deeper UV emission, down to the UVB range (between 305 nm and 320 nm) was shown. The electrical characteristics of the different $Al_yGa_{1-y}N$ LEDs were also studied. At this stage, the performance of these LEDs is still modest but the important result is that these devices show the possibility to use QDs as an active region for electrically injected devices emitting in the deep UV range. Therefore, those first results will serve as a solid base for further developments and optimization of electrically injected QD-based UV LEDs.

From a boarder perspective, we believe that further improvements of the growth conditions for $Al_yGa_{1-y}N$ QDs can lead to even better radiative efficiencies, similarly to the one obtained for GaN QDs. In addition, the samples studied in this work were grown using a low temperature GaN buffer layer (BL ~ 30 nm). As GaN can absorb in the UV range, this BL can impact the external quantum efficiency of UV LEDs. For the next structures, this layer should be replaced by an AlN BL. During this thesis, we also optimized the growth conditions of the AlN BL and the $Al_xGa_{1-x}N$ templates grown above, which structural and optical properties were as good as the ones obtained using GaN BL. The obtained results are not presented in the frame of this manuscript (based on a self-limitation length restriction). Finally in order to improve the electro-optical characteristics of the final QD-based UV LEDs, more work on the device fabrication process will be necessary. Also, the design of LED structures for efficient p type $Al_xGa_{1-x}N$ doped layers remains to be done and investigated including tunnel junctions in the framework of the ANR project DUVET.

Appendix A

Polarization study and symmetry of valence band states in GaN QDs / $Al_xGa_{1-x}N$

Figure 1 shows the PL integrated intensity temperature dependent measurements for the three GaN/$Al_xGa_{1-x}N$ samples (referred as samples A, B and C in chapter II). As we can see, the PL intensity remains roughly stable at low temperature then a decrease is obtained while reaching higher temperatures due to the escape of excitons from the QDs through the wetting layer, which increases the probability to recombine non radiatively with dislocations. However, another behaviour is observed around 140-180 K: the PL intensity shows a significant increase. This increase is found to be more important in the case of GaN / $Al_{0.7}Ga_{0.3}N$ QD structure. Such behaviour raised the question about its origin which could be related to a crossover of the Γ_9-Γ_7 valence band maxima in the hole ground state of the GaN QD layer while increasing x_{Al} in the $Al_xGa_{1-x}N$ barrier ($0.5 \leq x \leq 0.7$) together with a redistribution of the carriers, leading to a redistribution of the emission cones.

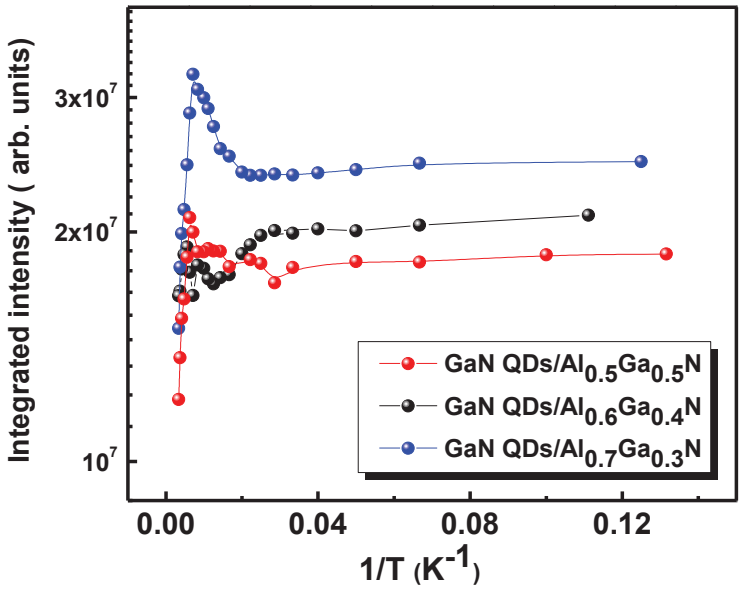

Figure 1. Temperature dependence of the integrated PL intensity for GaN QDs / $Al_xGa_{1-x}N$ (0001), with $0.5 \leq x \leq 0.7$.

As described in chapter I.1.3, the upper valence band state has a Γ_9 symmetry in GaN and a Γ_7 symmetry in AlN; this is due to the strong difference in the crystal field value, which is slightly positive in GaN and strongly negative in AlN [1]. In previous studies, it was shown that by increasing x_{Al} in $Al_xGa_{1-x}N$ alloys, the hole base state becomes progressively Γ_7, which means that photons polarized perpendicularly to the c-axis (i.e. the light emission is parallel to the c-axis) become progressively forbidden [1, 2]. A previous study on GaN / $Al_xGa_{1-x}N$ QWs showed

that a change of the hole ground state from Γ_9 to Γ_7 can occur by increasing the QW width (i.e. equivalent to the QD height in our case) at different x_{Al} compositions. It was also shown that the higher the electric field value in the QW (i.e. higher x_{Al} in the barrier), the larger the Γ_7 domain [2]. This is due to the shift of hole wave functions towards the barriers. For QDs, we can expect that this behaviour is stronger as the wave functions penetrate more in the barriers, compared to QWs, due to the lateral confinement.

In order to verify if this increase of intensity is related to the crossover of the Γ_9-Γ_7 valence band maxima in the $Al_xGa_{1-x}N$ barrier (which can induce a redistribution of the carriers and of the emission cones), we started a study by investigating the linear polarization (using a polarizer in front of the detector) of the QD PL emitted light under oblique observation ($\theta = 45°$). This means that the sample is excited and observed with an angle $\theta = 45°$. Under this configuration we can have access to the light polarization parallel to the c axes (emission originated from the Γ_7 hole states). Figure 2 presents a schematic of the setup. The X, Y and Z axes are those of the crystal, with Z // c. Using a holder with an angle of 45 ° on which the samples are placed, the luminescence is composed of **a wave s, with E perpendicular to the incidence plane**, and **a wave p, with E parallel to the incidence plane**. We recall that the incidence plane is defined by the normal to the surface and the direction of the ray we are studying (the PL emission). The transitions involving the X and Z parts of the wave functions will be observed in p geometry, and in s geometry for part Y (light polarization perpendicular to the incident plane). We recall that in (0001) biaxially strained nitrides, X and Y top valence band states are degenerated.

θ_i is the incident angle (angle between the unextracted luminescence and the normal to the sample surface (as presented on figure 2)) and is around 20°. This value was estimated using Descartes law: $n \sin \theta_i = \sin 45° = \sqrt{2}/2$; where n is the $Al_{0.7}Ga_{0.3}N$ refractive index (~ 2.05-2.15).

Figure 4 shows the PL intensity as a function of the polarization angle (using a polarizer in front of the detector) under oblique observation ($\theta = 45°$) for sample C. This experiment was made at different temperatures. We can see that by increasing the temperature from 11K (figure 4(a)) up to 140 K (figure 4(b)), the intensity diagram is inversed. Unfortunately, this study was not finished and more experiments should be performed. However, the first results indicate that probably an inversion of the cone emission intensity diagram is taking place between 11 K and 140 K.

Appendix A

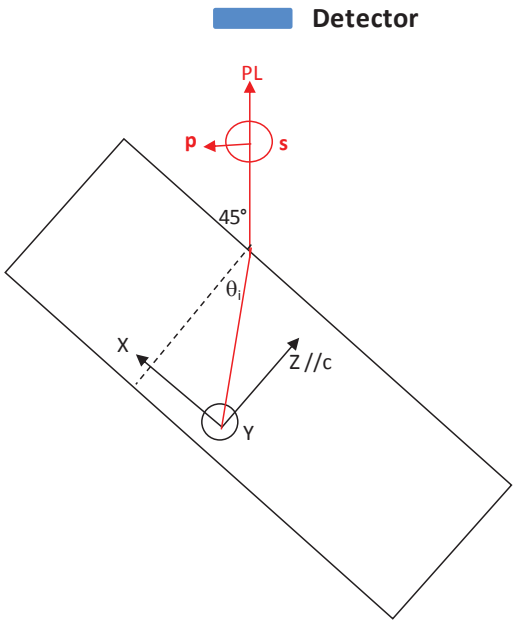

Figure 2. Schematic presenting the photoluminescence with a setup under oblique observation (θ ≈ 45°). The X, Y, Z axes are those of the crystal with Z//c (i.e. the growth direction). The luminescence is composed of a wave s (with E perpendicular to the incidence plane), and a wave p (with E parallel to the incidence plane). The transitions involving the X and Z parts of the wave functions will be observed in p geometry and in s geometry for part Y.

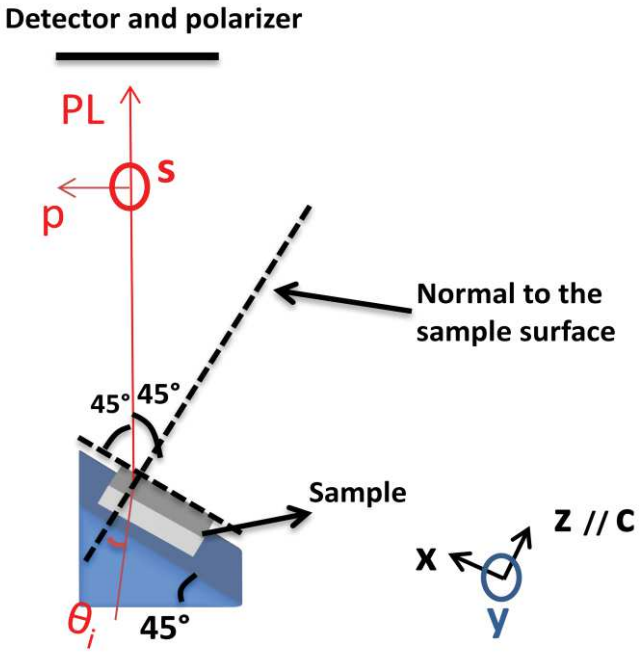

Figure 3. Different schematic representation of the photoluminescence setup under oblique observation (θ ≈ 45°).

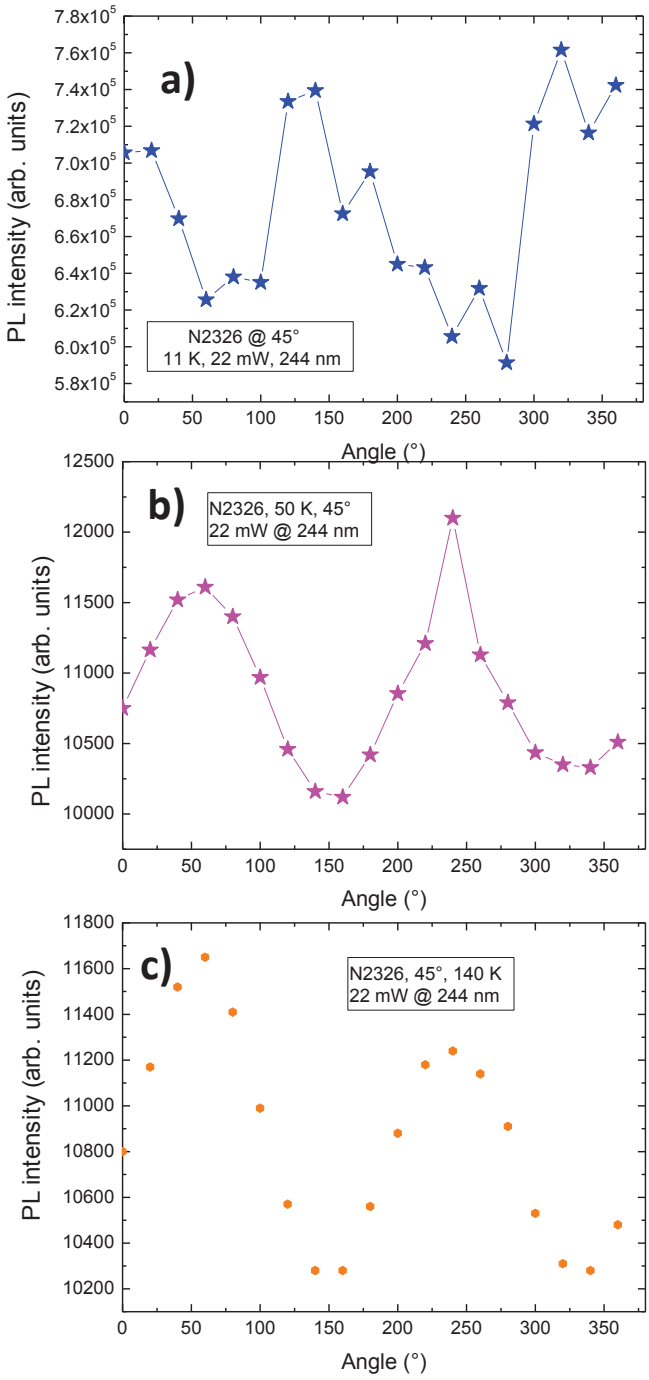

Figure 4. The PL intensity for GaN / $Al_{0.7}Ga_{0.3}N$ QDs (sample C in chapter II) as a function of the polarizer angle at: a) 11 K, 50 K, 140 K. The sample is observed under oblique observation (45°).

[1] M. Leroux, S. Dalmasso, F. Natali, S. Hélin, C. Touzi, S. Laügt, M. Passerel, F. Omnes, F. Semond, J. Massies, P. Gibart, Phys. Status Solidi b 234, 887 (2002).

[2] M. Leroux, F. Semond, F. Natali, D. Byrne, F. Cadoret, B. Damilano, A. Dussaigne, N. Grandjean, A.Le Louarn, S. Vézian, J. Massies, Superlattices and Microstructures 36, 659 (2004).

List of publications

Related publications

- **S. Matta,** J. Brault, T.-H. Ngo, B. Damilano, J. Massies, M. Leroux, and B. Gil Superlattices and Microstructures **114** (2018) 161-168: "Photoluminescence properties of (Al,Ga)N nanostructures grown on $Al_{0.5}Ga_{0.5}N$ (0001)".
- J. Brault, M. Al Khalfioui, **S. Matta**, B. Damilano, M. Leroux, S. Chenot, M. Korytov, J. E. Nkeck, P. Vennéguès, J. Y. Duboz, J. Massies, and B. Gil Semicond. Sci. tech. 33 (2018) 075007: "UVA and UVB light emitting diodes with $Al_yGa_{1-y}N$ quantum dot active regions covering the 305–335 nm range".
- **S. Matta,** J. Brault, T.-H. Ngo, B. Damilano, M. Korytov, P. Vennéguès, M. Nemoz, J. Massies, M. Leroux, and B. Gil Journal of Applied Physics **122** (2017) 085706: "Influence of the heterostructure design on the optical properties of GaN and $Al_{0.1}Ga_{0.9}N$ quantum dots for ultraviolet emission".
- J. Brault, **S. Matta,** T.-H. Ngo, M. Korytov, D. Rosales, B. Damilano, M. Leroux, P. Vennéguès, M. Al khalifioui, A. Courville, O. Tottereau, J. Massies, and B. Gil Japanese Journal of Applied Physics **55** (2016) 05FG06 : "Investigation of $Al_yGa_{1-y}N$/ $Al_{0.5}Ga_{0.5}N$ quantum dot properties for the design of ultraviolet emitters".
- J. Brault, **S. Matta,** T.-H. Ngo, D. Rosales, M. Leroux, B. Damilano, M. Al khalifioui, F. Tendille, S. Chenot, P. de Mierry, J. Massies, and B. Gil Materials Science in Semiconductor Processing **55** (2016) 95-101: "Ultraviolet light emitting diodes using III-N quantum dots".
- M. Leroux, J. Brault, **S. Matta**, M.Korytov, B.Damilano, B.Vinter, J.-H. Kim, Y.-H. Cho, D. El Maghraoui, S. Jaziri Nanotechnology (IEEE-NANO) **7388977** (2015) 278-281: "Optical Properties of $Al_{0.5}Ga_{0.5}N$/GaN Polar Quantum Dots and UV LEDs made of them".

Other publications

- **S. Matta,** J. Brault, M; Korytov, T. Q. P. Vuong, C. Chaix, M. Al Khalfioui, P. Vennéguès, J. Massies, and B. Gil. Journal of Crystal Growth, accepted (2018): "Properties of AlN layers grown on c-sapphire substrate using ammonia assisted MBE".
- Z. Zheng, Y. Li, O. Paul, H. Long, **S. Matta**, M. Leroux, J. Brault, L. Ying, Z. Zheng, B. Zhang Journal of Photonics **12** (2018) 043504: "Loss analysis in nitride deep ultraviolet planar cavity".

- R. Dagher, **S. Matta**, L. Nguyen, M. Portail, M. Zielinski, T. Chassagne, J. Brault, Y. Cordier, and A. Michon Physica Status Solidi A **214** (2017) 1600436: "High temperature annealing and CVD growth of graphene on bulk AlN and AlN templates".
- M. Nemoz, R. Dagher, **S. Matta**, Adrien Michon, P. Vennéguès, and J. Brault Journal of Crystal Growth **461** (2017) 10–15: "Dislocation densities reduction in MBE-grown AlN thin films by high-temperature annealing".
- J. Zheng, L. Wang, X. Wu, Z.Hao, C. Sun, B. Xiong, Y. Luo, Y. Han, J. Wang, H. Li, J. Brault, **S. Matta,** M. Al Khalfioui, J. Yan, T. Wei, Y. Zhang, and J. Wang Applied Physics Letters **109** (2016) 241105: "A PMT-like high gain avalanche photodiode based on GaN/AlN periodically stacked structure".
- S. Contreras, L. Konczewicz, J. Ben Messaoud, H. Peyre, M. Al Khalfioui, **S. Matta**, M. Leroux, B. Damilano and J.Brault Superlattices and Microstructures **98** (2016) 253-258: "High temperature electrical transport study in AlN Si-doped".

Abstract

This PhD deals with the epitaxial growth, structural and optical properties of $Al_yGa_{1-y}N$ quantum dots (QDs) grown on $Al_xGa_{1-x}N$ (0001) by molecular beam epitaxy (MBE), with the aim to study their potential as a novel route for efficient ultraviolet (UV) emitters.

First, we have studied the growth of GaN QDs using either plasma MBE (PAMBE) or ammonia MBE (NH_3-MBE) to find the most adapted nitrogen source for the fabrication of UV emitting QDs. It was shown that the growth process is better controlled using PAMBE, leading to the growth of GaN QDs with higher densities, better size uniformity and up to three times higher photoluminescence (PL) intensities. Also, the influence of the epitaxial strain on the QD self-assembling process was studied by fabricating GaN QDs on different $Al_xGa_{1-x}N$ surfaces (with $0.5 \leq x \leq 0.7$). We showed that QDs with higher densities and smaller sizes (heights) are formed by using a larger lattice-mismatch (i.e. a higher x_{Al} composition). However, photoluminescence (PL) measurements indicated a strong redshift in the emission energy as the Al content of the $Al_xGa_{1-x}N$ template increases due to the increase of the internal electric field discontinuity from 3 to 5.3 MV/cm.

Next, in-depth investigations of the growth conditions and optical properties of $Al_{0.1}Ga_{0.9}N$ QDs / $Al_{0.5}Ga_{0.5}N$ were done presenting the different challenges to be solved to grow efficient QDs. Changing the growth procedure, especially the post-growth annealing step, has shown a modification of the QD shape from elongated QDs, formed with an annealing at 740°C, to symmetric QDs, formed with an annealing at a temperature around or above 800°C. An additional band emission at lower energies was also observed for QDs grown with a lower annealing temperature (740°C). This additional band emission was attributed to the formation of QDs with higher heights and a reduced Al composition less than the nominal one of 10 % (i.e. forming Ga-rich QDs). The influence of the annealing step performed at higher temperature has been shown to strongly decrease the PL emission from this additional QD family. In addition, this annealing step strongly impacted the QD shape and led to an improvement of the QD radiative efficiency by a factor 3. Then, the $Al_xGa_{1-x}N$ barrier composition ($0.5 \leq x \leq 0.7$), the $Al_yGa_{1-y}N$ QD composition ($0.1 \leq y \leq 0.4$) as well as the deposited amount were varied in order to assess the range of accessible emission energies. Also, the influence of varying the $Al_xGa_{1-x}N$ barrier composition on the QD formation was studied. By varying these growth conditions, the QD wavelength emission was shifted from the UVA down to the UVC range, reaching a minimum wavelength emission of 270 - 275 nm (for water and air purification applications) with a high radiative efficiency. Time resolved photoluminescence (TRPL) combined with temperature dependent PL measurements enabled us to determine the internal quantum efficiencies (IQE) of $Al_yGa_{1-y}N$ QDs / $Al_xGa_{1-x}N$ (0001). IQE values between 50 % and 66 % were found at low temperature, combined with the ability to reach a PL integrated intensity ratio, between 300 K and 9 K, up to 75 % for GaN QDs and 46 % for $Al_yGa_{1-y}N$ QDs (versus 0.5 % in a similar quantum well structure emitting in the UVC range).

Finally, the demonstration of $Al_yGa_{1-y}N$ QD-based light emitting diode prototypes, emitting in the whole UVA range, using GaN and $Al_{0.1}Ga_{0.9}N$ QDs, and in the UVB range down to 305 nm with $Al_{0.2}Ga_{0.8}N$ QDs active regions, was shown.

Keywords: III-nitride, AlGaN, quantum dots, molecular beam epitaxy, ultraviolet

Résumé

Ce travail porte sur la croissance par épitaxie sous jets moléculaires (EJM) et sur les propriétés structurales et optiques de boîtes quantiques (BQs) $Al_yGa_{1-y}N$ insérées dans une matrice $Al_xGa_{1-x}N$ (0001). L'objectif principal est d'étudier le potentiel des BQs en tant que nouvelle voie pour la réalisation d'émetteurs ultraviolets (UV) efficaces.

Tout d'abord, nous avons étudié la croissance des BQs GaN en utilisant soit une source plasma (N_2, appelée PAMBE) soit une source ammoniac (NH_3, appelée NH_3-MBE) afin de choisir la meilleure approche pour former les BQs les plus efficaces. Il a été montré que le procédé de croissance est mieux contrôlé en utilisant l'approche PAMBE, conduisant à la croissance de BQs GaN avec des densités plus élevées, une meilleure uniformité en taille et des intensités de photoluminescence (PL) jusqu'à trois fois plus élevées. En outre, l'influence de la contrainte épitaxiale sur le processus d'auto-assemblage des BQs a été étudiée en fabriquant des BQs GaN sur différentes couche tremplins d'$Al_xGa_{1-x}N$ (avec $0,5 \leq x \leq 0,7$). Nous avons montré que des BQs avec des densités plus élevées et des hauteurs plus faibles sont formées en augmentant le désaccord de paramètre de maille (c.à.d en utilisant des tremplins avec x_{Al} plus élevé). Cependant, les mesures de photoluminescence (PL) indiquent un fort décalage de l'énergie d'émission vers le rouge lorsque x_{Al} augmente, en raison de l'augmentation de la discontinuité du champ électrique interne de 3 à 5,3 MV/cm.

Ensuite, des études approfondies sur les conditions de croissance et les propriétés optiques des BQs $Al_{0,1}Ga_{0,9}N$ / $Al_{0,5}Ga_{0,5}N$ ont été présentées, montrant les différents défis pour fabriquer des BQs efficaces. L'optimisation de la procédure de croissance, notamment l'étape de recuit post-croissance, a montré une modification de la forme des BQs. Plus précisément, un changement d'une forme allongée (pour un recuit à 740 °C), à une forme symétrique (pour un recuit à une température proche de ou supérieure à 800°C) a été observé. En plus, une bande d'émission supplémentaire vers les plus grandes longueurs d'onde a également été observée pour les BQs formées avec un recuit à 740°C. Cette bande a été attribuée à une fluctuation de composition des BQs, induisant la formation d'une famille additionnelle de BQs avec des hauteurs plus grandes et une compostions en Al inférieure à 10 %, estimée proche de l'alliage binaire GaN. Enfin, il a été démontré qu'en faisant un recuit à plus haute température ($\geq$ 800°C), l'émission de PL de cette famille supplémentaire de BQs (BQs riche en Ga ou (Al)GaN) diminue très fortement. De plus, cette étape de recuit impacte fortement la forme des BQs et a conduit à une amélioration de leur efficacité radiative d'un facteur 3. Ensuite, la variation de la composition en Al des BQs $Al_yGa_{1-y}N$ ($0,1 \leq y \leq 0,4$), ainsi que la quantité de matière déposée ont permis d'évaluer la gamme de longueurs d'onde d'émission accessibles. En ajustant les conditions de croissance, l'émission des BQs a été déplacée de l'UVA vers l'UVC, atteignant une émission autour de 270 - 275 nm (pour les applications de purification de l'eau et de l'air) avec des rendements radiatifs élevés. Les mesures de photoluminescence résolue en temps (TRPL), combinées avec les mesures de PL en fonction de la température, nous ont permis de déterminer les efficacités quantiques internes (IQE) des BQs GaN / $Al_xGa_{1-x}N$ (0001). Des valeurs d'IQE comprises entre 50 % et 66 % ont été obtenues à basse température, avec la possibilité d'atteindre un rapport d'intensité intégré de PL, entre 300 K et 9 K, allant jusqu'à 75 % pour les BQs GaN et 46 % pour les BQs $Al_yGa_{1-y}N$ (contre 0,5 % pour des structures équivalents à base de puits quantiques).

Enfin, nous avons montré la possibilité de fabriquer des DELs à base de BQs (Al,Ga)N couvrant une grande gamme de longueurs d'onde allant du bleu-violet jusqu'à l'UVB (de 415 nm à 305 nm).

Mots-clés: nitrures d'éléments III, AlGaN, boîtes quantiques, épitaxie sous jets moléculaires, ultraviolet